

## INFORMATION TO USERS

This manuscript has been reproduced from the microfilm master. UMI films the text directly from the original or copy submitted. Thus, some thesis and dissertation copies are in typewriter face, while others may be from any type of computer printer.

**The quality of this reproduction is dependent upon the quality of the copy submitted.** Broken or indistinct print, colored or poor quality illustrations and photographs, print bleedthrough, substandard margins, and improper alignment can adversely affect reproduction.

In the unlikely event that the author did not send UMI a complete manuscript and there are missing pages, these will be noted. Also, if unauthorized copyright material had to be removed, a note will indicate the deletion.

Oversize materials (e.g., maps, drawings, charts) are reproduced by sectioning the original, beginning at the upper left-hand corner and continuing from left to right in equal sections with small overlaps.

Photographs included in the original manuscript have been reproduced xerographically in this copy. Higher quality 6" x 9" black and white photographic prints are available for any photographs or illustrations appearing in this copy for an additional charge. Contact UMI directly to order.

Bell & Howell Information and Learning  
300 North Zeeb Road, Ann Arbor, MI 48106-1346 USA

**UMI**<sup>®</sup>  
800-521-0600



# Passive Radar Observations of the Aurora

by

Frank David Lind

A dissertation submitted in partial fulfillment of  
the requirements for the degree of

Doctor of Philosophy

University of Washington

1999

Program Authorized to Offer Degree: Geophysics

UMI Number: 9952861

Copyright 1999 by  
Lind, Frank David

All rights reserved.

UMI<sup>®</sup>

---

UMI Microform 9952861

Copyright 2000 by Bell & Howell Information and Learning Company.

All rights reserved. This microform edition is protected against  
unauthorized copying under Title 17, United States Code.

---

Bell & Howell Information and Learning Company  
300 North Zeeb Road  
P.O. Box 1346  
Ann Arbor, MI 48106-1346

© Copyright 1999  
Frank David Lind

In presenting this dissertation in partial fulfillment of the requirements for the Doctorial degree at the University of Washington, I agree that the Library shall make its copies freely available for inspection. I further agree that extensive copying of this thesis is allowable only for scholarly purposes, consistent with "fair use" as prescribed in the U.S. Copyright Law. Requests for copying or reproduction of this dissertation may be referred to University Microfilms, 1490 Eisenhower Place, P.O. Box 975, Ann Arbor, MI 48106, to whom the author has granted "the right to reproduce and sell (a) copies of the manuscript in microform and/or (b) printed copies of the manuscript made from microform."

Signature 

Date: 2 December 1999


University of Washington  
Graduate School

This is to certify that I have examined this copy of a doctoral dissertation by

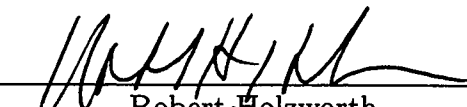
Frank David Lind

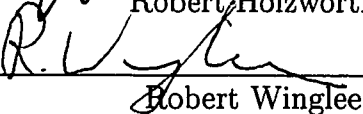
and have found that it is complete and satisfactory in all respects,  
and that any and all revisions required by the final  
examining committee have been made.

Chair of Supervisory Committee:

  
\_\_\_\_\_  
John David Sahr

Reading Committee:

  
\_\_\_\_\_  
Robert Holzworth

  
\_\_\_\_\_  
Robert Winglee

Date : 2 December 1999

University of Washington

Abstract

## Passive Radar Observations of the Aurora

by Frank David Lind

Chair of Supervisory Committee

Professor John David Sahr  
Electrical Engineering

In this dissertation I present the first observations of auroral E-region irregularities using a passive radar system. The Manastash Ridge Radar exploits commercial communications broadcasts to make radar observations. Compared to other contemporary radar techniques, passive radar provides significantly superior performance at a fraction of the cost. I have constructed the first passive radar system for non-defense applications.

I discuss observations of the August 27, 1998 geomagnetic event made using the radar. This event was simultaneously observed using the Ultraviolet Imager (UVI) on-board NASA's Polar spacecraft. I make a detailed comparison between the data from the radar and those from UVI. I then compute a lower bound for the current flowing in association with the observed auroral arc by combining data from the two instruments.

I also include the development of a three fluid theory for the E-region irregularities. Finally, I explore future directions in passive radar technology and ionospheric research.



# TABLE OF CONTENTS

<b>List of Figures</b>	<b>vi</b>
<b>List of Tables</b>	<b>xviii</b>
<b>Chapter 1: Introduction</b>	<b>1</b>
1.1 Motivation For This Work . . . . .	4
<b>Chapter 2: The Earth's Ionosphere</b>	<b>7</b>
2.1 Vertical Structure of the Ionosphere . . . . .	8
2.1.1 Neutral Composition . . . . .	9
2.1.2 Charged Particle Composition . . . . .	10
2.1.3 Plasma Parameters . . . . .	11
2.1.4 Conductivity . . . . .	17
2.2 Ionosphere Features . . . . .	19
2.2.1 Electrojets . . . . .	21
2.2.2 Coupling to the Magnetosphere . . . . .	22
<b>Chapter 3: The Ionospheric Two Stream Instability</b>	<b>24</b>
3.1 The Plasma Physics of the Two Stream Instability . . . . .	24
3.2 Linear Two Fluid Theories . . . . .	25
3.2.1 The Magnetic and Electric Field Geometries . . . . .	28
3.2.2 Ionospheric Two Stream Geometry . . . . .	30
3.2.3 The Ion Acoustic Speed . . . . .	31

3.2.4	The Irregularity Dispersion Relation . . . . .	32
3.2.5	The Instability Threshold . . . . .	34
3.3	Linear Kinetic Theories . . . . .	35
3.4	Nonlinear Theories . . . . .	36
3.4.1	Threshold Velocity and Phase Velocity Saturation . . . . .	36
3.4.2	Wave Heating . . . . .	37
3.4.3	Secondary Wave Generation . . . . .	38
3.4.4	Spectral Characteristics . . . . .	38
3.4.5	Anomalous Wave Velocities . . . . .	39
3.5	Simulations . . . . .	40
3.6	Additional Theoretical Issues . . . . .	40
3.6.1	Irregularity Electromagnetic Scattering . . . . .	41
3.6.2	Wave Generation Mechanisms . . . . .	41
3.6.3	The Importance of Inhomogeneities . . . . .	42
3.6.4	Multiple Ion Species and Dusty Plasmas . . . . .	42
<b>Chapter 4:</b>	<b>Observations of Auroral E-region Irregularities</b>	<b>43</b>
4.1	E-region Irregularity Experimental Radar Observations . . . . .	46
4.1.1	Irregularity Altitudes . . . . .	47
4.1.2	Irregularity Amplitudes . . . . .	49
4.1.3	Spectral Types . . . . .	49
4.1.4	Watermann Distributions . . . . .	50
4.1.5	Aspect Sensitivity . . . . .	51
4.1.6	Flow Angle Sensitivity . . . . .	53
4.1.7	Instability Threshold Conditions . . . . .	54
4.1.8	Saturation Velocity . . . . .	55
4.1.9	Spectral Shape . . . . .	56

4.1.10	Irregularity Energy Dissipation . . . . .	57
4.1.11	Seasonal and Solar Cycle Dependence . . . . .	58
4.2	Other Experiments . . . . .	58
4.2.1	Rocket Experiments . . . . .	59
4.2.2	Laboratory Experiments . . . . .	60
 <b>Chapter 5: A Three Fluid Model for Auroral E-region Irregularities</b>		 <b>62</b>
5.1	The Relation to Type-3 Irregularities . . . . .	62
5.2	Two Ion Species . . . . .	64
5.3	Three Fluid Dispersion Relation . . . . .	65
5.3.1	The Model Ionosphere . . . . .	68
5.3.2	Model Parameter Sweeps . . . . .	68
5.4	A Brief Interpretation . . . . .	87
5.5	The Production of Type-3 Waves . . . . .	89
 <b>Chapter 6: Radar Methods for Observing E-Region Irregularities</b>		 <b>90</b>
6.1	The Coherent Scatter Radar . . . . .	90
6.2	Theory of Observations . . . . .	91
6.2.1	Radar Technique . . . . .	92
6.2.2	Radar Resolution . . . . .	95
6.2.3	The Bragg Scattering Condition . . . . .	97
6.2.4	Irregularity Bandwidth and Aliasing . . . . .	100
6.3	Typical Radar Observations . . . . .	101
6.4	Typical Operating Configurations . . . . .	102
 <b>Chapter 7: The Manastash Ridge Radar</b>		 <b>104</b>

7.1	Passive Radar Systems . . . . .	104
7.2	Overview of the Manastash Ridge Radar . . . . .	105
7.2.1	Radar Field of View . . . . .	107
7.2.2	Properties of FM Radio Signals . . . . .	107
7.2.3	FM Radio Signal Variance . . . . .	114
7.2.4	The Challenges of Passive Radar . . . . .	115
7.3	Radar Capabilities and Performance . . . . .	119
7.3.1	Radar Sensitivity . . . . .	120
7.3.2	Radar Range Resolution . . . . .	120
7.3.3	Radar Velocity Resolution . . . . .	121
7.3.4	Radar Time Resolution . . . . .	122
7.3.5	Range and Velocity Aliasing . . . . .	122
7.3.6	Comparison to Other Coherent Scatter Radars . . . . .	122
7.4	Early Radar Observations . . . . .	123
<b>Chapter 8: Passive Radar Observations of E-Region Irregularities</b>		<b>126</b>
8.1	First Irregularity Observations . . . . .	126
8.1.1	Irregularity Spectral Fitting . . . . .	127
8.1.2	Irregularity Probable Location Maps . . . . .	136
8.1.3	Inferred Electric Field . . . . .	137
8.2	Summary of Observations . . . . .	141
<b>Chapter 9: Analysis of the August 27, 1998 Event</b>		<b>142</b>
9.1	Magnetometer Observations . . . . .	142
9.2	Ultraviolet Imager Observations . . . . .	142
9.2.1	UVI Photon Flux and Radar Data Comparison . . . . .	144
9.2.2	UVI and MRR View Line Cross-sections . . . . .	149

9.2.3	UVI Estimated Conductivity and MRR Vector Electric Field .	150
9.3	Ionospheric Current Density Estimate . . . . .	154
<b>Chapter 10:</b>	<b>Future Directions and Conclusion</b>	<b>161</b>
10.1	Passive Radar . . . . .	161
10.2	Conclusion . . . . .	165
<b>Bibliography</b>		<b>168</b>
<b>Appendix A:</b>	<b>Derivation of a 3-Fluid Model for Auroral E-region Ir-</b>	
	<b>regularities</b>	<b>205</b>
A.1	Assumptions . . . . .	205
A.2	Initial Equations . . . . .	206
A.3	Perturbed Equations . . . . .	208
A.3.1	Continuity Relations . . . . .	208
A.3.2	Ion Momentum Equations . . . . .	209
A.3.3	Electron Momentum Equations . . . . .	211
A.4	The Three Fluid Dispersion Relation . . . . .	214
<b>Appendix B:</b>	<b>The Manastash Ridge Radar Design</b>	<b>217</b>
B.1	Antenna Design . . . . .	217
B.2	Receiver Design . . . . .	218
B.3	Data Acquisition and Transport . . . . .	220
B.4	Signal Processing . . . . .	220
B.5	Computational Systems . . . . .	222
B.6	Software Systems . . . . .	223

## LIST OF FIGURES

2.1	An electron density profile for the Earth's ionosphere. This profile is computed from the International Reference Ionosphere (1995). Local electron density maxima can be seen in the E-region (100 km), and the F-region (300 km). . . . .	9
2.2	The primary composition of the neutral gas in the Earth's Ionosphere. This profile is from the MSIS-E-90 upper atmosphere model. . . . .	10
2.3	The ion composition of the Earth's Ionosphere. The four primary ion species are shown from the IRI-95 model. . . . .	11
2.4	Electron plasma frequency for the ionosphere as a function of altitude. This parameter is computed from the IRI-95 and the International Geomagnetic Reference Field Model (IGRF). The peak plasma frequency corresponds to the peak ionospheric electron density. . . . .	12
2.5	The ion and electron gyrofrequencies as a function of altitude as computed from the IRI-95 and IGRF models. . . . .	13
2.6	Ionospheric collision frequencies as a function of altitude. The collisions with the neutral gas dominate all other types of collisions at ionospheric altitudes. These collision frequencies are computed from the MSIS-E-90 model. . . . .	14
2.7	Model ionospheric ion and electron temperatures as a function of altitude as derived from IRI-95. The temperature of the ions and electrons can vary greatly as ionospheric conditions change. . . . .	15

2.8	Ionospheric gyro-collision coefficients computed from the IRI-95 and IGRF models. . . . .	16
2.9	The Specific, Pedersen, and Hall conductivities of the Earth's Ionosphere for undisturbed conditions, computed from the IRI-95 and IGRF models. . . . .	18
2.10	The Specific, Pedersen, and Hall conductivities of the lower E-region, computed from the IRI-95 and IGRF models. The Hall conductivity exceeds the Pedersen conductivity in the E-region. . . . .	19
2.11	A schematic of structures in the Earth's ionosphere as a function of latitude. The auroral zone is typically between 60° and 70° and the equatorial zone is between +/- 10°. The shaded portion of the diagram indicates the night side of the Earth and the arrows denote the typical convection direction. . . . .	20
2.12	An idealized northern hemisphere ionosphere convection pattern. Dashed lines denote the convection direction while the shaded arrows indicate the ionospheric electric field direction responsible for the convection. Latitude is denoted by the circles and notations indicating magnetic local time surround the outermost circle. A typical cross polar cap potential associated with this pattern is 80 kV. . . . .	22
2.13	The Earth's Ionosphere is coupled to the larger space environment as is shown in this cartoon looking at the Earth's equator. The sun is on the left hand side and the solar wind flows past the Earth at velocities between 400 and 1000 m/s. Currents are generated in the Earth's magnetosphere due to this flow and some of these currents close in the ionosphere. . . . .	23

3.1	The electric and magnetic field structure of the northern auroral ionosphere as a function of altitude. Field aligned currents flow down magnetic field lines to close in the E and F regions. The electric field drives ionospheric convection and drives a Hall current in the E-region. . . . .	29
3.2	The geometry of the two stream instability in the northern auroral E-region. The drift velocity $V_d$ is created by the $E \times B$ drift. The vector $\mathbf{k}$ denotes the wave vector of the irregularities generated by the instability for a sufficiently strong electric field. . . . .	30
3.3	The ion acoustic velocity as a function of altitude for a typical high latitude E-region ionosphere. This profile was computed from the IRI-95 model ionosphere. . . . .	32
4.1	The Watermann distribution of E-region irregularities from the Cornell University Portable Radar Interferometer (CUPRI), a 50 MHz pulse mode radar system (Sahr 1999, personal communication). The plotted data is from the ERRRIS-2 experiment conducted in northern Scandinavia in 1989 [Pfaff, et al., 1992]. . . . .	52
5.1	The geometry used for the one dimensional three fluid model. In the model the perturbations are assumed to be constrained to the $\hat{y}$ direction, the ambient electric field is in the $\hat{x}$ direction, and the magnetic field is downward in the $-\hat{z}$ direction. This configuration is appropriate for the northern auroral E-region ionosphere. . . . .	66
5.2	The phase velocity predicted by the three fluid model for variations in electron drift velocity. . . . .	69



5.3	The growth rate predicted by the three fluid model for variations in electron drift velocity. . . . .	70
5.4	The phase velocity predictions for variations in irregularity wavelength. . . . .	71
5.5	The growth rate predictions for variations in irregularity wavelength. . . . .	72
5.6	Model predictions of the phase velocity for variations in the ratio of the ion masses. One ion species, $NO^+$ , is held fixed while the mass of the other is varied. . . . .	73
5.7	Model predictions of the growth rate for variations in the ratio of the ion masses. One ion species, $NO^+$ , is held fixed while the mass of the other is varied. . . . .	74
5.8	Phase velocity predictions for variations in the electron plasma density. The ion plasma density is varied to maintain quasi-neutrality assuming a 50-50 mix of both ion species. . . . .	75
5.9	Growth rate predictions for variations in the electron plasma density. The ion plasma density is varied to maintain quasi-neutrality assuming a 50-50 mix of both ion species. . . . .	76
5.10	The phase velocity predictions for variations in the fraction of one ion species relative to another. The lack of variation points to a possible flaw in the model. . . . .	77
5.11	The growth rate predictions for variations in the fraction of one ion species relative to another. The lack of variation points to a possible flaw in the model. . . . .	78
5.12	Model phase velocity predictions due to electron temperature variations. . . . .	79
5.13	Model growth rate predictions due to electron temperature variations. . . . .	80
5.14	The phase velocity variations due to the ion temperature sweep. . . . .	81

5.15	The growth rate variations due to the ion temperature sweep. . . . .	81
5.16	The phase velocity predicted by the model for variations in the electron-neutral collision frequency. . . . .	82
5.17	The growth rate predicted by the model for variations in the electron-neutral collision frequency. . . . .	83
5.18	The model predictions of the phase velocity variation for a sweep of the ion-neutral collision frequency. The mode 1 velocity varies substantially as the ion-neutral collision frequency increases. . . . .	84
5.19	Model predictions of the growth rate variation for a sweep of the ion-neutral collision frequency. The mode 3 growth rates becomes weakly damped at high and low collision frequencies. . . . .	85
5.20	The phase velocity predictions of the three fluid model for an altitude sweep through a model ionosphere. . . . .	86
5.21	The growth rate predictions of the three fluid model for an altitude sweep through a model ionosphere. . . . .	87
6.1	The coherent scattering geometry in the northern hemisphere. Here a radar system illuminates the E-region ionosphere from the south. Irregularities in the E-region will scatter the radar signal allowing their detection. The auroral zone can move north and south somewhat due to changing ionospheric conditions. . . . .	91
6.2	The cross-section of the irregularities is strongly anisotropic relative to the Earth's magnetic field and very large compared to the cross-section for incoherent scatter. . . . .	92
6.3	The computed self ambiguity of a 1 ms pulse at 100 MHz. A single pulse provides a broad ambiguity that does not localize targets particularly well. . . . .	96

6.4	The computed self ambiguity of a random sequence for 0.125 seconds of data with a $4 \mu s$ baud length. The ambiguity is very compact and thus random codes make good radar waveforms. . . . .	97
6.5	The Bragg scattering geometry is shown for multistatic and backscatter geometries. The periodic density perturbations of the E-region irregularities forms a scattering lattice for the incident transmitter signal $\mathbf{k}_{tx}$ . The scatter occurs obeying energy and momentum conservation and results in a signal that returns to the receiver $\mathbf{k}_{rx}$ coherently. . . . .	98
6.6	The typical irregularity classification scheme that is used by coherent scatter radars consists of four irregularity types. The division into these classes is useful for discussing observations but is poorly motivated. . . . .	101
7.1	A typical passive radar system is shown for a multistatic configuration. The commercial FM broadcasts are intercepted to provide a reference signal. Scatter from the irregularities is then detected in a radio quiet environment created by favorable topography. . . . .	105
7.2	The Manastash Ridge Radar consists of two coherent digitizing receivers. The receivers and digitizers are synchronized using the global positioning satellite system. Data is transfered over the Internet to a central location where it is processed using a cluster computer. . . .	106

7.3	The view volume of the Manastash Ridge Radar in the Pacific Northwest. The transmitter and receiver sites are indicated on the diagram along with circles of multistatic range at 200 km intervals. The arrow points in the direction of magnetic north and the solid lines indicate the typical beamwidth of the antenna systems. The inner lines correspond to the +14 dB Yagi antenna, while the outer lines represent the +6 dB Log Periodic antenna. Contours of magnetic aspect angle are shown on the diagram with the 90° contour indicating the multistatic backscatter geometry. . . . .	108
7.4	The structure of an FM radio signal is complicated due to stereo modulation and optional data sidebands. The pilot carriers are suppressed and most of the signal energy is carried in the central channel. . . .	109
7.5	Plotting the inphase (I) and quadrature (Q) components of a received FM radio signal. The circle results from the constant amplitude (modulus) nature of the FM signal and the spread in the circle is due to variations in the transmitter, multi-path scatter, scattered targets, and receiver imperfections. . . . .	110
7.6	An FM radio power spectrum for 5 seconds of integration on 99.9 MHz. For long integrations the signal often appears to have a roughly Gaussian shape. . . . .	111
7.7	The FM radio spectrum versus time for 1 second of data. Substantial variation in the FM radio waveform creates the unique pattern that makes the signal work well for radar applications. . . . .	112
7.8	The self ambiguity of an FM radio signal for 10 seconds of integration. The globally compact ambiguity strongly resembles that of a random code and allows targets to be localized in range and velocity. . . .	113

7.9	Radar observations made with the Manastash Ridge Radar system have a unique ground clutter signature due to the presence of Mt. Rainier. This is a large mountain that is visible to both the transmitter and the remote receiver. . . . .	124
7.10	Occasionally the radar observes strong returns localized to a very small range and doppler extent. Some of these are aircraft and their range migration is consistent with their doppler velocities. . . . .	125
8.1	Two five second integrations of Manastash Ridge Radar data beginning at 09:52:34 UT on August 27, 1998. Here irregularities are visible over a range extent of 400 km. . . . .	128
8.2	Later in the August 27, 1998 event from 10:08:34 until 10:11:34 UT the irregularities appear at 600 km and appear to move away from the radar to 800 km. . . . .	129
8.3	Between 10:12:34 and 10:15:34 UT on August 27, 1998 the scatter from the irregularities intensifies considerably in two regions which appear to merge and fade away as time progresses. . . . .	130
8.4	After 10:16:34 UT the irregularities are barely detectable and the strongest portion of the August 27, 1998 event has passed. . . . .	131
8.5	Four consecutive one second integrations of Manastash Ridge radar data from the August 27, 1998 event. The irregularities are detectable in the radar data even with this short integration time. . . . .	132
8.6	The irregularities are plotted here on a linear scale for several ranges and times. This is how many other coherent scatter radars have displayed their data. The Manastash Ridge Radar's resolution is too high for this to be particularly effective. . . . .	133

8.7	In fitting a Gaussian spectral model to the irregularities the fitter often underestimates the peak amplitude of the data and over estimates the spectral width. Here the solid line is the model fit while the dashed line with circles represents the radar data. . . . .	134
8.8	The velocity-width distribution of the fitted Manastash Ridge Radar data from the August 27, 1998 event. This is also known as a Watermann distribution, and is a useful method for comparing data between radar systems. . . . .	135
8.9	The inferred probable location of the irregularities for all the data from the August 27, 1998 event. Only the right hand mapping of the data is shown as this is the likely one based on the radar view volume and comparison to other data. . . . .	137
8.10	A sequence of probable location maps for the irregularities observed during the August 27, 1998 event. Both the left and right mappings are shown. . . . .	138
8.11	A lower bound electric field magnitude along the radar view line for data from the August 27, 1998 event. The left and right mappings are shown, and the field appears relatively constant throughout the whole event. . . . .	140
8.12	A map of the vector electric field direction as inferred by the radar is shown for radar data from the August 27, 1998 event. Both the left and right mappings are shown. The electric field estimates are lower bounds. . . . .	140

9.1	August 27, 1998 magnetometer observations for two locations near to the Manastash Ridge Radar. The Newport magnetometer is located to the northeast of the radar under the view volume, while the Victoria magnetometer is located outside of the view volume to the northwest. . . . .	143
9.2	On August 27, 1998 the Ultraviolet Imager (UVI) aboard NASA's Polar spacecraft made observations of strong auroral emissions coincident with radar observations of E-region irregularities. . . . .	144
9.3	The observations from UVI are mapped onto the Manastash Ridge Radar's view volume in geographic coordinates. The fitted radar data is overlaid for the right hand mapping. The circle size indicates the relative strength of the irregularities. Note that the imager's filter cycles through LBHL, LBHS, 1304, and 1356 during the course of the observations. . . . .	147
9.4	The simultaneous observations from UVI and MRR are mapped onto the radar view volume. Here the irregularities are plotted using the left hand mapping. . . . .	148
9.5	Radar data from 10:14:34 UT matches the observed imager data from 10:15:13 UT better than radar data from 10:15:34 UT. This may be due to the imager integrating over changes in the aurora that the radar detects. . . . .	149
9.6	A comparison of velocity integrated radar data to UVI photon emissions along the presumed radar view line. Both the left and right hand mappings are given for 10:09:34 until 10:12:34 UT. Some structures are clearly observed by both the imager and radar while others are not. . . . .	151

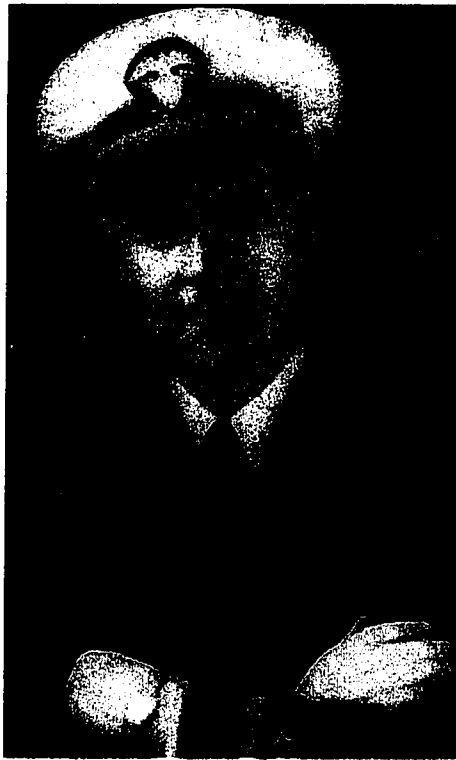
9.7	The velocity integrated radar data is compared to the UVI photon emissions along the presumed radar view line. Both the left and right hand mappings are given for 10:13:34 until 10:15:34 UT. The imager data from 10:15:13 UT is compared to radar data before and after the UVI observations. . . . .	152
9.8	UVI estimated Hall conductance (height integrated conductivity) for four times during the August 27, 1998 event. The vector electric field inferred by the radar for each period where irregularities were observed is overlaid using the right hand mapping. This mapping corresponds to the regions of greatest Hall conductance. . . . .	153
9.9	The UVI estimated Pedersen conductance for four times during the August 27, 1998 event. The vector electric field inferred by the radar is overlaid using the right hand mapping. . . . .	154
9.10	A combination of the UVI and MRR data allows a lower bound estimate of the Hall current density flowing in the ionosphere to be made along the radar view line for two periods during the event. . . . .	156
9.11	The vector current density can be overlaid on the UVI Hall conductance estimate and the radar view volume. . . . .	157
9.12	The lower bound magnitude of the Pedersen current is estimated to be an order of magnitude smaller than the Hall current along the radar view line. . . . .	158
9.13	The vector direction and magnitude of the Pedersen current density is overlaid on the UVI Pedersen conductance estimate and the radar view volume. . . . .	159



10.1	A national map of FM radio stations from the Federal Communications Commission database. Each dot on the map represents a single FM radio station. . . . .	164
B.1	The antenna pattern for the log periodic antenna used by the Manastash Ridge Radar. . . . .	218
B.2	The radar receiver design. . . . .	219
B.3	Blocks of raw data from the receivers are corrected by removing the mean and ensuring that the I and Q channels are orthogonal. . . . .	221
B.4	Each range of data is processed by forming the received sequence for a given range offset, decimating to a desired signal bandwidth, evaluating the correlation using the Fast Fourier Transform, and finally incoherently integrating. . . . .	221
B.5	The software for the Manastash Ridge Radar is divided between the receiver control computers and the radar operations server. Data processing and output is done on a cluster computer under the control of Perl scripts. The network time protocol and external web servers are not shown. . . . .	225

## LIST OF TABLES

4.1	Radar observations of E-region irregularities . . . . .	48
5.1	An overview of wave modes predicted by the three fluid theory. . . . .	67
7.1	A comparison of several modern VHF coherent scatter radars . . . . .	123
B.1	Useful software tools . . . . .	223



In memory of my grandfather Ralph Presley Lind.

## ACKNOWLEDGMENTS

Foremost I would like to thank my family for their love and support from the very beginning. In particular I would also like to thank my grandmother, Jane D. Lind, for all her efforts on my behalf.

I would like to thank my advisor John David Sahr for developing the idea of passive radar systems, obtaining support for this research, and for having had the courage to let a graduate student take on the project. My work has been all the richer for John's unselfish advice, friendship, and for the many things he has taught me that go well beyond radio science.

Special thanks to Jeff Morgan of the University of Washington Astronomy Department for his help and efforts at the Manastash Ridge Observatory.

Extra special thanks to the many Geophysics faculty who have helped me along the way, especially Robert Winglee, Bob Holzworth, George Parks, Marcia Baker, and John Ely.

Double extra special thanks to Dawn M. Gidner for her help, good humor, and for the development of a superb radar antenna.

I would also like to thank Damien Chua and Mitch Brittnacher of the UVI science team for providing me with data from the UVI imager for the August 27, 1998 event.

To the many graduate students present and past who have been my friends, helpers, and teachers you have my gratitude and my best wishes.

This work has been supported by the National Science Foundation, the Air Force Office of Scientific Research, and the Intel Corporation.

## Chapter 1

### INTRODUCTION

The earliest predictions of a conducting region at the top of the atmosphere are attributed to Gauss and Lord Kelvin in the mid 1800s [Bone, 1991]. These predictions did not draw much attention or take on practical importance until the development of radio in the 20th century.

With Marconi's initial radio communication across the Atlantic ocean in 1901 it became necessary to explain in detail the manner in which radio waves propagated in the Earth's atmosphere. The initial explanation given by Oliver Heaviside, that a layer of ionization in the upper atmosphere was responsible for the reception of radio waves at great distances, laid the foundation for the investigations that have produced our modern understanding of the ionosphere.

Scientific investigation of the ionosphere is driven by experimental observations of ionospheric motion, composition, conductivity, and field structure. These basic physical properties allow detailed models to be constructed that explain ionospheric phenomenon in terms of neutral gas dynamics, plasma physics, and chemistry.

To accomplish the measurements necessary to probe the ionosphere's behavior, many experimental techniques have been developed. These include numerous methods of ground based remote sensing, *in situ* techniques using satellites and sounding rockets, and satellite based remote sensing techniques using imagers, beacons, and top-side radio sounders.

Early investigations of ionospheric processes and structure were made using the innovation of the ionosonde [Breit and Tuve, 1926]. This type of radio sounder makes observations of the ionospheric electron density below an altitude limited

by the electron density peak. These systems operate between 1 and 30 MHz and make regular observations around the world every day.

The initial radio investigation of the ionosphere was continued and expanded upon following World War II. The most important development is probably the incoherent scatter radar [*Gordon, 1958, Bowles, 1958*]. This powerful type of instrument scatters radio waves from the thermal fluctuations in the electron population of the ionosphere through a process known as Thomson scatter. Such radars require very large antennas and extremely powerful transmitters, with the typical unit of merit for these systems being the MW-acre. Incoherent scatter radars provide many useful parameters: the electron density and temperature, the ion density of major species, electric fields, and convection velocities. Because of the high frequency at which these systems operate, they are able to profile the ionosphere at altitudes above the F-region peak which are inaccessible to the ionosonde.

It was realized early on that certain sections of the ionosphere sometimes presented extremely large scattering cross sections to radio waves at wavelengths on the order of a few meters. This fact has been exploited by radio amateurs for many years to transmit signals over great distances when the opportunity presents itself.

The first radar observations of this phenomenon were reported by *Eckersley* [1937]. He performed a surprisingly sophisticated experiment using radar interferometry at 9 MHz to determine that the irregularities he detected were located between 105 and 120 km in altitude. The association of the irregularities with the aurora was soon determined by *Harang and Stoffregen* [1938] who made backscatter observations in Norway at two frequencies simultaneously.

These early observations were interesting enough that many experiments have been conducted to observe the "radio aurora." The instrument that has been produced to make these measurements is the coherent scatter radar. These radars typically have transmitter powers on the order of a few tens of kW and relatively

small antenna systems. Functionally they are very similar to the incoherent scatter radar, but the lower transmitter powers and smaller antennas make them significantly less sensitive. Many incoherent scatter radars also make observations of the irregularities by substantially reducing their transmitter power, or even through inadvertent detection in the antenna side lobes. The reduced power is necessary because scatter from the irregularities will saturate the receivers when these systems are at full power. Thus incoherent scatter radars can also operate in a coherent scatter mode, usually at UHF frequencies.

Using coherent scatter radar E-region irregularities have been observed at the equator, in the auroral regions surrounding the Earth's poles, and occasionally at mid-latitudes. The experiments have allowed a number of basic facts to be determined. These include the electric field conditions necessary for the irregularity production, their characteristic alignment relative to the Earth's magnetic field, the extraordinary size of their scattering cross section, and their typical velocities and spectral shapes.

*Farley [1963a]* provided the first detailed theoretical explanation for the irregularities seen at the equator as the result of a streaming instability between electrons and ions. This physical interpretation correctly explains the general details of the radar observations. Many authors have expanded upon this basis and several good reviews of irregularity theory and experiment can be found in the literature [*Sahr and Fejer, 1996; Hanuise et al., 1993; Haldoupis, 1989; Keskinen and Ossakow, 1983*].

E-region irregularities are a natural example of nearly two dimensional plasma wave turbulence. They are initiated when sufficiently strong electric fields cause electrons to drift through ions at a speed which exceeds the local plasma sound speed. This situation is unstable because in most cases the sound speed is the fastest that linear density perturbations can propagate in a fluid. Waves are generated by

this super-acoustic motion converting energy from the flow to density perturbations which propagate out from the source of the disturbance.

The location of the irregularities is limited in altitude to the E-region of the ionosphere by increasing collisions with the neutral gas below, and by an increasing temperature, decreasing ion neutral collision frequency, and ion magnetization above. Ionospheric irregularities are observed at the equator in association with the equatorial electrojet, occasionally at mid-latitudes as sporadic-E, and frequently at auroral latitudes in association with the auroral electrojet.

The waves in the auroral zones are the result of electric fields created in the magnetosphere, a region of space surrounding the Earth. These electric fields are generated by the convection of solar wind plasma past the Earth's magnetic field. The associated distortion of the magnetosphere generates current systems. These current systems must form a closed circuit and some of them close within the Earth's ionosphere. The currents create the aurora through the precipitation of charged particles, they transfer energy to the ionosphere, and the ionospheric electric fields and convection patterns are a strong reflection of the magnetospheric conditions.

### ***1.1 Motivation For This Work***

The driving motivation of this work is to develop a new experimental technique called passive radar. In particular this technique allows for observation of the E-region irregularities at dramatically lower cost and with substantially higher performance than previous coherent scatter radar systems. By its very nature the technique also provides access to wavelengths currently used by commercial communications systems that are normally unavailable for use in radar applications. This is useful because theories of the irregularities often make predictions of their physical properties as a function of irregularity wavelength. An ability to probe the irregularities at new wavelengths allows for a more revealing comparison between



experiment and theory.

Using passive radar, the plasma physics of E-region irregularities can be investigated in the meter scale wavelength regime where the irregularity physics transitions from a plasma fluid behavior to a kinetic regime. At this length scale the nonlinear wave particle interactions begin to inhibit wave growth and dissipate energy within the system. The unprecedented spatial and velocity resolution provided by passive radar also allows for the investigation of the irregularities produced by spatial structures in the ionosphere having kilometer scales. Understanding the occurrence and behavior of the irregularities is also necessary for determining how energy from the magnetospheric current systems is dissipated within the ionosphere, as well as when and where this occurs.

In particular I am motivated to study E-region irregularities using the first observations made with the Manastash Ridge Radar. This is the first passive radar system for non-defense applications. The system uses a single FM radio station as its signal source, with a frequency of 99.9 MHz being typical. The observations I have taken of 1.5 meter E-region irregularities are the first reported in the literature, and are the most recent observations between the typical 1 m and 3 m scales since 1.3 m observations of the Antarctic auroral electrojet in 1994 [Ogawa, 1996].

These new radar observations demonstrate the efficacy of the passive radar technique as well as the potential for future applications. In addition to the novelty of the method by which these observations were made, the physical conditions which produced the irregularities and the ionosphere's response to them are also extremely interesting.

The events associated with these irregularity observations occurred August 27 1998, during an extraordinarily strong geomagnetic disturbance. This is a very fortunate event in that a great deal of contextual information is available from satellite based instrumentation. I analyze the radar results from this event in the

context of ionospheric plasma physics and the available satellite observations. In particular I examine the location of the irregularities relative to the auroral emissions seen by the Ultraviolet Imager, and I combine data from this imager and the radar to estimate the current flowing in association with the auroral arc.

In addition to the discussion of the radar and the observations made using it, I include some theoretical developments related to the generation of the E-region irregularities that help to explain the wide range of velocities observed by coherent scatter radar systems. In particular, this three fluid theory can explain waves whose velocity is substantially below the local ion acoustic speed. This speed is the lower limit of the wave velocity in the traditional linear fluid theory of the irregularities. By accounting for the equal presence of  $NO^+$  and  $O_2^+$  in the E-region of the ionosphere it is possible to produce a new wave mode whose properties correspond to a wider range of radar observations than has previously been possible.

## Chapter 2

### THE EARTH'S IONOSPHERE

The ionosphere is the region of charged particles that forms in the upper portion of the Earth's atmosphere. This region surrounds the Earth and extends upward from about 80 km in altitude, where the production of ionization by solar ultraviolet light substantially exceeds the recombination rate during the day. At its upper boundary the ionosphere transits smoothly from a region where collisions with the neutral gas are primarily dominant to a regime where the plasma physics of charged particle corotation with the Earth is most important.

Traditionally the ionosphere has been divided into a series of layers: the D-region, the E-region, and the F-region. This nomenclature was introduced by Appleton in 1924 who discovered the F-region. He renamed the Heaviside layer the E-region because the letter E was used to denote the electric field of a radio wave reflected from that layer. In his theory F was used to denote the same field when reflected from the newly discovered Appleton layer and so he named it the F-region. This left room above and below for new layers as they were discovered and it led naturally to naming the D-region which is just below the E-layer [*Ratcliffe, 1970*].

While the boundaries between the layers are not always physically distinct, it is possible to ascribe physical significance to each layer. The D-region, below 90 km is a region of mainly molecular ions where the physics is dominated by collisions with the neutral gas, primarily  $N_2$ . This layer is characterized by the tendency of radio waves to be absorbed there due to a combination of the moderate electron densities and high collision frequencies. The E-region, between 90 and 180 km, is a transitional region where the electrons become effectively collisionless while the ions

are still dominated by their collisions with the neutral gas. The E-region is composed primarily of molecular ion species with  $NO^+$  and  $O_2^+$  being equally dominant. The F-region, which lies above the E-region is where both the ions and the electrons are collisionless, i.e. the collisions with the neutral gas are much less frequent than the gyration of the particles around the geomagnetic field lines. This region of the ionosphere is composed primarily of atomic ions with  $O^+$  being the primary species at low altitudes and with  $H^+$  becoming dominant around 1000 km.

Due to the longer recombination times of the atomic ion species, the F-region experiences substantially less variation in electron density during the diurnal variation of solar ultraviolet radiation. The faster recombination of the molecular ion species below 150 km leads to the D and E layers effectively disappearing at night in the absence of other ionization sources. In the auroral ionosphere energetic particle precipitation often creates substantial ionization in the D and E layers.

## **2.1 Vertical Structure of the Ionosphere**

The ionospheric electron density profile shown in Figure 2.1 is a model profile (IRI-95 [Bilitza *et al.*, 1993]) for a mid-latitude quiet daytime ionosphere. This is a typical case but it should be understood that the ionosphere is a highly variable system with transient, diurnal, and solar cycle variations.

The most prominent feature visible is the F-region peak in the electron density, which results from the increasing neutral gas density with depth into the atmosphere, and the decreasing flux of solar ultraviolet radiation due to its absorption at higher altitudes. The E-region is then visible further down in altitude prior to a smooth decrease in electron density for the D-region at the very bottom of the ionosphere.

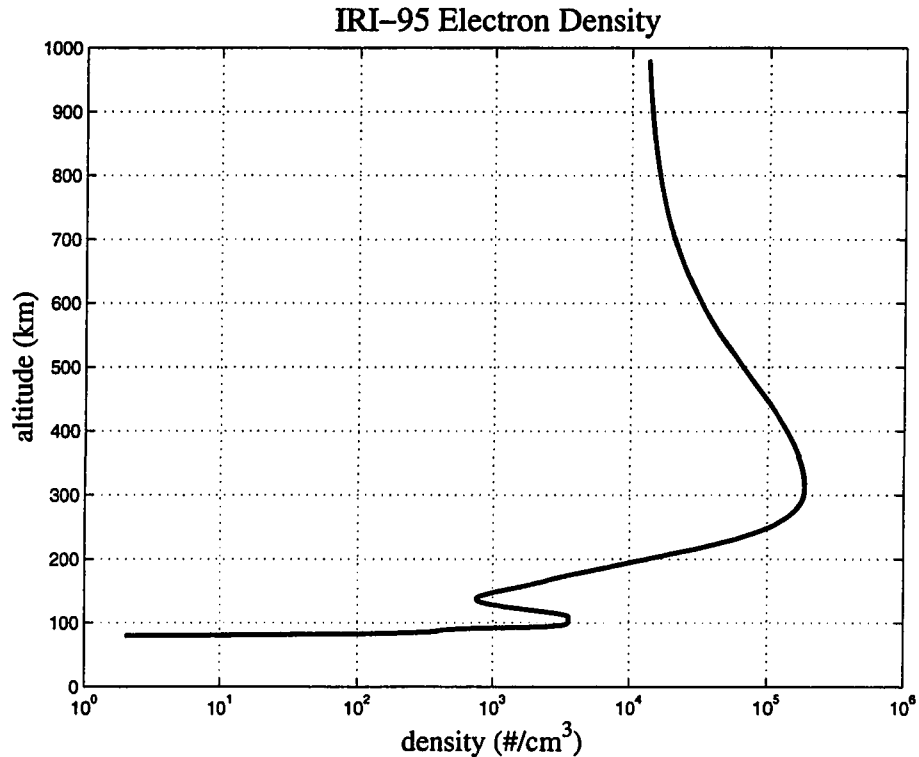


Figure 2.1: An electron density profile for the Earth's ionosphere. This profile is computed from the International Reference Ionosphere (1995). Local electron density maxima can be seen in the E-region (100 km), and the F-region (300 km).

### 2.1.1 Neutral Composition

The composition of the neutral gas atmosphere as a function of altitude is shown in Figure 2.2 from the MSIS-E-90 atmospheric model [Hedin, A. E., 1991]. Nitrogen ( $N_2$ ) dominates up to about 200 km, and Oxygen (O) is the primary neutral species at higher altitudes. Substantial amounts of other species such as  $O_2$ , Ar, and He are also present in the E and F-regions.

The neutral species which are present in the ionosphere provide a source for the ions and electrons and determine the chemistry of their recombination. This chemistry directly effects ionospheric dynamics. For example, the disappearance of the D and E-regions during the night is due to the shorter recombination times

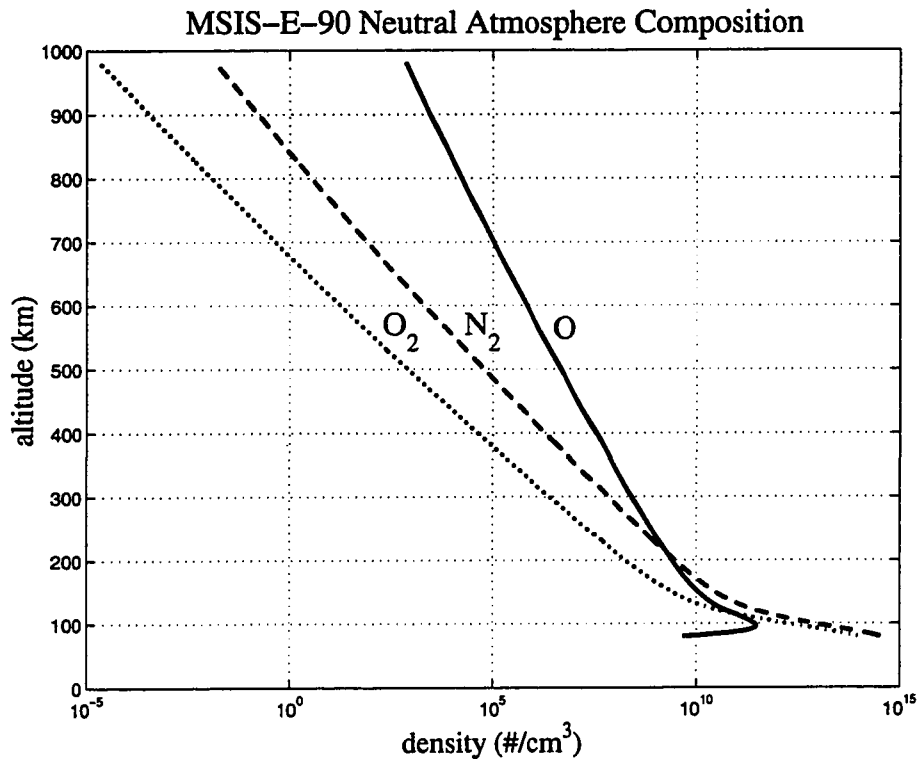


Figure 2.2: The primary composition of the neutral gas in the Earth's Ionosphere. This profile is from the MSIS-E-90 upper atmosphere model.

scale of molecular ion species. This demonstrates quite clearly that the atmospheric chemistry of the ionosphere can play an important role on relatively short time scales.

The neutral atmosphere also impacts the behavior of the ionosphere significantly through the role that neutral winds, tides, and gravity waves play. These neutral gas motions can directly influence the plasma in the lower ionosphere by convecting plasma, modulating densities and temperatures, and creating density gradients.

### 2.1.2 Charged Particle Composition

The role of charged particles is of great importance to the properties of the ionosphere. A typical profile showing the predominant ion species in the ionosphere is

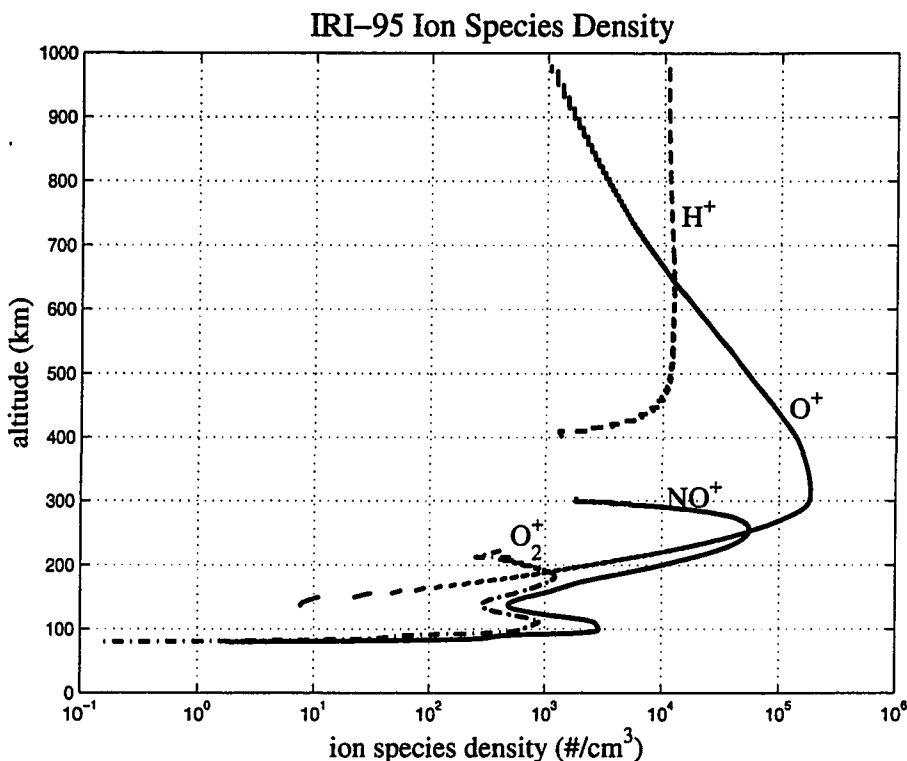


Figure 2.3: The ion composition of the Earth's Ionosphere. The four primary ion species are shown from the IRI-95 model.

shown in Figure 2.3. The nearly equal densities of  $NO^+$  and  $O_2^+$  in the E-region, give way to the predominance of  $O^+$  at higher altitudes.

This is in contrast to the charged particle composition of the magnetosphere which is dominated by  $H^+$  ions. The role of different ion species in the E-region is not limited to that of  $NO^+$  and  $O_2^+$ , meteors often deposit layers of metallic ions in sufficient density to strongly influence the plasma parameters of the region and this influences the formation of E-region irregularities.

### 2.1.3 Plasma Parameters

The electron plasma frequency is shown as a function of altitude in Figure 2.4 as computed from the IRI-95 ionosphere model and the International Geomagnetic

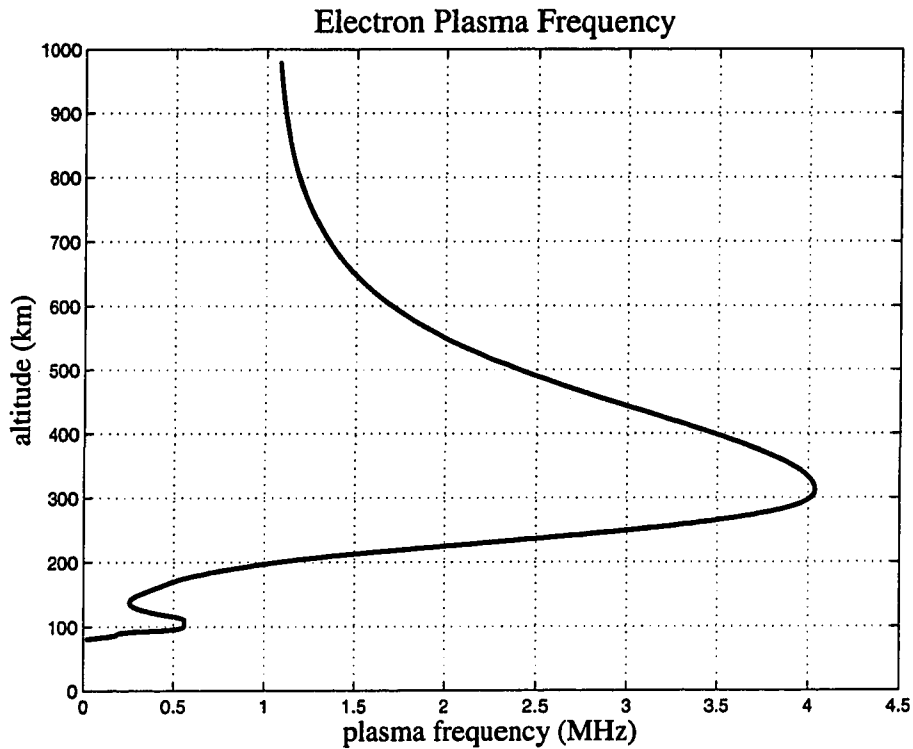


Figure 2.4: Electron plasma frequency for the ionosphere as a function of altitude. This parameter is computed from the IRI-95 and the International Geomagnetic Reference Field Model (IGRF). The peak plasma frequency corresponds to the peak ionospheric electron density.

Reference Field model [Barton, C. E., 1997]. This is the inherent frequency that electrons oscillate about the ions at when perturbed. Radio waves that are transmitted at frequencies near the peak plasma frequency (4-12 MHz typically) will be refracted back towards the Earth's surface by the ionosphere. This is the basic reason why radio broadcasts below about 30 MHz travel long distances around the globe. It is also the basis for the operation of the ionosonde. These devices transmit a succession of radio frequencies in order to determine ionospheric parameters such as the plasma density and the bottom side profile.

The ion and electron gyrofrequencies are shown in Figure 2.5, with the ion mass used for the calculation being the average of all the ion species at a given altitude.



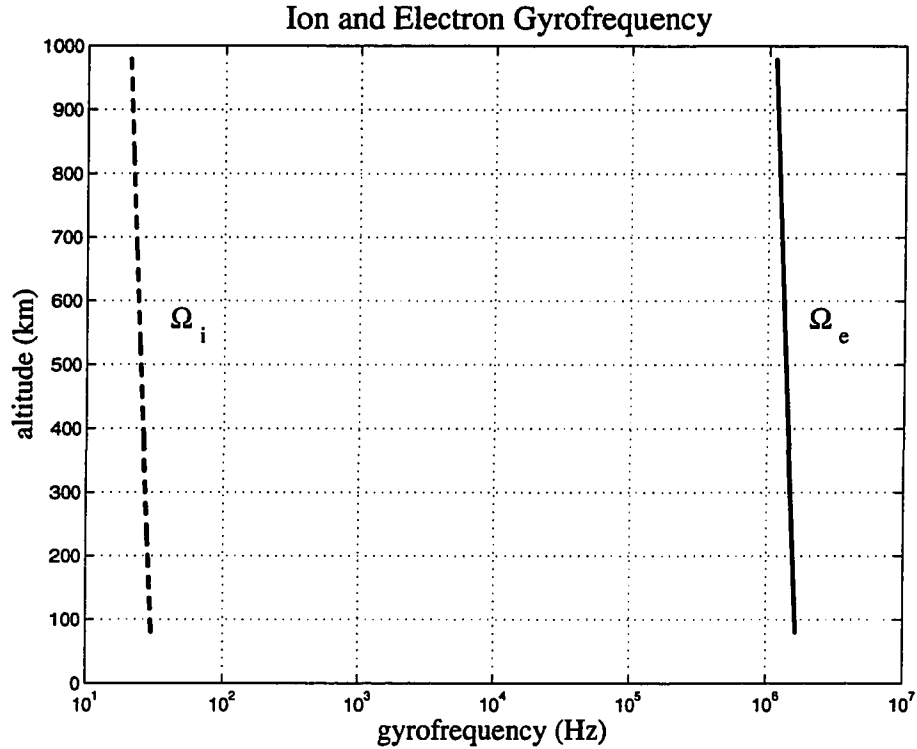


Figure 2.5: The ion and electron gyrofrequencies as a function of altitude as computed from the IRI-95 and IGRF models.

The gyrofrequency for a species  $\alpha$  is simply

$$\Omega_\alpha = \left| \frac{q_\alpha B}{m_\alpha} \right| \quad (2.1)$$

where  $q_\alpha$  is the species charge and  $m_\alpha$  is the species mass. The impact of the large ion mass can be seen by the large ratio between the electron and ion gyrofrequencies. This is due to the predominance of molecular and atomic ions in the ionosphere.

The ion-neutral and electron-neutral collision frequencies are shown in Figure 2.6 and were computed using data from the MSIS-E-90 model. The ion-ion and ion-electron collisions are so infrequent compared to the collisions with the neutral gas that they can usually be neglected. In general collision frequencies are very

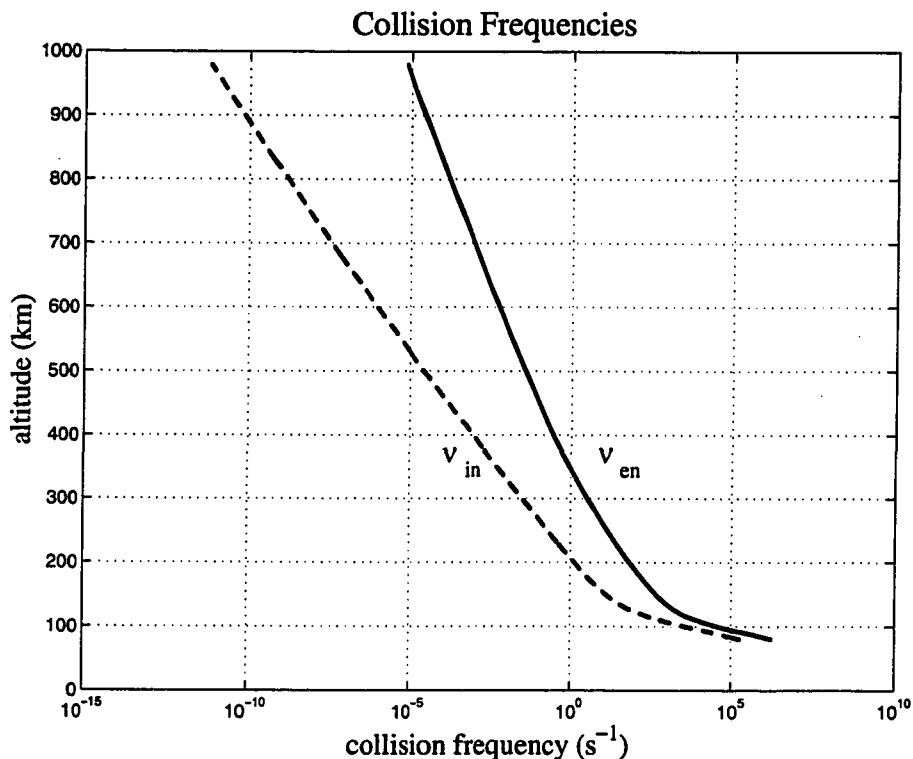


Figure 2.6: Ionospheric collision frequencies as a function of altitude. The collisions with the neutral gas dominate all other types of collisions at ionospheric altitudes. These collision frequencies are computed from the MSIS-E-90 model.

complicated because they depend upon the densities of the species, their velocities, and a velocity dependent cross-section for collision with every other species. In the ionosphere it is usual to use parameterized collision frequency formulas such as those derived from *Schunk and Nagy* [1980].

$$\nu_{en} = 5.4 \times 10^{-10} n_n T_e^{\frac{1}{2}} \quad (2.2)$$

$$\nu_{in} = 4.34 \times 10^{-10} (n_{N_2}) + 4.28 \times 10^{-10} (n_{O_2}) + 2.44 \times 10^{-10} (n_O) \quad (2.3)$$

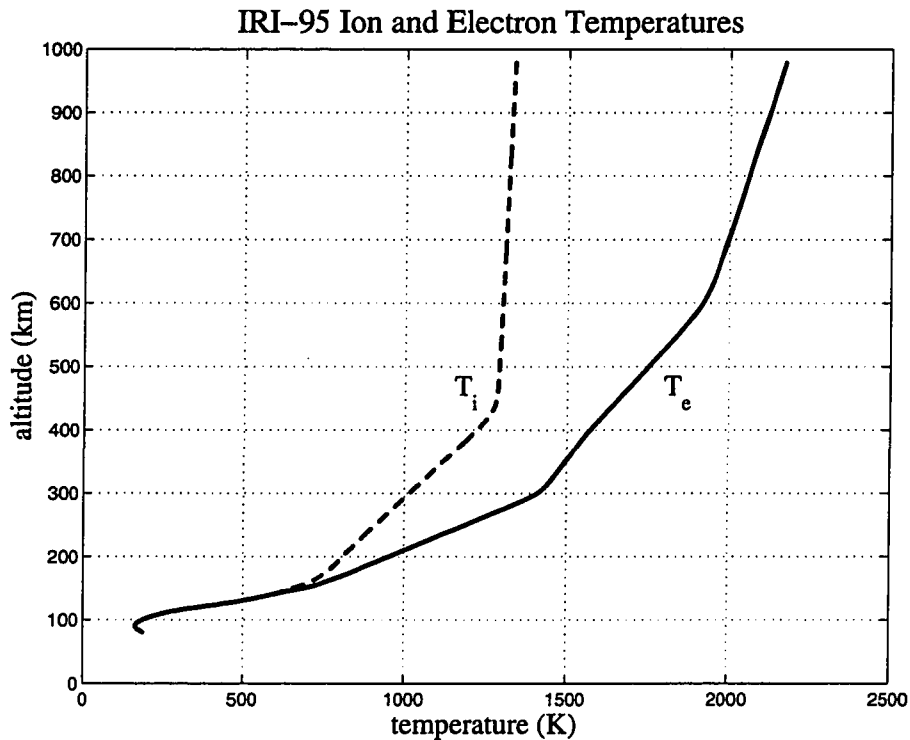


Figure 2.7: Model ionospheric ion and electron temperatures as a function of altitude as derived from IRI-95. The temperature of the ions and electrons can vary greatly as ionospheric conditions change.

Here,  $n_\alpha$  is the density for a given species  $\alpha$  and  $\alpha = n$  denotes the mean neutral density. The temperature of the electrons is  $T_e$  and the densities are given per  $cm^3$ .

A typical ionospheric electron and ion temperature profile is shown in Figure 2.7. Temperatures in the lower E-region are on the order of 300 K with equilibrium being maintained between the ions, electrons, and neutral gas by collisions on short time scales (seconds). The ionospheric temperature increases with altitude and above 150 km the neutral gas density is low enough that substantial temperature differences between the ions and electrons can sometimes occur.

It is really the relationship between the gyrofrequency and collision frequency that dominates the physics of the ionospheric plasma. This gyro-collision ratio is shown for ions  $\kappa_i$  and electrons  $\kappa_e$  in Figure 2.8. When this ratio is somewhat

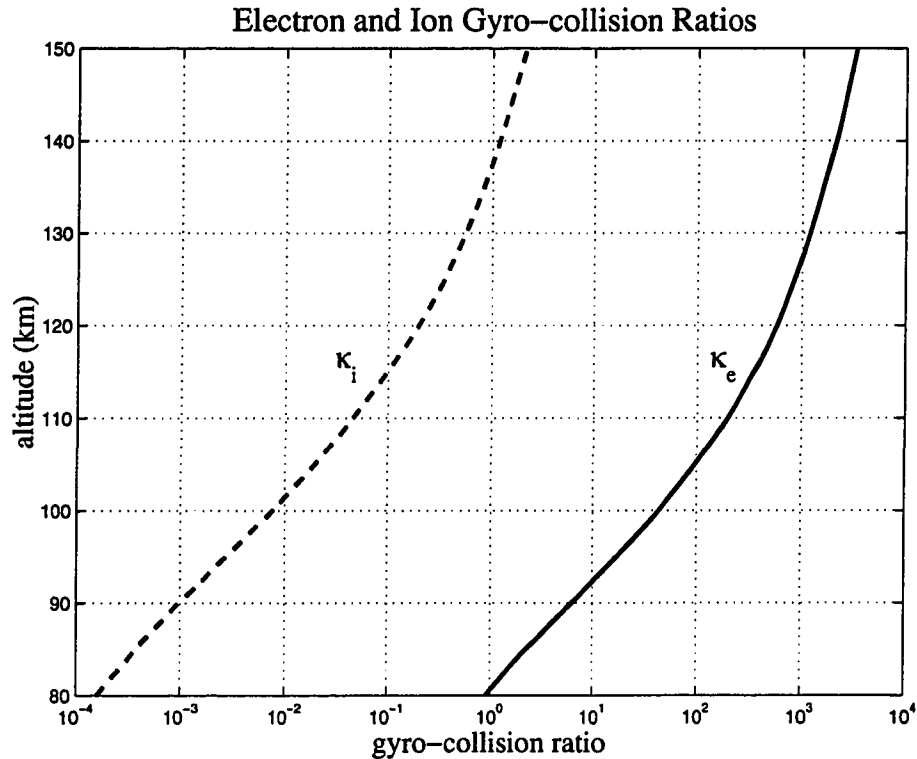


Figure 2.8: Ionospheric gyro-collision coefficients computed from the IRI-95 and IGRF models.

above 1.0, the plasma is magnetized and an accurate treatment must address the presence of the Earth's magnetic field. For low values of the ratio, the plasma is demagnetized because the species collides more frequently than it gyrates about the magnetic field.

By comparing the gyrofrequencies of the electrons to their collision frequency we see that they are magnetized throughout the ionosphere above about 85 km, while the ions are demagnetized below about 150 km. This demagnetization of the ions is one of the defining features of the E-region and it determines, to first order, the altitude extent of the E-region irregularities.

### 2.1.4 Conductivity

The conductivity of the ionosphere can be expressed through a tensor relationship

$$\mathbf{J} = \overset{\leftrightarrow}{\sigma} \cdot \mathbf{E} \quad (2.4)$$

where the conductivity tensor  $\overset{\leftrightarrow}{\sigma}$  is given by

$$\overset{\leftrightarrow}{\sigma} = \begin{pmatrix} \sigma_P & -\sigma_H & 0 \\ \sigma_H & \sigma_P & 0 \\ 0 & 0 & \sigma_S \end{pmatrix} \quad (2.5)$$

The conductivity tensor is useful for understanding of the phenomena that are present in the ionosphere and their relationship to the larger environment of the magnetosphere. The specific ( $\sigma_S$ ), Hall ( $\sigma_H$ ), and Pedersen ( $\sigma_P$ ) conductivities are determined primarily by the mobility of the ion species relative to the electrons. After *Brekke* [1997]

$$\sigma_S = \frac{ne}{B} (\kappa_e + \kappa_i) \quad (2.6)$$

$$\sigma_P = \frac{ne}{B} \left[ \frac{\kappa_e}{1 + \kappa_e^2} + \frac{\kappa_i}{1 + \kappa_i^2} \right] \quad (2.7)$$

$$\sigma_H = \frac{ne}{B} \left[ \frac{\kappa_e^2}{1 + \kappa_e^2} - \frac{\kappa_i^2}{1 + \kappa_i^2} \right] \quad (2.8)$$

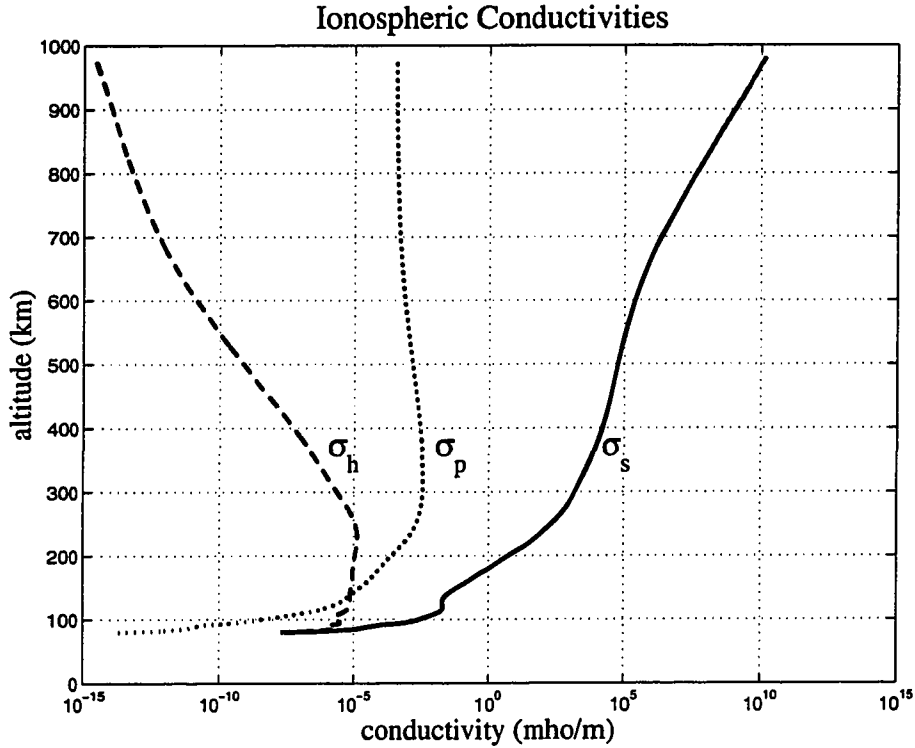


Figure 2.9: The Specific, Pedersen, and Hall conductivities of the Earth's Ionosphere for undisturbed conditions, computed from the IRI-95 and IGRF models.

where the gyro-collision ratio of a species  $\kappa_\alpha$  is determined for species  $\alpha$  by

$$\kappa_\alpha = \frac{\Omega_\alpha}{\nu_{\alpha n}} \quad (2.9)$$

for a plasma density  $n$ , magnetic field  $B$ , electron charge  $e$ , gyrofrequency  $\Omega_\alpha$ , and collision frequency  $\nu_{\alpha n}$ .

A model run showing these conductivities for a typical vertical profile of the ionosphere during undisturbed conditions is shown in Figure 2.9, while a more detailed view of the E-region is given in Figure 2.10.

Here we can see that the Hall conductivity maximizes in the E-region, and the Pedersen conductivity has a maximum in the F-region. The specific conductivity

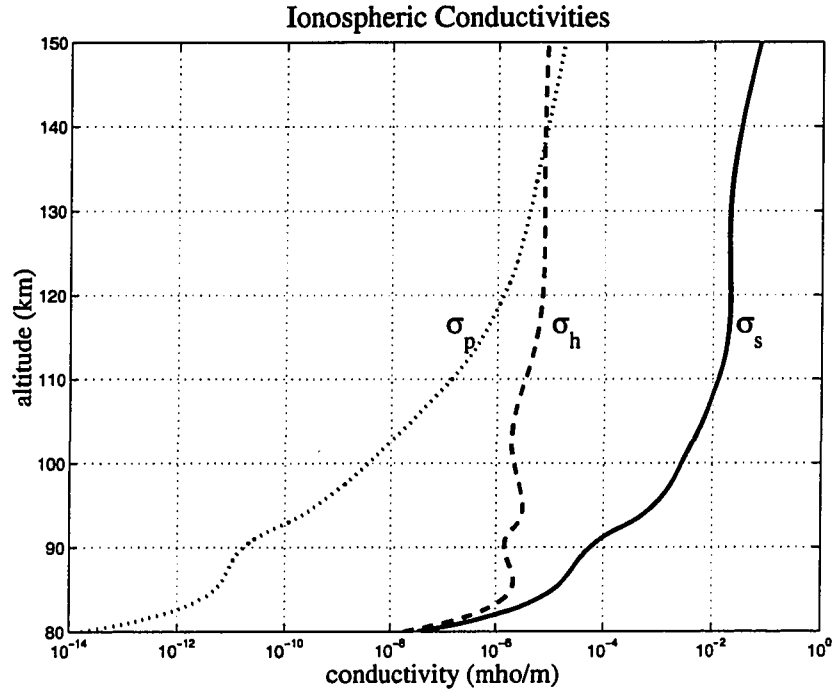


Figure 2.10: The Specific, Pedersen, and Hall conductivities of the lower E-region, computed from the IRI-95 and IGRF models. The Hall conductivity exceeds the Pedersen conductivity in the E-region.

increases rapidly with altitude becoming dominant above about 250 km. This concentrates horizontal ionospheric current systems in the E-region and lower F-region of the ionosphere. At high latitudes these Hall and Pedersen currents connect to the magnetosphere via field aligned currents which are in part possible due to the high conductivity along the magnetic field lines. The electric fields associated with these magnetospheric current systems are also responsible for the strong convection of plasma in the polar ionosphere.

## 2.2 Ionosphere Features

The ionosphere shows more than the simple vertical structure that I have described in detail. There are many large scale features such as quiescent current systems,

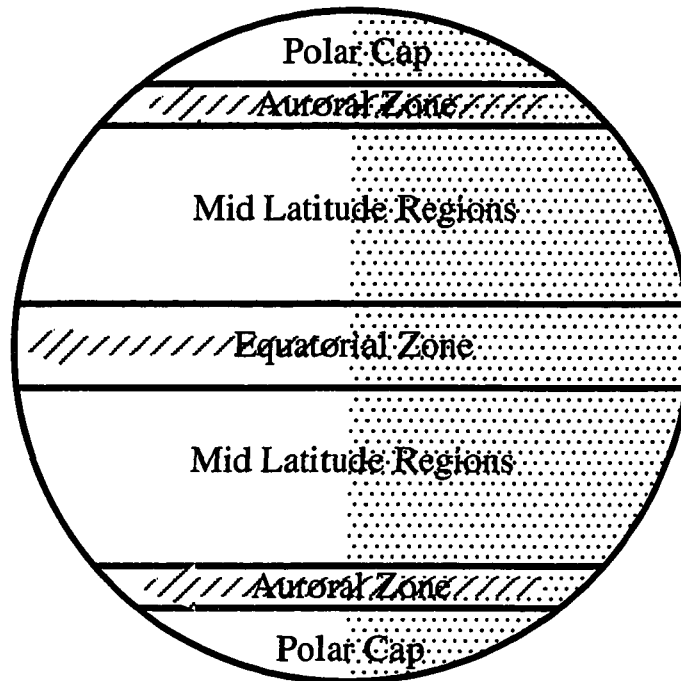


Figure 2.11: A schematic of structures in the Earth's ionosphere as a function of latitude. The auroral zone is typically between  $60^\circ$  and  $70^\circ$  and the equatorial zone is between  $\pm 10^\circ$ . The shaded portion of the diagram indicates the night side of the Earth and the arrows denote the typical convection direction.

the auroral zones, sporadic ionospheric layers, E and F-region tides, the equatorial dynamo, and the auroral and equatorial electrojets. An inventory of the physics of these phenomenon is beyond the scope of this work and is treated elsewhere [Kelley, 1989].

Figure 2.11 is a schematic showing the location of some important ionospheric features. These include the auroral zones and polar caps, the mid-latitude regions, and the equatorial zone.

There is no strong demarcation for many of these divisions and the boundaries between them should be taken as approximate. For example, the auroral zones often expand equatorward to mid-latitudes in response to strong geomagnetic disturbances.



### *2.2.1 Electrojets*

One prominent phenomenon of the ionosphere that is related to the study of E-region irregularities is the formation of electrojets. Electrojets are ionospheric currents that are generated by large scale electric fields. The scope and generation mechanisms of these electric fields limit the spatial extent of the electrojets. They flow in the E-region where the Hall conductivity is highest and they can carry an integrated current of several million amps.

There are electrojets in the auroral zones and at the equator. Electrojets in these locations share many characteristics but their generation mechanisms are different. The equatorial electrojet is located at the equator and flows perpendicular to the Earth's magnetic field. The electrojet flow is in a westward direction during the day and eastward at night. The flow during the night is restricted in duration after sunset because the E-region disappears as its molecular ions recombine in the absence of solar ultraviolet light. The equatorial electrojet occurs due to an electric field generated by a dynamo that is driven by solar heating of the ionosphere at the equator.

The auroral electrojets occur in the auroral zones surrounding the Earth's polar caps. These currents are created by electric fields generated in the magnetosphere and coupled to the ionosphere via field aligned currents. The auroral electrojets flow in the E-region of the ionosphere and can occur during the day or night, with the typical flow direction being toward magnetic midnight. They are most intense during strong geomagnetic storms. During these times the magnetospheric electric fields are enhanced and strong particle precipitation creates the aurora. This particle precipitation enhances the conductivity of the E-region and allows large ionospheric currents to flow. A diagram of the typical convection pattern of the north polar ionosphere is given in Figure 2.12. The currents associated with this convection form the auroral electrojets.

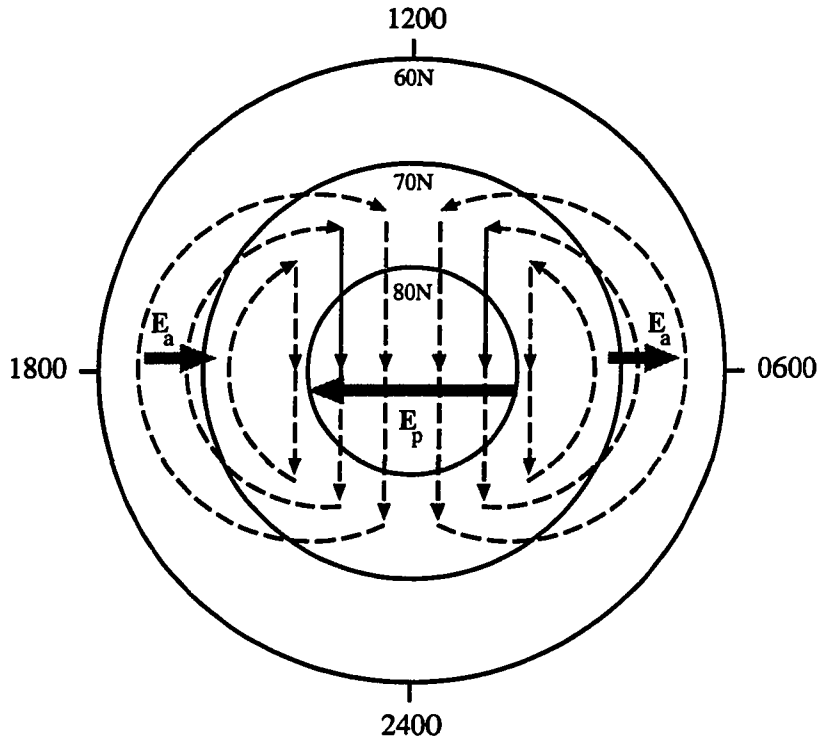


Figure 2.12: An idealized northern hemisphere ionosphere convection pattern. Dashed lines denote the convection direction while the shaded arrows indicate the ionospheric electric field direction responsible for the convection. Latitude is denoted by the circles and notations indicating magnetic local time surround the outermost circle. A typical cross polar cap potential associated with this pattern is 80 kV.

The E-region irregularities are often associated with the electrojets both at the equator and in the auroral zone. The large scale field and conductivity structures that are favorable for the formation of electrojets also produce E-region irregularities when the electric fields are sufficiently strong.

### 2.2.2 Coupling to the Magnetosphere

The Earth's ionosphere is coupled to the larger space environment primarily by field aligned currents which occur in the auroral regions that surround the Earth's poles. These currents are driven by electric fields generated in the Earth's magnetosphere. The electric fields arise from the convection of the solar wind past the Earth's

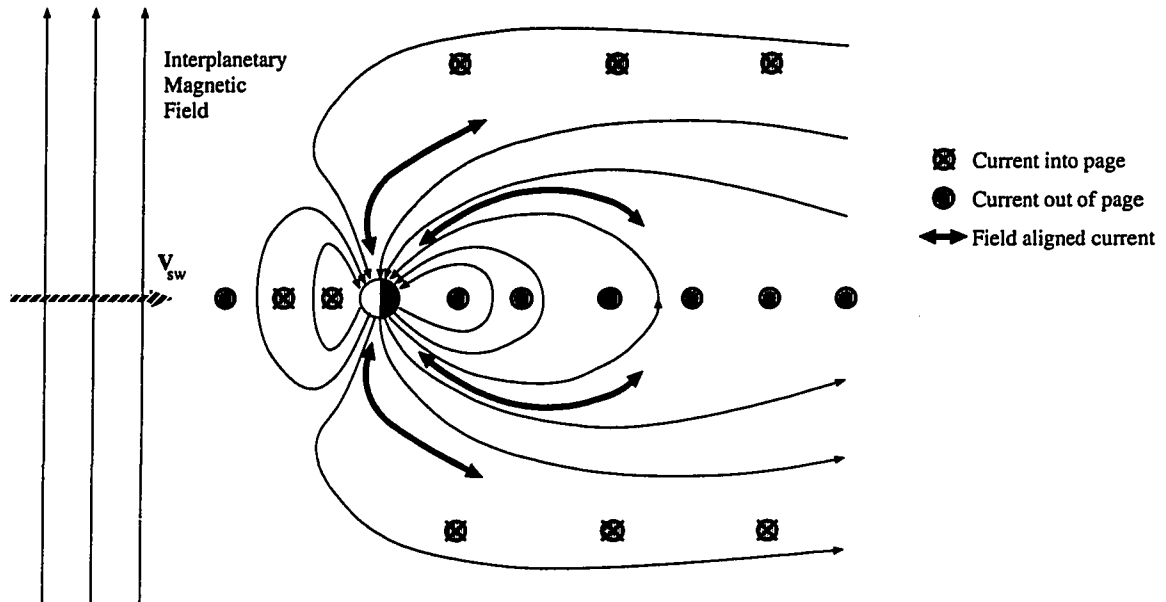


Figure 2.13: The Earth's Ionosphere is coupled to the larger space environment as is shown in this cartoon looking at the Earth's equator. The sun is on the left hand side and the solar wind flows past the Earth at velocities between 400 and 1000 m/s. Currents are generated in the Earth's magnetosphere due to this flow and some of these currents close in the ionosphere.

magnetic field.

Figure 2.13 illustrates how this occurs, with field aligned currents at high latitudes linking the auroral regions into the magnetospheric current systems. The ionosphere acts as a dynamic load on the system with most of the energy dissipation occurring in the E and F-regions as the magnetospheric currents close their circuit there.

It is the generation of electric fields in the magnetosphere, by a flow driven dynamo process, that ultimately produces large-scale electric fields in the auroral ionosphere and provides energy for the formation of E-region irregularities.

## Chapter 3

### THE IONOSPHERIC TWO STREAM INSTABILITY

The auroral electrojet is a phenomenon of the ionosphere where a relatively large current system is driven by electric fields generated in the magnetosphere. This current system is confined to a narrow range of altitudes in the E-region of the ionosphere where the Hall conductivity maximizes. The flow of this current is also favored, especially at night, by enhancements in the conductivity due to the energetic particle precipitation that creates the aurora. In the electrojet the geometry of the electric and magnetic fields is often favorable for the formation of the plasma wave turbulence known as E-region irregularities.

#### ***3.1 The Plasma Physics of the Two Stream Instability***

The ionospheric two stream instability, where one component of the ionospheric plasma streams through another, is the instability that is responsible for the generation of the E-region irregularities. In particular it is this streaming instability that allows the free energy of flowing electrons to be coupled into wave growth, and this ultimately acts as a dissipation mechanism for energy carried into the ionosphere by field aligned currents.

It was first recognized by [Farley, 1963a] that the physics of the two stream instability was fundamental for understanding the ionospheric turbulence that had been observed by radar systems. The initial explanation was proposed to explain observations made of strong radio scatter from plasma turbulence in the equatorial electrojet. It soon became apparent that the two stream instability could be

important anywhere in the E-region under appropriate conditions. In the ionosphere this instability has become known as the Farley instability, or sometimes the Farley-Buneman instability [*Buneman, 1963*].

The basic concept is that electrons, driven by a sufficiently strong electric field, Hall drift through ions at velocities exceeding the local ion acoustic speed. This situation is unstable because the ion acoustic speed is the greatest velocity at which electric field mediated density perturbations can linearly propagate in the E-region of the ionosphere. When the electrons undergo this 'supersonic' drift motion the flow becomes unstable in the volumes of electrons that have exceeded the acoustic speed. The electrons couple energy from their drift motion into the growth of ion acoustic waves which radiate away from the disturbed volume. Energy may be transferred between different wave modes and this energy is ultimately thermalized through nonlinear wave-particle interactions at short wavelengths. This results in heating of the surrounding plasma and neutral background gas on time scales that are large compared to the growth and decay times of individual waves.

### **3.2 Linear Two Fluid Theories**

It is easiest to approach the physics of the irregularities using a linear fluid theory. This is the approach taken by many authors who have progressively added additional details and refinements [*Buneman, 1963; Sudan et al., 1973; Lee and Kennel, 1973; Wang and Tsunoda, 1975; St. Maurice et al., 1981; Huba et al., 1983; Fejer et al., 1984a; Fejer and Providakes, 1987; Kissack et al., 1995; Hamza and St. Maurice, 1995*].

The fluid theory allows a direct derivation of several important irregularity properties, without the complications of kinetic theory. These include the dispersion relation of the waves produced by the electron's drift motion, the conditions for wave growth, and the basic physical regimes in which the instability is important.

The theory has been extensively developed for the irregularities of the auroral electrojet with the addition of density gradients [*Huba et al.*, 1983]. The importance of gradients is such that the mechanism is often referred to as the “gradient drift” instability. This instability primarily generates waves with wavelengths greater than 10 m. Sharp density gradients are often present at high latitudes near auroral arcs and the gradient drift instability can play an important role in such cases.

A simple linear fluid theory cannot explain many important properties of the irregularities such as their observed spectral shapes, aspect angle dependence, or even the diversity of velocities observed by radar systems. The theory also gives predictions of the irregularity growth rates at short wavelengths that differ unrealistically from those predicted by kinetic theories. It is however a very good starting point for forming a basic understanding of the physics that is involved in the formation of E-region irregularities.

The theory begins by approximating electrons and ions of the ionospheric plasma as being well represented by the fluid equations for a magnetized plasma. The continuity and momentum equations are taken for the electrons and a single ion species that is assumed to be the mean ion species present in the E-region. After *Fejer and Providakes* [1987]

$$\frac{\partial N_e}{\partial t} + \nabla \cdot (N_e \mathbf{V}_e) = Q - \alpha_{ei} N_e N_i \quad (3.1)$$

$$\frac{D\mathbf{V}_e}{Dt} = \frac{-e}{m_e} (\mathbf{E} + \mathbf{V}_e \times \mathbf{B}) - \frac{\nabla P}{m_e N_e} - \nu_{en} \mathbf{V}_e \quad (3.2)$$

$$\frac{\partial N_i}{\partial t} + \nabla \cdot (N_i \mathbf{V}_i) = Q - \alpha_{ei} N_e N_i \quad (3.3)$$

$$\frac{D\mathbf{V}_i}{Dt} = \frac{q_i}{m_i} (\mathbf{E}) - \frac{\nabla P}{m_i N_i} - \nu_{in} \mathbf{V}_i \quad (3.4)$$

where the electric field is given by the gradient of a scalar potential

$$\mathbf{E} = -\nabla\phi \quad (3.5)$$

and here  $\alpha_{ei}$  represents a recombination coefficient for a non-catalytic binary chemical recombination and  $Q$  represents a constant source term.

Both *Robinson and Honary* [1993] and *Kissack et al.* [1995] use an energy relation at this point, but this significantly complicates the analysis and results in new wave modes that are not well motivated experimentally. The more usual approach is to assume an isothermal ideal gas law  $\gamma = 1$ , or in some cases an adiabatic ideal gas law  $\gamma = \frac{5}{3}$ .

$$P = \gamma N_\alpha k_b T_\alpha \quad (3.6)$$

Where  $k_b$  is the Boltzmann constant,  $N_\alpha$  is the density of a species  $\alpha$ , and  $T_\alpha$  is the temperature of that species.

Other authors have selected an approximation where the ions are isothermal and the electrons are adiabatic [*Farley and Providakes*, 1989], and this seems to fit the experimental data more accurately in some cases. The correctness of this is not well

motivated physically and it is not clear that all data is better fit using this approach.

There also has been an attempt by *Kissack et al.* [1995] to accurately account for the transport and conduction of heat in a fluid theory context, and these approaches have produced relations that are very similar to those predicted by the kinetic theories [*Stubbe*, 1989].

The resulting set of fluid equations is then evaluated using first-order linear perturbation theory, and the system is solved for the dispersion relation.

### 3.2.1 The Magnetic and Electric Field Geometries

Figure 3.1 shows the geometry of the electric and magnetic fields that are necessary for the generation of the E-region irregularities. In this particular case the magnetic field is oriented appropriately for the northern polar regions of the Earth's ionosphere.

As can be seen, the electric field is perpendicular to the magnetic field and the electron plasma will drift with a velocity given by

$$V_d = \left[ 1 - \frac{\Omega_i^2}{\Omega_i^2 + \nu_i^2} \right] \frac{\mathbf{E} \times \mathbf{B}}{B^2} - \left[ \frac{\nu_e}{\Omega_e} + \frac{\nu_i \Omega_i}{\Omega_i^2 + \nu_i^2} \right] \frac{\mathbf{E}}{B} + V_z \hat{\mathbf{z}} \quad (3.7)$$

which is the drift motion for a magnetized collisional plasma in an applied electric field. This equation neglects neutral winds and is for a given velocity parallel to the magnetic field  $V_z$ . In the E-region this drift is reasonably approximated by the drift motion in a collisionless plasma

$$V_{d\perp} \cong \frac{\mathbf{E} \times \mathbf{B}}{B^2} \quad (3.8)$$

for a simple applied electric field. The ion plasma is governed by a similar equation.



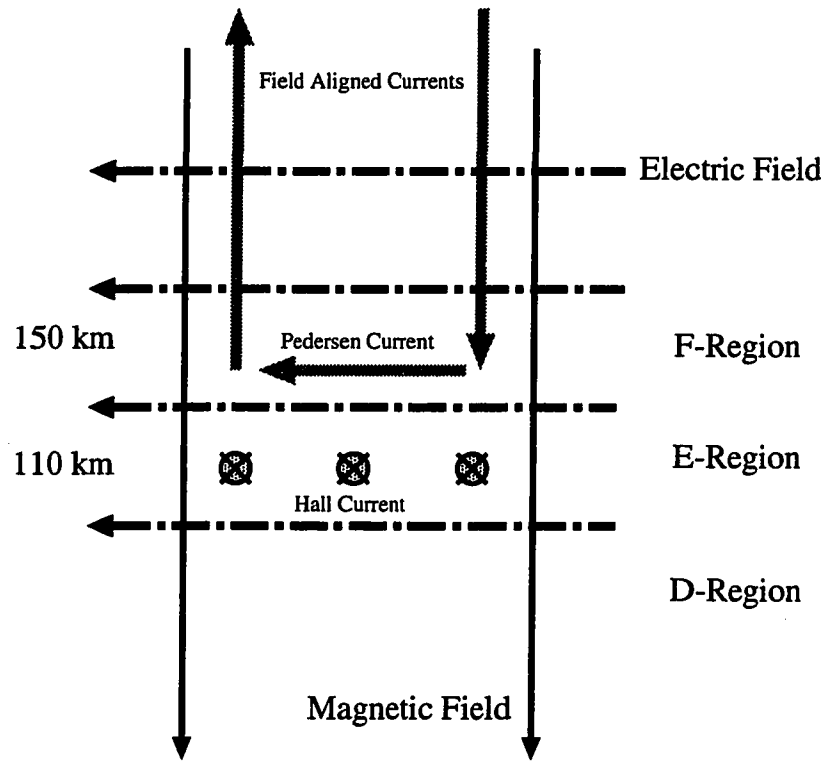


Figure 3.1: The electric and magnetic field structure of the northern auroral ionosphere as a function of altitude. Field aligned currents flow down magnetic field lines to close in the E and F regions. The electric field drives ionospheric convection and drives a Hall current in the E-region.

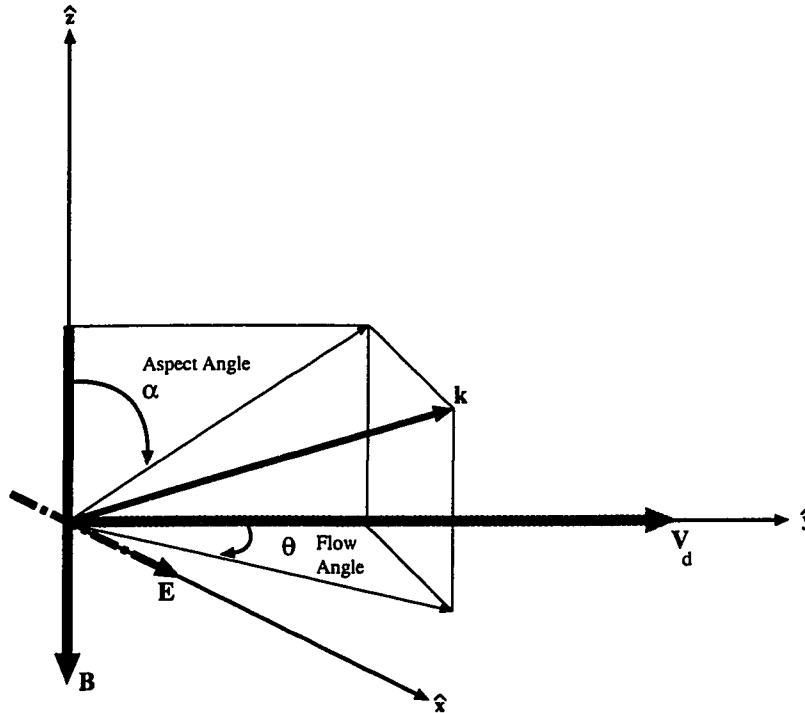


Figure 3.2: The geometry of the two stream instability in the northern auroral E-region. The drift velocity  $V_d$  is created by the  $E \times B$  drift. The vector  $\mathbf{k}$  denotes the wave vector of the irregularities generated by the instability for a sufficiently strong electric field.

However, being collisionally bound to the neutral gas in the E-region, the ions are effectively demagnetized and they drift in a direction determined by the applied electric field and the ambient neutral wind.

### 3.2.2 Ionospheric Two Stream Geometry

The geometry of the two stream instability in the E-region is shown in Figure 3.2. The aspect angle  $\alpha$  and flow angle  $\theta$  are typically confined to a relatively narrow drift cone around the drift direction. Here the neutral wind is taken to be zero, which to first-order is usually a good approximation when compared to the electron drift velocity.

The ion drift in the direction of the applied electric field is relatively slow while

the electrons drift rapidly through ions. The situation becomes unstable when the electron drift exceeds the local ion acoustic speed. Whether this happens locally within the plasma, or in bulk where an entire region of electrons exceeds the acoustic speed en masse, is not yet clear from theory or experiment. It has, however, been determined by sounding rocket measurements that the E-region plasma can contain instabilities of extremely large amplitude with 5-15% of the ambient plasma density being a typical maximum. Of course for such large perturbations the basic linear theory assumption does not hold. A full non-linear treatment is then necessary which does not make the small perturbation assumption, and the testable predictions of these theories are rather limited.

### *3.2.3 The Ion Acoustic Speed*

The fundamental velocity at which the two stream instability becomes unstable is known as the ion acoustic speed. This is the velocity at which linear density perturbations in the plasma of the ionosphere propagate. The density perturbations are propagated as plasma sound waves where the pressure force is conveyed by electric fields, and not by binary collisions as in the neutral atmosphere. The formula for the ion acoustic speed in the ionosphere is given by

$$C_s = \sqrt{\frac{k_b(T_i + T_e)}{m_i}} \quad (3.9)$$

under the assumption of isothermality and using a mean mass for the approximated single ion species. In the auroral E-region ionosphere velocities between 300 and 450 m/s are typical as is shown in Figure 3.3. This velocity can be modified significantly by heating from particle precipitation and wave particle interactions.

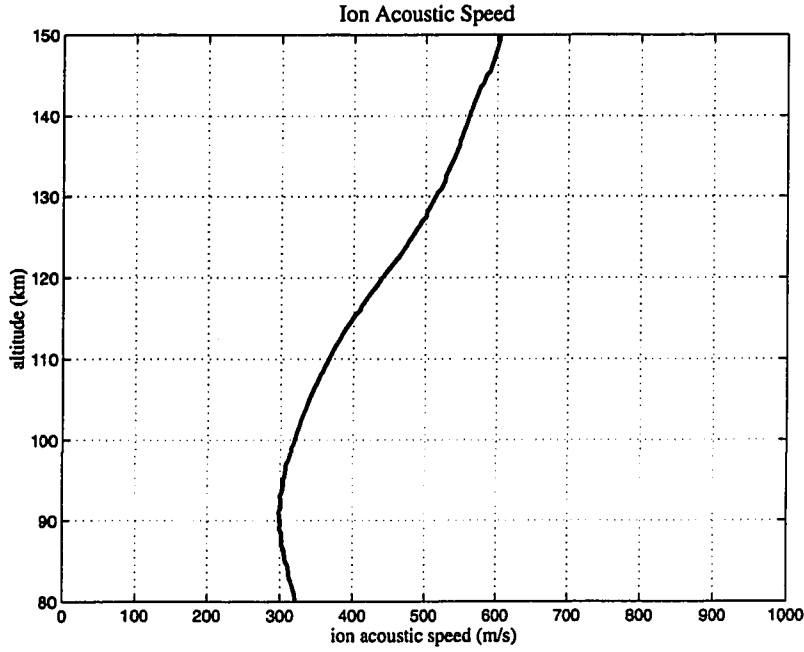


Figure 3.3: The ion acoustic velocity as a function of altitude for a typical high latitude E-region ionosphere. This profile was computed from the IRI-95 model ionosphere.

### 3.2.4 The Irregularity Dispersion Relation

By considering small wave like perturbations  $e^{i\mathbf{k}\cdot\mathbf{r}-\omega t}$  and solving the system of perturbed fluid equations it is possible to arrive at the following dispersion relation for the irregularities. After *Fejer and Providakes* [1987]

$$\omega_r = \frac{\mathbf{k} \cdot \mathbf{V}_d}{1 + \psi} \quad (3.10)$$

$$\Gamma = \frac{1}{1 + \psi} \left[ \frac{\psi}{\nu_{in}} (\omega_r^2 - k^2 C_s^2) + \frac{\omega_r \nu_{in}}{k L_N \Omega_i} \right] - 2\alpha N_0 \quad (3.11)$$

$$\psi = \frac{\nu_e \nu_{in}}{\Omega_e \Omega_i} \left[ 1 + \frac{\Omega_e^2 k_{\parallel}^2}{\nu_{en}^2 k^2} \right] \quad (3.12)$$

$$L_N = \frac{N_0 |\mathbf{k} \times \mathbf{B}|}{\mathbf{k} \cdot \nabla N \times \mathbf{B}} \quad (3.13)$$

where equation 3.10 is the real part of the irregularity dispersion relation and 3.11 is the imaginary part. The wave frequency  $\omega_r$  is linearly related to the electron drift velocity  $\mathbf{V}_d$  for a given irregularity wave vector  $\mathbf{k}$ . This relation determines the phase velocity of the irregularities. It is important to note that the propagation of the irregularities is predicted by linear theory to occur at the electron drift velocity and not the ion acoustic speed. Some observations support the linear relationship while others show the phase velocity reaching saturation near the ion-acoustic speed. This is an unresolved issue because the ion-acoustic speed is not measured during the majority of coherent scatter radar observations.

The imaginary portion of the dispersion relation represents wave growth and decay in the system. The first term represents the streaming instability, the second the importance of density gradients, and the third incorporates the effect of recombinational damping. The parameter  $\psi$  controls the region of the ionosphere where wave growth is important by determining the relative magnetization of the ions and electrons. The second term of 3.12 results in strong damping for waves propagating with a component  $k_{\parallel}$  along the magnetic field direction. This is the fundamental reason that the irregularities are strongly “field aligned.”

The density gradient scale length  $L_n$  incorporates the influence of density gradients on the irregularities. Weak gradients serve either to stabilize or destabilize the system based on the direction of the density gradients relative to the electric field.

The gradient is destabilizing if

$$[\mathbf{E} \cdot \mathbf{k} \times \mathbf{B}] [\nabla N \cdot \mathbf{k} \times \mathbf{B}] > 0 \quad (3.14)$$

Strong density gradients can actually destabilize the plasma through the gradient drift instability even in the absence of an electric field. This destabilization is wavelength dependent, with long wavelengths ( $> 10$  m) being excited first in the plasma. Under most conditions density gradients only serve to modify the electric field required to excite the meter scale two stream instability.

The irregularity growth rate relation (Equation 3.11) is also not an accurate picture at short wavelengths because the fluid theory approximations are only valid at wavelengths greater than the ion mean free path. Below this scale kinetic effects such as Landau damping limit the growth rate of the irregularities. This becomes important for wavelengths below about 1 m under typical auroral ionosphere conditions.

### 3.2.5 *The Instability Threshold*

It is relatively straightforward to solve for the drift velocity at which the instability begins to grow. Under the assumption of no density gradients, and neglecting recombination, it is possible to derive a threshold condition for instability

$$\mathbf{k} \cdot \mathbf{V}_d > C_s(1 + \psi) \quad (3.15)$$

This instability threshold indicates that when the drift velocity of the electrons exceeds the local ion acoustic speed the plasma becomes unstable and wave growth will occur. A typical electric field strength sufficient to exceed the threshold is

around 25 mV/m in the auroral ionosphere.

### 3.3 Linear Kinetic Theories

The initial development of the linear theory for the two stream instability in the E-region of the ionosphere was done using kinetic theory by *Farley* [1963a]. Since then most of the development of irregularity theory has been done with the fluid theories because they are significantly simpler in their formulation. It would be wrong to think that the kinetic approaches have been in any way abandoned. A number of authors have continued and extended the early work substantially [*Schmidt and Gary*, 1973; *Schlegel and St. Maurice*, 1983; *Schlegel*, 1983; *Stubbe*, 1989; *Pecseli et al.*, 1989; *Dimant and Sudan*, 1995; *Gurevich et al.*, 1995; *Rosenberg and Chow*, 1998].

These kinetic theories proceed from the Boltzmann kinetic equations for the distribution functions of the various species with some approximate collision term.

It is normal for ions of similar mass to simply consider a single ion distribution, instead of each species that is present. The usual approach then proceeds similarly to fluid theory in that first order linear perturbations are taken with the assumption of wave like solutions so that the system can be solved in the frequency domain. The perturbation to the density function is derived and this result is used with Poisson's equation to obtain a dispersion relation. The fluid limit can always be recovered by taking the appropriate moments of the distribution functions. As is noted by *Stubbe* [1989], the primary problem in the kinetic theory is the appropriate description of the collisional effects and the usual approach is to pick an appropriate relaxation model.

The kinetic theories inherently handle Landau damping correctly and with the proper collision term can realistically describe momentum and energy transfer. In practice this makes the results from kinetic theory extraordinarily complicated. For

wavelengths greater than a meter the linear fluid and kinetic theories make essentially identical predictions, so that the complexity of the kinetic theory is not rewarded by “better” results. At wavelengths below a meter the kinetic theory makes significantly more realistic predictions of the irregularity growth and dissipation rates.

### 3.4 *Nonlinear Theories*

Linear theories of the Farley-Buneman instability predict many important features, such as the threshold for instability, a characteristic dispersion relation, alignment perpendicular to the magnetic field, and why the irregularities are confined to the E-region. They are not, however, sufficient to explain many features of the irregularities that are commonly observed such as the spectra shape, saturation of wave growth, wave phase velocities that are too low or high relative to the ion acoustic speed, ionospheric wave heating, irregularity amplitudes, and scattering cross-sections.

Nonlinear approaches have been used on many of these outstanding questions of irregularity theory. There is a continuum of techniques, some of which make similar predictions in different ways. In general the problem has been that the theories are not sufficiently distinguished or predictive to make measurements that select between them.

#### 3.4.1 *Threshold Velocity and Phase Velocity Saturation*

The threshold velocities at which instability growth occurs have been treated extensively by several authors. *Chaturvedi et al.* [1987] found that field aligned electron drifts could modify the threshold criteria and generate oblique sound waves. More recently *Karashtin and Tsimring* [1993] examined the effect that plasma inhomogeneities have on the threshold velocity. *Kissack et al.* [1997] have looked at the



impact of electron neutral energy exchange has on the Farley-Buneman threshold through nonlinear heating of the neutral background.

There are some observations of the irregularities [*Primdahl and Bahnsen, 1985*] that show the irregularity phase velocities are limited to the ion acoustic speed  $C_s$ . This has been explained by *Sudan [1983b]* as being due to an effective increase in the electron neutral collision frequency in the presence of turbulence. Other theories predict a similar saturation velocity for the irregularities, although for different reasons. Three wave interactions [*Kustov et al., 1988*], resonance broadening [*Robinson, 1992*], and mode coupling [*Hamza and St.-Maurice, 1993a*] all can produce a similar limit to the phase velocity of the irregularities. It is not entirely clear how to experimentally select between these different models, or even that their underlying physical mechanisms are actually distinct. They also do not explain observations of the irregularities that seem to closely follow the linear dispersion relation, where the phase velocity of the irregularities depends on the electron drift velocity  $V_d$ . More theoretical and experimental work will be required to resolve this issue, and it would be interesting to determine if this saturation velocity has a wavelength dependence.

### 3.4.2 Wave Heating

A major question that must be addressed by the nonlinear theories is how the energy in the turbulence generated by the instabilities is dissipated in the E-region. This question is worth answering because it addresses the larger problem of energy balance in the system and how energy from the magnetosphere is dissipated in the ionosphere.

Wave heating mechanisms have been considered extensively in several studies. Early on it was shown that there is sufficient energy in the waves to account for observed electron temperature profiles in the ionosphere and that the wave heating

could be a significant fraction of joule heating for sufficiently strong electric fields [St. Maurice *et al.*, 1981; St. Maurice and Laher, 1985]. This is especially true if the wave propagation direction is not exactly perpendicular to the magnetic field.

Other work has focused on anomalous resistivity and diffusion causing conductivity changes which lead to or are the result of wave heating [St. Maurice, 1987; Robinson, 1992; Hamza and St. Maurice, 1995; Robinson, 1998]. Some work on wave particle interactions via a plasmon-electron interaction theory has also been developed by Robinson [1986]. All these approaches provide mechanisms for wave heating of the E-region but they are not always sufficiently distinguished in their predictions to be experimentally validated.

### 3.4.3 Secondary Wave Generation

Much of the work on heating is based on ideas that have been developed regarding the generation of secondary waves in the turbulent plasma. The idea, as applied to the ionosphere, traces its roots back to work with the equatorial electrojet by Sudan, *et al.* [1973]. He described a turbulent cascade of energy from long to short wavelengths where the energy produced by the streaming instability ultimately heats the plasma and surrounding neutral gas. Some authors have continued in this vein [Schlegel and St.-Maurice, 1983], while there has been a definite shift toward considering more restricted three wave interaction theories by others [Kustov *et al.*, 1988; Sahr and Farley, 1995]. The three wave interaction models address a slightly different set of questions, primarily considering how irregularities that propagate at high or low phase velocities can be generated.

### 3.4.4 Spectral Characteristics

A forward theory capable of predicting irregularity spectral shape would be very useful. It would allow construction of an inverse problem based on radar observa-

tions, and the potential extraction of useful ionospheric parameters from a single coherent scatter radar. It may be too much to hope for such a predictive theory because many of the effects on irregularity spectral shapes seem to be subtle and hard to deconvolve. This is especially true when both electric field and density gradient drifts are of comparable magnitude. Because most of the irregularity observations are made using radars there are also questions as to what features of the irregularity spectrum are due to “scattering physics” of the radar signals as opposed to “plasma physics” of ion-acoustic wave generation and interaction.

There have been a number of attempts to produce models of the spectrum with varying success [*Rosenbluth and Sudan*, 1986; *Sahr*, 1990], while others have concentrated on specific characteristics such as the doppler width [*Hamza and St. Maurice*, 1993b]. The boldest attempt to date has been by *Pivovarov et al.* [1996] who use a nonlinear current model to predict spectral shapes and then compare them to experimental data in an attempt to determine electron drifts and electric fields. This attempt seems quite promising, with realistic electron drifts and fields being derived from the experimental data. It is, however, necessary to see this technique applied to a larger set of data and calibrated using other methods before its predictions can be used with confidence.

#### 3.4.5 Anomalous Wave Velocities

Many observations of the E-region irregularities have been made in which phase velocities other than those likely under the linear theory have been observed. These velocities are either well below or above the nominal ion acoustic speed. The theoretical interpretation of the experimental results is often complicated by the fact that the ion acoustic speed is not known for the majority of radar experiments.

Early work on the low velocity echoes focused on possible electrostatic ion cyclotron waves (EIC) [*Ossakow and Chaturvedi*, 1979; *Chaturvedi*, 1981; *Fejer et al.*,

1984b; *Fejer and Providakes, 1987*]. However, this theory was later abandoned based on experimental evidence [*Watermann et al., 1989a; Sahr et al., 1991; Watermann, 1994*].

Recent theories to explain these anomalous velocities have either focused on extraordinarily sharp density gradients [*St.-Maurice et al., 1994*], or three wave interaction theories [*Haldoupis et al., 1991; Haldoupis et al., 1993b; Sahr and Farley, 1995*]. The predictions of these theories may be testable with sufficiently well designed experiments.

### **3.5 Simulations**

Numerical simulations may be the best hope for developing an in-depth understanding of the many complicated features that the irregularities display. Unfortunately, because of the molecular ion species in the E-region of the ionosphere, the electron to ion mass ratio is very large, and this ensures that accurate fluid and particle simulations are difficult to construct. A summary of simulation and theory for the E-region irregularities can be found in *Janhunen [1995]*.

Several simulations have been attempted using various approaches, most being in two dimensions perpendicular to the magnetic field. All of them show some degree of success in predicting irregularity features [*Machida and Goertz, 1988; Janhunen, 1992; Janhunen, 1994a; Schlegel and Theimann, 1994; Oppenheim et al., 1995; Oppenheim and Otani, 1996; Oppenheim et al., 1996*].

### **3.6 Additional Theoretical Issues**

The theoretical work on the E-region irregularities is well developed but stymied. The simple linear fluid theories are the best understood but do not predict many important properties of the E-region irregularities. Linear kinetic theories provide some insight, especially for short wavelengths, but are extraordinarily complicated.

Nonlinear theories currently make a large number of hard to distinguish predictions that are not easily testable, and simulations are limited by computing power for the near future.

If these were the extent of the difficulties it would certainly be enough; however there are other issues (described below) which have not been addressed to date. The plasma instabilities in the E-region of the ionosphere form an extraordinarily complicated system and progress in this field may be slow.

### *3.6.1 Irregularity Electromagnetic Scattering*

A fundamental limitation involved in interpreting data collected by ionospheric radars is a lack of clear understanding of the irregularity scattering cross-section and the importance of multiple scatter. These issues increase the difficulty involved in constructing an accurate theory of irregularity spectral shape; it helps to know what you are predicting. Some work has been done on the cross-section by *Moorcroft* [1985], and the work on multiple scattering by *Donovan and Moorcroft* [1992] shows that it may be important for VHF frequency radars at large magnetic aspect angles. These issues need substantial investigation both experimentally and theoretically.

### *3.6.2 Wave Generation Mechanisms*

Current theories and experiments do not make clear what portion of the plasma undergoes the transition to instability. They are also not predictive of how this transition occurs. Do small regions of the plasma go unstable and then decay, or does the whole system exceed the instability threshold in bulk?

This is an area that may be best addressed by simulations as it is not clear that radar experiments can ever resolve the spatial and temporal scales necessary to answer this question.

### 3.6.3 *The Importance of Inhomogeneities*

Some work on the role of inhomogeneities in the plasma and neutral background has been done [Huba *et al.*, 1983; Sverdlov, 1988], but how density structures on multiple scales interact with the turbulent wave field of the irregularities is not clear. This is an area where high resolution incoherent scatter radar observations of the E-region prior to the onset of instability might be very useful. By measuring the position of density inhomogeneities prior to instability onset it may be possible to experimentally determine their relationship to the irregularities.

### 3.6.4 *Multiple Ion Species and Dusty Plasmas*

The E-region of the ionosphere actually consists of two ion species  $NO^+$  and  $O_2^+$  of similar mass (6% difference) in roughly equal densities. The usual approximation is to take the mean ion mass and use a single ion species. This removes an ion-acoustic mode from the system that is important when nonlinear wave-wave interactions occur. I discuss this idea more thoroughly in Chapter 5.

Some other work has been done along these lines for dusty plasmas by Rosenberg and Chow [1998]. This area of investigation may be very important for understanding the role of meteors in the ionosphere and the role of ion production in irregularity physics.

## Chapter 4

# OBSERVATIONS OF AURORAL E-REGION IRREGULARITIES

The very first scientific observations of E-region irregularities were reported by *Eckersley* [1937]. In many ways this initial work was the most impressive to be done for the next 30 years. Utilizing an early 9.127 MHz commercial transmitter that was modified to emit pulses, and a receiver situated 19.2 km away in Chelmsford Essex, *Eckersley* performed his radar observations. He detected the presence of scatterers and localized them to between 85-155 km in height using interferometry. His initial conclusion that the scatter was produced by irregularities or clouds in the E-region of the ionosphere began a large effort to probe and understand the irregularities that continues to this day.

Following shortly after *Eckersley's* observations, *Harang and Stoffregen* [1938] used a 41 MHz system to detect scatter from high altitude reflecting layers at a height of more than 100 km. This work, which was done with a 50 kW pulse transmitter located near Tromso Norway is the last significant work on the E-region irregularities reported prior to World War II.

Beyond the initial disruption of work, the war caused substantial development in radar technology and the era following it showed an immediate increase in sophistication. *Lovell et al.* [1947] reported the first irregularity observations after the war, simultaneously utilizing both 3 and 106.5 MHz transmitters located at the Jodrell Bank experimental station. These observations are novel because the 106.5 MHz observations are the first substantially above the ionosphere's critical frequency.

The 1950s saw rise to a number of different programs dedicated to investigating the irregularities. *Forsyth et. al.* [1950] established the first of a large series of radars in Canada, and reported echoes at ranges between 600 and 1000 km in association with the aurora.

During this early period of investigation it rapidly became clear that at high latitudes the irregularities were strongly associated with the presence of the aurora. It was also understood that the scatter occurs when the radio waves were incident perpendicular to the Earth's magnetic field. This field alignment is a prominent feature of the irregularities and many researchers found it difficult to accept that this condition could be strictly maintained. The work of *Harang and Landmark* [1953], using simultaneous 35 and 75 MHz pulse mode radars detected irregularities at ranges between 300 and 500 km, but not when aurora was clearly visible at distances of 80 km. Harang and Landmark commented:

*It has been assumed that reflexions from an aurora mainly occur when the waves are incident normally to the direction of the earth's magnetic field. In this case we should get no reflexions from the aurorae observed visually in Tromso. But it is difficult to imagine that this condition is so strictly maintained that the most violent aurora at 80 km distance does not give the slightest trace of echoes.*

Investigations of the irregularities during this early period were mainly confined to detecting the location of the scatterers. A final bit of sophistication was the development of the Range Time Intensity plot (RTI) [*Bullough and Kaiser, 1954*], where the amplitude of the scattered signal is recorded as a function of range and time. This technique allowed for the long term monitoring of the irregularities.

The work of *Bowles* [1954] marked the beginning of a new era with the first doppler spectra of equatorial irregularities. Bowles utilized a 25.4 MHz radar system that was capable of alternating between CW and pulse mode transmission.



Even with his modest 100 W transmitter power, he was easily able to detect the irregularities.

*McNamara* [1955] used a more advanced system in the auroral zone that was capable of distinguishing between positive and negative doppler shifts. His observations provided doppler information at 90.7 MHz, along with simultaneous backscatter observations at 50 and 106 MHz. The doppler shifts of the observed irregularities were reported to be several thousand meters per second.

Several other interesting results round out the end of the 1950s, and the early part of the 1960s. These works show the beginning of a systematic attempt to understand the irregularities and their relation to other phenomenon.

An extensive set of observations at 72 MHz was analyzed by *Bullough et al.* [1957] to show the close correlation between magnetic disturbances and the appearance of the irregularities. The first UHF observations were begun by *Leadabrand et al.* [1959] and the irregularities were determined to be strongly field aligned by *Bowles* [1960]. Extensive backscatter information was also recorded at 41.0 MHz as part of International Geophysical Year observations, and this data showed a good correspondence between echo locations and the location of the visual aurora [*Leonard*, 1959; *Gartlein et al.*, 1960]. *Flood* [1960] collected simultaneous observations at 49.7, 143.5, and 226 MHz and examined the wavelength dependence of the scatter from the irregularities. This marks the start of the experimental program at Cornell University that was a powerful complement to the theoretical work being done there [*Booker*, 1954; *Booker et al.*, 1955]. The azimuthal distribution of the echoes was investigated by [*Kelly et al.*, 1961] in Canada, and work by Russian investigators was also reported [*Bagaryatskii*, 1961].

Properly this middle period of irregularity investigation was brought to an end by *Bowles et al.* [1963] who determined that the equatorial irregularities were produced by ion-acoustic waves in the ionosphere. He inferred a similar case for auroral zone

echoes and this, combined with the theoretical model of *Farley* [1963a], marks the beginning of the modern era of irregularity investigation.

An excellent summary of work from these early years can be found in *Leadabrand et al.* [1965], where extensive modern observations from Fraserburgh, Scotland at 30, 401, and 800 MHz are also described.

#### **4.1 E-region Irregularity Experimental Radar Observations**

Observations of the E-region irregularities have been reported by many investigators on at least 38 frequencies ranging from 3 MHz to 1.295 GHz (see Table 4.1). Almost all of these investigations have included range information, and most modern ones include doppler spectra. A few simultaneous multi-frequency experiments have been done, as have several interferometry experiments. The experiments have investigated many different aspects of irregularity physics, while at the same time advancing the state of radar technique.

Modern auroral E-region irregularity investigations have primarily been conducted with VHF and UHF radar systems. For the VHF systems, most observations have been made at 50 and 140 MHz, while recent UHF observations are usually made using the incoherent scatter radars currently in operation at their operating frequencies.

Because of the diverse nature of the radar experiments and the dramatic variations in ionospheric conditions it is often difficult or impossible to compare different E-region irregularity experiments in a meaningful and quantitative way. The only real exceptions to this are common volume experiments where multiple radars examine a single spatial region simultaneously. Furthermore most of the irregularity observations have been “event driven” and this may significantly bias our current understanding of irregularity behavior. Despite the experimental difficulties many important issues underlying the irregularity physics have been addressed in a rea-

sonably systematic manner.

New coherent scatter radars are few and far between, and issues such as multiple scatter, wave-wave interactions, wavelength dependence, and large scale coupling are difficult to address without a larger scale program of systematic observations.

#### *4.1.1 Irregularity Altitudes*

The first reported observations of the irregularities made clear that they were a phenomenon of the E-region of the ionosphere [Eckersley, 1937]. Two main techniques for ascertaining irregularity altitude exist, the first is to use narrow antenna beams to localize observations to a particular point in space, and the second is to use interferometry to effectively synthesize such angular resolution.

Extensive investigations by Leadabrand *et al.* [1965] and Abel and Newell [1969] using UHF radars with steerable dishes established clearly that the average height of the irregularities is near 110 km in altitude. Some observations have put the peak altitude as low as 103 km [Moorcroft and Schlegel, 1990] and it is likely that the height is highly dependent on ionospheric conditions.

Other experimenters have used interferometry to investigate the irregularities and obtain altitude and thickness observations [Timofeev and Miroshnikov, 1982; Providakes *et al.*, 1983; Ruohoniemi and Moorcroft, 1985; Ierkic *et al.*, 1992]. These observations are consistent with the irregularities being sharply bounded below 95 km and having typical vertical extents of 5-10 km.

Observations of altitude extent with steerable dishes are similar in their conclusions [Schlegel *et al.*, 1990; Foster *et al.*, 1992], although they observe some altitude variation as a function of magnetic aspect angle.

There is also some evidence that low velocity echoes are more restricted in their altitude extent than echoes near the ion-acoustic velocity [Moorcroft and Ruohoniemi, 1987].

Table 4.1: Radar observations of E-region irregularities

frequency (MHz)	range	doppler	altitude	first reference
3.0	yes	no	no	[ <i>Lovell et al.</i> , 1947]
9.1	yes	no	yes	[ <i>Eckersley</i> , 1937]
14.0	yes	yes	no	[ <i>Eglitis et al.</i> , 1995]
19.0	yes	no	no	[ <i>Basu et al.</i> , 1974]
30.0	yes	yes	no	[ <i>Leadabrand et al.</i> , 1965]
35.0	yes	no	no	[ <i>Harang and Landmark</i> , 1953]
41.0	yes	no	no	[ <i>Harang and Stoffregen</i> , 1938]
42.0	yes	yes	no	[ <i>Haldoupis and Sofko</i> , 1979]
46.9	yes	yes	yes	[ <i>Providakes et al.</i> , 1988]
48.5	yes	yes	no	[ <i>McNamara et al.</i> , 1982]
49.2	yes	yes	yes	[ <i>Providakes et al.</i> , 1983]
49.7	yes	no	no	[ <i>Flood</i> , 1960]
50.0	yes	yes	yes	[ <i>Balsley et al.</i> , 1972]
53.5	yes	yes	yes	[ <i>Unwin and Johnston</i> , 1981]
55.0	yes	no	no	[ <i>Unwin</i> , 1967]
60.0	yes	yes	no	[ <i>Koehler et al.</i> , 1990]
65.0	yes	no	no	[ <i>Ogawa</i> , 1996]
72.0	yes	no	no	[ <i>Bullough et al.</i> , 1957]
73.1	yes	no	no	[ <i>Bullough and Kaiser</i> , 1954]
74.0	yes	no	no	[ <i>Harang and Landmark</i> , 1953]
80.0	yes	no	no	[ <i>Ogawa</i> , 1996]
83.0	yes	no	no	[ <i>Kustov et al.</i> , 1993]
90.0	yes	yes	yes	[ <i>Timofeev and Miroshnikov</i> , 1982]
90.7	no	yes	no	[ <i>McNamara</i> , 1955]
99.9	yes	yes	no	[ <i>Lind et al.</i> , 1999]
106.5	yes	no	no	[ <i>Lovell et al.</i> , 1947]
112.0	yes	yes	no	[ <i>Ogawa</i> , 1996]
140.0	yes	yes	no	[ <i>Greenwald et al.</i> , 1978]
143.5	yes	no	no	[ <i>Flood</i> , 1960]
145.0	yes	yes	no	[ <i>Jones et al.</i> , 1981]
226.0	yes	no	no	[ <i>Flood</i> , 1960]
398.0	yes	yes	yes	[ <i>Tsunoda et al.</i> , 1974]
400.0	yes	no	yes	[ <i>Leadabrand et al.</i> , 1959]
401.0	yes	yes	yes	[ <i>Leadabrand et al.</i> , 1965]
440.0	yes	yes	yes	[ <i>Foster and Tetenbaum</i> , 1991]
800.0	yes	yes	yes	[ <i>Leadabrand et al.</i> , 1965]
933.0	yes	yes	yes	[ <i>Moorcroft and Schlegel</i> , 1990]
937.5	yes	yes	yes	[ <i>Eglitis et al.</i> , 1995]
1295.0	yes	yes	yes	[ <i>Abel and Newell</i> , 1969]

#### 4.1.2 *Irregularity Amplitudes*

Almost all coherent scatter radar observations determine the relative amplitude of the backscattered power from the irregularities. Some information of this kind has even been compiled in relatively large statistical surveys of the irregularities [Schlegel *et al.*, 1986; Shand *et al.*, 1996].

There have, however, been relatively few absolute measurements of the backscattered power due to the irregularities [Schlegel and Moorcroft, 1989; Foster and Tetenbaum, 1991]. These observations are generally referenced to the cross-section of the incoherent scatter floor and are made using incoherent scatter radars.

Sounding rocket observations of the irregularities have been made in coordination with radar observations. The rocket experiments are able to measure the absolute level of the density fluctuations in the E-region irregularities. These fluctuations are typically between 5-15% of the total plasma density in a disturbed E-region.

Unfortunately, it is very difficult to relate the backscattered power directly to the irregularity density perturbations. This is primarily due to complications produced by the scattering of the radar signals by the irregularities.

#### 4.1.3 *Spectral Types*

The spectral type nomenclature was first introduced by Balsley and Ecklund [1972]. In their studies of the E-region irregularities they found that there were three main types observed.

Type-1 irregularities are generally thought to be the wave mode corresponding most closely to that produced by the linear two stream instability. They tend to have high amplitude, narrow spectral width, and velocities near the ion acoustic speed.

The Type-2 mode is a very common, low amplitude irregularity type, that has broad spectral width. It is generally believed to be the result of a turbulent cascade

from long to short wavelengths and is observed to occur over a large range of flow angles.

Type-3 spectra have a unique history among the irregularities. These radar returns have narrow spectral width, high amplitude, and velocities substantially below the ion acoustic speed. Type-3 echoes are difficult to explain using current theories and much effort has been expended in attempting to explain them. For a complete discussion of these theories see *Haldoupis et al.* [1995a].

A fourth type of irregularity, named Type-4, has been observed and categorized [*Haldoupis*, 1989]. These irregularities have narrow spectral width, large amplitudes, narrow distribution around the electron drift direction, and velocities that seem to always be near 1000 m/s [*Haldoupis et al.*, 1991].

Several other types of irregularities have been proposed but have yet to gain wide acceptance in the community [*Tanaka et al.*, 1990; *Kunitake et al.*, 1993].

In many ways the type nomenclature for the irregularities is actually misleading. It is also not supported well by statistical distributions of the irregularities [*Sahr and Fejer*, 1996]. It is certainly true that many coherent scatter radar observations of the irregularities can be classified as one of the types if your definitions are flexible enough. There is, however, no clear physical definition of the different types and there are no distinct boundaries between them.

#### 4.1.4 *Watermann Distributions*

Comparisons between radar systems are problematic as many have very different resolutions, sensitivities, significantly different operating modes, wildly divergent geometries, and insufficient agreement about the shape of the irregularity auto-correlation function. A more useful approach than the type nomenclature is the Watermann distribution [*Watermann et al.*, 1989a].

In a Watermann distribution, the number of observed spectra for a given phase

velocity and irregularity spectral width are plotted using fits from a presumed model for the irregularity spectral shape. An example of such a distribution is shown in Figure 4.1 for about 60,000 fitted spectra from the 50 MHz CUPRI radar system [Sahr and Fejer, 1996].

#### 4.1.5 Aspect Sensitivity

Perhaps the most investigated property of the irregularities is the sensitivity of the irregularity scattering cross-section to the angle between the irregularity wave vector and the Earth's magnetic field.

The E-region irregularities were observed very early to be extraordinarily field-aligned (i.e. their scattering cross-sections are only large when the irregularity wave vector is perpendicular to the Earth's magnetic field). The alignment is so dramatic that some early authors conceived of alternate explanations for their observations than field aligned scatter [Harang and Landmark, 1953].

The work of Bowles [1960] with equatorial E-region irregularities showed definitively that the irregularities were in fact extraordinarily field aligned, and it was inferred that those in the auroral zone were similar.

Many experiments have been undertaken to investigate the aspect sensitivity of the irregularities. Some of the initial work by McDiarmid [1972] estimated a sensitivity of 1.3-1.5 dB/deg at 50 MHz. Other observations by 50 MHz radars in Canada also show less aspect angle dependence than the typical 10 dB/deg expected from theory and experiment [Haldoupis et al., 1986; Haldoupis et al., 1987; Watermann et al., 1989b].

This is substantially different from the measured values at other frequencies. Indeed Moorcroft and Schlegel [1990] found a 6 dB/deg dependence between 5.8° - 7.6° at 933 MHz, and Foster et al. [1992] measured aspect sensitivity that varied smoothly between 15 and 7 dB/deg over a range of 0 to 9 degrees at 440 MHz.

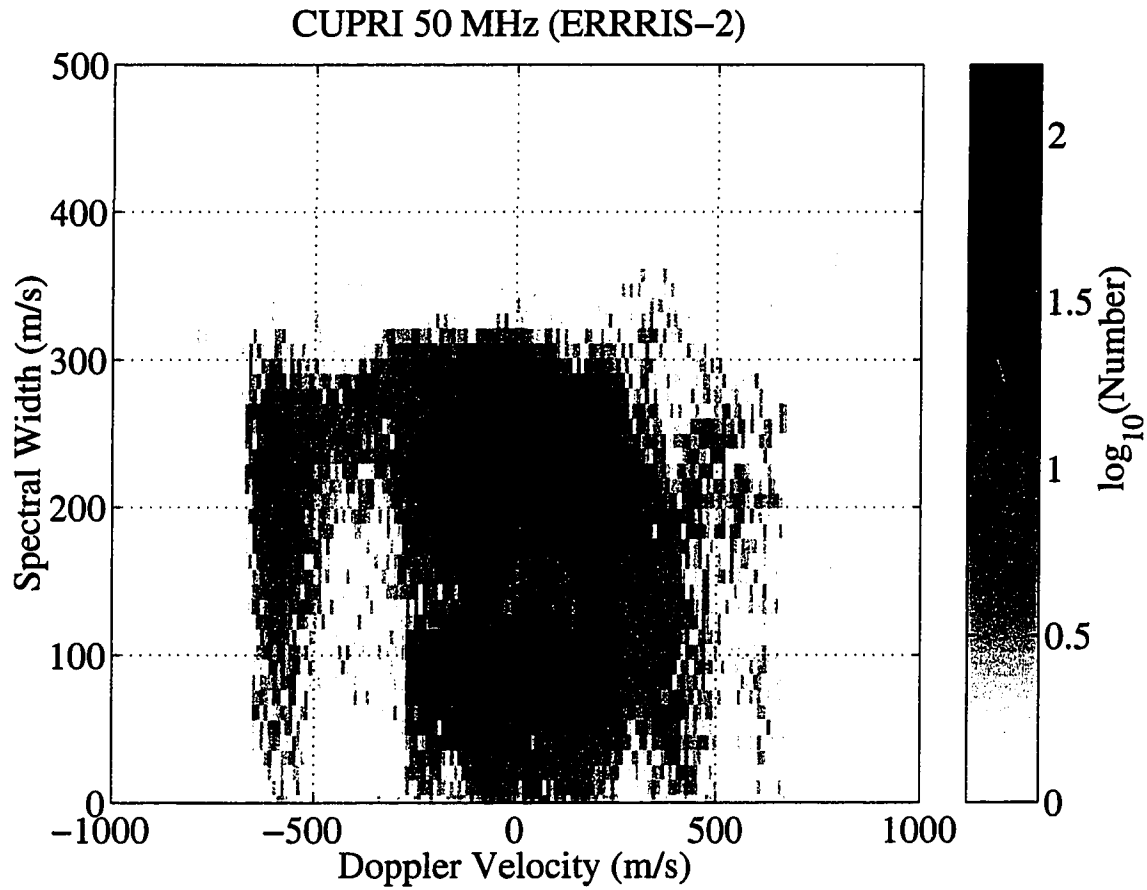


Figure 4.1: The Watermann distribution of E-region irregularities from the Cornell University Portable Radar Interferometer (CUPRI), a 50 MHz pulse mode radar system (Sahr 1999, personal communication). The plotted data is from the ERRRIS-2 experiment conducted in northern Scandinavia in 1989 [Pfaff, *et al.*, 1992].



*Waldock et al.* [1985] found sensitivity between 0 and 10 dB/deg depending on the absolute intensity of the backscatter in a statistical study of STARE data, while *Koehler et al.* [1985a] in a similar study of Canadian 50 MHz VHF data found that aspect angle was not well correlated with other phenomenon and that the spectral characteristics were strongly dependent upon it.

It is generally thought that the low values of aspect angle sensitivity and the variability in the measurements of the 50 MHz data sets is due to ionospheric refraction effects [*Uspensky and Williams*, 1988; *Moorcroft*, 1989; *Watermann*, 1990]. These are negligible above about 70 MHz, and so the aspect angle sensitivity between 7 and 15 dB/degree found by the UHF radars is the more likely value. This does not however explain the STARE data which was taken at 140 MHz and so further experiments at intermediate wavelengths will be necessary to determine the frequency dependence of the aspect angle sensitivity.

A number of experiments have also shown a substantial dependence of the irregularity phase velocity on the aspect angle [*Tsunoda*, 1976; *Nielsen*, 1988; *Moorcroft and Schlegel*, 1990; *Foster et al.*, 1992]. There is also some evidence that the most intense irregularities are also the most narrowly confined in aspect angle [*Foster and Tetenbaum*, 1991].

#### 4.1.6 Flow Angle Sensitivity

A complement to aspect angle sensitivity is a dependence of irregularity properties on flow angle. This is the angle between the flow of the electrons that drives the two stream instability and the incident radar signal. In general a cosine rule is expected from linear theory for waves near zero flow angle. Some observations seem to support this [*Foster et al.*, 1992], while others show velocities that are lower than expected [*Nielsen et al.*, 1983].

It is more difficult to examine flow angle effects due to the radar geometries

that are involved. As such they have not been as well investigated as aspect angle sensitivity.

The multi-static nature of the STARE radar lends itself to analysis of flow angle effects. *Nielsen et al.* [1984] and *Haldoupis et al.* [1984] both examined the spectral dependence on flow angle for STARE data. They find that there is substantial variation of the spectrum with flow angle, with narrow type 1 spectra at up to 60 degrees from the electron drift direction. At larger angles broader less stable spectra are observed.

*Kustov et al.* [1997] utilized two orthogonal 50 MHz CW radar beams to examine type-2 spectra at large magnetic aspect angles. Periodic electron flow direction changes allowed the observation of an asymmetry in the observed spectra that had the same sign as the mean doppler shift perpendicular to the flow.

Flow angle effects need to be investigated further as there are theoretical indications that the maximum growth rate of the irregularities may occur at slight angles to the flow [*Janhunen, 1994a; Janhunen, 1994b; Oppenheim et al., 1996*]. It is also possible that non-linearly excited wave modes may propagate at large angles to the flow direction [*Oppenheim et al., 1995*] and several of the wave-wave interaction theories predict preferred directions for the generation of secondary waves [*Sahr and Farley, 1995*].

#### 4.1.7 Instability Threshold Conditions

One of the most important predictions of the linear theories of the E-region irregularities is the existence of an instability threshold. In the E-region ionosphere this threshold is essentially the ion-acoustic speed. When the electron drift velocity exceeds this acoustic speed, small perturbations in the plasma can grow into waves which derive their energy from the electron flow and then propagate away from the instability region.

In most cases in the E-region ionosphere a combination of an ambient electric field and density gradients creates the drifts that generate the instabilities. In radar experiments there is usually a focus on the electric field necessary to drive the plasma unstable.

Most of the early work associated with the instability threshold was done using the 398 MHz Chatanika incoherent scatter radar in Alaska [*Tsunoda and Presnell, 1976; Moorcroft, 1979*]. Thresholds ranging from 20 to 30 mV/m were observed using this system.

More recently *Kustov et al.* [1989] has investigated the instability threshold using the STARE radar system. Interestingly the observations show a threshold of 5-15 mV/m, with a substantial increase in fluctuations above 15 mV/m. This is below the value typically associated with the instability threshold and this is attributed to unresolved microstructure (relative to the low spatial and temporal radar resolution) in the plasma causing “threshold spreading.” Some work has also shown that, near the instability threshold, sudden increases in the electron density can cause the onset of the irregularities [*Kustov et al., 1993*].

The instability threshold condition is another area where more definitive measurements can be made. In particular a coherent scatter radar capable of deriving the convection with relatively high resolution might resolve the microstructure that may be confusing the STARE threshold measurements. Another important experiment would be simultaneous coherent and incoherent scatter measurements of the same volume. This could allow the effect of density gradients to be deconvolved from that of the electric field.

#### 4.1.8 Saturation Velocity

The linear fluid theory predicts a linear relation between the phase velocity of the irregularities and the electron drift velocity. In all cases so far observed there is a

saturation velocity where increased electron drift does not lead to higher wave phase velocities.

This saturation velocity, in most cases, appears to be near the ion acoustic speed in the plasma [*Moorcroft*, 1980; *Nielsen and Schlegel*, 1985; *Haldoupis and Schlegel*, 1990]. Such a saturation is consistent with nonlinear theoretical models and simulations, although it is not predicted by the linear theory.

In observations by *Foster and Tetenbaum* [1992] phase velocities as high as 700 m/s have been observed. The saturation is still near the ion acoustic speed, but that speed is higher due to elevated electron temperatures. Work by *Prikryl et al.* [1995] shows that higher electron temperatures can indeed lead to higher saturation thresholds, and this is consistent with the idea of  $C_s$  as the limiting speed.

#### 4.1.9 Spectral Shape

The irregularity spectral shapes measured by many experimental observations show a rather diverse character. The early spectral observations of the irregularities showed the predominance of two main spectral types [*Balsley and Ecklund*, 1972; *Balsley et al.*, 1972; *Greenwald et al.*, 1975a; *Greenwald et al.*, 1975b; *Greenwald et al.*, 1975c]. Powerful narrow spectra (Type-1, Type-3) generated by the two stream instability and much weaker broad spectra (Type-2) thought to be produced by a turbulent cascade from long to short wavelengths.

Double peaked spectra [*Haldoupis and Sofko*, 1979] have been reported once and long discrete echoes are observed equatorward of the electrojet for low electric field strengths [*Haldoupis and Nielsen*, 1986]. Other work has shown that the spectral shape is aspect angle dependent with broad spectra being predominant at large flow angles [*Nielsen et al.*, 1984; *Koehler et al.*, 1985a].

Some larger studies of irregularity spectral shape have been conducted. *Schlegel et al.* [1986] examined 77,000 STARE spectra and found that few of the weak broad

spectra were detected. *Eglitis et al.* [1995] did a comprehensive comparison of spectra between three radars PACE (14 MHz), SABRE (144 MHz), and COSCAT (937.5 MHz). This study found type-1 like irregularities had minimum width near the ion acoustic speed with the mean scattered power going down as the width increased. Interestingly the type-2 like irregularities had minimum widths near 0 m/s but their scattered power went up with increasing width.

The lack of a predictive theory of spectral shape has limited the ability of coherent scatter radars to extract useful physical parameters from the observations. Work by *Pivovarov et al.* [1996] attempted to use a spectral shape prediction model to fit data and determine the electric field and electron drift motions. This effort was fairly successful on the limited data set to which it was applied, but it is doubtful that it would work well in less constrained circumstances.

#### 4.1.10 Irregularity Energy Dissipation

Energy dissipation by the irregularities is a very important problem that has not been addressed in a comprehensive manner by experiments. Observations such as that by *Schlegel and St.-Maurice* [1981] showing ionospheric temperatures near 110 km of 1200 K cannot be easily explained using a classical heating process and are probably the result of plasma wave heating.

Work by *Haldoupis et al.* [1993a] using both incoherent (EISCAT) and coherent (STARE) scatter measurements of a common volume during anomalous E-region electron heating events shows that irregularity backscatter is always present during heating events. Further there may be an electric field threshold for substantial electron temperature increases of 40 mV/m.

There has also been a curious observation by *Robinson et al.* [1998] during an RF heater experiment where the electron temperature was reduced between 100 - 115 km when the heater was activated. This may be explainable in terms

of induced E-region irregularities transporting energy away from the heating zone or alternatively by the temperature being ill-defined for strongly non-Maxwellian plasma distributions.

How the irregularities dissipate energy on a large scale, and what impact this has on the larger magnetospheric current systems has not been well addressed experimentally.

#### *4.1.11 Seasonal and Solar Cycle Dependence*

Long term observation observations using coherent scatter radars have been relatively rare with some systems only running for short periods. Most work has also focused on understanding irregularity generation mechanisms and the underlying instability plasma physics. There have been some efforts to examine the seasonal and solar cycle dependence of E-region irregularity occurrence using coherent scatter radars [*Hultqvist and Egeland, 1964; Ogawa, 1996*]. The results of these studies have been consistent with known seasonal and solar cycle effects on geomagnetic activity and ionospheric electric fields.

There has also been work by *Shand et al. [1996]* on irregularity amplitudes over a solar cycle which showed a solar cycle dependence for the westward electrojet but not the eastward electrojet. Other potential dependencies, such as spectral characteristics and velocities have not been examined to date.

## **4.2 Other Experiments**

There have been several novel experiments involving coherent scatter radar observations that deserve mention. *Keys [1970]* used a balloon borne X-ray detector under a VHF radar beam at Slope Point New Zealand. He showed that particle precipitation was not the direct cause of the radar echoes.

*Hagfors et al.* [1971] compared radar data to satellite measurements of particle fluxes. This work found that strong echoes were coincident with proton precipitation but not electron precipitation.

Finally, the boldest experiment of all was by *Forsyth and Fulford* [1979] where a radar was placed on a sounding rocket and used to observe ion acoustic waves that had a phase velocity of 380 m/s.

#### 4.2.1 Rocket Experiments

Sounding rockets have been used to probe the auroral E-region of the ionosphere since the 1960s [*McNamara*, 1969]. Sounding rocket borne instrumentation is very useful for its ability to provide *in situ* measurements of ionospheric parameters. Direct measurements of E-region electric fields, plasma density, and density fluctuations can be made using appropriate instruments. In particular, sounding rockets are the only way in which the absolute level of E-region irregularity density fluctuations are known. These density fluctuations can be as large as 5-15% of the background plasma density. Sounding rockets have shown that the phase speeds and directions of the irregularities are consistent with radar observations, that fine altitude structure exists on scales from 100 m to several kilometers, that the irregularities are strongly field aligned, and that threshold electric fields are around 20 mV/m. There is also evidence that instabilities with wavelengths as short as 35 cm can be excited in the E-region [*Margot and McNamara*, 1991].

A brief summary of sounding rocket observations can be found in *Sahr and Fejer* [1996] and a more comprehensive discussion is in *Pfaff* [1986]. The observations made by sounding rockets are consistent with the radar observations but it is often difficult to compare the two. Several experiments have been done where simultaneous observations of the same volume have been made by sounding rockets and coherent scatter radars [*Pfaff et al.*, 1992; *Rose et al.*, 1992]. The results from

these experiments have not substantially shifted ideas regarding the irregularities and their observation using radar.

#### 4.2.2 Laboratory Experiments

There have been some attempts to study the Farley-Buneman instability in the laboratory. These begin with *D'Angelo et al.* [1974] who used a cesium plasma device in an attempt to generate the instability. D'Angelo found that the plasma perturbations were strongly elongated along the magnetic field lines of the device, and he was able to measure the wave vector spectrum of the perturbations [*D'Angelo et al.*, 1974]. This experiment also showed that the power at a given wavelength obeyed a power law

$$P(k) = k^{-\beta} \quad (4.1)$$

where  $\beta = 3.5 - 3.8$ . Other work has attempted to simulate equatorial electrojet conditions obtaining  $\beta = 2 - 3.5$  [*John and Saxena*, 1975]. In a novel experiment, *Alport et al.* [1981] attempted to understand the Bragg backscatter by scattering 3 cm waves in an experimental device. Finally, *Kustom et al.* [1985] showed that increases in the electric field above the instability threshold increase the power level of the fluctuations but don't change the spectral shape, which he found to have  $\beta = 3.5$ .

Laboratory experiments to understand the irregularities have gone out of fashion. This is probably due to the limited degree of comparison that is possible between the laboratory devices and the ionosphere. It is very difficult (if not impossible) to create true ionospheric conditions in a laboratory device. The E-region consists of low temperature plasma that is relatively pure in its composition. It is also not clear that the physics should scale correctly between the devices and the E-region



or even how this scaling is best done.

## Chapter 5

# A THREE FLUID MODEL FOR AURORAL E-REGION IRREGULARITIES

A fundamental assumption underlying the evaluation of fluid and kinetic theories for the E-region irregularities is that a single ion species can be used. This is certainly a good approximation to first order as  $NO^+$  and  $O_2^+$  are similar in mass (30 and 32 amu respectively). The resulting theories predict two modes, one the growing Farley-Buneman mode and the other strongly damped.

In general there has been little work on the role that different ion species play in the electrodynamics of the E-region irregularities. The theory is complicated to start with and most effort has been directed toward understanding the effect of non-linear terms on irregularity behavior. These non-linear theories have not been particularly successful at explaining the full range of irregularity radar observations.

Understanding the role of multiple ion species may provide the insight into the radar observations that is missing from current theories. A fluid model that includes two ion species instead of the normal one is a reasonable starting point for understanding the role of multiple ion species in the formation and evolution of E-region irregularities. I focus on a plasma composed of electrons,  $NO^+$ , and  $O_2^+$  because this is the typical composition of the E-region ionosphere.

### ***5.1 The Relation to Type-3 Irregularities***

The power spectra produced by VHF radar has resulted in a type nomenclature which loosely categorizes a spectrum using its mean doppler velocity and doppler

width. This categorization is generally based on the morphology of the echo and its evolution in time. Distinctions between different echo types are not always clear. In many cases the observed echo properties are not easily explained by the linear irregularity theories. The Type-2, Type-3, and Type-4 irregularities all fall into this category.

In evaluating the three fluid model I will focus on comparisons to Type-3 irregularities. These irregularities are the least understood of irregularity types. The initial work on Type-3 echoes by *Fejer et al.* [1984b] identified their properties and proposed an interpretation in terms of scatter from electrostatic ion cyclotron waves. This EIC hypothesis enjoyed nearly a decade of favor before being invalidated experimentally [*Watermann et al.*, 1989a; *Sahr et al.*, 1991]. A good review of the rise and fall of the EIC hypothesis is given by *Watermann* [1994].

The demise of the EIC hypothesis leaves a large body of experimental observations without adequate explanation. Three main theories have been advanced to explain the Type-3 echoes, the first by *Haldoupis et al.* [1992] explains the Type-3 echoes in terms of the presence of a destabilizing plasma density gradient. A similar approach was also taken by *St.-Maurice et al.* [1994] using sharp density gradients at the boundaries of discrete optical arcs and a non-linear two stream turbulence model. The second approach suggested by *St.-Maurice et al.* [1994] involves a non-linear wave-wave coupling which produces secondary waves corresponding to the Type-3 echoes. This approach has also been pursued by *Sahr and Farley* [1995] who produced a detailed three wave coupling model. The third model suggested by *Shalimov and Haldoupis* [1995] relies on a new instability generated when the electron temperature is strongly elevated relative to the ion temperature.

An excellent summary of the observations and theory concerning the Type-3 radio aurora can be found in *Haldoupis et al.* [1995a]. As noted in his review, more work is needed on the models to explain all the observations and the existing

experimental results are not sufficient to select a particular model as being the most likely explanation for the Type-3 radio aurora. Further, designing experiments to test the proposed models may be difficult because most of the theories rely on some form of non-linear mode coupling which implies the necessity of radar observations at multiple wavelengths and scattering geometries.

## 5.2 *Two Ion Species*

To date all theories that attempt to explain the radar observations of echoes in the auroral E-region have made the simplifying assumption of a single ion species. The consequence of this approximation is that several modes of oscillation are removed from the system. These modes result from the presence of the two ion species and their different masses. By retaining the two ion species in the derivation of a fluid model for the auroral E-region it is possible to examine the behavior of the plasma for different parameter variations.

The single ion assumption seems justified in the E-region because the two principle ion species are  $NO^+$  and  $O_2^+$ . These species are present in roughly equal density and have very similar masses of 30 and 32 amu respectively; a single mean ion species of 31 amu is often assumed in linear fluid theories. This approximation simplifies the mathematics greatly and allows for the derivation of an analytical solution that explains the observed phase velocities and instability thresholds of the Type-1 echoes. Applying the linear three fluid model to  $NO^+$  and  $O_2^+$  does not produce a new growing wave mode. However, it is a useful endeavor because it highlights potential paths for the non-linear coupling of energy between waves and the ultimate dissipation of energy in the system.

### 5.3 Three Fluid Dispersion Relation

A full analytic derivation of the three fluid dispersion relation is given in Appendix A. The derivation begins from the fluid equations appropriate for an E-region plasma and follows a linear perturbation approach. The resulting wavelike solutions give a dispersion relation that is composed of a density response function for each species in the plasma. By using Gauss' law the system of equations can be closed and the resulting dispersion relation is written below.

$$1 - \frac{\omega_{pi1}^2}{-k^2 V_{ti1}^2 + \omega^2 + i\nu_i \omega} - \frac{\omega_{pi2}^2}{-k^2 V_{ti2}^2 + \omega^2 + i\nu_i \omega} + \frac{\omega_{pe}^2}{-i\nu_e \kappa_e^2 (\omega - kV_d) + k^2 V_{te}^2} = 0 \quad (5.1)$$

This is equation A.31 in Appendix A and is the dispersion relation for a one dimensional system. The parameters  $\omega_{pi1}$ ,  $\omega_{pi2}$ , and  $\omega_{pe}$  are the plasma frequencies associated with each species while  $V_{ti1}$ ,  $V_{ti2}$ , and  $V_{te}$  are the thermal velocities. We will also be assuming that the electrons and ions are isothermal so that  $\gamma = 1$ .  $V_d$  is the electron drift that creates the instability and this term is determined by the electric field. The collision frequencies  $\nu_e$  and  $\nu_i$  are for collisions with the neutral background gas. The irregularity wavenumber is given by  $k$ , while the frequency is given by  $\omega$ . The geometry of this system is shown in Figure 5.1 and is appropriate for the northern auroral E-region.

Any new wave modes that result from equation 5.1 will result from differences in the ion plasma frequencies (i.e., the species inertial response to perturbation), or from differences in the thermal velocities. In evaluating the system I will assume that the ion temperatures are identical ( $T_{i1} = T_{i2} = T_i$ ) and this reduces the difference in the thermal velocities to a mass dependence. This is a reasonable assumption because collisions with the neutral background gas should maintain temperature

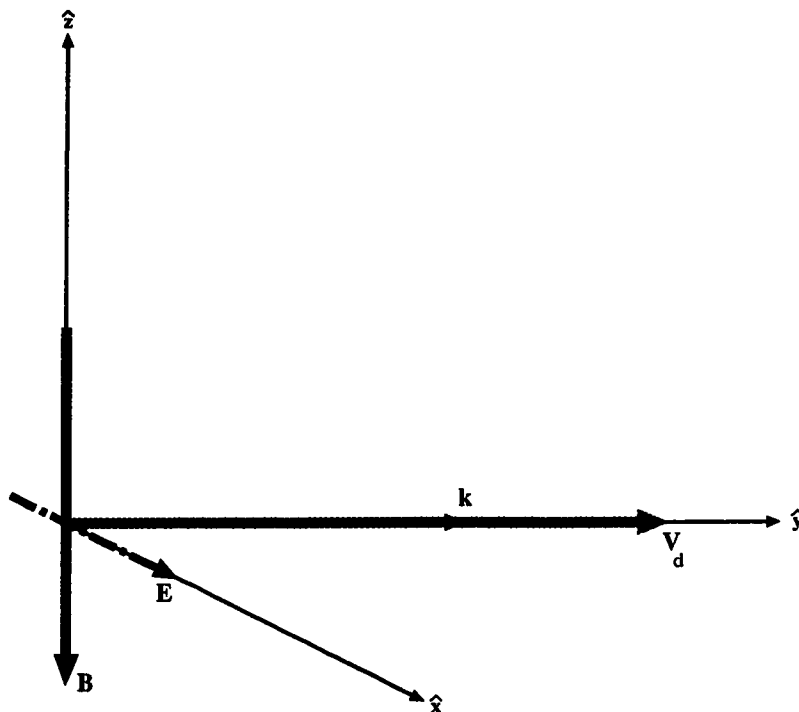


Figure 5.1: The geometry used for the one dimensional three fluid model. In the model the perturbations are assumed to be constrained to the  $\hat{y}$  direction, the ambient electric field is in the  $\hat{x}$  direction, and the magnetic field is downward in the  $-\hat{z}$  direction. This configuration is appropriate for the northern auroral E-region ionosphere.

equilibrium on time scales shorter than one second. Because radar observations have integration times at least this long, any effects from ion temperature differences are not likely to be recognizable in the observations.

In order to understand the meaning of the three fluid dispersion relation it is useful to solve equation A.31 for the frequency response  $\omega$  in terms of the wave vector  $k$ . The result is a fifth order polynomial in  $\omega$ . This is equation A.32 and the expanded form is the most tractable for numerical root finding. By solving for the real and imaginary portion of  $\omega$  with an assortment of possible ionospheric parameters five wave modes are revealed. These modes are summarized in Table 5.1, where  $C_{s3}$  is an ion-ion acoustic mode velocity.

$$C_{s3} = \sqrt{\frac{k_b(T_{i1} + T_{i2})}{m_{i1} + m_{i2}}} \quad (5.2)$$

Table 5.1: An overview of wave modes predicted by the three fluid theory.

wave mode	characteristic velocities	typical growth or damping
mode 1	$V_d$ electron drift velocity	growth for $V_d > C_s$
mode $3_p$	$C_{s3}$	weakly damped
mode $3_m$	$-C_{s3}$	weakly damped
mode $4_p$	positive high velocity	strongly damped
mode $4_m$	negative high velocity	strongly damped

The most relevant wave modes are those that are growing or weakly damped. Growing modes in the system will form waves that are likely to be observable by radars or sounding rockets, and weakly damped modes may have energy coupled into them by non-linear processes such as wave-wave interactions. The weakly damped modes may be important for dissipating energy accumulated by the growing modes, especially when the damping rate is comparable to the growth rate of the growing modes. Strongly damped modes are not likely to be excited by any process and in

general I do not focus on mode  $4_p$  and mode  $4_m$ .

### *5.3.1 The Model Ionosphere*

To evaluate the three fluid model in as realistic a manner as possible it is necessary to have an ionospheric model. In order to provide all the parameters necessary I have combined output from three models: the International Reference Ionosphere (IRI-95), the Mesosphere Stratosphere Incoherent Scatter Model with E-region (MSIS-E-90), and the International Geomagnetic Reference Field Model (IGRF). The models were evaluated for August 27, 1998 at 10:00 UT at a location of  $60^\circ$  N latitude and  $120^\circ$  W longitude.

### *5.3.2 Model Parameter Sweeps*

The three fluid model is evaluated for a given set of model parameters by numerically finding the roots of equation A.32. The root finder sometimes gets a bit confused, especially when solutions cross, and gaps in the model parameter sweeps are produced by the exclusion of these glitches.

In most cases the real portion of this equation is divided by the wave vector  $k$  in order to convert it to a phase velocity. The imaginary portion is not divided and simply gives the growth rate. When varying a parameter to determine the response of the system the other parameters are set using the ionospheric model at an E-region altitude of 110 km. The normal wavelength the irregularities are evaluated for is 1.5 m, the wavelength observed by the Manastash Ridge Radar system. The ion acoustic speed at this altitude is 372 m/s for the model parameters.

### *Drift Velocity*

Figure 5.2 shows the phase velocity response to variations in the electron drift velocity. Mode 1 responds as is expected from two fluid theory with a linear relationship



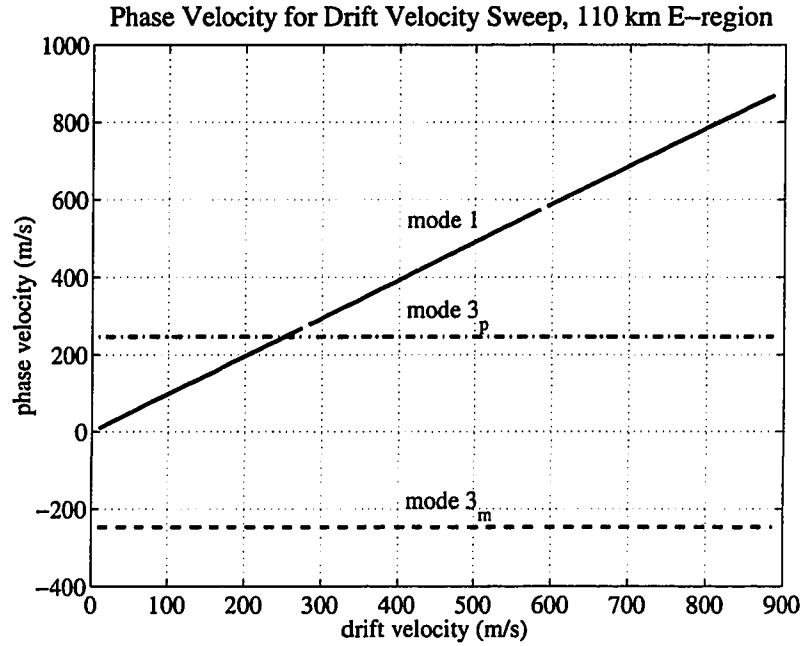


Figure 5.2: The phase velocity predicted by the three fluid model for variations in electron drift velocity.

between drift velocity and the phase velocity. Mode  $3_p$  has a positive phase velocity that is independent of the drift velocity, while mode  $3_m$  has a matching negative phase velocity. The phase velocity of mode  $3_p$  and mode  $3_m$  is significantly below the local ion acoustic speed and corresponds to that predicted for an acoustic mode between the two ion species. It is in the range that would be expected for Type-3 irregularities.

Examining the growth rate versus drift velocity in Figure 5.3 shows that mode 1 is damped until the drift velocity exceeds the ion acoustic speed and the growth increases with increasing drift. Mode  $3_p$  and  $3_m$  have the same growth rate and are moderately damped at this altitude.

The damping of the mode 3 solutions is probably too large to allow the mode to grow due to non-linear mode coupling. Any energy coupled into this mode would be rapidly dissipated without wave growth under these particular ionospheric con-

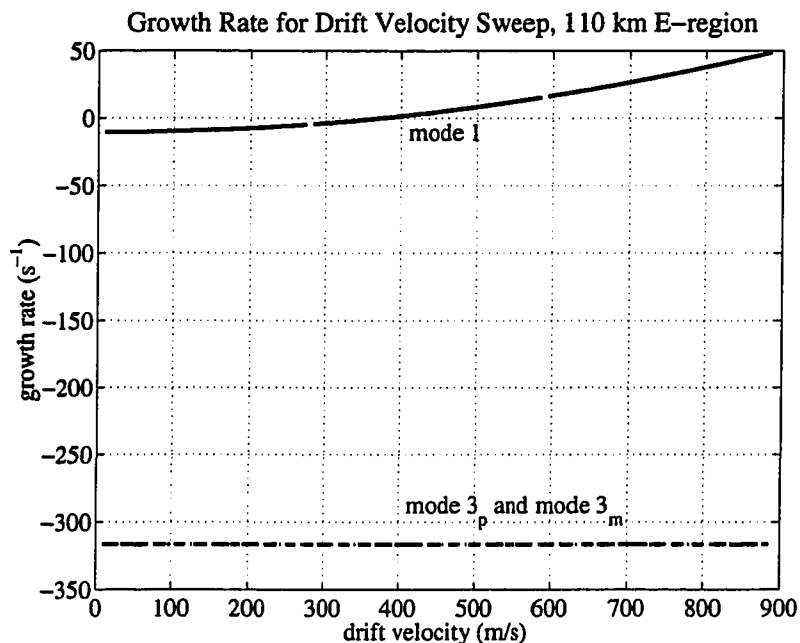


Figure 5.3: The growth rate predicted by the three fluid model for variations in electron drift velocity.

ditions.

### *Wavelength Dependence*

Irregularity wavelength is another fundamental parameter of the system. It is directly related to the wave vector by the standard relation.

$$k = \frac{2\pi}{\lambda} \quad (5.3)$$

The phase velocity wavelength dependence is shown in Figure 5.4. Typical irregularity wavelengths observed by radars are between 1 and 3 m. Here the mode 1 phase velocity does not have any significant wavelength dependence and this is again consistent with the results from two fluid theory predictions.

The mode 3 solutions have an interesting wavelength dependence with the 3<sub>p</sub>

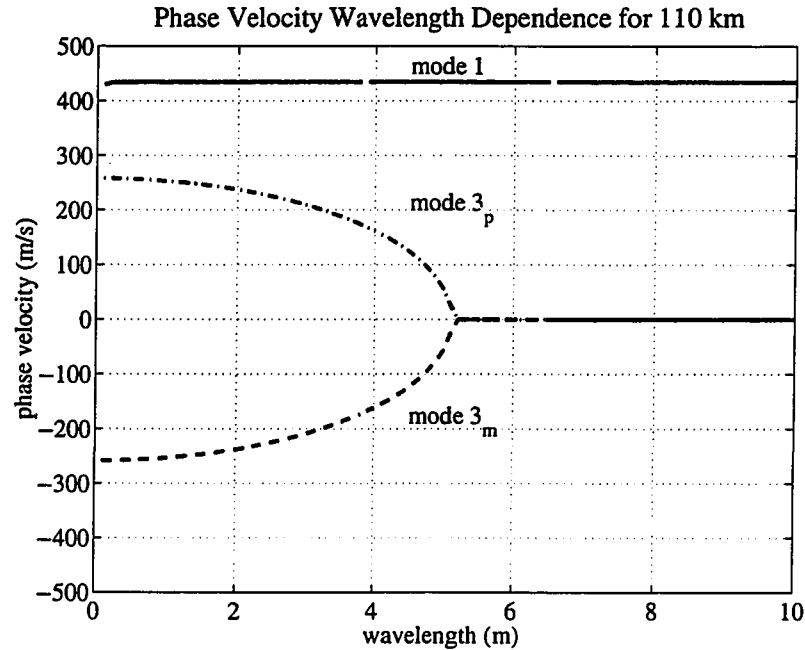


Figure 5.4: The phase velocity predictions for variations in irregularity wavelength.

and  $3_m$  modes ceasing to propagate for sufficiently long wavelength. The wavelength where the mode 3 solutions join shows a distinct altitude dependence (not shown) and goes to longer wavelengths at higher altitude.

Figure 5.5 shows the growth rate variation with wavelength. Mode 1 shows the unrealistic growth at short wavelengths that is characteristic of fluid models. The lower wavelength limit of these models is set by the ion mean free path and from kinetic theories is established to be at about 1 m.

The mode 3 solutions shows the complementary behavior of the equation with the mode degeneracy being opposite that of the phase velocity solution. Although mode  $3_m$  becomes weakly damped at long wavelength its wave frequency has gone to zero in this region and so it is not likely that any energy could be coupled into the mode at large wavelengths.

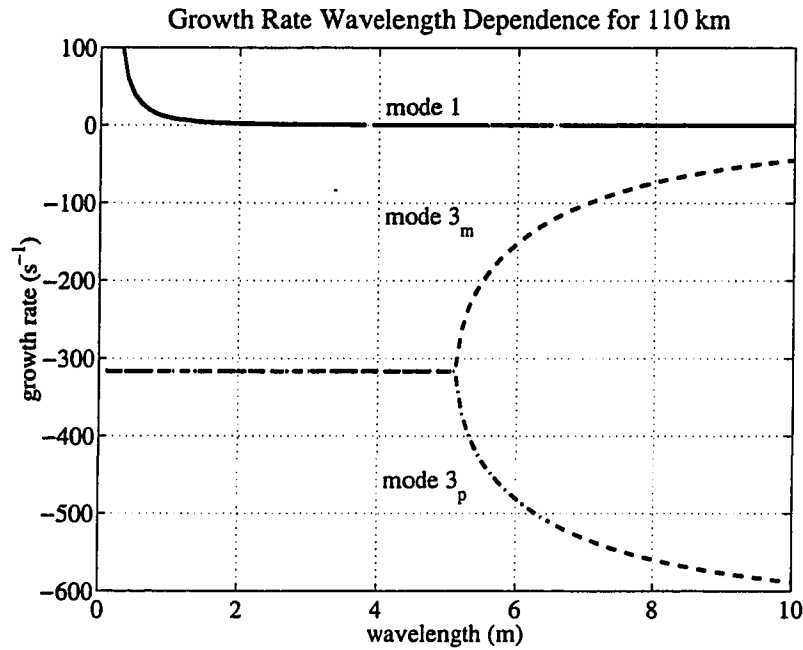


Figure 5.5: The growth rate predictions for variations in irregularity wavelength.

### *Ion Mass*

In examining the dependence of the three fluid model to ion mass I am only going to explore conditions that are reasonably realistic for the E-region ionosphere. To do so I hold one ion to be  $NO^+$  and allow the other ion to vary in mass. This represents a background ionosphere in which half the plasma is another ion species that has been deposited. One way for this to occur is the disintegration of a meteorite and the three fluid theory may be applicable to such situations. The system's behavior may be more interesting for other combinations of masses but investigating the full range of plasma compositions is beyond the scope of this work.

Figure 5.6 shows the phase velocity dependence of the three fluid model as the mass ratio of the ions is varied. Here the mode 1 is independent of the ion mass, being set by the electron drift velocity. In actual radar observations the Type-1 velocity would show variation as the ion acoustic speed varies, but the linear fluid theory is not able to predict this effect.

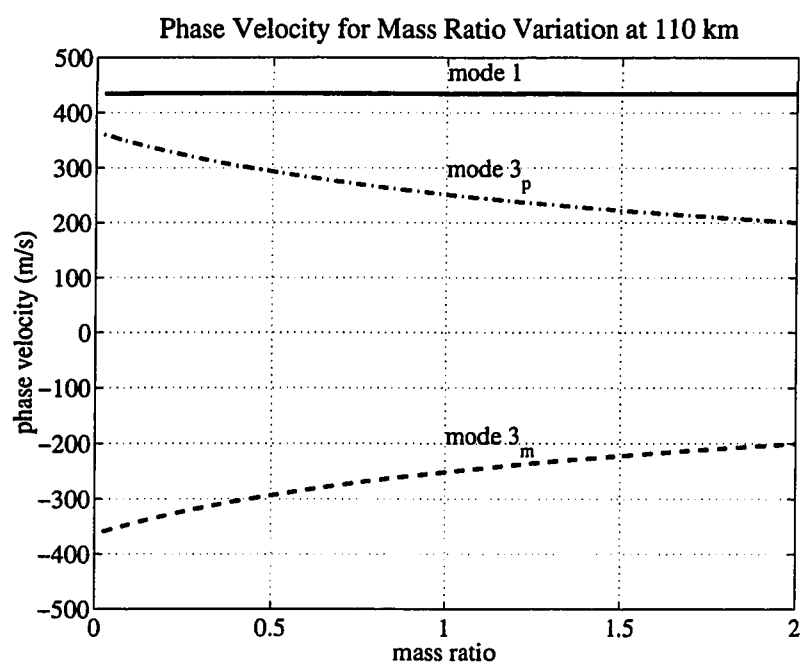


Figure 5.6: Model predictions of the phase velocity for variations in the ratio of the ion masses. One ion species,  $NO^+$ , is held fixed while the mass of the other is varied.

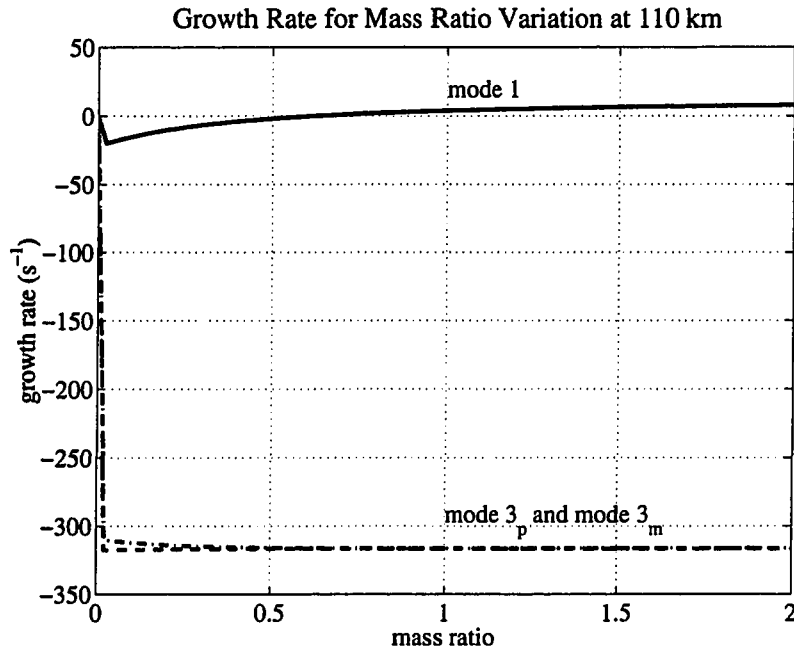


Figure 5.7: Model predictions of the growth rate for variations in the ratio of the ion masses. One ion species,  $NO^+$ , is held fixed while the mass of the other is varied.

The mode 3 phase velocities vary strongly in response to the ion mass variations. At the lower mass ratio limit the phase velocity approaches the ion acoustic speed  $C_s$ . If the mode 3 waves could be excited in the plasma, their phase velocity could be a good indication of the ion mass ratio of the plasma.

Figure 5.7 shows the growth rate variation with ion mass ratio. Here mode 1 shows a significant variation as the increase in ion acoustic speed causes the mode to be damped as the mean mass of the plasma becomes smaller. In a corresponding fashion the growth becomes stronger as the mean mass increases.

The mode 3 growth rates appear to be largely independent of the ion mass ratio, especially when the second ion is more massive than  $NO^+$ . A satisfying result is that the mode 3 solutions join the mode 1 solution when the second ion mass goes to zero. This implies that these modes disappear as we go to a single ion plasma.

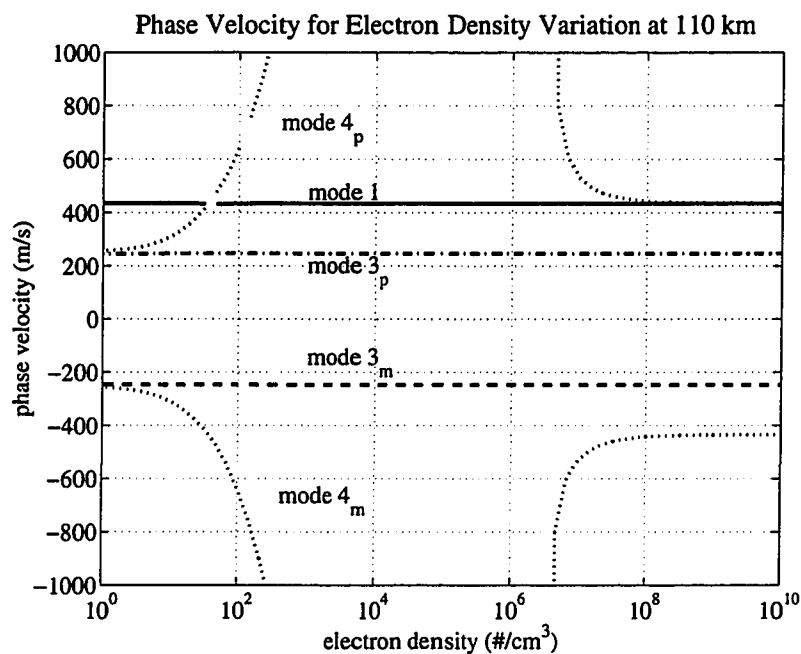


Figure 5.8: Phase velocity predictions for variations in the electron plasma density. The ion plasma density is varied to maintain quasi-neutrality assuming a 50-50 mix of both ion species.

### *Plasma Density*

In varying the plasma density I proceed by varying the electron density and using quasi-neutrality to set the ion density. Figure 5.8 now shows modes  $4_p$  and  $4_m$  because these modes now cross the solutions for the other modes and they are highly dependent on the electron density. The phase velocity of mode 1, mode  $3_p$ , and mode  $3_m$  is independent of the electron density. This is not surprising as the mode 1 velocity is dominated by the electron drift velocity and the mode 3 velocities are determined by the ion masses.

The mode 4 velocities are interesting and become very large (10 km/s) in the region of realistic E-region densities between  $10^4$  and  $10^6$  electrons per  $cm^3$ . These modes appear to be fast electron plasma waves that are strongly damped in the E-region.

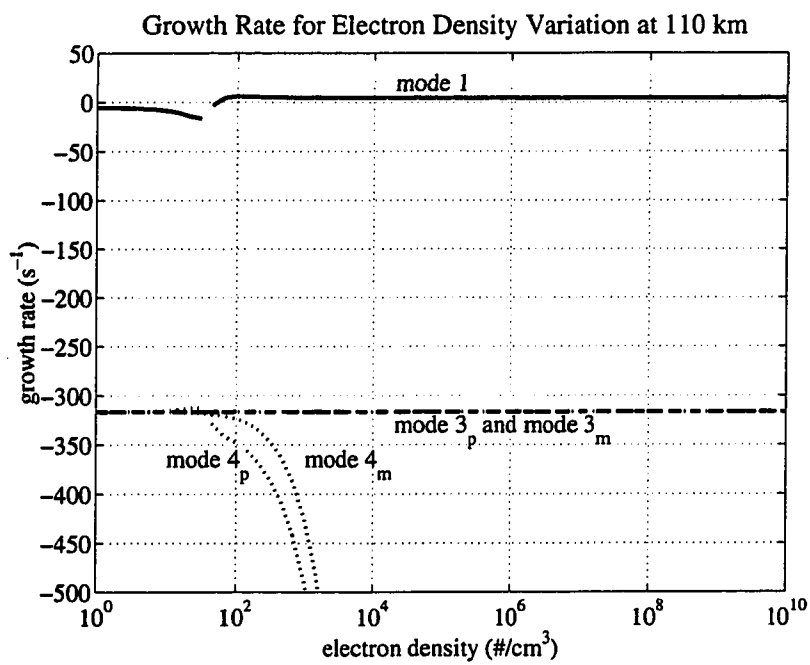


Figure 5.9: Growth rate predictions for variations in the electron plasma density. The ion plasma density is varied to maintain quasi-neutrality assuming a 50-50 mix of both ion species.



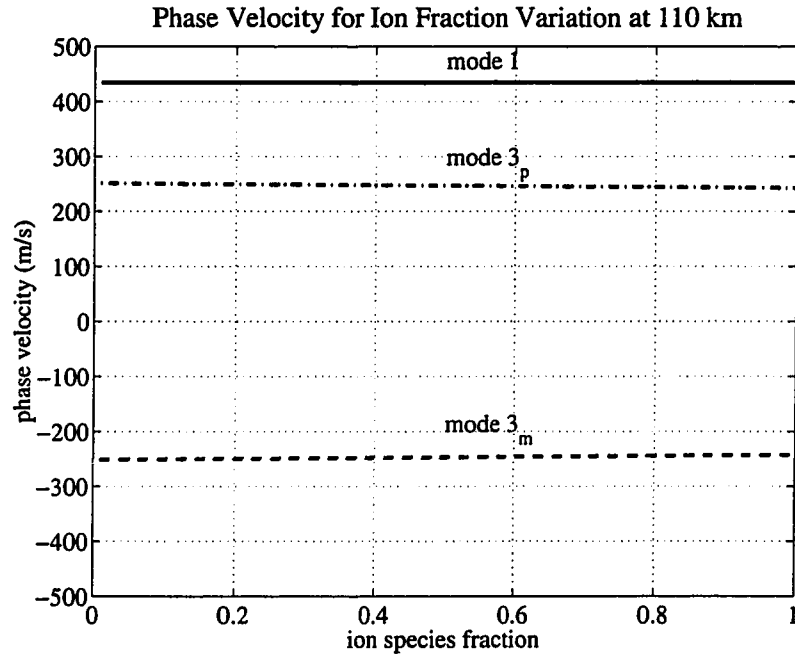


Figure 5.10: The phase velocity predictions for variations in the fraction of one ion species relative to another. The lack of variation points to a possible flaw in the model.

Examining the growth rates in Figure 5.9 clarifies that the mode 4 waves are at best moderately damped at low electron densities. It is highly unlikely that this mode is ever important in the E-region. The growth of the mode 3 waves is independent of the electron density, and the mode 1 wave shows a transition to damping when the electron density is low enough. Electron density variations over realistic E-region will not produced changes in irregularity behavior unless they are accompanied by variations in other parameters.

### *Ion Fraction*

Figure 5.10 shows the effect of varying the fraction of  $O_2^+$  relative to  $NO^+$ , while holding the total ion density constant. The mode 3 phase velocities have only a slight dependence and mode 1 is independent of this variation.

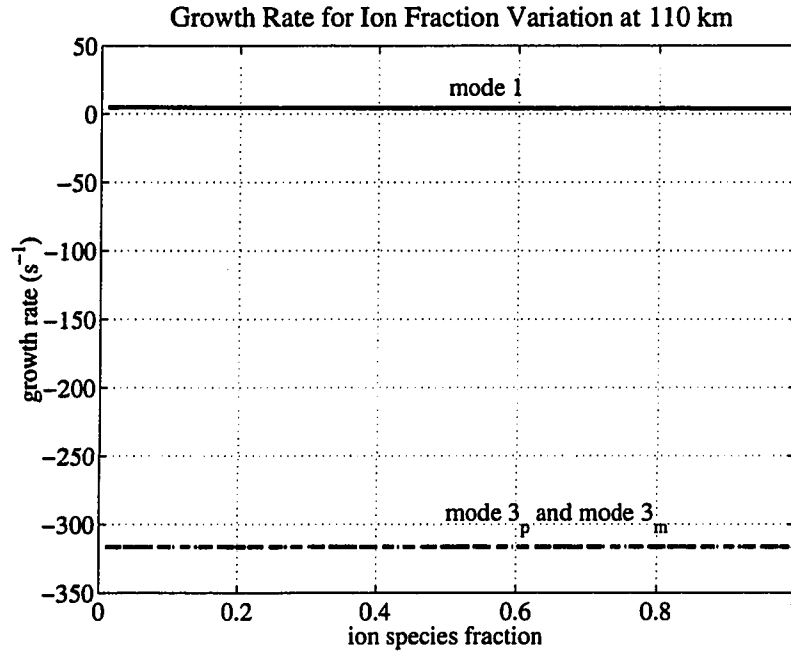


Figure 5.11: The growth rate predictions for variations in the fraction of one ion species relative to another. The lack of variation points to a possible flaw in the model.

The growth rates of modes 1, 3<sub>p</sub>, and 3<sub>m</sub> are shown in Figure 5.11 and are independent of the ion species fraction. This is not particularly surprising for mode 1 which should be unaffected so long as the total ion density remains the same.

What is surprising is that the mode 3 waves do not respond to the fraction of one ion species relative to the other. In fact, I would expect the mode to disappear completely as the fraction goes to zero. This indicates that the model may have a problem with how it is incorporating the ion density. The most probable cause is the simplification of a single ion neutral collision frequency. When this is combined with the fact that the collision model [*Schunk and Nagy, 1980*] does not take account of ion density variations it could produce the observed lack of variation.

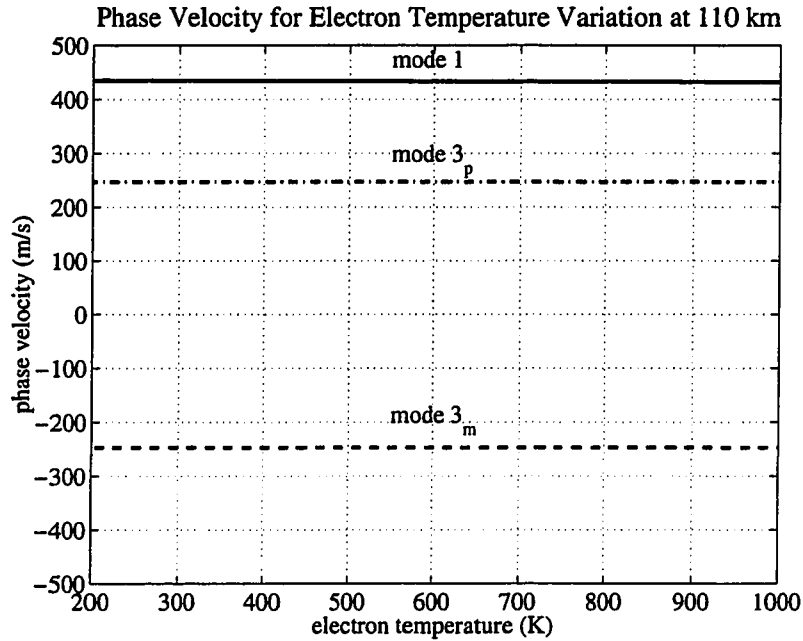


Figure 5.12: Model phase velocity predictions due to electron temperature variations.

### *Electron Temperature*

The phase velocity variation with electron temperature is shown in Figure 5.12 and mode 1,  $3_p$ , and  $3_m$  are all independent of  $T_e$ .

The independence of mode 1 is not surprising because the linear fluid theory does not incorporate phase velocity effects due to changes in the ion acoustic speed. The mode 3 waves are clearly produced by ion-ion inertial effects with ion-electron effects not being well modeled by the linear theory.

The growth rate dependence is shown in Figure 5.13 and the change in acoustic speed as the electron temperature increases clearly shows a transition at the drift velocity.  $V_d$  is set to 410 m/s in this model run, and this is where mode 1 stops growing. The growth of the mode 3 waves is clearly independent of the electron temperature.

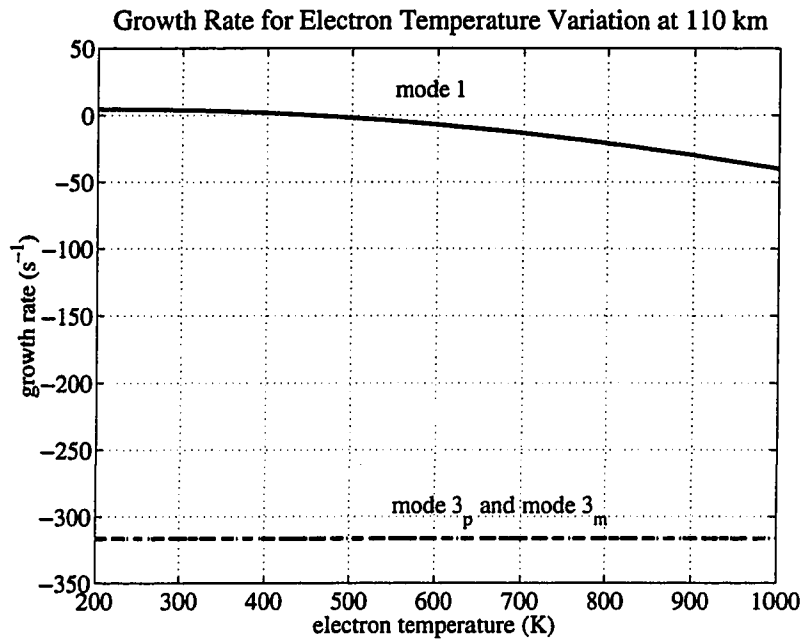


Figure 5.13: Model growth rate predictions due to electron temperature variations.

### *Ion Temperature*

The situation for ion temperature variations is quite different. The phase velocity variation is shown in Figure 5.14 and again mode 1 is independent of the variation in  $T_i$ . The mode 3 phase velocities are strongly dependent on the ion temperature. Variation in temperature can produce a range of possible velocities that is comparable to the whole range of irregularity velocities observed by coherent scatter radars. Thus if one of the mode 3 waves were to be excited it might not be possible to distinguish it from a mode 1 wave by phase velocity alone.

The growth rate variation is shown in Figure 5.15 and here the growth of the mode 3 waves is independent of temperature. Ion temperature is an equal contributor to the ion acoustic speed so the mode 1 wave behaves exactly as it did for electron temperature variations. As the acoustic speed exceeds the drift velocity, the mode 1 wave stops growing.

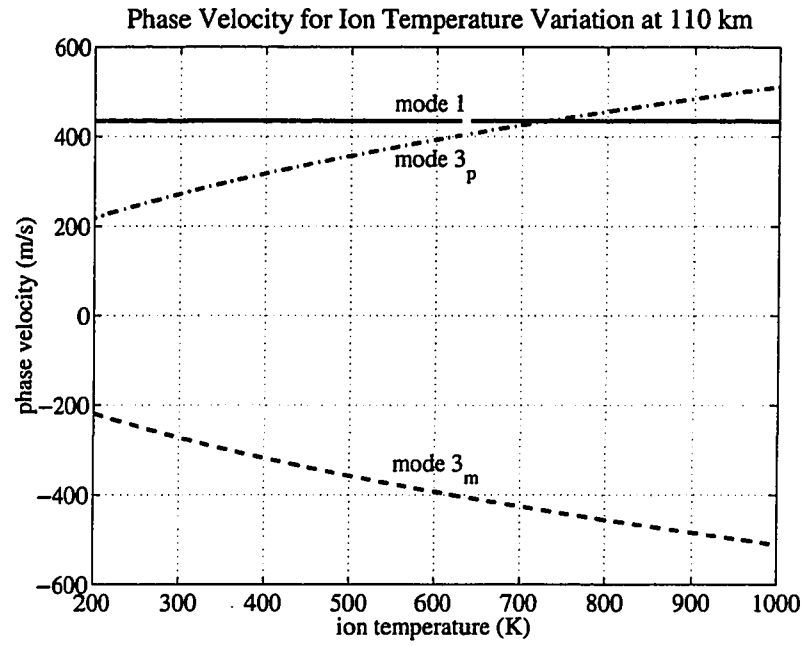


Figure 5.14: The phase velocity variations due to the ion temperature sweep.

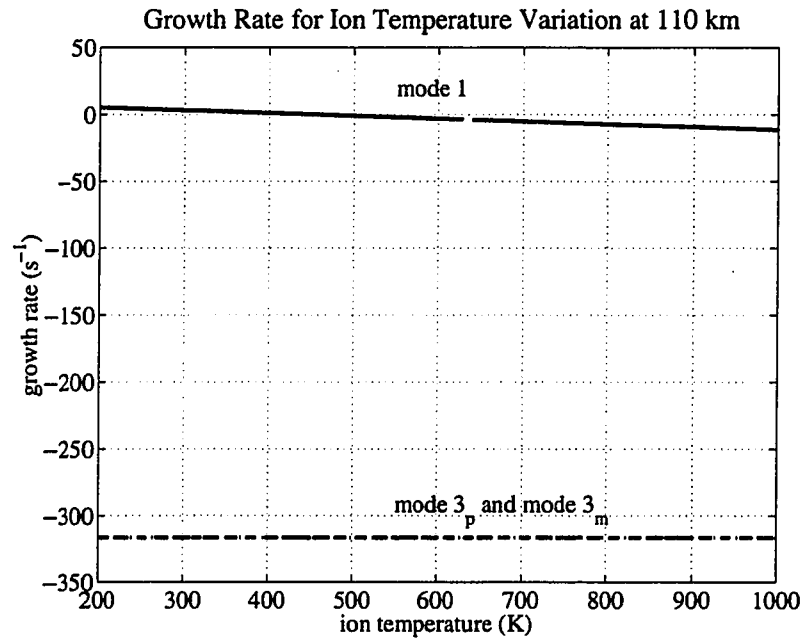


Figure 5.15: The growth rate variations due to the ion temperature sweep.

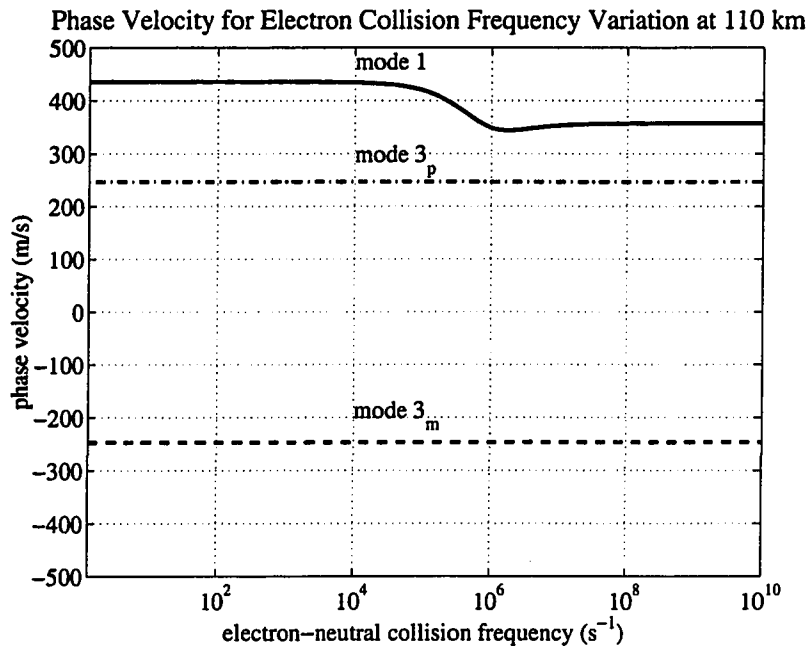


Figure 5.16: The phase velocity predicted by the model for variations in the electron-neutral collision frequency.

### *Electron Collision Frequency*

The effect of electron collision frequency variation in Figure 5.16 show that the mode 3 waves are independent of this parameter. Mode 1 shows a transition in phase velocity to roughly the ion acoustic speed as the collision frequency increases to the point where the electrons become demagnetized. This is essentially a statement that the streaming instability has stopped because there is no longer a Hall drift.

This is reflected in the growth rate as can be clearly seen in Figure 5.17. Here the peak mode 1 growth is just prior to the transition to moderate damping. It is very interesting that this damping level is the same as that maintained by the mode 3 waves. This implies that as the electron streaming instability shuts off it is the ions that become most important in the plasma dynamics.

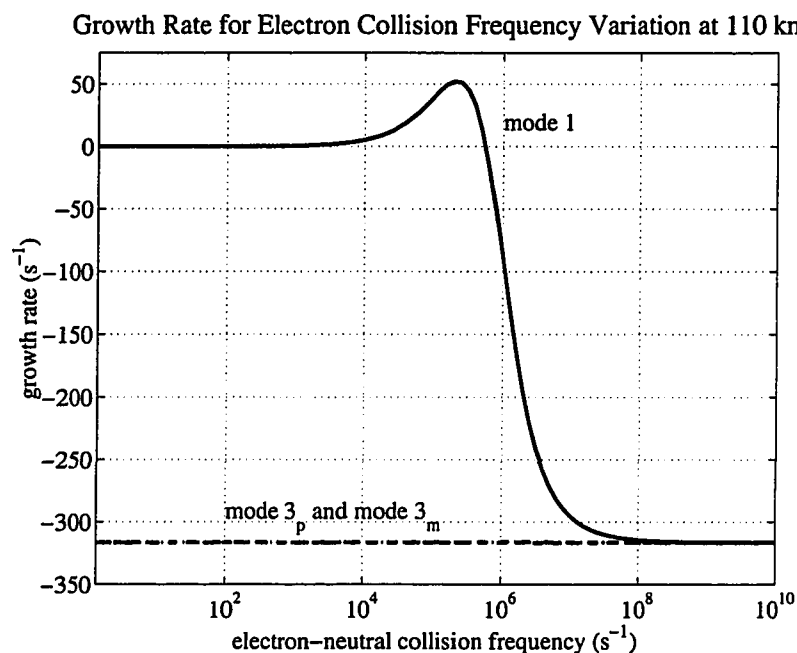


Figure 5.17: The growth rate predicted by the model for variations in the electron-neutral collision frequency.

### *Ion Collision Frequency*

By now it is clear that we should expect the ion neutral collision frequency to play an important role in the mode 3 waves. Figure 5.18 demonstrates that this is true for the phase velocity.

Here the mode 3 waves merge to zero phase velocity for sufficiently large collision frequency due to the wave frequency going to zero. The mode 1 wave is strongly effected by the increased ion-neutral collision frequencies although as can be seen from Figure 5.19 this variation occurs once mode 1 becomes damped.

The mode 3 waves also show a dramatic variation in growth rate with ion neutral collision frequency. Here we finally see that there are conditions for which both mode  $3_p$  and  $3_m$  are weakly damped. Interestingly this is outside the collision frequency range that is most associated with the growth of mode 1 irregularities. There are some complications with this particular parameter sweep as the root structure is

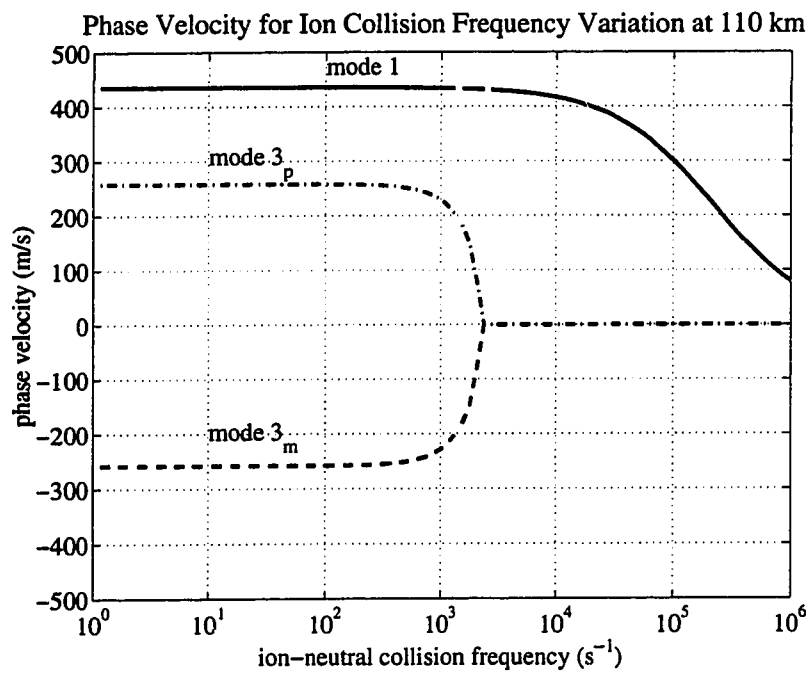


Figure 5.18: The model predictions of the phase velocity variation for a sweep of the ion-neutral collision frequency. The mode 1 velocity varies substantially as the ion-neutral collision frequency increases.



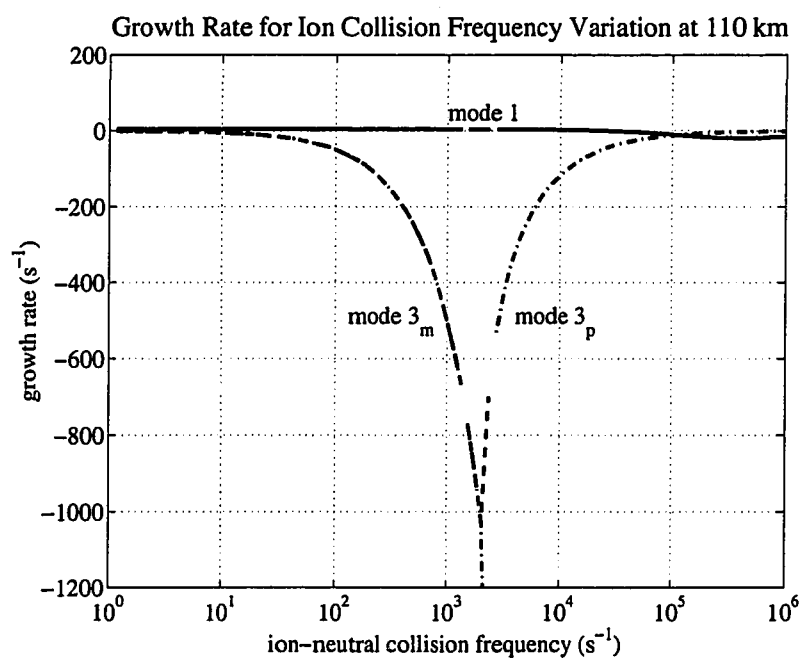


Figure 5.19: Model predictions of the growth rate variation for a sweep of the ion-neutral collision frequency. The mode 3 growth rates becomes weakly damped at high and low collision frequencies.

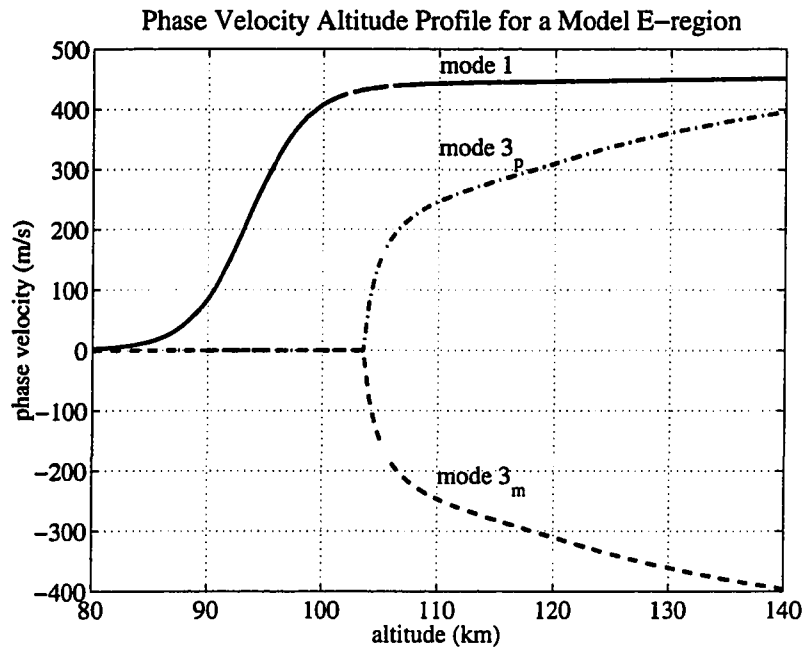


Figure 5.20: The phase velocity predictions of the three fluid model for an altitude sweep through a model ionosphere.

complicated for the root finder to resolve. At high collision frequencies it is also notable that mode  $3_p$  is less damped than mode 1.

#### *Model E-region Altitude Sweep*

The last evaluation of the three fluid model involves sweeping over altitude. In many ways the altitude sweep is very similar to the ion collision frequency variation above. Figure 5.20 shows the altitude dependence of the mode 3 velocities with the degeneracy into positive and negative going modes just below 105 km. The phase velocity of the mode 1 wave also varies significantly towards the bottom of the E-region and this is another possible explanation for the Type-3 irregularities. This variation is primarily due to the increase in ion-neutral collision frequency.

Figure 5.21 again shows similar results to the ion-neutral collision frequency plots. Here the mode 3 waves are strongly damped in the central E-region where

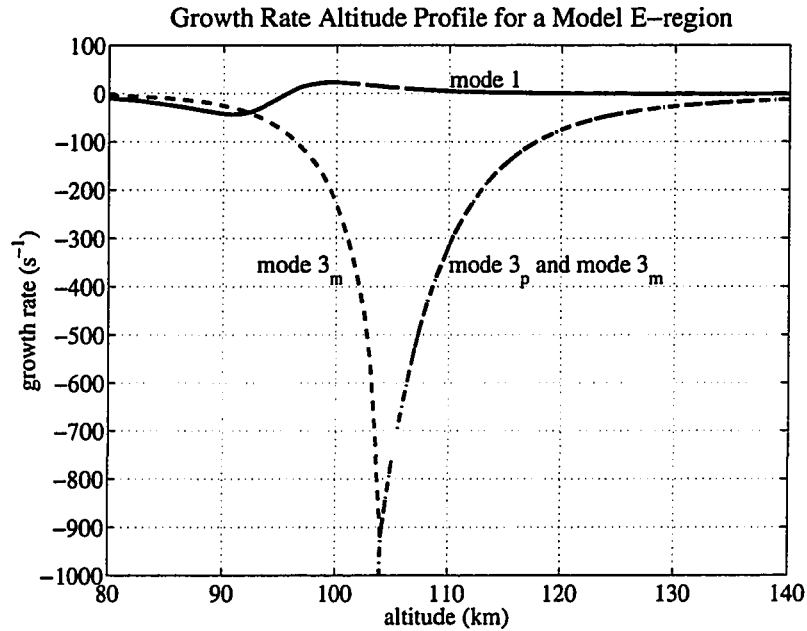


Figure 5.21: The growth rate predictions of the three fluid model for an altitude sweep through a model ionosphere.

the mode 1 waves are expected to grow. Only at high and low altitude does the growth rate of the mode 3 waves become weakly damped. Mode  $3_p$  which propagates in the same direction as the drift velocity does not appear to grow at low altitudes, and while mode  $3_m$  has a weakly damped growth rate the phase velocity in the lower E-region is zero. It is likely that if energy can be coupled into either mode  $3_p$  or  $3_m$  it will be in the upper E-region.

#### 5.4 A Brief Interpretation

The three fluid model reveals interesting behavior for both mode 1 and mode 3 waves. The mode 1 wave clearly behaves in a similar manner to the traditional two stream instability that is derived from two fluid theory. This mode is an ion-electron acoustic mode that derives its growth under conditions of strong electron drift. The phase velocities in the lower E-region diverge greatly from the electron drift velocity

$V_d$  that is the normal speed predicted by two fluid theory. The range covered is sufficient to explain the observations of Type-3 waves for somewhat enhanced mode 1 growth. The controlling parameter for these lowered phase velocities appears to be the ion-neutral collision frequency.

Interpretation of the mode 3 waves is more problematic. The mode behaves as a damped ion-ion acoustic mode and even obeys the expected acoustic velocity relationship  $C_{s3}$  at high altitudes. This mode might have positive growth rate for a differential drift between ion species but it is difficult to see how such a selective drift could occur in the E-region. The mode 3 waves are clearly always damped and so will not arise from the linear theory of the instability. It may be possible to couple energy into these modes from strong mode 1 instabilities through nonlinear wave-wave interactions. I have not shown that this can occur and the three fluid system is complicated enough without nonlinearities being introduced. This is a potential direction for theoretical investigation.

It is also not clear that this mode can generate electron density perturbations that are observable with radar. This would depend on the relative phase relationship between any ion perturbations and I have not evaluated this relationship here.

The mode 3 waves may be important for dissipation of energy from mode 1 instabilities, especially at upper E-region altitudes. Modes of this type may also be important in situations where the ion composition of the E-region ionosphere has been substantially modified by deposition of other ion species by meteors. One possibility for detecting the presence of mode 3 waves is to observe their response to ion temperature enhancements but not to electron temperature enhancements. This would require very high time resolution with a coherent scatter radar and an independent measure of ion and electron temperature in the scattering volume.

### 5.5 The Production of Type-3 Waves

Perhaps the most fundamental observed property of the Type-3 radio aurora is the existence of a preferred phase velocity between about 150 and 250  $ms^{-1}$ , this is well below the nominal ion acoustic speed in the region. This preferred velocity is clearly shown in work done with the Cornell 50-MHz CUPRI radar [Fejer *et al.*, 1984b; Providakes *et al.*, 1985; Providakes, 1985; Fejer and Providakes, 1987; Sahr, 1990; Sahr *et al.*, 1991], as well as in results from STARE 140-MHz measurements [Haldoupis and Nielsen, 1989a; Haldoupis *et al.*, 1992]. The narrow doppler widths of the spectrum also imply a resonant like production mechanism [Haldoupis *et al.*, 1995a].

As I have demonstrated with the three fluid model, it may be possible to produce mode 1 waves having an appropriate velocity for conditions of enhanced ion-neutral collision frequency. Collision frequencies of between  $10^5$  and  $10^6$  should be sufficient to produce the full range of observed velocities. This implies that the Type-3 wave is simply the Type-1 wave under different and somewhat rarer conditions. A direct test of this hypothesis is to measure the ion-neutral collision frequency while simultaneously observing Type-3 radio aurora with a coherent scatter radar. Such an experiment may be possible with the combination of a coherent scatter radar and incoherent scatter or sounding rocket observations. This is probably a difficult experiment to perform.

## Chapter 6

# RADAR METHODS FOR OBSERVING E-REGION IRREGULARITIES

E-region irregularities occur at altitudes too high for balloon borne payloads and too low for direct satellite observations. To date the primary observations of the irregularities have been from a relatively small number of sounding rocket flights and a somewhat larger collection of radar observations (see Table 4.1).

### ***6.1 The Coherent Scatter Radar***

The primary radar technique for observing the irregularities is termed “coherent scatter” for the way in which the scattered radar signals sum in-phase (or coherently) at the receiver. Coherent scatter radars take advantage of the large radar cross section presented by the irregularities (for certain geometries) to make observations using relatively modest radar systems.

By making observations using radar it is possible to observe the spatial structure, velocities, spectral shapes, and amplitudes of the irregularities. At the present time it is difficult to relate these observations to more physical parameters, as a model capable of accurately predicting even the full range of observed velocities and spectral shapes has not been successfully developed.

This is in contrast to the technique of “incoherent” scatter in which the Thomson scatter from thermal fluctuations of the ionospheric plasma is well understood. However, this lack of a comprehensive understanding of coherent scatter, combined with the importance of the irregularities to the physics of the larger magnetospheric

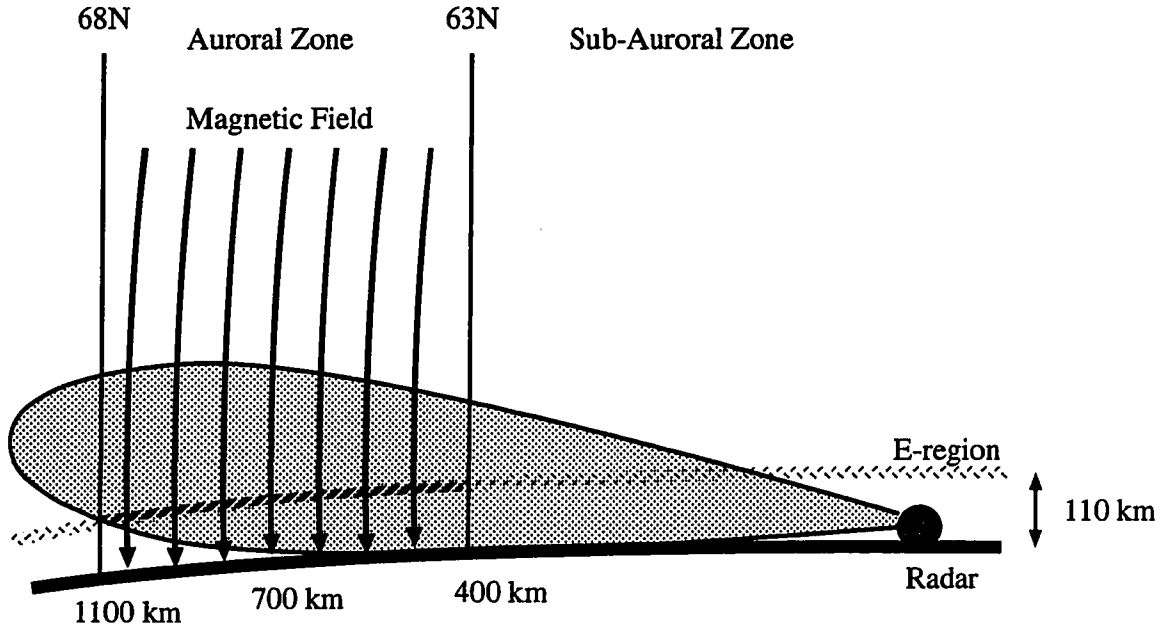


Figure 6.1: The coherent scattering geometry in the northern hemisphere. Here a radar system illuminates the E-region ionosphere from the south. Irregularities in the E-region will scatter the radar signal allowing their detection. The auroral zone can move north and south somewhat due to changing ionospheric conditions.

environment, makes them interesting to study.

## 6.2 Theory of Observations

The geometry of a typical coherent scatter radar experiment is shown in Figure 6.1 for the case of auroral E-region irregularities. The radar system is sited several hundred kilometers equatorward of the auroral zone, looking poleward. Radio signals are transmitted into the ionosphere where they can scatter from the E-region irregularities. This scattered signal is then detected by the radar and is greatest when the radar signal is nearly perpendicular to the Earth's magnetic field.

Figure 6.2 shows the volume scattering cross-section of E-region irregularities relative to that of incoherent scatter. The large cross-section allow the irregularities to be observed with relatively low power radar systems.

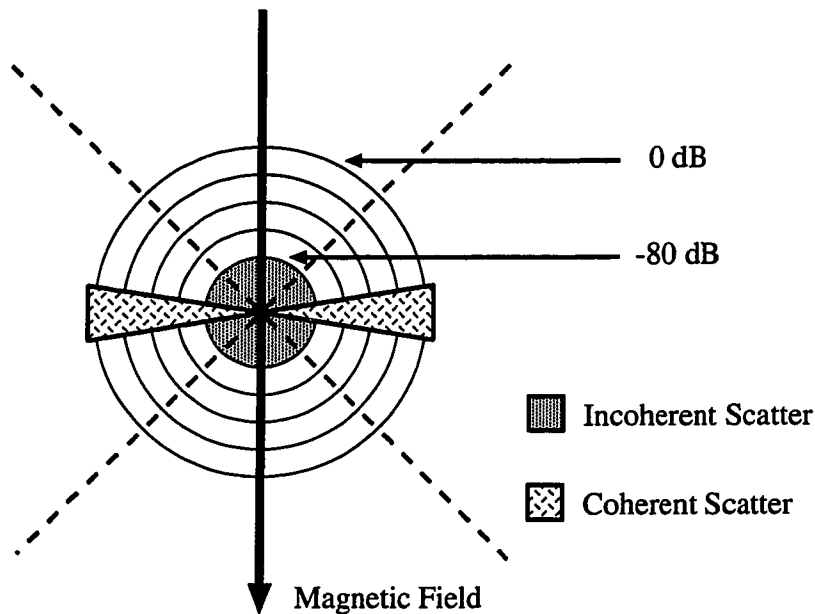


Figure 6.2: The cross-section of the irregularities is strongly anisotropic relative to the Earth's magnetic field and very large compared to the cross-section for incoherent scatter.

The scattering cross section of the irregularities falls off rapidly (10-15 dB per degree) away from perpendicular, and most coherent scatter radars are not sensitive enough to detect the irregularities at large aspect angles. Measuring the aspect angle dependence of the irregularities is most easily done using incoherent scatter radars because the large transmitter powers and high antenna gains make these systems extraordinarily sensitive.

### 6.2.1 Radar Technique

In general a radar transmits a signal that is scattered from a target or medium where there are inhomogeneities in the dielectric constant  $\epsilon$ . These inhomogeneities may be due to aircraft, plasma density irregularities, or even thermally excited fluctuations in ionospheric electron densities. This signal propagates to the target, is scattered, and then at some later time the return signal is received by the radar system. The



signal strength at the end of this process is much lower because it has propagated a great distance, moving spherically outwards. Assuming a narrow-band signal, this process is described by the radar equation

$$P_R = \frac{P_t G_t G_r \lambda^2 \sigma}{(4\pi)^3 R_t^2 R_r^2} \quad (6.1)$$

which relates the power transmitted to the power received in terms of the transmit and receive antenna gains  $G_t$  and  $G_r$ , the system wavelength  $\lambda$ , the scattering cross-section  $\sigma$ , the distance traveled from transmitter to target  $R_t$ , and from target to receiver  $R_r$ . The radar system performs the detection of the scattered signal in the presence of noise that is a combination of thermal background noise and that generated by the radar receiver. The noise power is given by

$$P_{noise} = F k_b T_{sys} B \quad (6.2)$$

where  $F$  is the receiver noise figure, and  $B$  is the receiver bandwidth. The received power must exceed the noise power (usually after additional signal processing) in order for the scatterer to be detected. This is usually defined as the signal to noise ratio (SNR)

$$SNR = \frac{P_R}{P_{noise}} \quad (6.3)$$

before signal processing, and when the SNR is large a scatterer is directly detectable. In many cases the detection of a particular target of interest is more complicated than is implied by this basic approach. Often scatter from more than one targets may be simultaneously received by a radar. This “clutter” contribution is not actually

noise, but it can prevent the detection of a signal of interest.

One approach to studying a geophysical target using a radar system lies in estimating the autocorrelation function of the target as a function of range [*Sahr and Lind, 1997*]. Assuming stationarity this is given by

$$R_{\sigma\sigma}(r, \tau) = \langle \sigma(r, t) \sigma^*(r, t - \tau) \rangle \quad (6.4)$$

where  $\sigma$  is the target scattering amplitude at time  $t$  and range  $r$ , and  $\tau$  is the correlation lag variable (which through a Fourier transform can be related to the doppler shift of the target). For a transmitter signal  $x(t)$  and a scattering amplitude  $\sigma(r, t)$ , the received signal is given by

$$y(t) = \int_0^\infty x(t - r) \sigma\left(\frac{r}{2}, t - \frac{r}{2}\right) dr \quad (6.5)$$

where the scattering amplitude of the target  $\sigma(t, r)$  is defined in time-like units for a time  $t$  and a range  $cr$ . The estimation of the target autocorrelation function proceeds from the cross-correlation of the transmitted and received signals,

$$Q\left(\frac{r}{2}, \tau\right) = \frac{1}{T} \int_{-\frac{T}{2}}^{\frac{T}{2}} y(t) x^*(t - r) y^*(t - \tau) x(t - r - \tau) dt \quad (6.6)$$

where the estimate is an average over a time period  $T$ . By evaluating the expected value of the cross-correlation  $\langle Q(\frac{r}{2}, \tau) \rangle$  it is possible to estimate  $R_{\sigma\sigma}(r, \tau)$ , although this can be complicated in practice.

In order for the estimation process to be useful, it is also necessary that the variance in the estimator be small. The variance is given by computing

$$\text{Var}(Q) = \langle |Q - \langle Q \rangle|^2 \rangle = \langle QQ^* \rangle - QQ^* \quad (6.7)$$

and it is directly dependent on the characteristics of the transmitter waveform  $x(t)$  and the target scattering amplitude  $\sigma(t, r)$ .

Different waveforms can be designed for detecting a particular type of target. Often these transmitter signals are designed to minimize the variance in the estimates of the target's autocorrelation function and maximize the probability of detecting the target. In other cases it is desirable to accept limitations that allow the signal to be optimized for the measurement of a particular parameter such as range or doppler shift.

### 6.2.2 Radar Resolution

Radars attempt to localize scatterers in time, range, azimuth, elevation, and velocity. A radar will have a resolution associated with each of these parameters. In many cases a particular radar system may not measure one or several of these variables. For example, many radars for irregularity research do not measure velocity.

The ability of a radar system to resolve a target in range, velocity, and time is directly related to the nature of the waveform that is transmitted. The self ambiguity of the transmitter signal is one way to evaluate the range and velocity resolution of a radar waveform. It is computed by

$$\chi(r, \nu) = \int_{-\infty}^{\infty} x(t)x^*\left(t - \frac{r}{c}\right)e^{2\pi i\nu t} dt \quad (6.8)$$

and represents the “blurring” that is produced by the radar waveform  $x(t)$ . Figure 6.3 shows the self ambiguity for single pulse of the type that might be transmitted

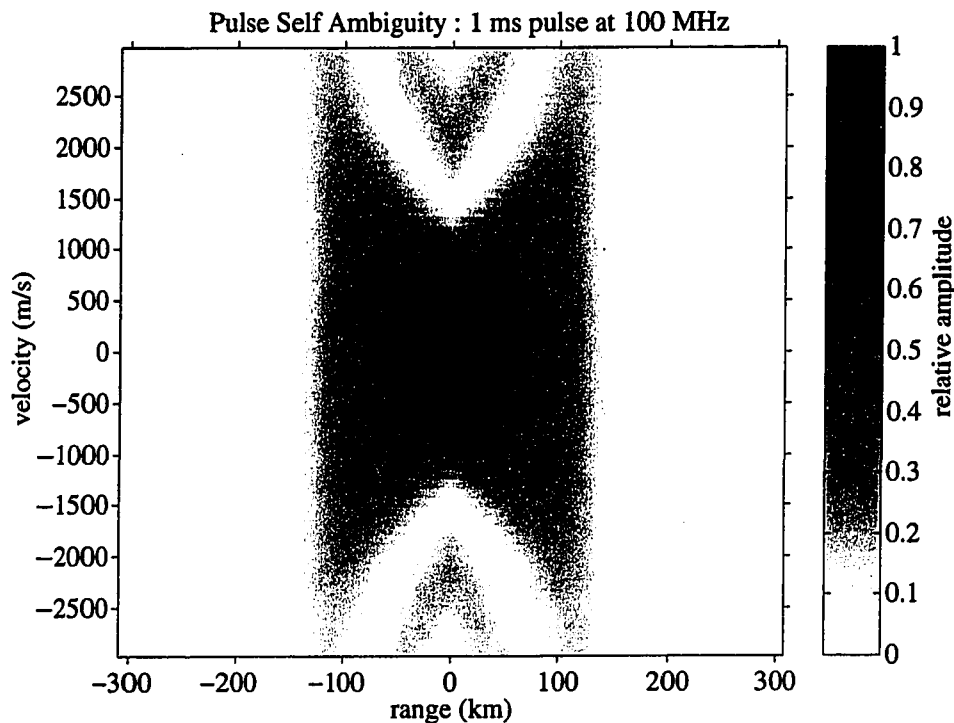


Figure 6.3: The computed self ambiguity of a 1 ms pulse at 100 MHz. A single pulse provides a broad ambiguity that does not localize targets particularly well.

by a traditional pulse mode radar.

The more “compact” the self ambiguity of the transmitted waveform, the better its ability to localize a target in range and velocity. An ideal radar has a delta function like self ambiguity, localizing a target to one particular point in range-velocity space.

Radar waveforms that produce compact self ambiguity are known as pulse compression methods because they attempt to shape the transmitted signal so that the self ambiguity is localized in range, velocity, or both. Examples of pulse compression techniques include Barker codes, pseudo noise sequences, and random codes. These techniques are largely beyond the scope of this work but details can be found in *Skolnik* [1990].

Figure 6.4 shows the self ambiguity of a random waveform. Random waveforms

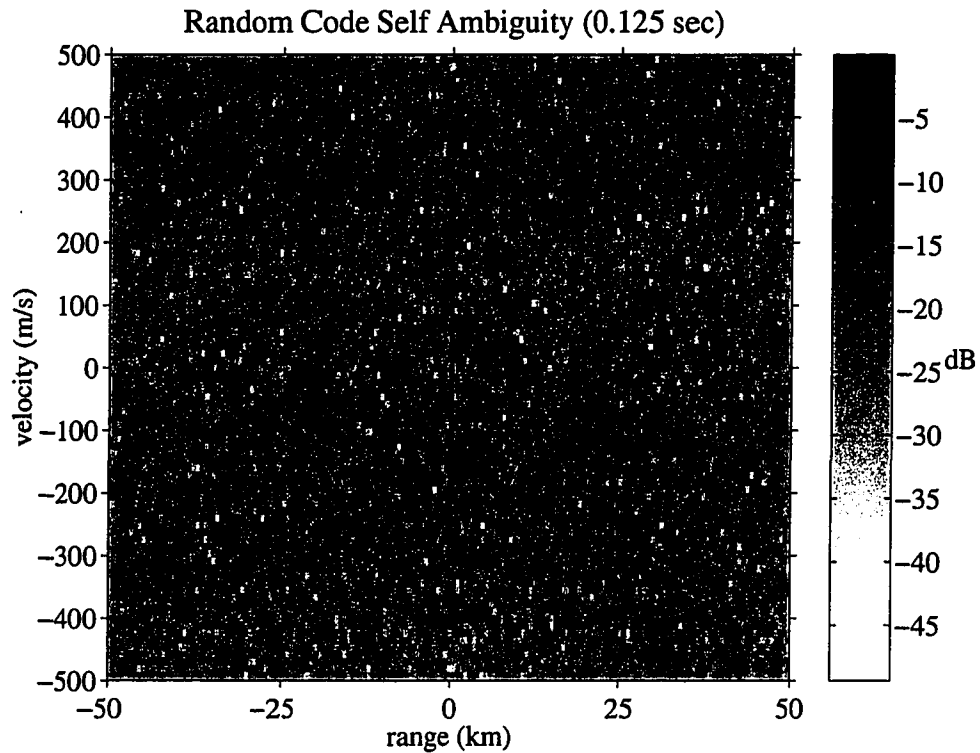


Figure 6.4: The computed self ambiguity of a random sequence for 0.125 seconds of data with a  $4 \mu\text{s}$  baud length. The ambiguity is very compact and thus random codes make good radar waveforms.

have very compact ambiguity and have been used in planetary and atmospheric radar experiments [Hagfors and Kofman, 1991; Sulzer, 1986]. They have the additional property of being completely alias free in range and velocity and so are also an example of an “overspread” radar technique. It is only recently that the computational power has become available to make random codes feasible for regular use.

### 6.2.3 The Bragg Scattering Condition

For E-region irregularities the incident ( $tx$ ), scattering ( $s$ ), and return ( $rx$ ) wave geometries must satisfy an energy ( $\hbar\omega$ ) and momentum ( $\hbar\mathbf{k}$ ) conservation relation in order for a significant return signal to be present.

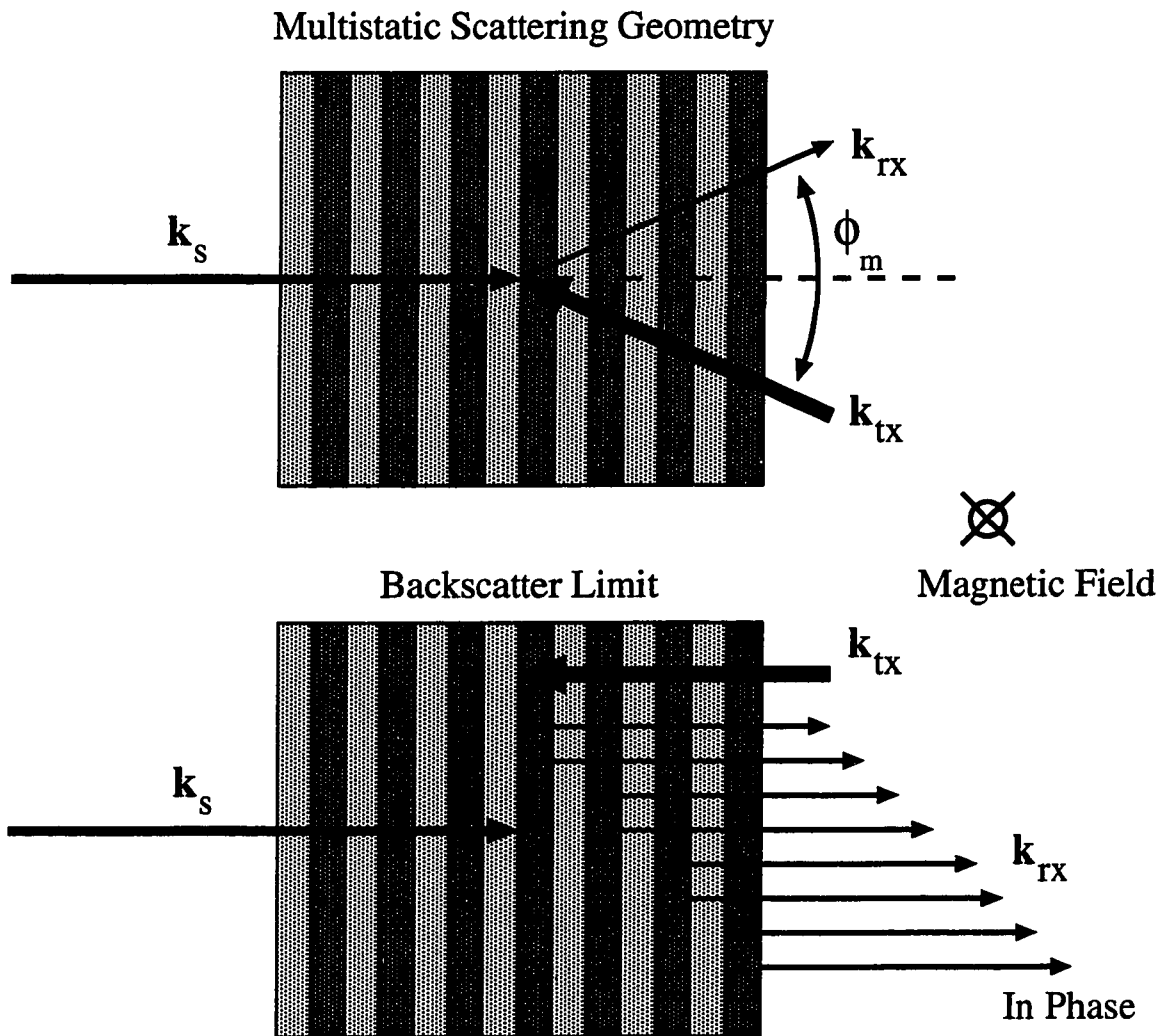


Figure 6.5: The Bragg scattering geometry is shown for multistatic and backscatter geometries. The periodic density perturbations of the E-region irregularities forms a scattering lattice for the incident transmitter signal  $\mathbf{k}_{tx}$ . The scatter occurs obeying energy and momentum conservation and results in a signal that returns to the receiver  $\mathbf{k}_{rx}$  coherently.

$$\omega_{tx} = \omega_{rx} + \omega_s \quad (6.9)$$

$$\mathbf{k}_{tx} = \mathbf{k}_{rx} + \mathbf{k}_s \quad (6.10)$$

This is often referred to as a Bragg scattering geometry, and is shown in Figure 6.5. The particular radar experiment determines the radar wave vector and frequency, the locations of the transmitters and receivers determine the geometrical relationship of the wave vectors, and nature determines if a scattering wave vector satisfying the relationship exists. Most radars have their transmitters and receivers in one location (monostatic) and the scattering geometry is constrained by

$$\mathbf{k}_{rx} = -\mathbf{k}_{tx} \quad (6.11)$$

which is just the condition for backscatter. The scattering wave vector  $\mathbf{k}_s$  is then constrained to be

$$\mathbf{k}_s = 2\mathbf{k}_{tx} \quad (6.12)$$

and this makes the wavelength of the scatterer half that of the transmitted radar signal. Other wavelengths can be probed with either different transmitter signals or different transmit-receive geometries.

The analogy to Bragg scattering in a crystal lattice occurs due to the successive plasma density enhancements and rarefactions that are associated with the ion

acoustic waves of the E-region irregularities, which in a sense form a scattering lattice. In reality the transmitter wavelength and radar geometry select a particular spatial Fourier component of the ion acoustic wave field for observation, so the analogy is not exact.

#### *6.2.4 Irregularity Bandwidth and Aliasing*

The irregularities are most often seen at distances between 300 and 1000 km, with most doppler velocities near the ion acoustic speed of the E-region (typically around 370 m/s). For a 100 MHz radar system, and the highest velocity irregularities, this corresponds to a doppler bandwidth typically on the order of 3 kHz. When the product of a radar target's range extent and doppler bandwidth exceeds the speed of light the target is said to be overspread [*Skolnik, 1990*].

$$\Delta f \Delta r > c \quad (6.13)$$

For such targets traditional periodic pulse mode radar measurements will be aliased in either range or doppler shift. This is the case for VHF observations of auroral electrojet irregularities and as a result many observations to date have had significant aliasing problems in either range, velocity, or both.

To produce unambiguous measurements of the target's autocorrelation function it is necessary to use methods that directly address this aliasing problem. These "overspread" radar techniques utilize transmitter waveforms that are carefully structured to allow ranges and velocities to be uniquely determined by the correlation function.



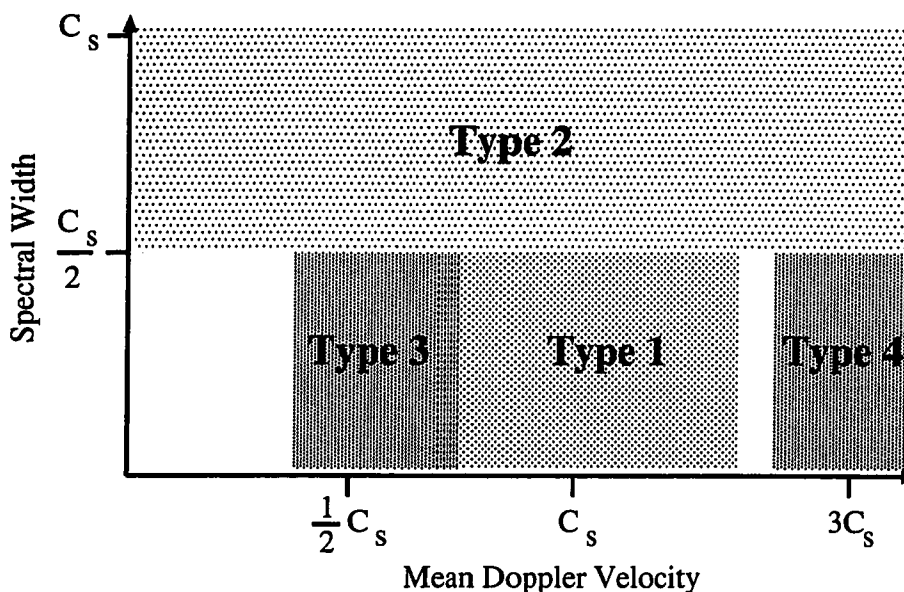


Figure 6.6: The typical irregularity classification scheme that is used by coherent scatter radars consists of four irregularity types. The division into these classes is useful for discussing observations but is poorly motivated.

### 6.3 Typical Radar Observations

The radars which make coherent scatter observations of ionospheric irregularities form a diverse group. These radar are so diverse that inter-comparison of the radar observations has proven very difficult. Most comparisons of auroral irregularity radar observations have preceded from an ill defined phenomenological classification scheme, an interpretation of which is shown in Figure 6.6. Unfortunately, this scheme is not really so well-defined as the figure implies, and it means different things to different people.

The irregularity type classification scheme can be assigned physical significance in a somewhat ad hoc manner. The type-1 wave is most often considered to be the fundamental ion acoustic mode that is generated by the two stream instability in the ionosphere. It has relatively narrow spectral width, large amplitude, and is observed to propagate in the drift direction of the electrons at or near the ion acoustic speed.

Type-2 waves are a form of relatively low amplitude scatter that is thought to be formed by a cascade of energy longer to shorter wavelengths. These waves have very broad spectral widths, and a wide range of propagation velocities below the ion acoustic speed.

The type-3 wave has a relatively colorful history, it was originally believed to be an electrostatic ion cyclotron wave. However, after a more than a decade it was proven experimentally that this explanation was unlikely. Type-3 waves are observed to propagate with doppler shifts well below any realistic ion acoustic speed, but with high amplitude and narrow spectral width. The current trend is to explain them using strong density gradients or nonlinear wave-wave interactions, but these theories are difficult to test and none of them have been conclusive in their predictions.

Type-4 waves have extraordinarily large amplitude, narrow spectral widths, and are thought to be produced either by extremely sharp density gradients, a heated ionosphere with elevated ion acoustic speed, or both processes in some combination. These echoes are extremely rare and have not been observed by all coherent scatter radar systems.

Recently there have been attempts to develop a more rational classification system for the irregularities. The Watermann plot examines the Doppler velocity of the irregularities versus their spectral width. Despite difficulties involved in defining a theoretically optimal definition of irregularity spectral width this is a promising approach.

#### **6.4 Typical Operating Configurations**

Contemporary coherent scatter radar systems used for observing the E-region irregularities typically operate on frequencies of 50 MHz or 140 MHz, primarily due to limitations on the available radio wave spectrum imposed by communications

regulating authorities (FCC). Transmitter powers on the order of 30 kW with duty cycles of a few percent are common, leading to average transmitter powers on the order of a few kilowatts.

There is diversity in the waveforms transmitted by these systems, but three major categories have been used. Pulse mode monostatic radars such as CUPRI [*Providakes et al.*, 1983], double pulse multistatic radars like STARE [*Greenwald et al.*, 1978], and the CW multistatic radars such as SAPPHIRE [it Koehler et al., 1995b].

There does, however, appear to be a recent trend towards multistatic systems that utilize much higher duty cycles and which exploit transmitter signals appropriate for overspread radar targets [*Popple et al.*, 1997; *Moorcroft and Schlegel*, 1990].

## Chapter 7

### THE MANASTASH RIDGE RADAR

The use of passive radio techniques is a growing trend in ionospheric radio science. VLF beacon broadcasts have been used for many years to observe lightning related signatures [*Pasko and Inan, 1994*], and more recently to detect the occurrence of red sprites, blue jets, and the auroral electrojet [*Cummer et al., 1996*]. GPS and other satellite borne signals have been exploited, through networks of ground based receivers, to perform ionospheric tomography and produce large-scale maps of ionospheric total electron content [*Fremouw et al., 1992; Leitinger et al., 1997; Ruzhin et al., 1998*]. HF radio broadcasts also been used to detect and study traveling ionospheric disturbances [*Beley et al., 1995*].

So far these techniques have been of relatively low resolution, averaging over large regions of space or large periods of time. Indeed, the signals that have been exploited so far are neither the most predominant nor the most powerful man made signals that are present in the environment. Commercial broadcasts are ubiquitous AM radio, FM radio, Television, and most recently Digital Television, occupy a large portion of the radio spectrum. These broadcasts are among the most powerful signals transmitted for any purpose.

#### **7.1 *Passive Radar Systems***

Passive radar is a new technology that exploits the presence of powerful communications signals in the environment. By intercepting these signals and the echoes from interesting scatterers it is possible retrieve alias free range and doppler infor-

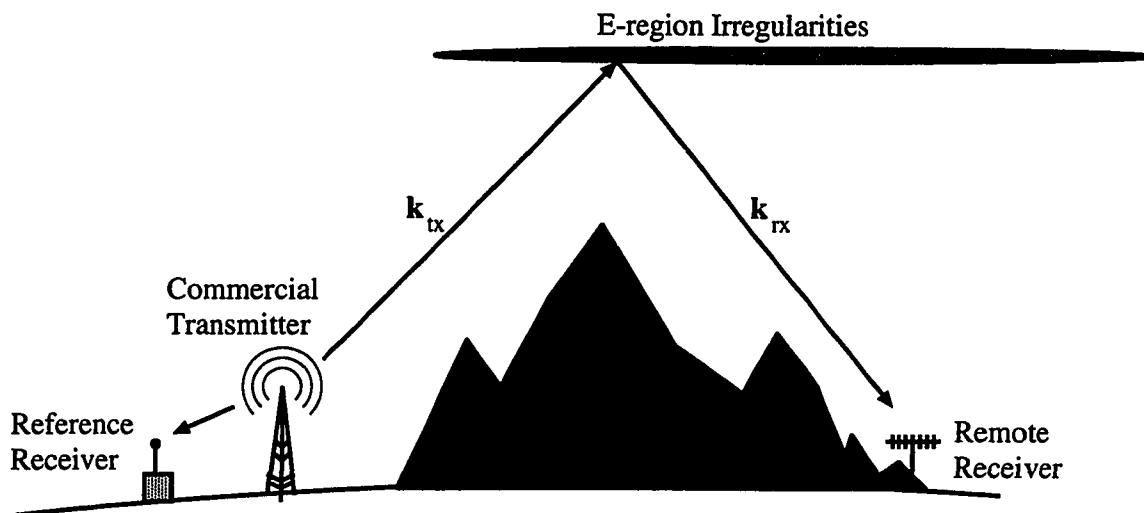


Figure 7.1: A typical passive radar system is shown for a multistatic configuration. The commercial FM broadcasts are intercepted to provide a reference signal. Scatter from the irregularities is then detected in a radio quiet environment created by favorable topography.

mation of extraordinarily high quality. Radar systems which operate in this manner have many benefits, especially for scientific applications. They are compact, low in cost, and have high resolution in range, velocity, and time. They use ambient signals to exploit wavelength regimes that are unavailable to conventional active radar systems. The transmitters, FM radio and Digital Television stations, are operated independently of the passive radar and are maintained, serviced, and paid for by their operating interests. In many locations there are a large number of independent transmitters operating on a variety of frequencies and having high average output power. Because passive radar systems have no transmitter they are also inherently low in emissions and safe to operate.

## 7.2 Overview of the Manastash Ridge Radar

The Manastash Ridge Radar system is the first example of a passive coherent scatter radar for observing E-region irregularities. This multistatic passive radar system

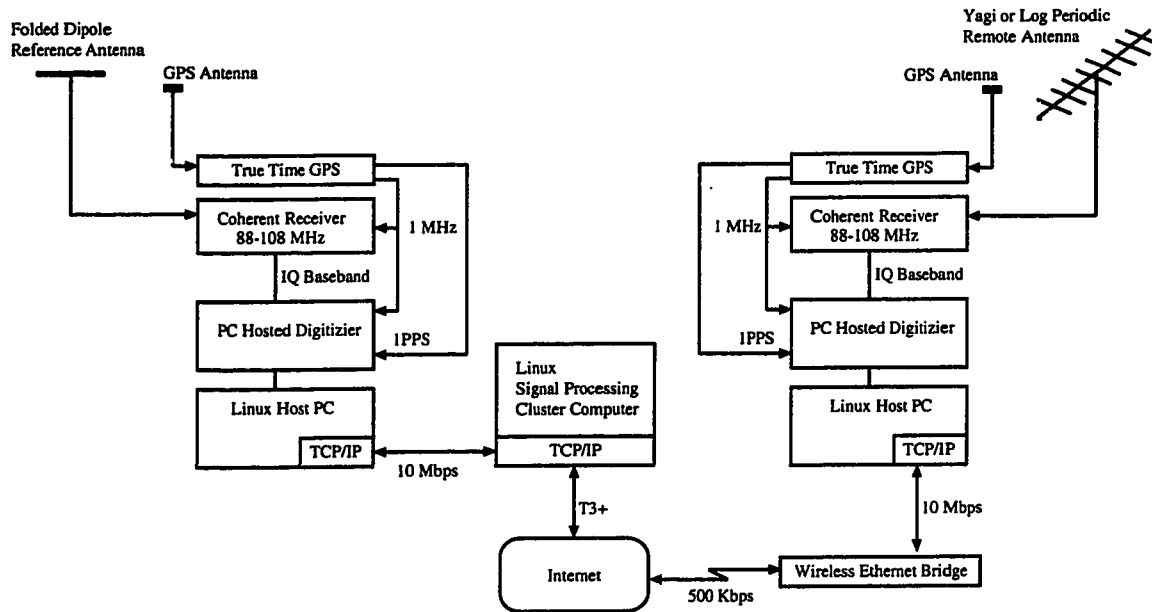


Figure 7.2: The Manastash Ridge Radar consists of two coherent digitizing receivers. The receivers and digitizers are synchronized using the global positioning satellite system. Data is transferred over the Internet to a central location where it is processed using a cluster computer.

utilizes a single FM radio station that provides a transmitter signal of opportunity. This radar is the first passive radar developed for any use outside of aircraft tracking and other military applications [Howland, 1994; Griffiths et al., 1992].

A simple overview of the radar system is shown in Figure 7.2. Two receivers are synchronized in time and frequency using the Global Positioning System. The reference receiver located on the University of Washington campus intercepts the signal that is initially transmitted by an FM radio station in the Seattle area. The FM radio signal propagates into the ionosphere, where for the appropriate near backscatter geometry, it scatters from E-region irregularities and is ultimately detected by the remote receiver. The remote receiver is located at the Manastash Ridge Observatory in eastern Washington State, USA.

By cross-correlating the transmitted signal  $x(t)$  with the scattered signal  $y(t)$ , it is possible to make true radar observations [Sahr and Lind, 1997]. For FM radio

signals these observations have high range, time, and velocity resolution [*Hansen, 1994; Hall, 1995*].

### *7.2.1 Radar Field of View*

Figure 7.3 shows the view volume of the Manastash Ridge Radar. The radar is located in the northwest United States with a field of view over Canada. The arrow indicates the direction of magnetic north toward which the remote antenna is aligned. The beam width of the main antenna lobe is indicated by the solid lines. Two sets of lines are shown, one for the 6 dB log periodic antenna, and one for the 14 dB yagi. The transmitter and receiver locations are shown along with range indicators spaced at 200 km intervals. Contours of magnetic aspect angle are plotted to indicate the likely scattering volume.

The 90° aspect angle contour corresponds to the multistatic backscatter geometry that is most favorable for the detection of the irregularities. Because of the highly field aligned nature of the irregularities scatter from non perpendicular magnetic aspect angles is significantly attenuated. A typical value is 10 dB/deg, and this ensures that any echoes detected by the radar are likely to be within 1° of the backscatter contour due to the system's limited sensitivity. It is also likely that the current radar system is limited in its ability to observe irregularities located to the east of the remote receiver location. This is due to the presence of the Cascade mountain range in that direction. These mountains may prevent the radar from making observations at low elevation angles in that direction.

### *7.2.2 Properties of FM Radio Signals*

Commercial FM broadcast stations typically transmit their signals between 88 and 108 MHz in frequency. The stations encode a stereo audio signal into a constant amplitude frequency modulated signal. Typical stations broadcast 30 - 100 kW of

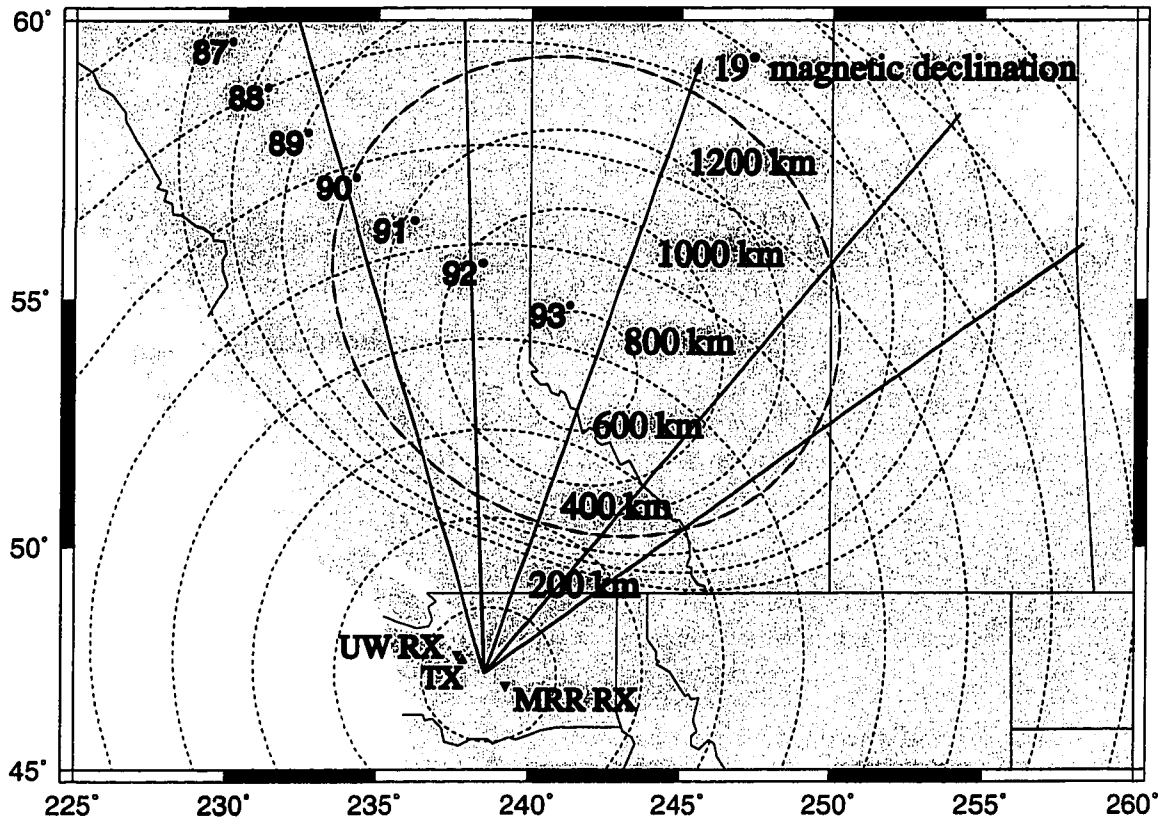


Figure 7.3: The view volume of the Manastash Ridge Radar in the Pacific Northwest. The transmitter and receiver sites are indicated on the diagram along with circles of multistatic range at 200 km intervals. The arrow points in the direction of magnetic north and the solid lines indicate the typical beamwidth of the antenna systems. The inner lines correspond to the +14 dB Yagi antenna, while the outer lines represent the +6 dB Log Periodic antenna. Contours of magnetic aspect angle are shown on the diagram with the 90° contour indicating the multistatic backscatter geometry.



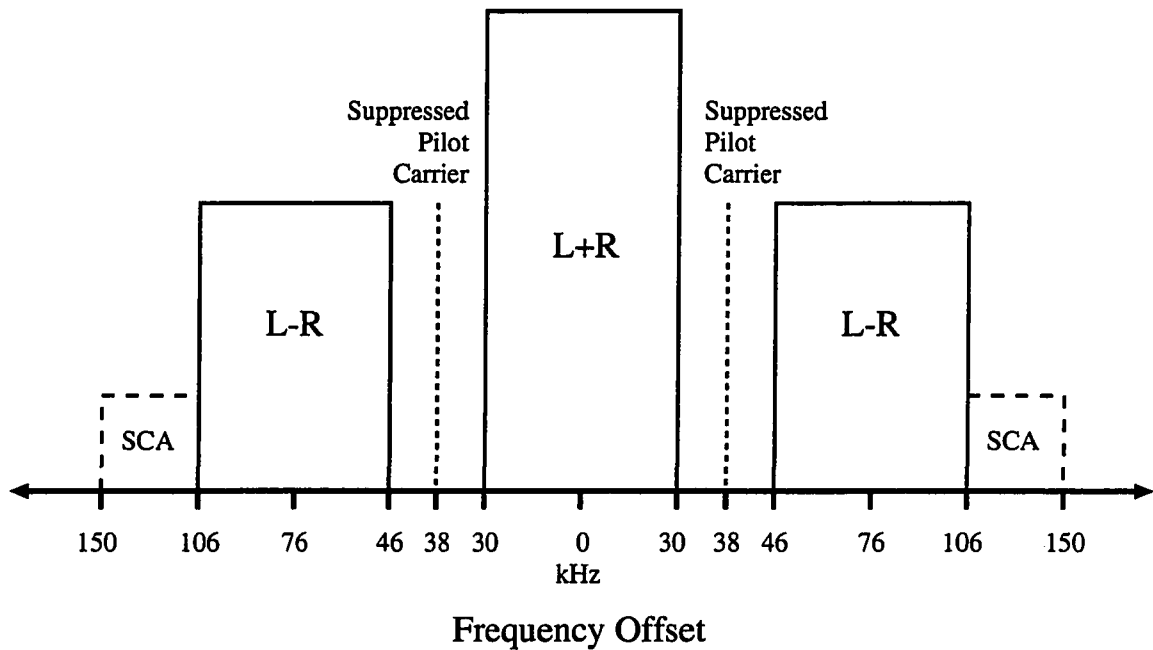


Figure 7.4: The structure of an FM radio signal is complicated due to stereo modulation and optional data sidebands. The pilot carriers are suppressed and most of the signal energy is carried in the central channel.

effective radiated power over a bandwidth of about 200 kHz with channel spacings on the order of 200 kHz but allocated about 800 kHz apart in the same geographical regions.

Prior to modulation the stereo audio signals are in the range of 10 Hz to 15 kHz. These audio signals are encoded into a central L+R channel with a signal between 50 Hz and 15 kHz which is suitable for a monaural receiver. Two suppressed pilot carriers are generated at 19 kHz and the second harmonics of these carriers at 38 kHz form the center for the L-R channels that encode the stereo modulation. These stereo channels range from 23 kHz to 53 kHz. Data subcarriers (SCA) may also be transmitted with their modulation between 53 kHz and 75 kHz. Frequency modulation is then applied with a modulation index of about 2.0. This results in a L+R modulated signal between 100 Hz and 30 kHz, a suppressed 38 kHz pilot carrier, L-R stereo signals between 46 kHz and 106 kHz centered on 76 kHz, and

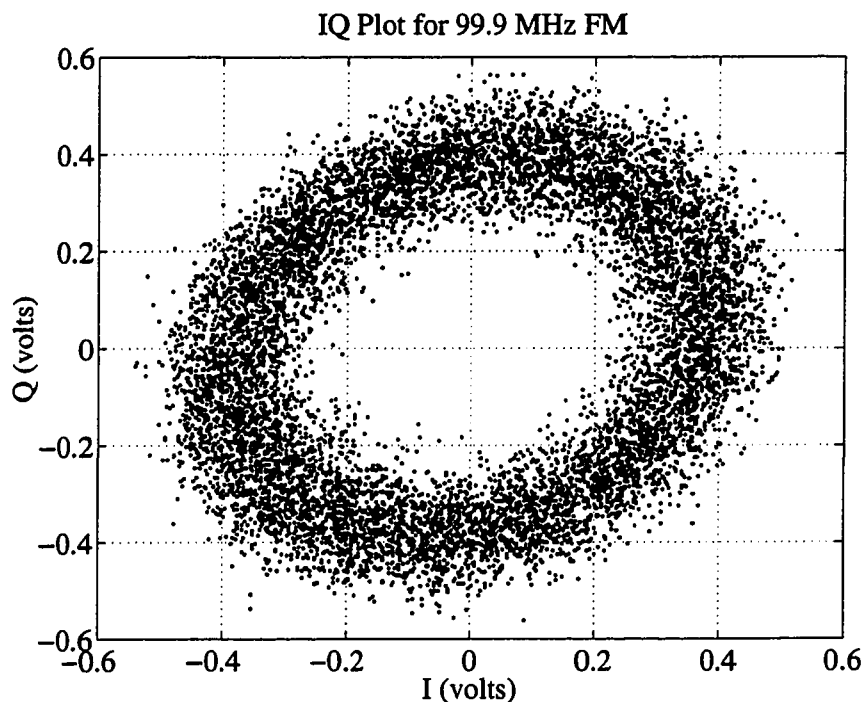


Figure 7.5: Plotting the inphase (I) and quadrature (Q) components of a received FM radio signal. The circle results from the constant amplitude (modulus) nature of the FM signal and the spread in the circle is due to variations in the transmitter, multi-path scatter, scattered targets, and receiver imperfections.

SCA channels between 106 kHz and 150 kHz [FCC 47CFR73.322, 1998].

The net result of this process is that audio information is non-linearly spread across a much larger bandwidth. Because this signal is unique over time scales longer than about  $10 \mu s$  the FM radio signal is essentially a CW random code that forms a unique pattern in frequency and time.

Random codes make good radar signals although at the expense of a large signal processing burden. They have been used in radio astronomy by *Hagfors and Kofman* [1991] and suggested for incoherent scatter radar [Sulzer, 1986].

Using a receiver with quadrature sampling to preserve phase information, the FM radio signal can be plotted in the inphase (I) and quadrature (Q) plane and this is shown in Figure 7.5. The constant amplitude nature of the CW FM radio

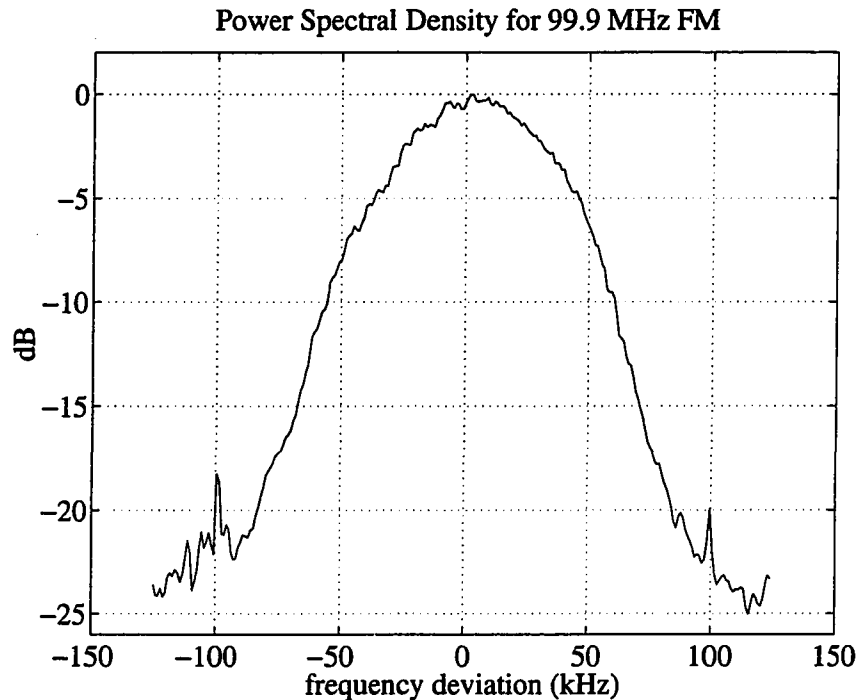


Figure 7.6: An FM radio power spectrum for 5 seconds of integration on 99.9 MHz. For long integrations the signal often appears to have a roughly Gaussian shape.

broadcast is immediately evident from the circular appearance of the IQ plot. The width of the circle is related to variations in the received signal strength. These may be due to multi-path propagation, variations in the transmitter signal, receiver flaws, and scatter from targets.

Figure 7.6 is the power spectrum of a typical FM radio station in the Seattle area. The power in the signal is distributed in a roughly Gaussian manner around the central transmitter frequency.

This spectral character varies substantially with time as can be seen in Figure 7.7. Spectra are plotted as a function of time here and the signal power has strong variation in bandwidth as the signal is modulated. The consequence of this is that the quality of the FM radio signal as a radar waveform varies substantially from moment to moment.

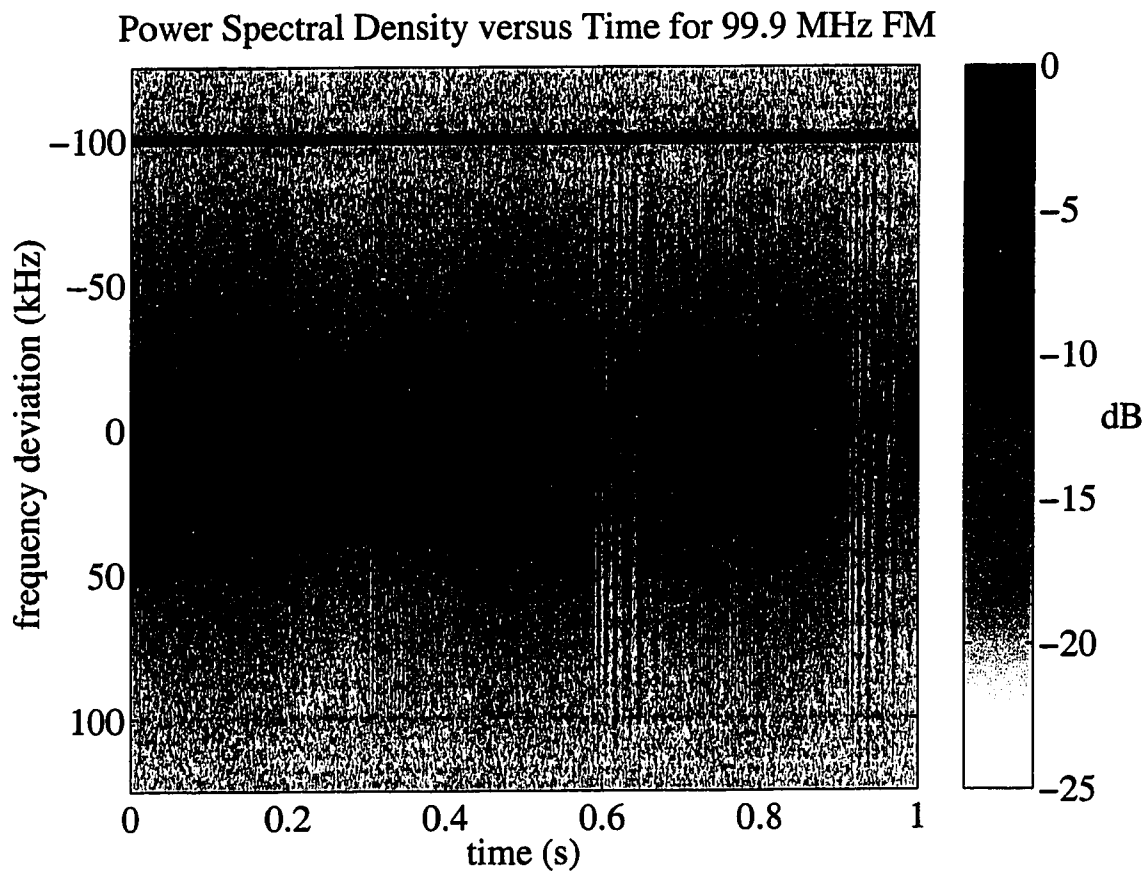


Figure 7.7: The FM radio spectrum versus time for 1 second of data. Substantial variation in the FM radio waveform creates the unique pattern that makes the signal work well for radar applications.

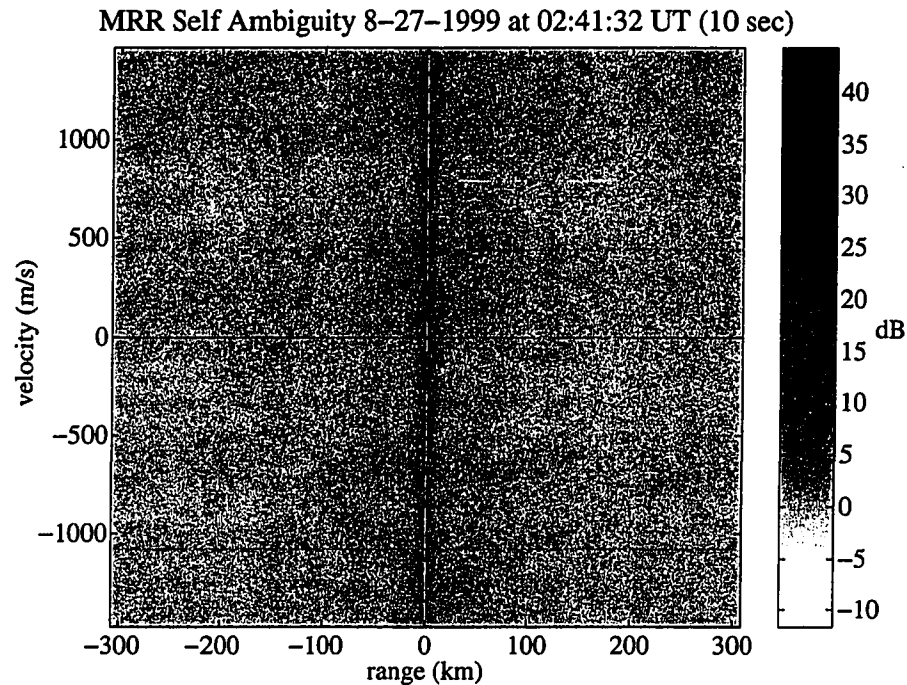


Figure 7.8: The self ambiguity of an FM radio signal for 10 seconds of integration. The globally compact ambiguity strongly resembles that of a random code and allows targets to be localized in range and velocity.

The self ambiguity of the FM radio signal shown in Figure 7.8 is very similar to that of a random code under most circumstances. There is some variation in the character of the ambiguity as the transmitter signal varies, and this variation is most pronounced when the bandwidth of the transmitter signal falls significantly for long periods of time. For example, it becomes badly distorted when the radio station broadcasts silence. The consequence of the reduced signal bandwidth is substantially reduced range resolution and distortion of the transmitter self ambiguity.

Some stations also transmit FM radio sidebands that contain information such as elevator music, stock quotes, and traffic information. These sidebands cause the ambiguity function computed from FM radio signals to depart from its nearly ideal delta function character. In particular they result in symmetric structures offset in frequency and range around the central self-ambiguity peak. These structures are

usually 30 dB or more below the central peak and their effect can be mitigated by appropriate signal processing.

### 7.2.3 FM Radio Signal Variance

When using FM radio signals to detect targets it is important to have some idea of how good the signal is for making estimates of the target auto-correlation function. In order for these estimates to be useful the variance of the estimator must be small. An evaluation of this variance for a Gaussian FM radio signal model is discussed in *Sahr and Lind* [1997]. The approximate form of the resulting variance for over-spread targets is

$$\frac{\Delta Q}{Q} = \sqrt{\frac{T_{acf}}{T}} \sqrt{1 + \frac{T_r P^2}{T_{acf} R_\sigma^2(\frac{r}{2}, 0)}} \quad (7.1)$$

where  $Q$  is the estimate of the target autocorrelation function,  $T$  is the integration time,  $T_{acf}$  is the target correlation time,  $T_r$  is the target range extent (in time like units),  $R_\sigma$  is the zero lag power at a given range, and  $P$  is the typical power. This essentially states that the uncertainty in the estimate is inversely proportional to the number of independent samples subject to the effects of the clutter. The clutter contribution can be suppressed through incoherent and coherent integration.

The variance in the estimates produced by the radar appear to be on the order of 30% - 50% depending on the integration time of the radar. The major complication in making a stronger statement about the FM radio signal variance is that real FM radio signals are not the Gaussian ideal. The signals have significant structure and can vary greatly in time. This can lead to changes in the quality of the estimator during the course of an observation.

### *7.2.4 The Challenges of Passive Radar*

In order to utilize signals intercepted from the environment as radar signals, there are many problems that must be adequately addressed. The most basic condition is that suitable signals must be present in the region that is to be observed. For much of the world FM radio signals are broadcast continuously with high transmitter powers.

#### *Synchronization*

It is necessary to synchronize the receivers in the system so that the phase relationship between the receivers does not vary rapidly relative to the delay and doppler resolution that needs to be resolved. For a doppler resolution of 1.5 m/s at a frequency of 100 MHz, it is necessary to synchronize the system to 1 Hz in 100 MHz or 1 part in  $10^8$ . The initiation of data taking and the sampling must also be coordinated so that the digitized signals can be aligned accurately for processing.

The Manastash Ridge Radar utilizes the global positioning system (GPS) to providing the timing signals that stabilize its oscillator, sampling clock, and data acquisition trigger. Using GPS it is relatively easy to obtain synchronization of 1 mHz at 100 MHz for all portions of the system.

#### *Dynamic Range*

Dynamic range is the ability to resolve a weak signal in the presence of a stronger one. It is necessary for any radar intercepting signals in the environment to be able to detect the signal scattered by a target in the presence of noise, interference, and clutter. This signal is usually very weak and so the radar system must have a large dynamic range.

In most radar systems, dynamic range is achieved in time by turning off the transmitter and receiving the scattered signals on a quiet channel. In passive radar

the signal that is intercepted is often broadcast continuously. This forces the system to be able to detect the scattered signal in the presence of a strong signal on the same channel. For FM radio this dynamic range requirement is on the order of 100 dB. Such dynamic range is extraordinarily difficult to achieve using a traditional monostatic radar system.

In the Manastash Ridge Radar an alternate approach is taken to achieving dynamic range. A multistatic geometry is used where the dynamic range is achieved by separation in distance and the exploitation of favorable topography. By locating a reference receiver in Seattle, the transmitter signal can be intercepted by the radar. This signal is strongly attenuated by distance and the Cascade mountain range as it travels to the remote receiver located at the Manastash Ridge Observatory near Ellensburg Washington.

Because FM radio is a continuous wave (CW) signal it illuminates potential clutter sources at all times and delays. This produces a strong clutter signal in the remote receiver. Ground clutter can be clearly observed by its characteristic zero doppler velocity. In the Manastash Ridge Radar ground clutter is especially evident due to the visibility of Mt. Rainier at both the transmitter and receiver site. This large mountain is the strongest scatterer detected by the radar during most operations.

### *Data Transport and Management*

The collection, transport, and management of data produced by a radar system is not a trivial issue. The Manastash Ridge Radar generates approximately 500 Ksamples  $\text{sec}^{-1}$  receiver $^{-1}$  in its basic operating mode. For the unpacked 12 bit samples (in 16 bit words) this corresponds to 1 Mbyte  $\text{sec}^{-1}$  receiver $^{-1}$ . Because the system is multistatic this data must be moved to a central location for processing over a distance of 150 km.



The remote receiver is located in a region selected both for convenience and its relative lack of strong radio interference. The Manastash Ridge Observatory is located 10 km from the nearest urban center. A 500 Kbit/sec microwave communications link serves to connect the observatory to the Internet and this link is used to transport the data from the remote site to the University of Washington. The data collection rate exceeds the available bandwidth and the result of this is that either data acquisition must happen with at most a 6% duty cycle or the data must be compressed by at least 20:1.

Currently the system operates in a low duty cycle mode, although some experiments with data compression have been attempted (using 1 bit sampling). There is good evidence that rather aggressive compression schemes produce usable results, with ratios as high as 40:1 [*Gidner, D. private communications*]. It is also possible to use coherent averaging to reduce the bandwidth of the received signals and thus limit the subsequent data rates at the receivers. This requires sufficient signal processing power at all receiver sites.

Once the data has been processed it must be examined for the presence of interesting targets. Currently this is not automated and is rather time consuming. To accurately detect and record "interesting" events a sufficiently robust algorithm must be developed to recognize the presence of irregularities in the radar output.

### *Signal Processing and Computational Burden*

All of the data collection, management, transport, and processing takes significant computational power. In fact, radar system designs can easily be formulated to utilize any conceivable amount of computational power available in the foreseeable future. This is the real cost of utilizing the passive radar technique. Moore's law makes this price less painful to pay.

The basic signal processing algorithm of a passive radar system is the discrete

computation of the ambiguity function [*Sahr and Lind, 1997*]. This is given by

$$\chi \left[ \frac{r}{2}, \tau \right] = \sum_t y[t]x^*[t-r]y^*[t-\tau]x[t-r-\tau] \quad (7.2)$$

where  $\chi \left[ \frac{r}{2}, \tau \right]$  is the target correlation function as a function of range,  $r$  is the delay variable,  $\tau$  the lag variable, and the summation is over time  $t$ . The reference transmitter signal is given by  $x[t]$  and the remote detected signal is given by  $y[t]$ .

A large computational gain can be obtained by reorganizing the computation in terms of a “detected” signal

$$yx[t; r] = y[t]x^*[t-r] \quad (7.3)$$

which can then be coherently averaged when the scattering amplitude of the target varies more slowly than the transmitter signal. This decimation step gives

$$YX[t_d; r] = \sum_{t=0}^{N-1} yx[t_d + t; r] \quad (7.4)$$

where  $N$  is the number of consecutive samples to average. The correlation then becomes

$$\chi \left[ \frac{r}{2}, \tau \right] = \sum_t YX[t_d; r]YX^*[t_d - \tau; r] \quad (7.5)$$

This computation is over a finite set of delay and lag offsets, corresponding to the desired range-doppler extent of the radar data. The actual evaluation of this four

correlation can be performed in either the time or frequency domains.

The computational complexity of the Fourier transform evaluation of the correlation in the time domain is

$$O(R_s, N_d, M_f) = \frac{1}{N_d + M_f} [R_s N_d M_f + R_s M_f \log_2(M_f) + R_s M_f] \quad (7.6)$$

where  $N_d$  is the number of consecutive samples that are decimated,  $R_s$  is the sample rate, and  $M_f$  is the Fourier transform window length (in samples). The computation is dominated by its first term  $R_s N_d M_f$ . This is the decimation or “coherent integration” step, and optimizations can be made by building fast decimators or limiting the sample rate. For radar sample rates of  $R_s = 250,000$  samples per second, decimation of  $N_d = 256$  samples, and Fourier window lengths of  $M_f = 512$  samples, the computation burden per range is about  $10^7$  operations for one second of data (ops). Evaluation of a typical range extent of 2500 ranges requires on the order of  $10^{10}$  ops.

### **7.3 Radar Capabilities and Performance**

Passive radar using FM radio signals as transmitter waveforms of opportunity is not a weak compromise in order to avoid having a transmitter. The performance of a passive radar system is extraordinarily good. Available transmitter power is large, the range and velocity resolution are superb, the time resolution is excellent, and the system is sufficiently sensitive to make useful geophysical observations.

The only component of the ideal radar that is missing is large antenna gain on the transmit side, but for E-region irregularity studies this is not necessary and the wide illumination pattern provides the opportunity for observing large regions of the ionosphere.

### 7.3.1 Radar Sensitivity

The greatest current limitation of the Manastash Ridge Radar system is its clutter limited dynamic range. Though no absolute calibration of the radar's sensitivity has been performed, it is clear that the system is limited at all delay and lag offsets by ground clutter and self correlations between the system receivers.

The strongest irregularity signatures observed have been about 15 dB above the clutter floor, while the strongest ground target (Mt. Rainier) is at about 30 dB with the antenna directed toward it. Significant improvement should be possible with more antenna gain, improved receivers, and clutter rejection methods.

### 7.3.2 Radar Range Resolution

The range resolution of the radar is directly related to the compactness of the self ambiguity of the transmitter signal. By utilizing a Gaussian spectral model for the transmitter signal it is possible to directly evaluate the self ambiguity and compute a form that is approximately correct for FM radio signals. This was done by *Hall* [1995] in the Fourier domain resulting in

$$|\chi(t)| = e^{-\frac{1}{2}t^2(2\pi B^2 + \frac{1}{4W^2})} \quad (7.7)$$

where  $\chi(t)$  is the delay portion of the Fourier space self ambiguity for the Gaussian model,  $B$  is the bandwidth of the received signal, and  $W$  is the length of the Fourier transform window. If we define the range resolution to be the 3 dB half width of this function relative to its maximum, it is easy to show that

$$\Delta r_{3dB} = \frac{c}{2} \sqrt{\frac{|\ln(\frac{1}{2})|}{2\pi B^2 + \frac{1}{4W^2}}} \quad (7.8)$$

where  $\Delta r_{3dB}$  is the range resolution, and  $c$  is the speed of light. For typical Fourier window lengths this expression is dominated by the signal bandwidth. When evaluated for appropriate FM radio like parameters ( $B = 250,000$  Hz,  $W = 0.25$  sec), the range resolution is  $\Delta r = 200m$ . This can be thought of as the lower bound for a radar signal consisting of an ideal Gaussian random waveform. This also assumes perfect sampling, with no variance or timing errors. In practice the sampling is not perfect and the FM radio transmitter signal varies substantially with time. The actual range resolution is on the order of 600 meters for good transmitter waveforms and much worse for poor ones.

### 7.3.3 Radar Velocity Resolution

The velocity resolution is similarly related to the self ambiguity of the transmitter signal. Again after *Hall* [1995]

$$|\chi(\nu)| = e^{-\pi^2 \nu^2 W^2} \quad (7.9)$$

where  $\chi(\nu)$  is the frequency portion of the self ambiguity,  $\nu$  is the frequency in Hz, and  $W$  is again the length of the Fourier transform window. Now defining the velocity resolution to be the 3 dB half width of this function relative to its maximum, it follows that

$$\Delta \nu_{3dB} = \sqrt{\frac{|\ln(\frac{1}{2})|}{W^2}} \quad (7.10)$$

so the frequency resolution of the ideal Gaussian waveform is simply limited by the length of the Fourier transform window. In practice this is not actually true because there is a finite limit to the frequency synchronization of the radar. In most cases the FM radio transmitter signals provide a velocity resolution of at best about 1.5

m/s.

#### *7.3.4 Radar Time Resolution*

The time resolution of the radar is limited by a combination of the Fourier transform window length and the variance in the spectral estimates that is desired. Typical integration times for the radar system are between 5 and 10 seconds, although irregularities have been observed and are detectable with 1 second integration times.

There are also additional limits on the system for long integration times as the transmitter ambiguity varies with time. The longer the integration, the more likely the transmitter ambiguity is to become poor at some point during the integration. Thus there is a variable upper bound on the integration time that can vary dramatically depending on what signals are being intercepted.

#### *7.3.5 Range and Velocity Aliasing*

Because of the nature of the FM radio signal, observations made using the Manastash Ridge Radar are free of range and doppler aliasing problems. This is true even for large range and doppler extents, and this is a very uncommon feature for any radar system. It is primarily a reflection of the FM radio signal's globally compact self ambiguity. The FM radio signal essentially forms a random code that identifies a particular point in time, space, and velocity.

#### *7.3.6 Comparison to Other Coherent Scatter Radars*

By taking advantage of the relatively high power (100 kW) CW FM radio signals and exploiting their compact ambiguity it is possible to make "true" radar observations. The resulting radar system is capable of high range, velocity, and time resolution, can make observations across a range of frequencies, and is very inexpensive to build. A comparison to the best operating modes of several modern coherent scatter radars

is shown in Table 7.1.

Table 7.1: A comparison of several modern VHF coherent scatter radars

Instrument		Best Resolution			
name	frequency (MHz)	range (km)	velocity (m/s)	time (s)	
Canadian CW	50	50.0	10.0	10.0	
SAPPHIRE	50	50.0	15.0	10.0	
CUPRI	50	5.0	10.0	2.0	
Manastash Ridge	88 - 108	0.6	1.5	1.0	
RAPIER	140	7.5	5.0	8.0	
STARE/SABRE	140	20.0	150.0	20.0	

The Manastash Ridge Radar has superior range and velocity resolution compared to the other VHF coherent scatter radars. Its typical time resolution is similar for integration times on the order of 5 to 10 seconds.

#### 7.4 Early Radar Observations

Early observations made with the Manastash Ridge Radar system show characteristic features that are worth commenting on here. Figure 7.9 shows the ground clutter that is typically observed by the radar. The clutter appears at a range of 55 km, with the strongest clutter source being located at 70 km and corresponding to Mt. Rainier (a large mountain visible to both the transmitter and receiver).

Ground clutter can be visible along the zero doppler line for a distance that strongly depends on the integration time. The non-zero doppler component of the Mt. Rainier signal is visible flanking the strong zero doppler echo, and this corresponds to the secondary structure in the transmitter self ambiguity. It is visible here due to the extraordinary strength of the signal from Mt. Rainier.

One interesting feature of the multistatic radar geometry is that the first few hundred ranges are always free of any scatterers. This is determined by the transmitter - receiver distance and the propagation of light between them. It is a very

## MRR Ambiguity 8-27-1998 10:13:34 UT (99.9 MHz, 5 seconds)

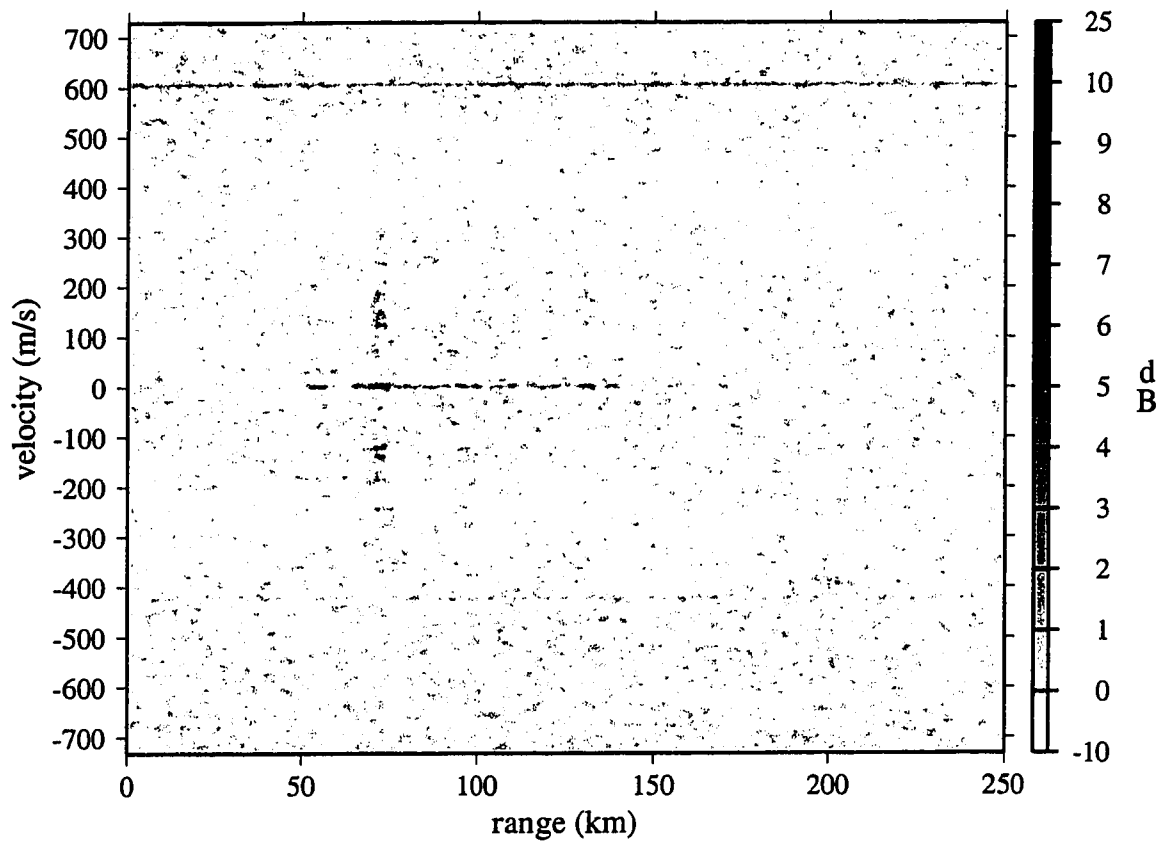


Figure 7.9: Radar observations made with the Manastash Ridge Radar system have a unique ground clutter signature due to the presence of Mt. Rainier. This is a large mountain that is visible to both the transmitter and the remote receiver.



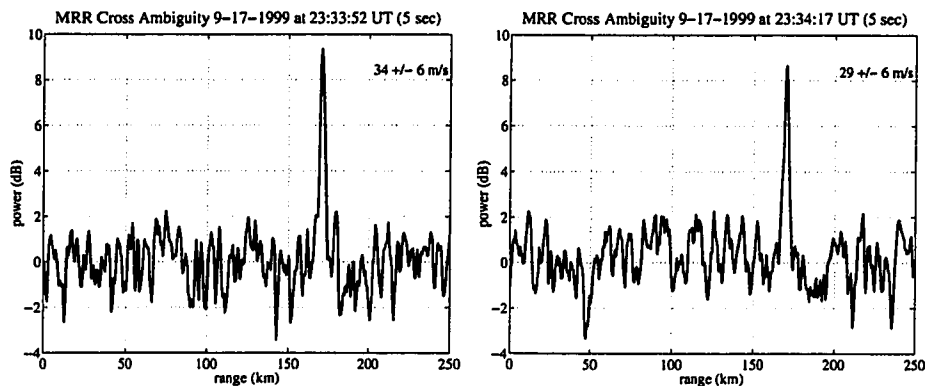


Figure 7.10: Occasionally the radar observes strong returns localized to a very small range and doppler extent. Some of these are aircraft and their range migration is consistent with their doppler velocities.

useful reference for calibrating the clutter floor of the receivers for every set of radar data.

After observing a sufficiently large quantity of data, it became clear that occasionally the system would detect point targets such as aircraft and meteors. An excellent example of an aircraft observation is shown in Figure 7.10.

The detection of aircraft by the current system is limited by sensitivity, dynamic range, and the Cascade mountain range. Only high flying aircraft, in the right locations, and of sufficient cross-section are likely to be detected.

## Chapter 8

# PASSIVE RADAR OBSERVATIONS OF E-REGION IRREGULARITIES

On August 27, 1998 a strong geomagnetic storm drove expansion of the auroral oval southward into the field of view of the Manastash Ridge Radar. This was a fortunate event because such strong storms are relatively rare, and the radar had only recently become sufficiently automated for regular operations.

### ***8.1 First Irregularity Observations***

The radar was operated for six hours on the morning of August 27, 1998 beginning at 6:58:34 UT. During this time an intense geomagnetic event caused substantial southward expansion of the auroral oval beginning the previous day.

A frequency of 99.9 MHz was selected for observation. This frequency contains a 100 kW FM radio station located in the Seattle area, and is relatively free of interference at the remote receiver site. Data was collected at a rate of 5 seconds per minute. The low duty cycle was necessary to accommodate limited data storage.

After data collection was completed, the system automatically transferred the 1800 seconds of data over the Internet to a computer located at the University of Washington. Processing the 3.6 G-bytes of data required about a day of computer time on a modern quad-processor.

A sequence of range - velocity ambiguity planes are shown in Figures 8.1, 8.2, 8.3, and 8.4. The radar returns have been processed to provide 1.5 m/s velocity resolution, 600 m range resolution, and five second integration times. The irreg-

ularities extend in range from 760 km to 1100 km, and are between 200 m/s and 375 m/s in velocity. The region of turbulence may well extend beyond 1100 km, but at this range the E-region falls below the radar horizon. Ground clutter at zero doppler is visible out to about 200 km and the feature at 70 km backscatter range is the result of strong scatter from Mt. Rainier. This is a large mountain visible to both the transmitter and receiver and it appears in all our data. The non-zero velocity component near this ground clutter is due to second order structure in the self ambiguity of the transmitted signal that is visible due to the strength of the Mt. Rainier scatter. Additionally there are several horizontal lines, the strongest at about -950 m/s, that are due to interference at the remote receiver site.

Figure 8.5 shows several range - velocity plots with one second integration times for data taken at 9:53:38 UT. This image is processed at 6 m/s velocity resolution, and 600 m range resolution. The lower velocity resolution is necessary to allow for sufficient signal power in each velocity bin for the irregularities to be easily detectable. Here the irregularities extend from 550 km to 850 km in range and have velocities between 250 m/s and 325 m/s.

The irregularities observed during this event had signals between 1 and 6 dB above the clutter floor, which was calibrated from the first ten ranges of the ambiguity plane. The early ranges will never contain any targets due to the multi-static nature of the system and thus are very useful for determining a reference clutter floor. An absolute power calibration of the radar has not yet been attempted. Such a calibration will prove difficult because we do not control the transmitter and the antenna pattern is not well known.

### *8.1.1 Irregularity Spectral Fitting*

Although the underlying passive radar technique provides excellent range, velocity, and time resolution it is important to understand that the power spectral density

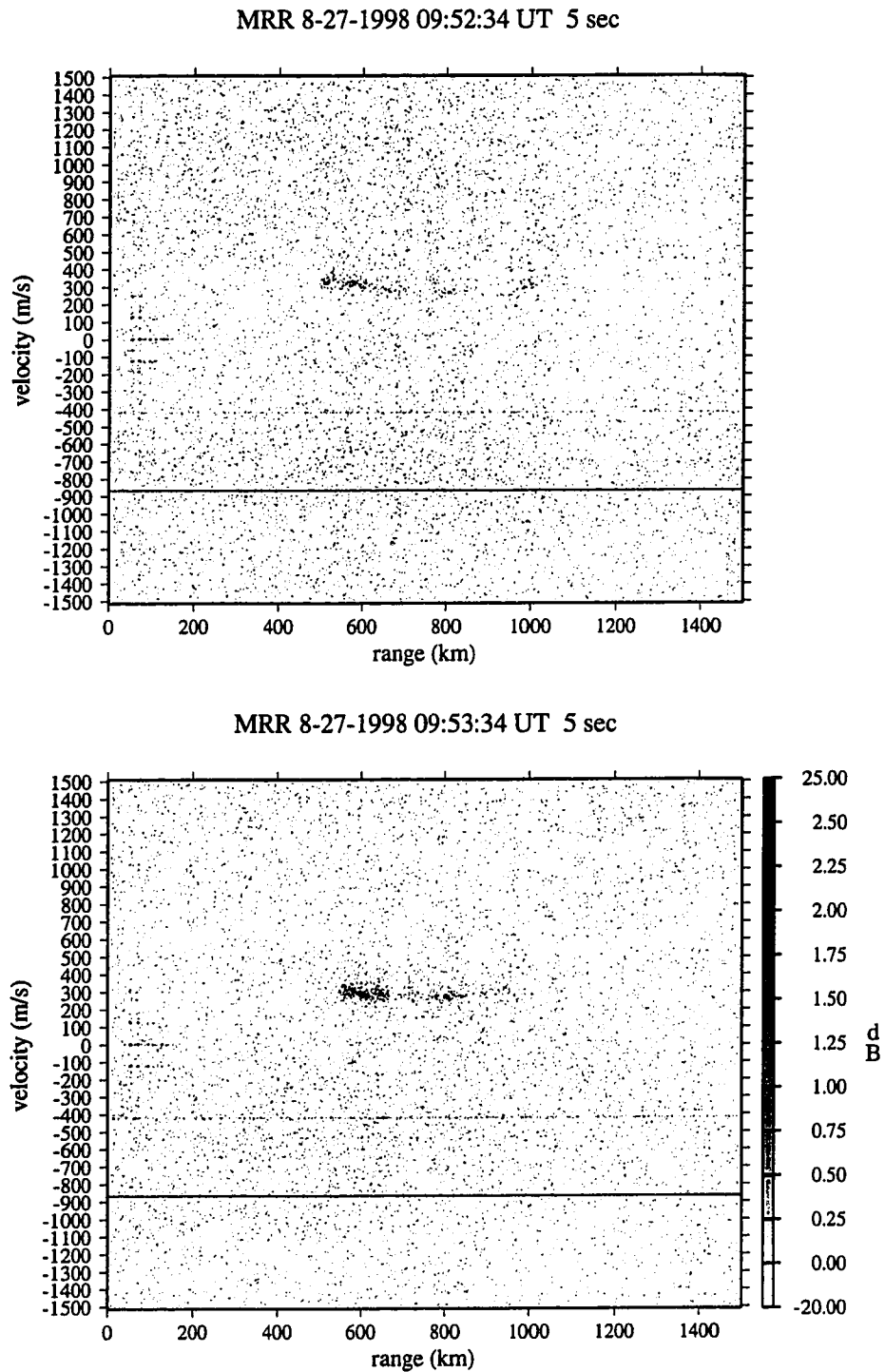


Figure 8.1: Two five second integrations of Manastash Ridge Radar data beginning at 09:52:34 UT on August 27, 1998. Here irregularities are visible over a range extent of 400 km.

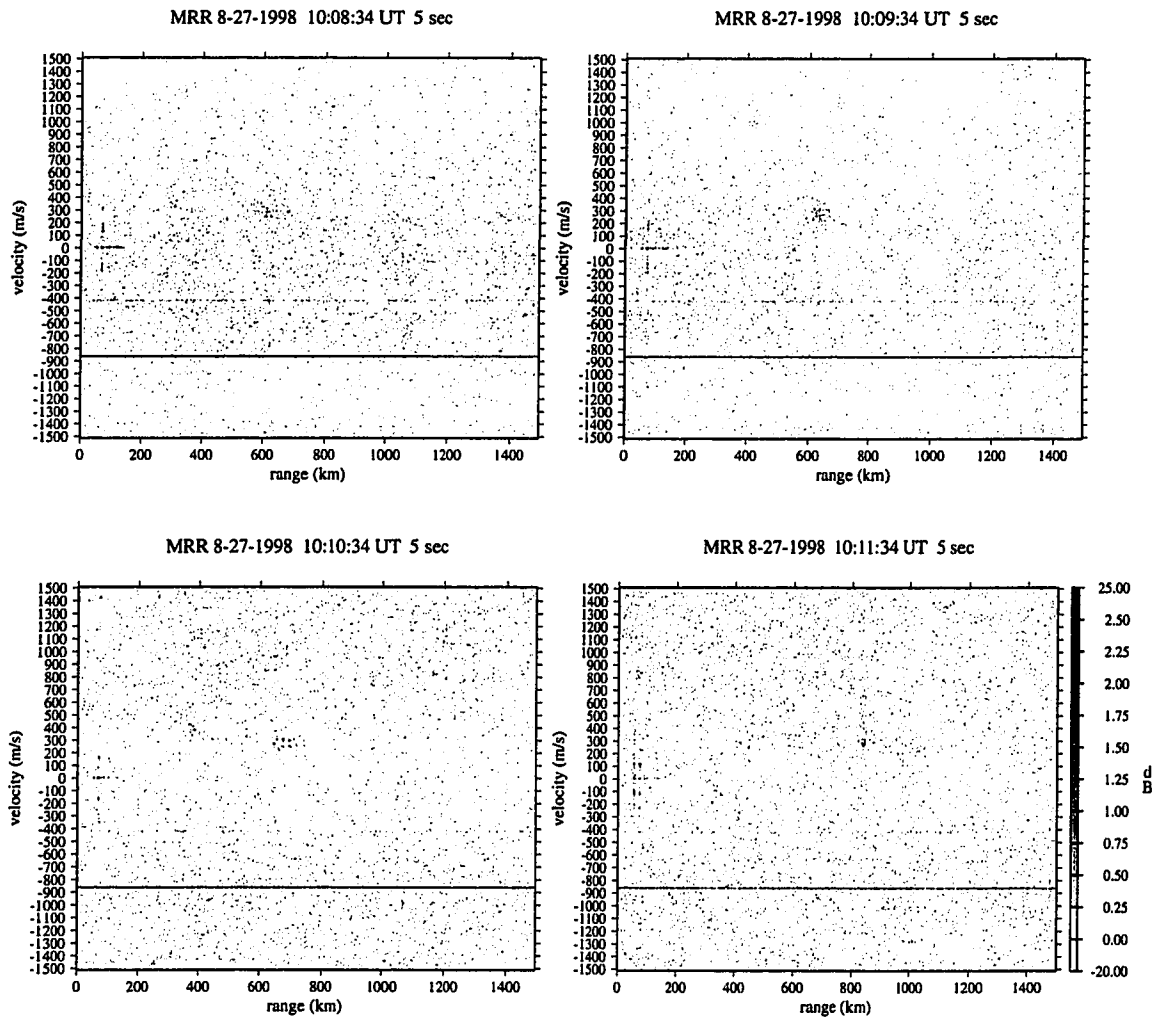


Figure 8.2: Later in the August 27, 1998 event from 10:08:34 until 10:11:34 UT the irregularities appear at 600 km and appear to move away from the radar to 800 km.

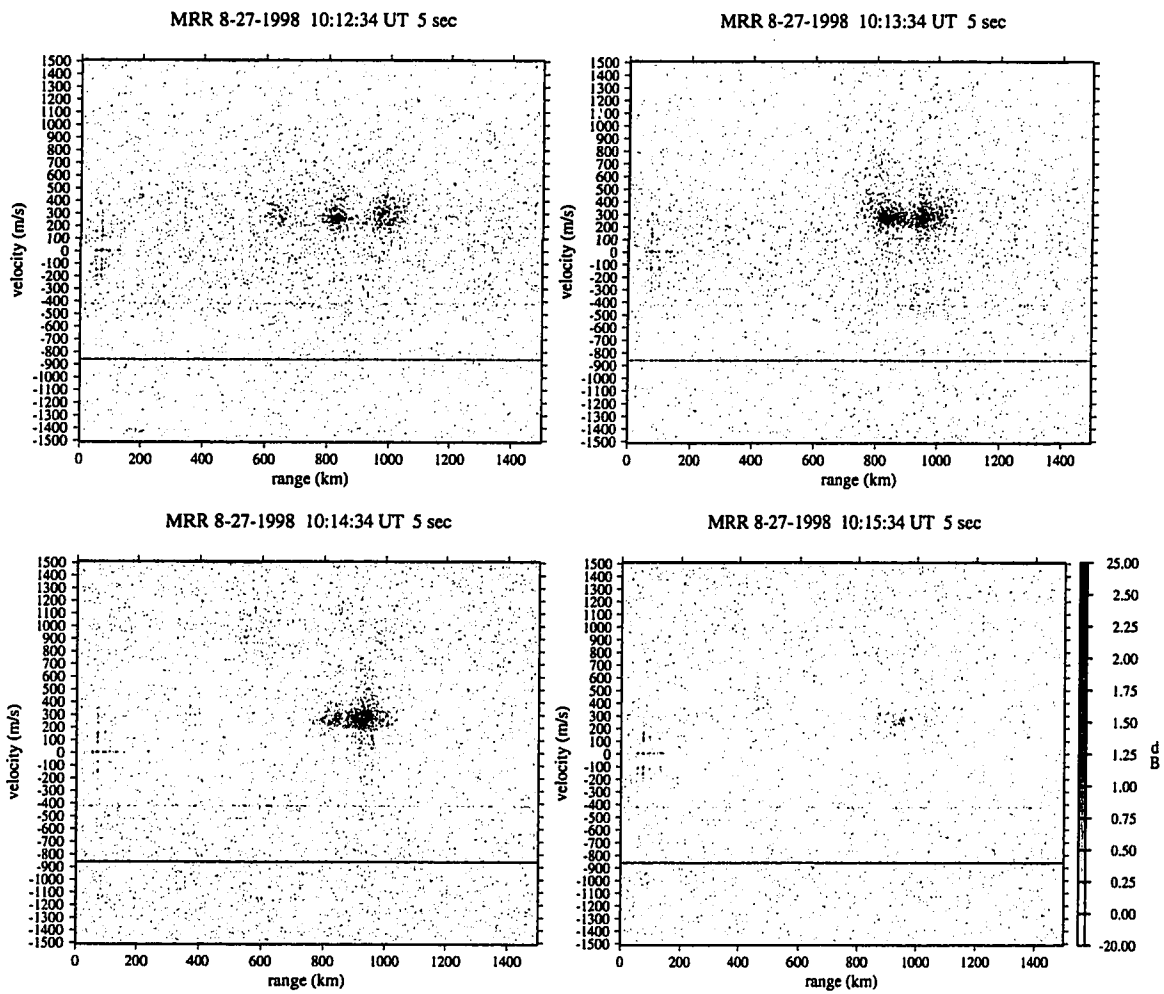


Figure 8.3: Between 10:12:34 and 10:15:34 UT on August 27, 1998 the scatter from the irregularities intensifies considerably in two regions which appear to merge and fade away as time progresses.

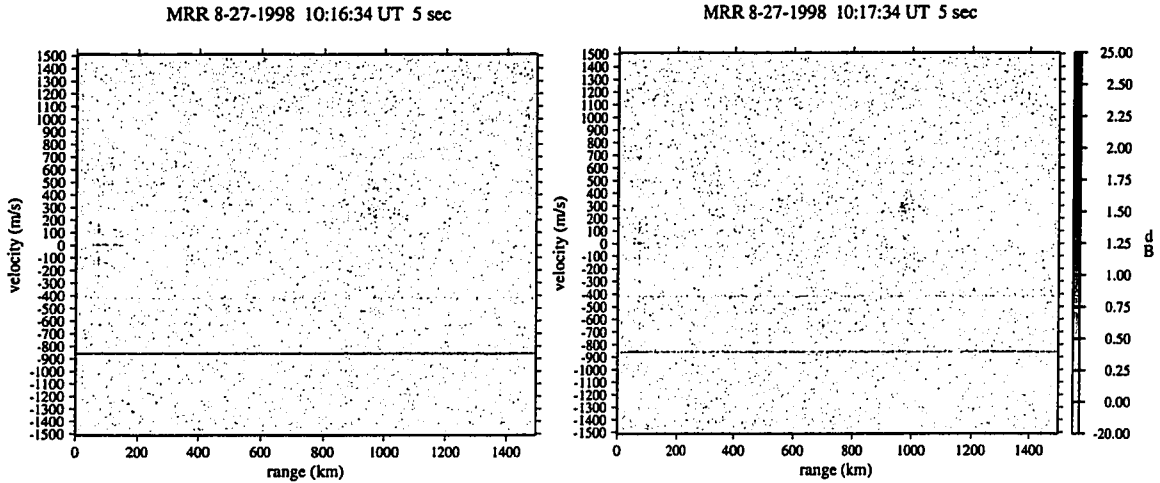


Figure 8.4: After 10:16:34 UT the irregularities are barely detectable and the strongest portion of the August 27, 1998 event has passed.

estimates of the irregularities may have substantial variance. Thus the fine structure that can be seen in the velocity observations may simply be an artifact of the relatively short integration times. Fortunately it is always possible to re-process the passive radar data, reducing its variance at the expense of lower resolution in time, range, or velocity.

Figure 8.7 shows an example from the fitting procedure using a Gaussian model.

$$P(v) = \alpha e^{\left(\frac{v-v_{mean}}{\sigma_v}\right)^2} + \beta \quad (8.1)$$

In the model,  $\beta$  represents the clutter floor,  $\alpha$  the irregularity amplitude,  $v_{mean}$  the mean velocity, and  $\sigma_v$  the spectral width. The model is fit to the data in a given radar frame at each range. The fitting is done using the nonlinear fitter in Matlab which is essentially a Levenberg-Marquardt type algorithm. The velocity, amplitude, spectral width, and offset are determined from the fit, which is done in the ambiguity space.

Using the fitted data it is possible to create Watermann distributions that

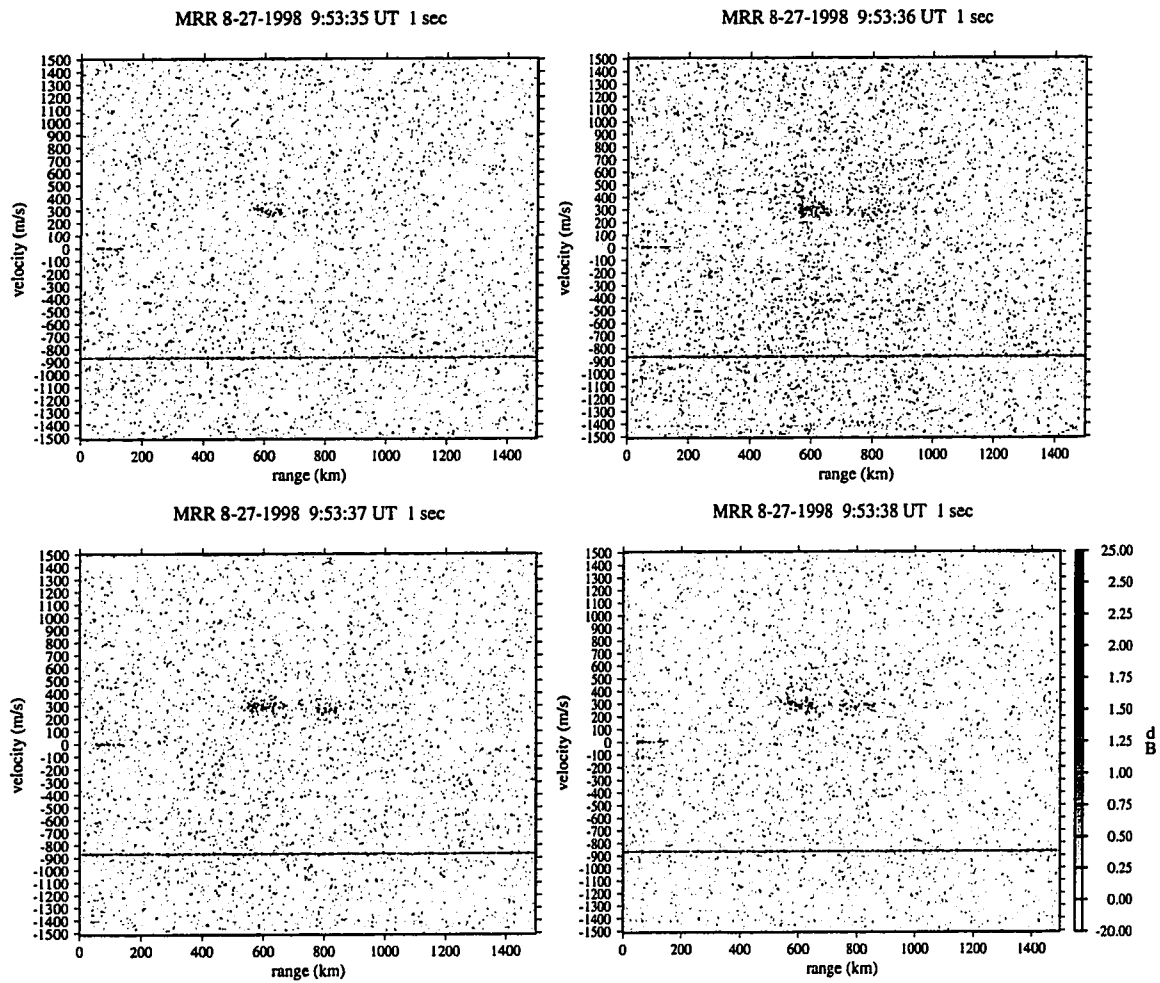


Figure 8.5: Four consecutive one second integrations of Manastash Ridge radar data from the August 27, 1998 event. The irregularities are detectable in the radar data even with this short integration time.



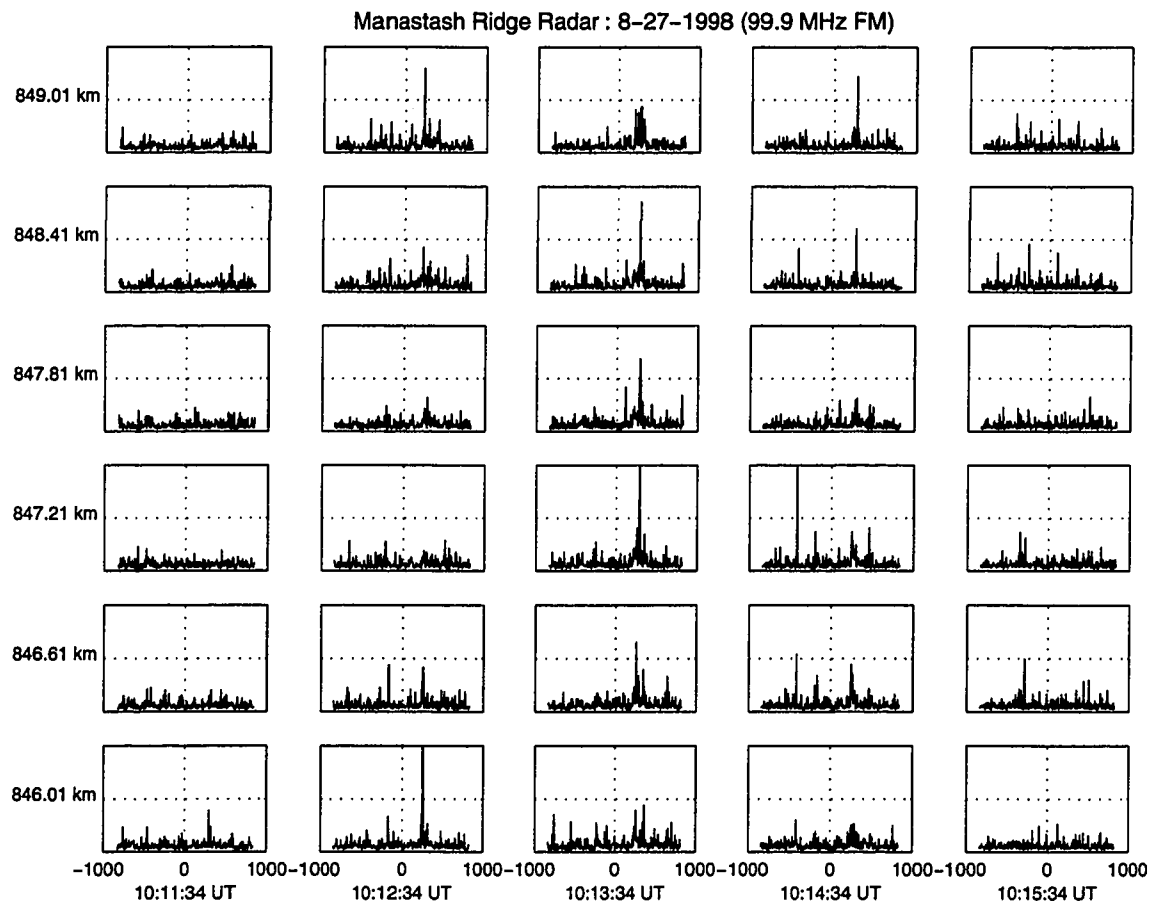


Figure 8.6: The irregularities are plotted here on a linear scale for several ranges and times. This is how many other coherent scatter radars have displayed their data. The Manastash Ridge Radar's resolution is too high for this to be particularly effective.

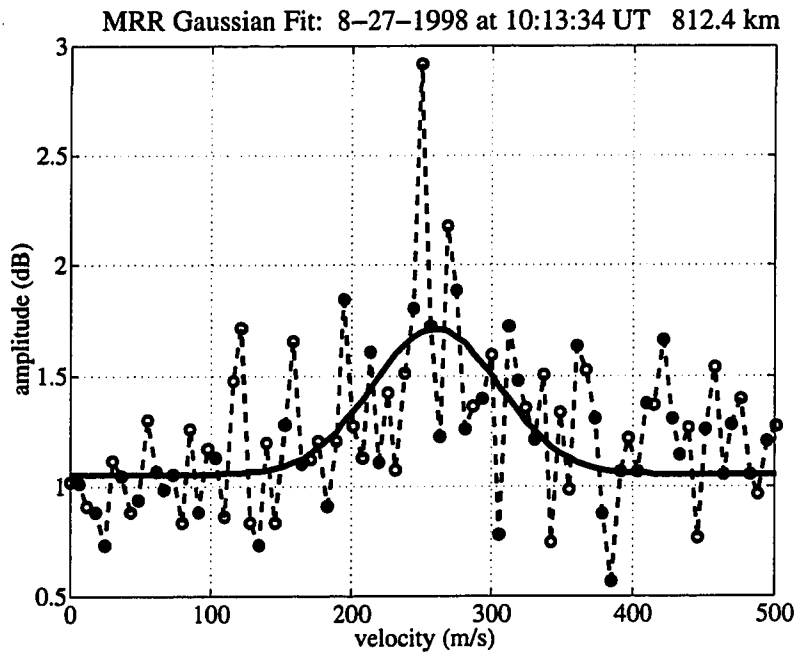


Figure 8.7: In fitting a Gaussian spectral model to the irregularities the fitter often underestimates the peak amplitude of the data and over estimates the spectral width. Here the solid line is the model fit while the dashed line with circles represents the radar data.

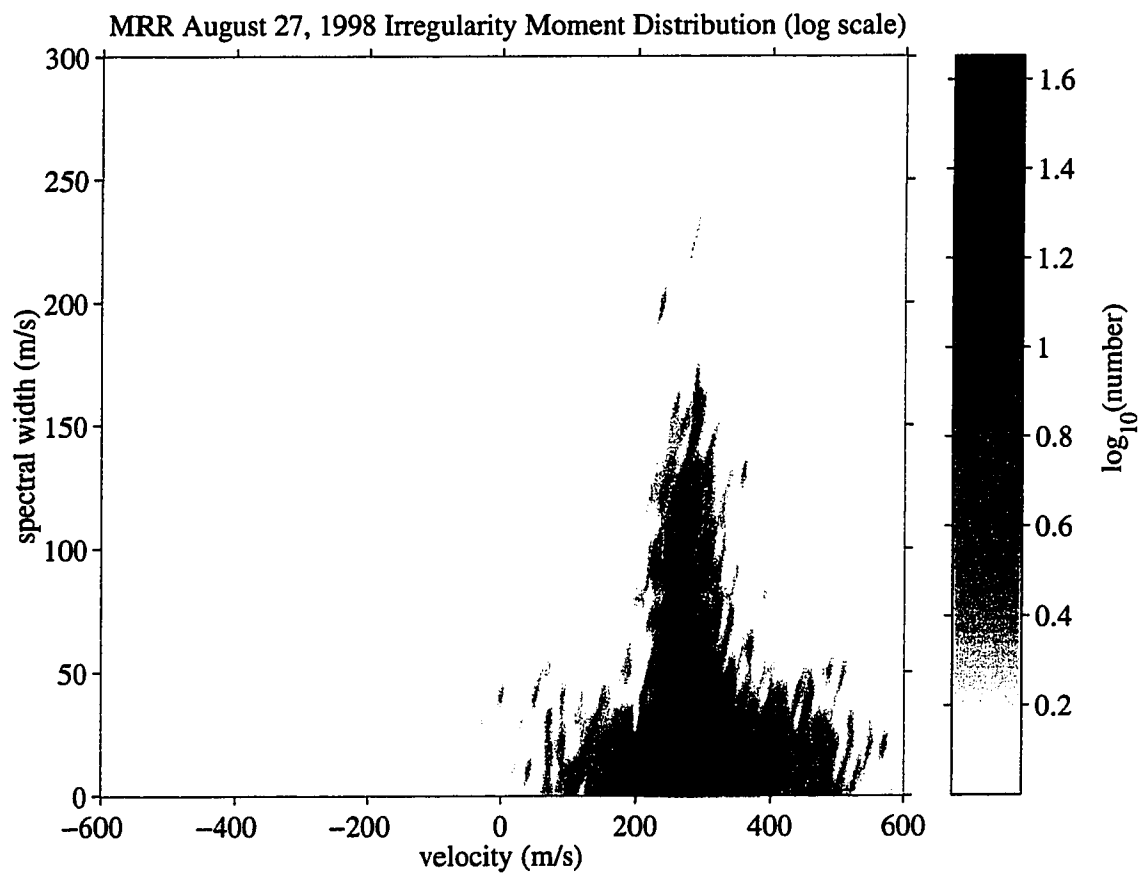


Figure 8.8: The velocity-width distribution of the fitted Manastash Ridge Radar data from the August 27, 1998 event. This is also known as a Watermann distribution, and is a useful method for comparing data between radar systems.

are useful for intercomparison between different radar systems [Watermann *et al.*, 1989a]. These distributions plot the mean velocity of the irregularities versus their spectral width. A Watermann distribution for the data from the Manastash Ridge Radar system is given in Figure 8.8.

### 8.1.2 Irregularity Probable Location Maps

Because the cross-section of the irregularities falls at approximately 10 dB/deg away from an aspect angle of  $\alpha = 90^\circ$  it is very likely that all the irregularities observed by the Manastash Ridge Radar are along this perpendicularity contour. The radar simply does not have the dynamic range to observe irregularities at large aspect angles unless they are extraordinarily large.

Because of this it is possible to map distance from the radar onto positions along the contour. This must be done taking into account the multi-static geometry and assuming an altitude for the irregularities.

For the magnetic aspect angle profile visible from the radar there are two possible locations associated with most distances. With the doppler shift of the irregularities consistently toward the radar it is likely that they lie either on the right hand side of the perpendicularity contour or the left. It is possible that they are actually on both sides but this would require an electric field that flips direction across the radar field of view. This is admittedly possible during such disturbed conditions but seems unlikely.

The probable location map is shown in Figure 8.9 for the right hand mapping of the data. This mapping is the most likely because of the antenna pattern, the Cascade mountains to the west, and observations by other instruments during the event. In many cases I will also show the left hand mapping which is more consistent with the typical electron drift direction during quiet time convection after magnetic midnight.

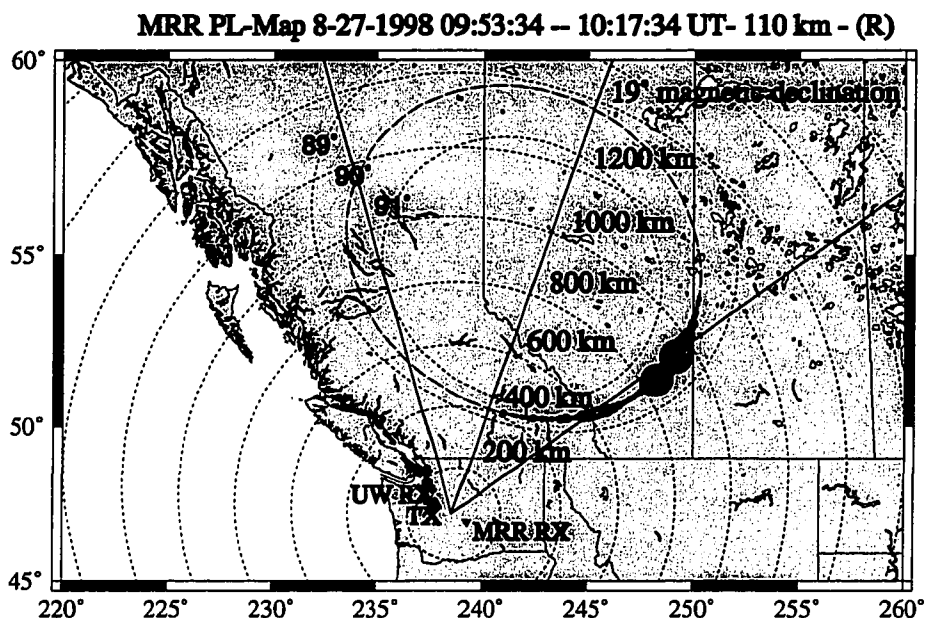


Figure 8.9: The inferred probable location of the irregularities for all the data from the August 27, 1998 event. Only the right hand mapping of the data is shown as this is the likely one based on the radar view volume and comparison to other data.

The largest error in the location of the irregularities using this method is an angular uncertainty on the order of  $7 - 8^\circ$ . It would be very useful to test this technique once an interferometric capability is developed for the radar. Probable location maps for three assumed altitudes and the left and right mappings are shown for 10:14:34 UT in Figure 8.10.

### 8.1.3 Inferred Electric Field

Once the irregularities have been located in space it is possible to infer a lower bound for the electric field in the E-region of the ionosphere. There are several more assumptions that must be made in order for this to be done.

The first assumption is that the drift velocity of the irregularities  $V_d$  is the observed doppler shift. This is just the assumption that the flow angle  $\theta = 0$ . In general the flow angle is within about  $20^\circ$  of the electron drift direction. Despite

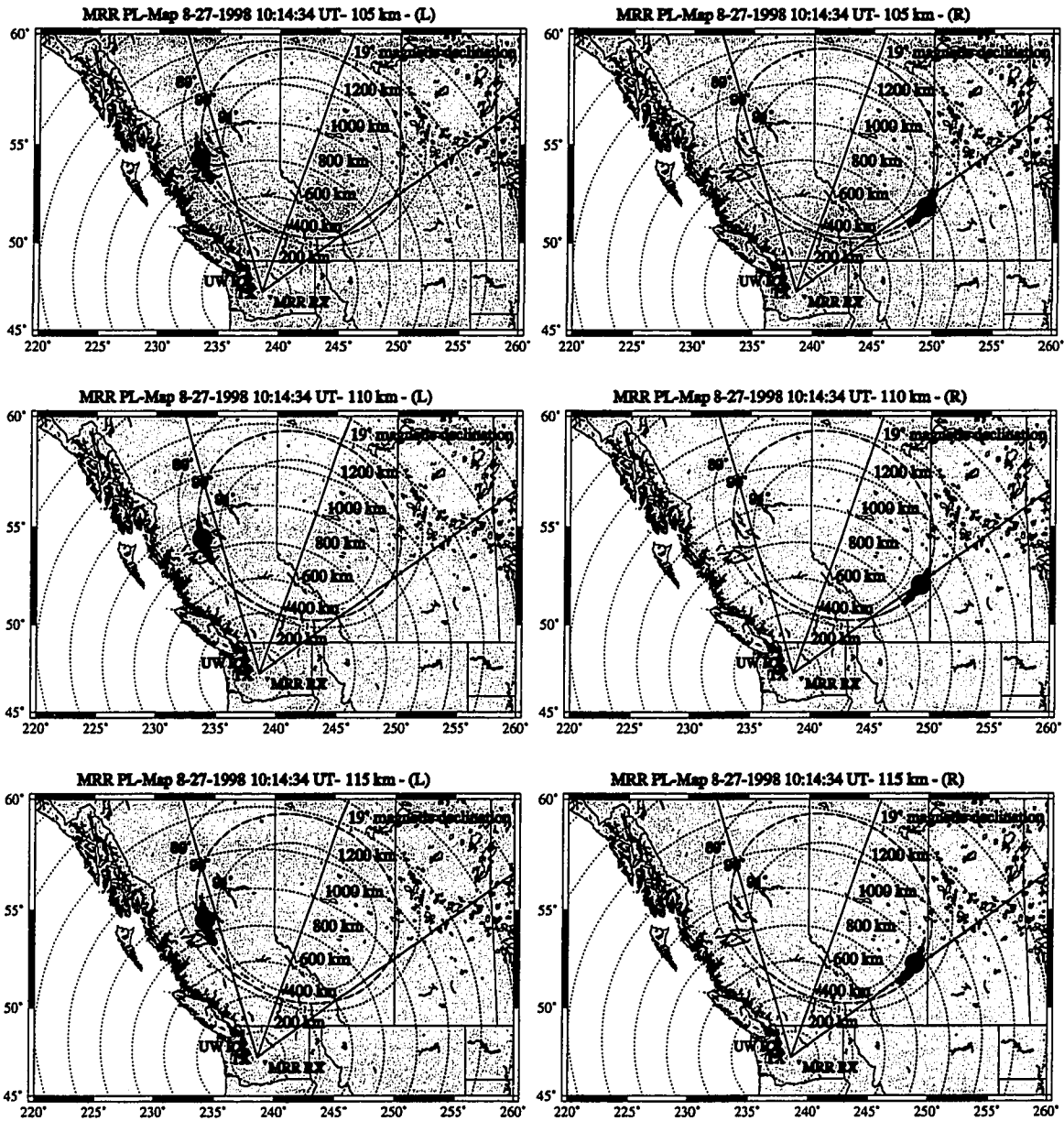


Figure 8.10: A sequence of probable location maps for the irregularities observed during the August 27, 1998 event. Both the left and right mappings are shown.

this there is no way of knowing the flow direction with the current radar system, and this means I can only put a lower bound on the electric field. Using

$$V_{doppler} = \frac{V_d \cos(\theta)}{1 + \psi} \cong \frac{V_d}{1 + \psi} \quad (8.2)$$

we assume to  $\psi = 0.25$  which is a typical value for the E-region. By combining this with

$$V_{d\perp} \cong \frac{\mathbf{E} \times \mathbf{B}}{B^2} \quad (8.3)$$

it is straightforward to infer a lower bound for the electric field given a magnetic field value. To obtain the magnetic field I presume that the irregularities map cleanly to the  $\alpha = 90^\circ$  magnetic aspect angle contour as a function of range. I then identify a location for each irregularity and compute the magnetic field value at a presumed altitude of 110 km using the IGRF magnetic field model.

The result of this process for all data from the August 27, 1998 event is shown in Figure 8.11 where both the left and right hand mapping are shown due to the ambiguity in the irregularity location. The electric field magnitude was relatively constant during the entire period and had a lower bound average value of  $19.8 \pm 5.1$  mV/m.

By using the vector direction of the magnetic field and the wave vector of each irregularity computed from the radar view geometry it is possible to also infer a vector direction for the electric field. This vector direction is shown overlaid on the radar view volume in Figure 8.12.

These estimates are rather crude lower bounds but it is difficult to do more with a single coherent scatter radar. In the future it should be possible to make

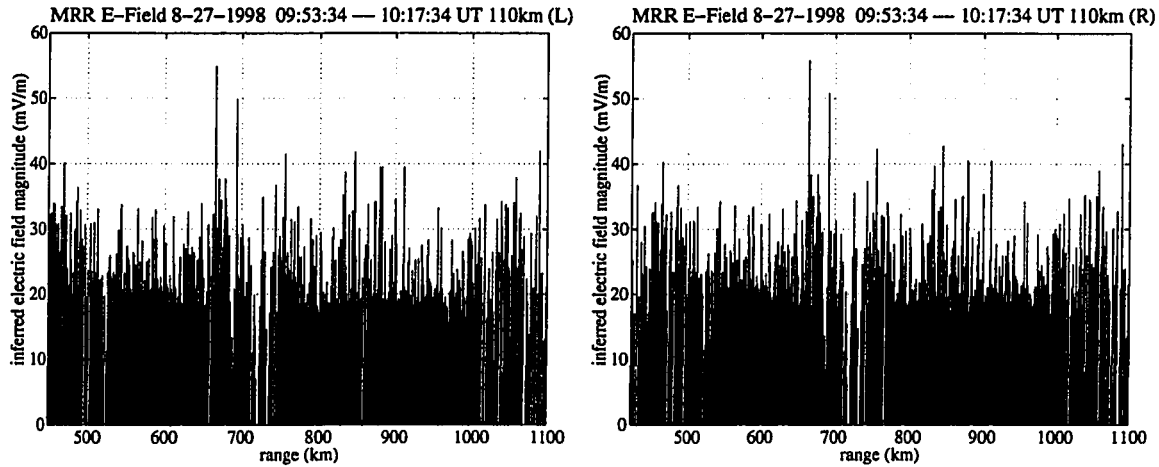


Figure 8.11: A lower bound electric field magnitude along the radar view line for data from the August 27, 1998 event. The left and right mappings are shown, and the field appears relatively constant throughout the whole event.

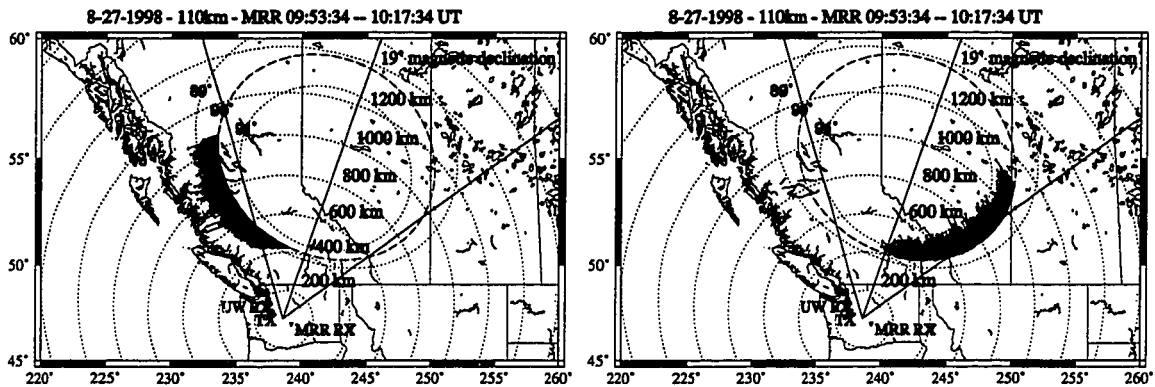


Figure 8.12: A map of the vector electric field direction as inferred by the radar is shown for radar data from the August 27, 1998 event. Both the left and right mappings are shown. The electric field estimates are lower bounds.



more accurate estimates by using interferometry to locate the irregularities in range, azimuth, and elevation.

## **8.2 Summary of Observations**

With the Manastash Ridge Radar we observed 88 seconds of data containing irregularities out of the 1800 seconds of data collected the morning of August 27, 1998. The nearest irregularities were observed at ranges of 500 km while the most distant were 1100 km away from the radar. The irregularities had velocities between 200 m/s and 400 m/s with predominantly narrow spectral widths. These observations correspond most closely to type-1 irregularities observed by other radar systems. The range-doppler extent of the irregularities was often large, but the passive radar technique prevented any range or doppler aliasing problems.

Because the radar is located at relatively low geomagnetic latitude (52.9° N CGM) a substantial expansion of the auroral oval is required to move the auroral electrojet into a position suitable for observation by the radar. This makes the Manastash Ridge Radar most useful in its current deployment for observing irregularities during highly active conditions.

These are the first E-region irregularity observations reported using a passive radar system, as well as being the first observations of 1.5 m irregularities reported in the literature. These are also the first observations reported between the 3 m (50 MHz radars) and 1 m (140 MHz radars) irregularity wavelengths since those reported at 1.3 m by *Ogawa* [1996].

## Chapter 9

### ANALYSIS OF THE AUGUST 27, 1998 EVENT

Observations of the August 27, 1998 Geomagnetic Storm by the Manastash Ridge Radar system were complemented by data from other instruments. In particular it is the observations using the Ultraviolet Imager onboard NASA's Polar spacecraft that provide the best context for understanding the radar data. By combining the radar data with conductances determined using the images it is also possible to estimate a lower bound for the ionospheric current density along the radar line of view.

#### **9.1 Magnetometer Observations**

Figure 9.1 shows the record from several magnetometers located closest to the Manastash Ridge Radar. These magnetometers show strong magnetic perturbations that are due to ionospheric currents. The perturbations are as large as 1000 nT and are greatest between 8:00 UT and 14:00 UT. The Newport, Washington magnetometer is closest to the radar view volume and shows its maximum deviation centered around 10:00 UT. This is nearly simultaneous with the observations of irregularities by the radar.

#### **9.2 Ultraviolet Imager Observations**

The Ultraviolet Imager (UVI) is an instrument on board NASA's Polar spacecraft. UVI takes pictures of the aurora through several filters that are changed at regular intervals during the spacecraft's polar orbit. Details of the imager's characteristics

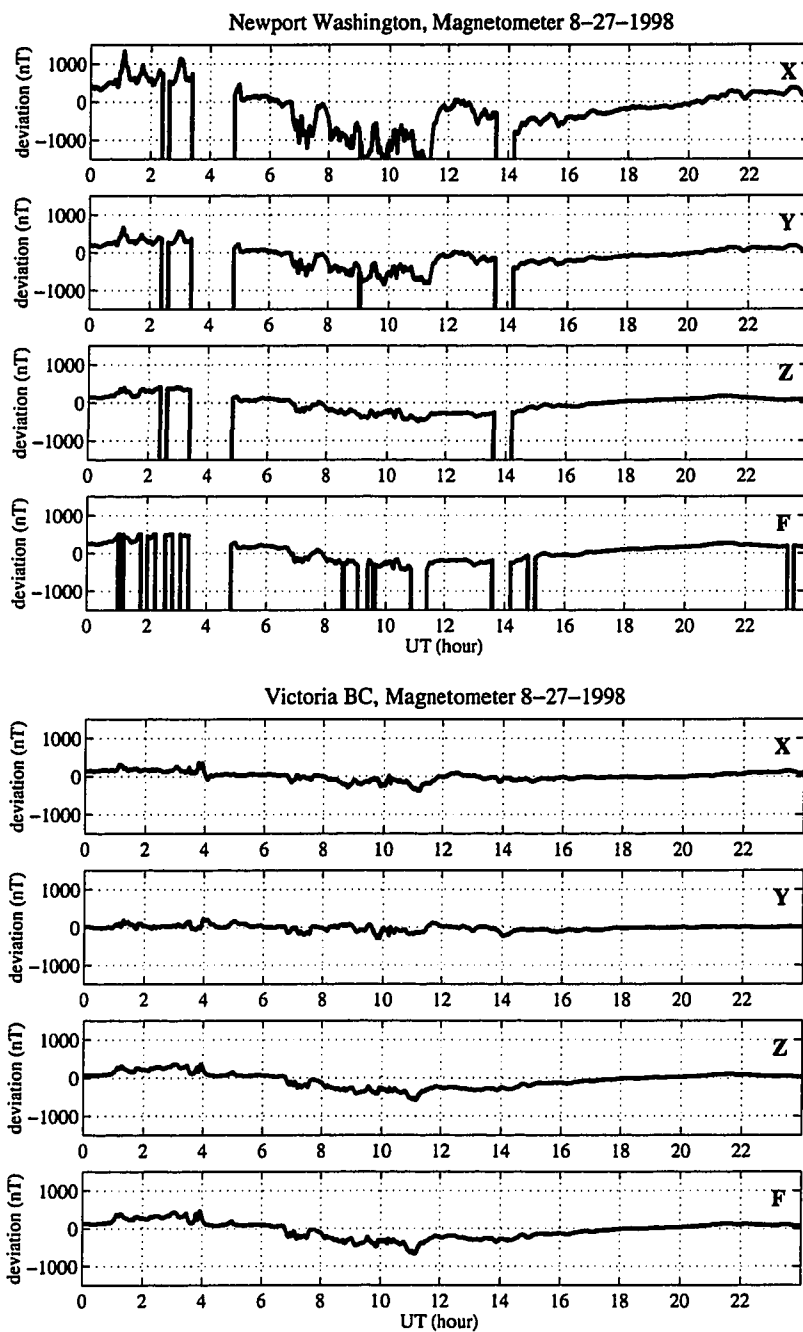


Figure 9.1: August 27, 1998 magnetometer observations for two locations near to the Manastash Ridge Radar. The Newport magnetometer is located to the northeast of the radar under the view volume, while the Victoria magnetometer is located outside of the view volume to the northwest.

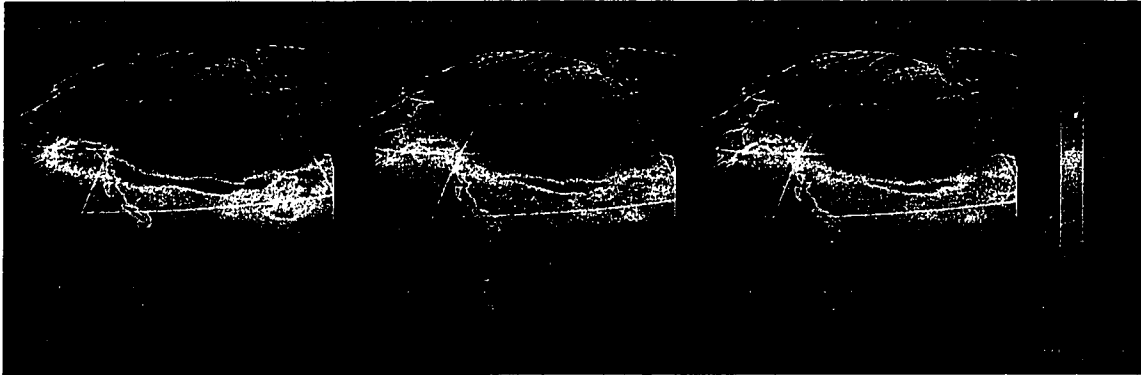


Figure 9.2: On August 27, 1998 the Ultraviolet Imager (UVI) aboard NASA's Polar spacecraft made observations of strong auroral emissions coincident with radar observations of E-region irregularities.

and other observations can be found in *Brittnacher et al.* [1997].

On August 27, 1998 UVI made observations of the aurora produced by the geomagnetic storm. During the period from 10:08:00 UT until 10:27:00 UT the imager recorded data directly over the view volume of the Manastash Ridge Radar. Three consecutive images from this period are shown in Figure 9.2, and these images clearly show an intense auroral arc located over southern Canada. It is the electric fields associated with this structure that created the irregularities observed by the radar.

### 9.2.1 UVI Photon Flux and Radar Data Comparison

By comparing the radar observations to the photon fluxes observed using the imager it is possible to examine where the irregularities occur relative to the auroral structures and how the irregularities and the arc evolve relative to each other in time and space.

There are many difficulties and uncertainties involved in making this comparison. The most problematic is the ambiguous angular resolution of the radar system. Although the radar has very fine resolution in range, the wide antenna pattern pro-

vides only minimal localization in azimuth. In order to move beyond this situation for the comparison with UVI I exploit constraints on the scattering geometry, consistency arguments, and relationships between the time evolution of the imager and radar data. It must be emphasized that this comparison is rough at best and should mainly be taken as a profitable direction for future experiments with higher angular resolution.

The scattering geometry provides the best constraint on the location of the irregularities. Because the scatter occurs most strongly where the radar beam is perpendicular to the Earth's magnetic field there is a single line of magnetic aspect angle ( $\alpha = 90^\circ$ ) where scatter from the irregularities is likely. Based on previous radar observations the scatter falls off away from this line at approximately 10 dB/degree. For all but the most extraordinarily strong irregularity returns the Manastash Ridge Radar currently has insufficient dynamic range to observe irregularities more than a degree off of perpendicular. To proceed I assume that the irregularities are constrained to the perpendicular scattering geometry.

The quality of this assumption is also limited by the accuracy of the IGRF magnetic field model used to compute the magnetic aspect angle contours, perturbations in the ionospheric magnetic field due to auroral current systems, variations due to refraction in the atmosphere, and uncertainty in the altitude of the irregularities.

There is no method of determining the altitude of the irregularities using the present radar system. Typically an antenna with narrow beam width in elevation is used, or interferometry is employed to effectively synthesize one. The irregularities are strongly confined to the E-region because of the physics of their generation. Variation in altitude between 100 km and 120 km leads to a one degree uncertainty in presumed azimuth of the irregularities. This is probably the dominant error in estimating the azimuth at this time. I assume an altitude of 110 km which is consistent with the average altitude of the irregularities as observed by other radar

systems.

For the comparison I utilize the range information from the irregularity Gaussian fits described in chapter 8. The irregularities are filtered for those having amplitude above an arbitrary lower cutoff. Unfortunately the perpendicular magnetic aspect angle line has two locations associated with each range, one left of magnetic north and one right. This ambiguity is not easy to resolve. Because the irregularities have a consistent sign to their doppler velocity throughout the event it is likely that they lie on one side or the other and not both. Structures and temporal variation in the imager data make it seem that the right side is the more likely. It is however not possible to resolve this matter convincingly and I present both the left and right mappings.

In order to perform this comparison it was necessary to map the UVI images into the radar's view volume on a  $0.25^\circ$  grid, averaging the photon flux at each grid region. This reduces the imager's effective resolution somewhat but also has the consequence of reducing the impact of uncertainty in the geographic coordinate mapping of the images.

Figure 9.3 shows the comparison between the irregularity observations and the imager data for the right hand mapping of the radar data, while Figure 9.4 shows it for the left hand side. The radar data was selected to be that closest to the start of the imager's integration period. Consecutive frames are shown from 10:09:05 UT until 10:21:21 UT and the imager uses four different filters during this time. The LBHL and LBHS filters show ultraviolet emissions from nitrogen while the 1304 and 1356 filters show oxygen emissions [*Brittnacher et al.*, 1997].

The mapping show a general correspondence between changes in the morphology of the auroral ultraviolet emissions and the irregularity locations and strengths. In both mappings the irregularities seem to occur preferentially on the equatorward side of the auroral arc.

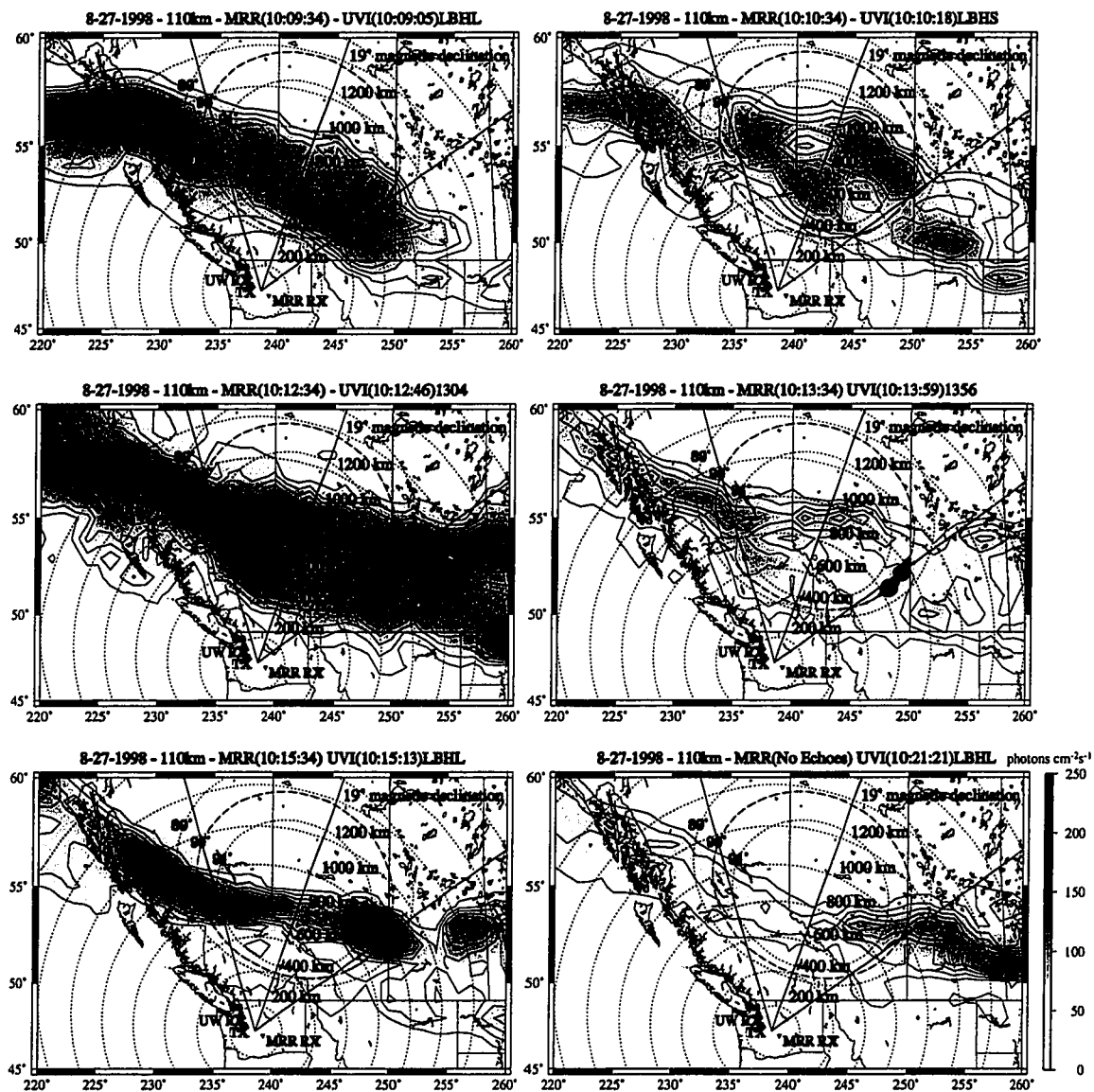


Figure 9.3: The observations from UVI are mapped onto the Manastash Ridge Radar's view volume in geographic coordinates. The fitted radar data is overlaid for the right hand mapping. The circle size indicates the relative strength of the irregularities. Note that the imager's filter cycles through LBHL, LBHS, 1304, and 1356 during the course of the observations.

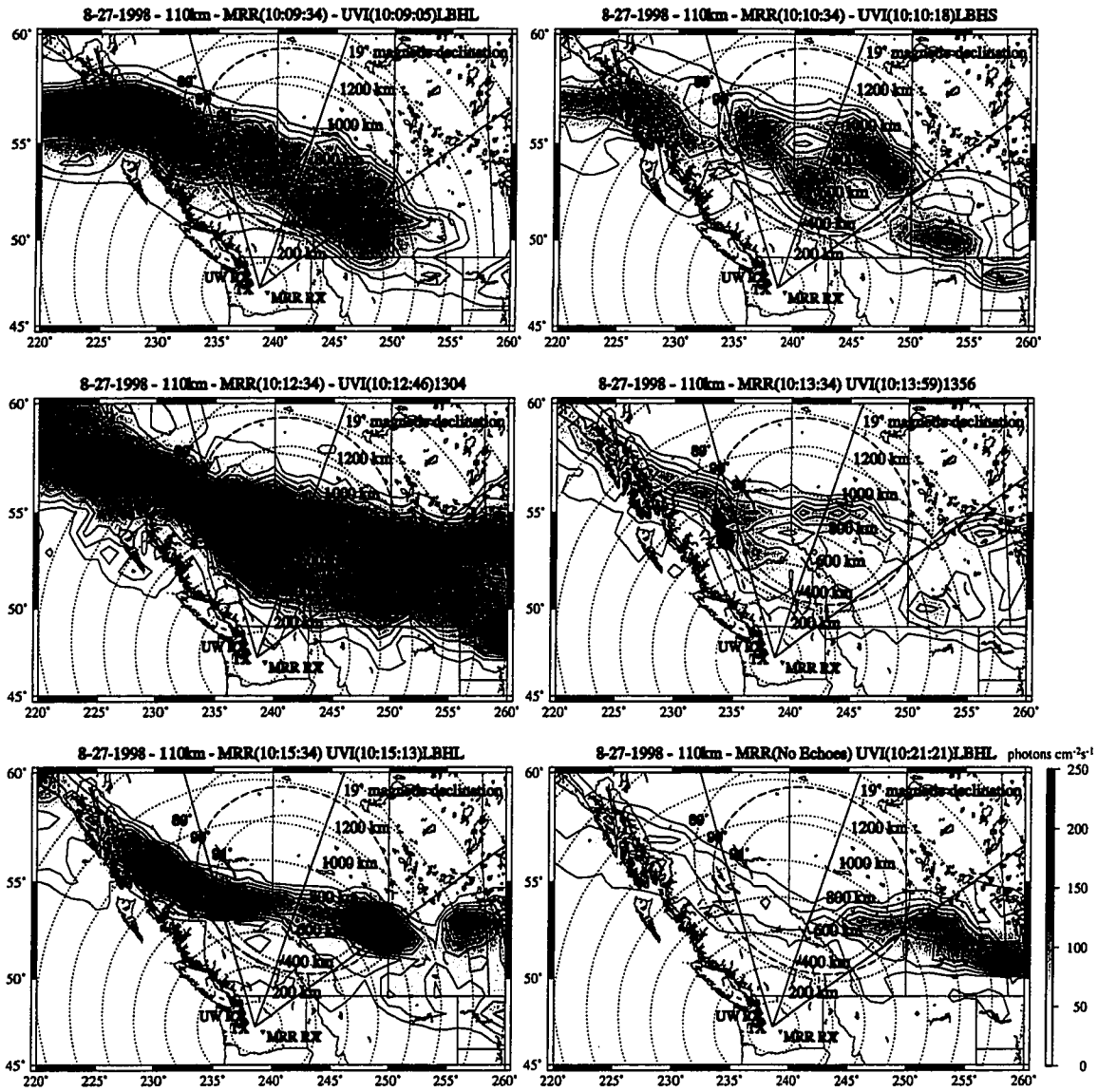


Figure 9.4: The simultaneous observations from UVI and MRR are mapped onto the radar view volume. Here the irregularities are plotted using the left hand mapping.



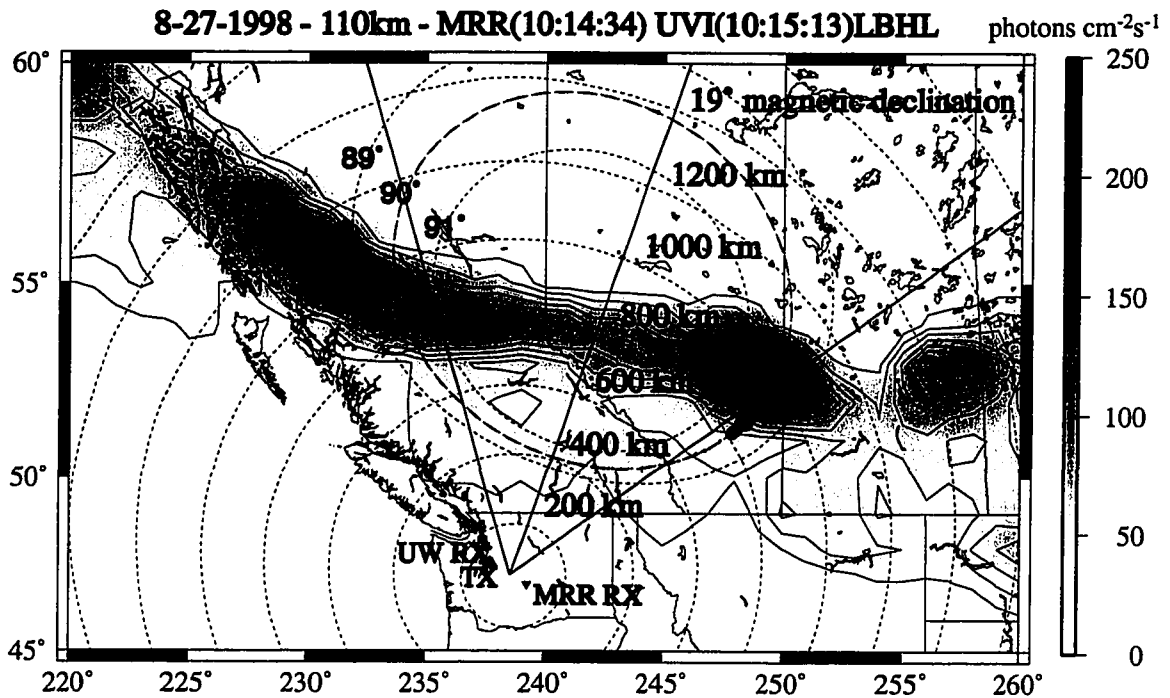


Figure 9.5: Radar data from 10:14:34 UT matches the observed imager data from 10:15:13 UT better than radar data from 10:15:34 UT. This may be due to the imager integrating over changes in the aurora that the radar detects.

In one case where the imager data proceeds the closest radar data the structure in the image seems to be better represented by the previous radar time period. This mapping is shown in Figure 9.5. This may indicate that the imager has integrated over temporal variation in the aurora and the radar observes this in the irregularity turbulence.

### 9.2.2 UVI and MRR View Line Cross-sections

In order to compare the observations of the radar with those of the imager it is useful to take slices of the image along the presumed radar view line. This is done by averaging those pixels whose geographic coordinates lie within  $0.5^\circ$  of the radar perpendicular magnetic aspect angle line at a particular range. This is done for both the left and right sides of the radar view volume at six different times, represented

in Figure 9.6 and Figure 9.7.

The radar data for this comparison is unfitted and is integrated in velocity to show the structures along the radar view line with reduced variance. The comparison between radar data at 10:12:34 UT and imager data at 10:12:46 UT for the right hand mapping is particularly striking. Here we can see that the observed structure and its spatial scale is very similar in both the irregularities and the ultraviolet emissions.

In many cases the radar data shows structure that the imager does not observe and vice versa. This may be due to that fact the radar is really observing the consequences of electric field and density gradient structures. These structures can extend beyond the regions where electron precipitation is actually producing ultraviolet emissions. Uncertainty in the alignment of the radar data with the imager photon flux pixels is also a likely cause of the differences.

### *9.2.3 UVI Estimated Conductivity and MRR Vector Electric Field*

The Ultraviolet Imager is capable of estimating ionospheric conductances (height integrated conductivities) from observations using its different filters. The basic process is described in *Germany et al.* [1994], and has large uncertainties during rapid auroral variations. Despite the limitations of the technique a comparison to the electric fields inferred from the radar data is interesting.

The conductances are mapped to a  $1^\circ$  grid and averaged over several frames to reduce the impact of the auroral variations on the estimates. This results in two integrated periods and the Hall conductance is shown in Figure 9.8 along with the radar inferred electric field during that time period for the right hand mapping. The enhanced Hall conductance on the right hand side of the radar view volume further increases the likelihood that the right hand mapping is the correct one.

The Pedersen conductance inferred from the imager data is shown in Figure 9.9

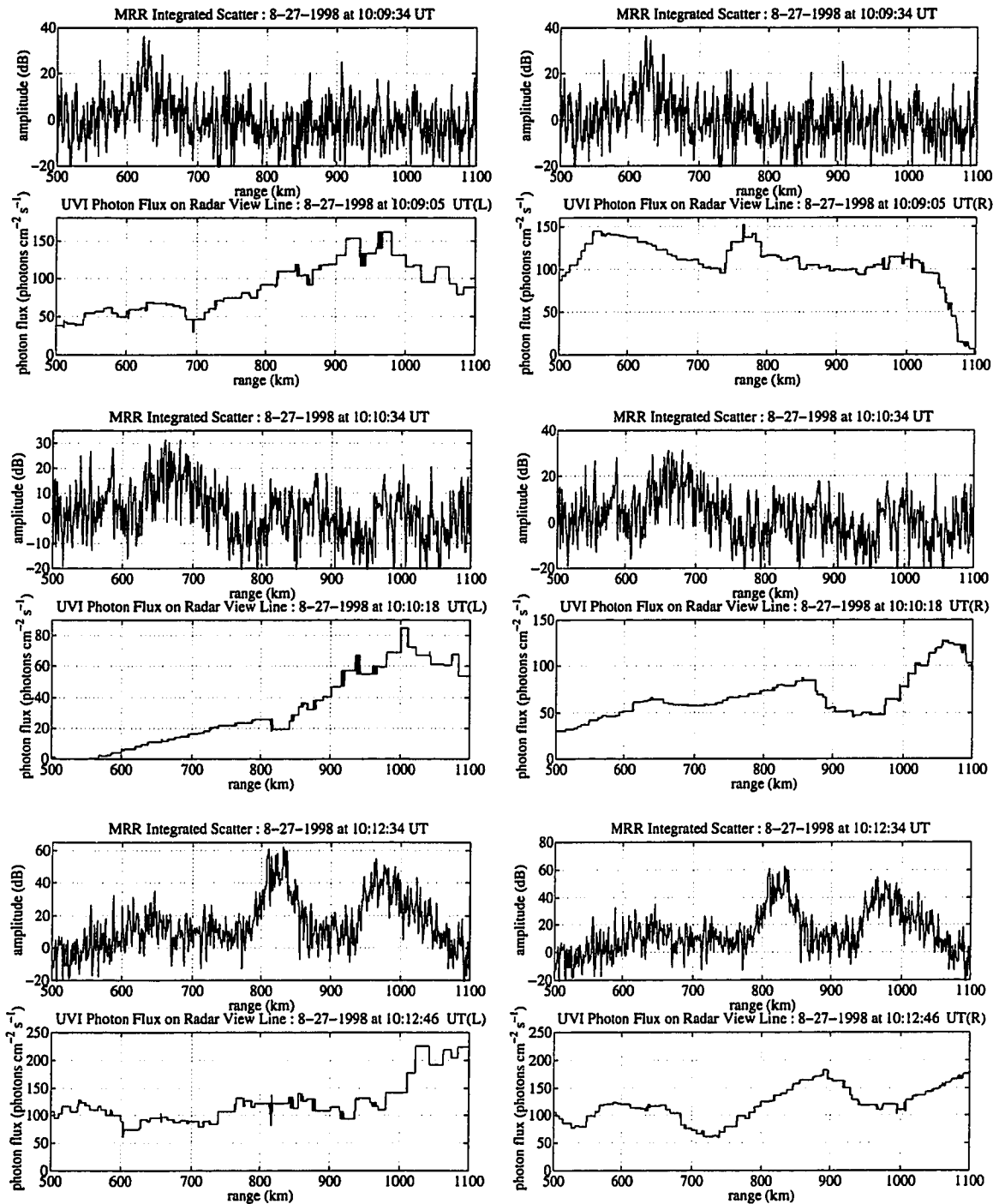


Figure 9.6: A comparison of velocity integrated radar data to UVI photon emissions along the presumed radar view line. Both the left and right hand mappings are given for 10:09:34 until 10:12:34 UT. Some structures are clearly observed by both the imager and radar while others are not.

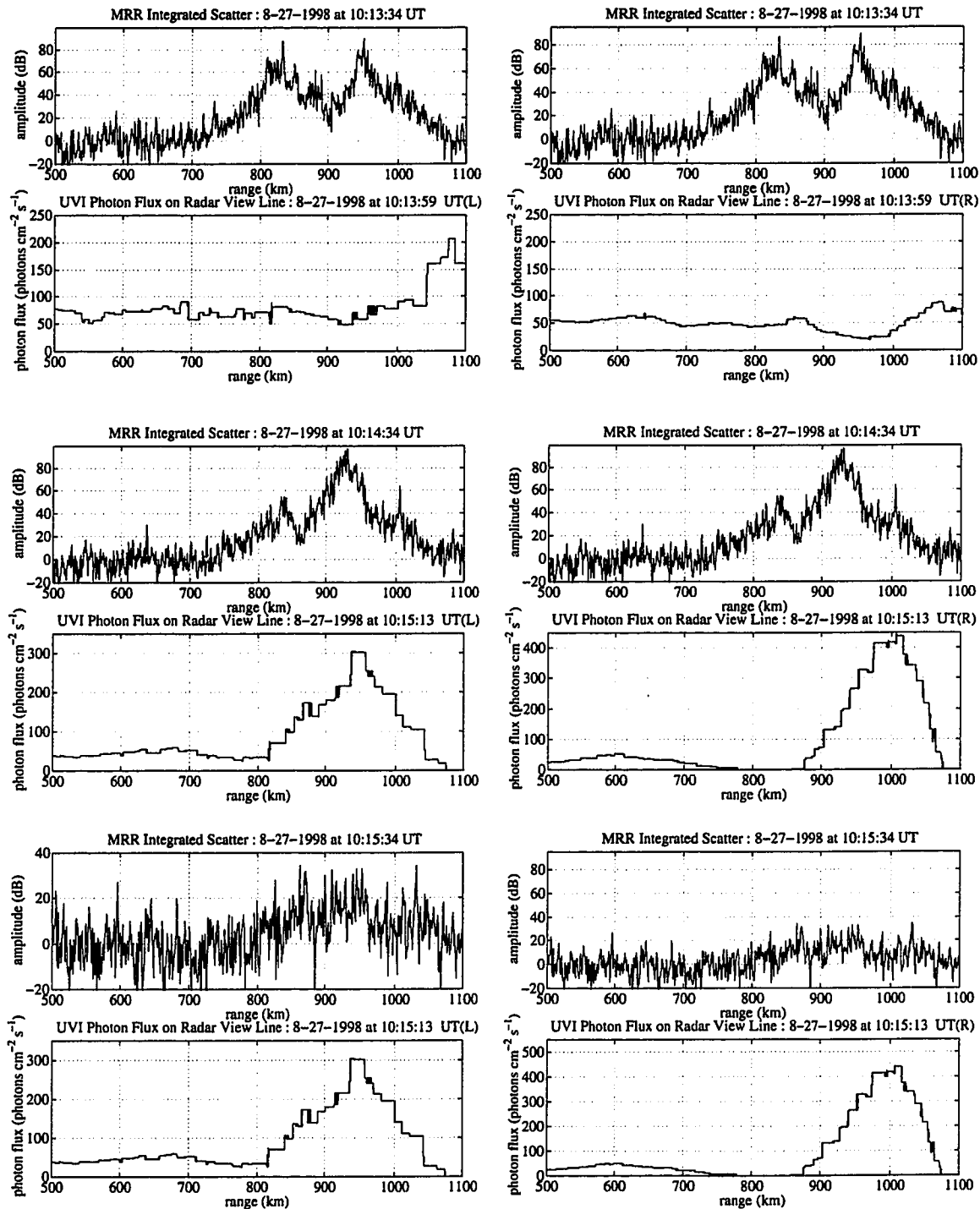


Figure 9.7: The velocity integrated radar data is compared to the UVI photon emissions along the presumed radar view line. Both the left and right hand mappings are given for 10:13:34 until 10:15:34 UT. The imager data from 10:15:13 UT is compared to radar data before and after the UVI observations.

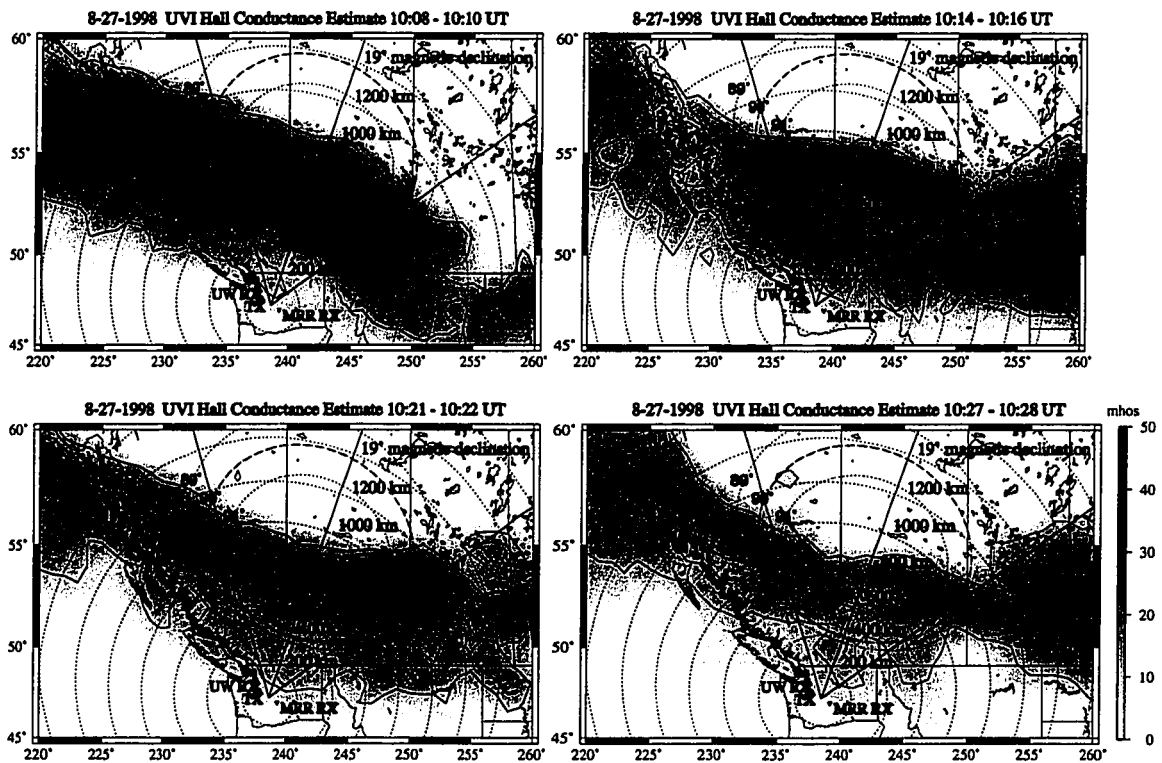


Figure 9.8: UVI estimated Hall conductance (height integrated conductivity) for four times during the August 27, 1998 event. The vector electric field inferred by the radar for each period where irregularities were observed is overlaid using the right hand mapping. This mapping corresponds to the regions of greatest Hall conductance.

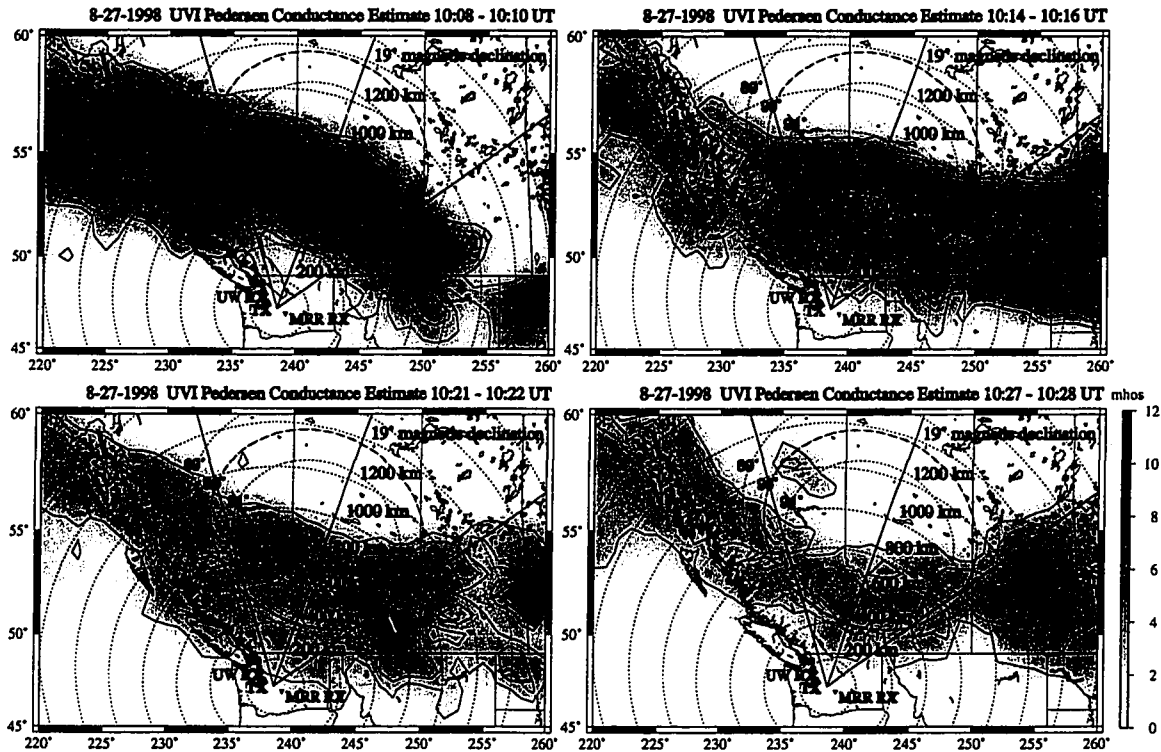


Figure 9.9: The UVI estimated Pedersen conductance for four times during the August 27, 1998 event. The vector electric field inferred by the radar is overlaid using the right hand mapping.

for the same two periods. In this case the Pedersen conductance is an order of magnitude smaller than the Hall conductance. This implies immediately that most of the current perpendicular to the magnetic field is being carried by the Hall current associated with the auroral electrojet.

### 9.3 Ionospheric Current Density Estimate

By presuming that the current is all flowing perpendicular to the magnetic field along the radar view line, it is straightforward to estimate a lower bound for the Hall and Pedersen current densities using the relation

$$J_{pedersen} + J_{hall} = \Sigma_p(\nabla_{\perp} \cdot \mathbf{E}) + \Sigma_h(-\nabla_{\perp} \times \mathbf{E}) \quad (9.1)$$

where  $\Sigma_h$  is the Hall conductance,  $\Sigma_p$  is the pedersen conductance,  $\mathbf{E}$  is the electric field, and  $\nabla_{\perp}$  is effectively a scale length perpendicular to the magnetic field. In order to estimate this scale length from the data we use  $\nabla_{\alpha=90}$  which is the scale length along the radar view line. This is another approximation but there is no other way to obtain a scale length from the electric field data that is not arbitrary. It is essentially an assumption that the scale of ionospheric features along the radar view line is similar to the scale in all directions.

The magnitude of the Hall current density lower bound is shown in Figure 9.10 along with the vector current density in the plane perpendicular to the magnetic field in Figure 9.11.

The inferred Hall current lower bound is  $0.77 \pm 0.78 \mu A m^{-2}$  for 10:08 - 10:10 UT, and  $0.33 \pm 0.45 \mu A m^{-2}$  for 10:14 - 10:16 UT. Despite the large uncertainty this estimate has reasonable values for a lower bound. The Hall current is confined to the E-region and this is the current that forms the auroral electrojet.

The Pedersen current density estimate is somewhat less certain because the conductance is distributed throughout the E and F-regions in an unknown manner. The Pedersen current density magnitude is shown in Figure 9.12 as a function of radar range and the vector direction and magnitude is shown in Figure 9.13 along with the imager derived conductance.

Here the Pedersen current density lower bound is significantly lower due to the difference in Pedersen conductance. The inferred lower bound is  $0.13 \pm 0.12 \mu A m^{-2}$  for 10:08 - 10:10 UT, and  $0.07 \pm 0.10 \mu A m^{-2}$  for 10:14 - 10:16 UT.

These current density estimates are very crude reductions of the data in light of the significant uncertainty in the irregularity locations. Future observations should

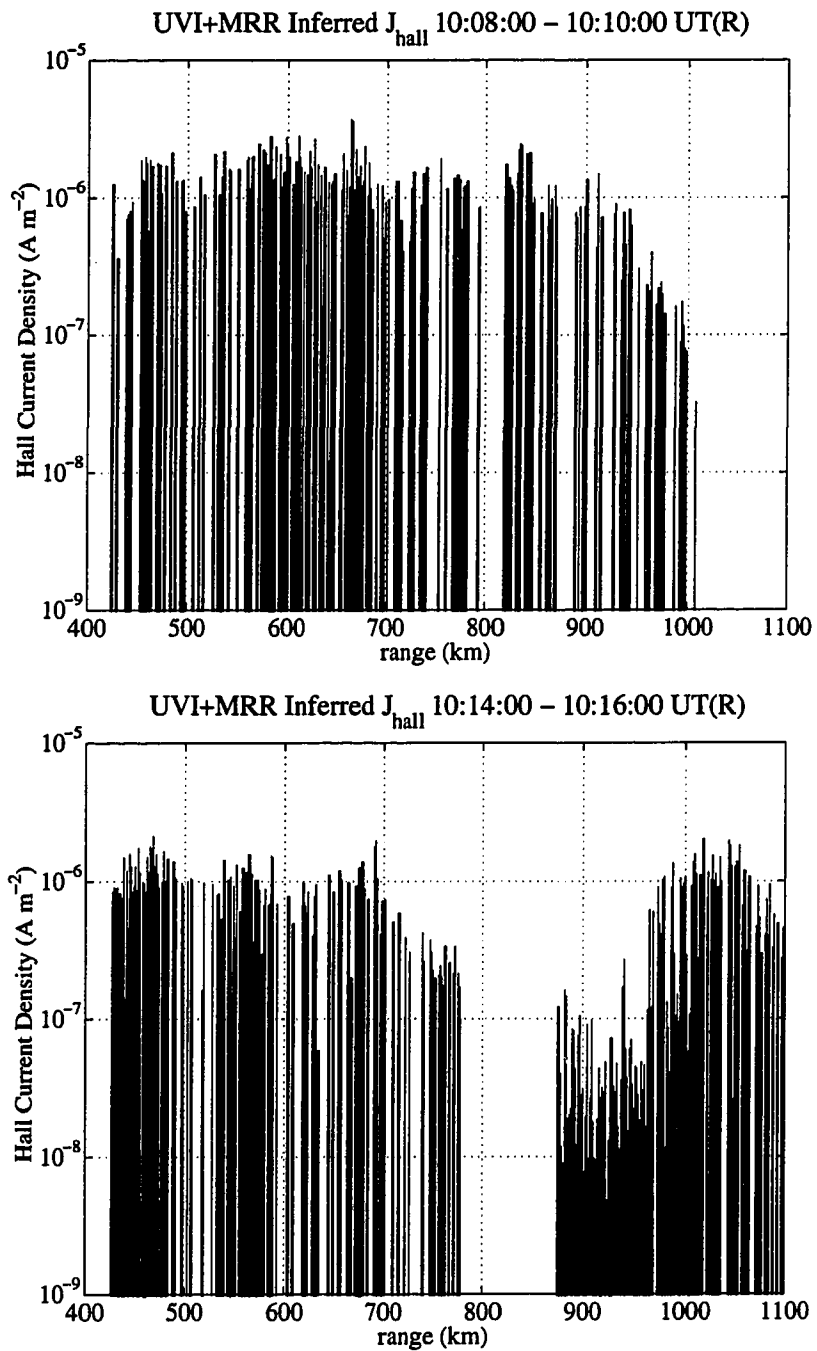


Figure 9.10: A combination of the UVI and MRR data allows a lower bound estimate of the Hall current density flowing in the ionosphere to be made along the radar view line for two periods during the event.



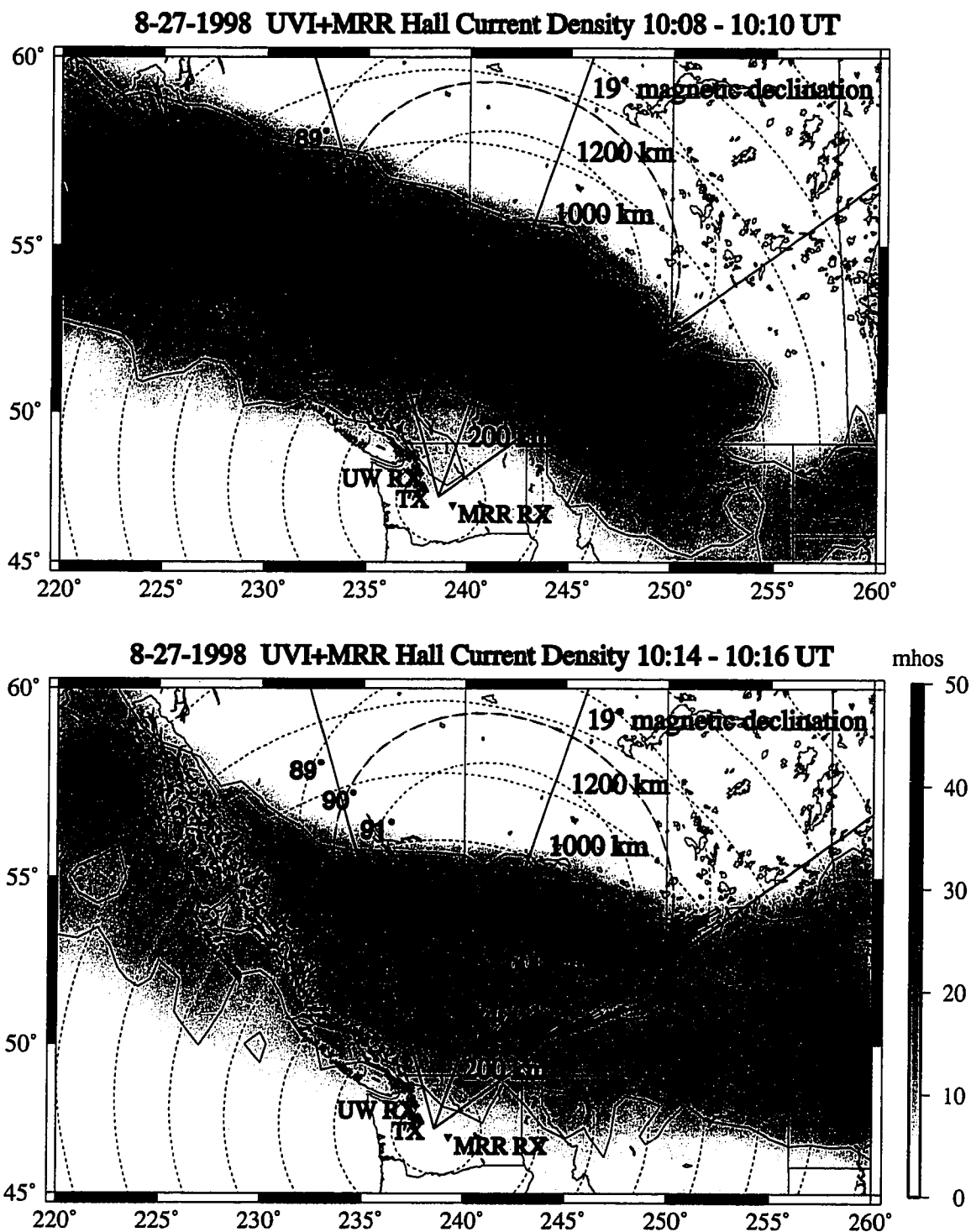


Figure 9.11: The vector current density can be overlaid on the UVI Hall conductance estimate and the radar view volume.

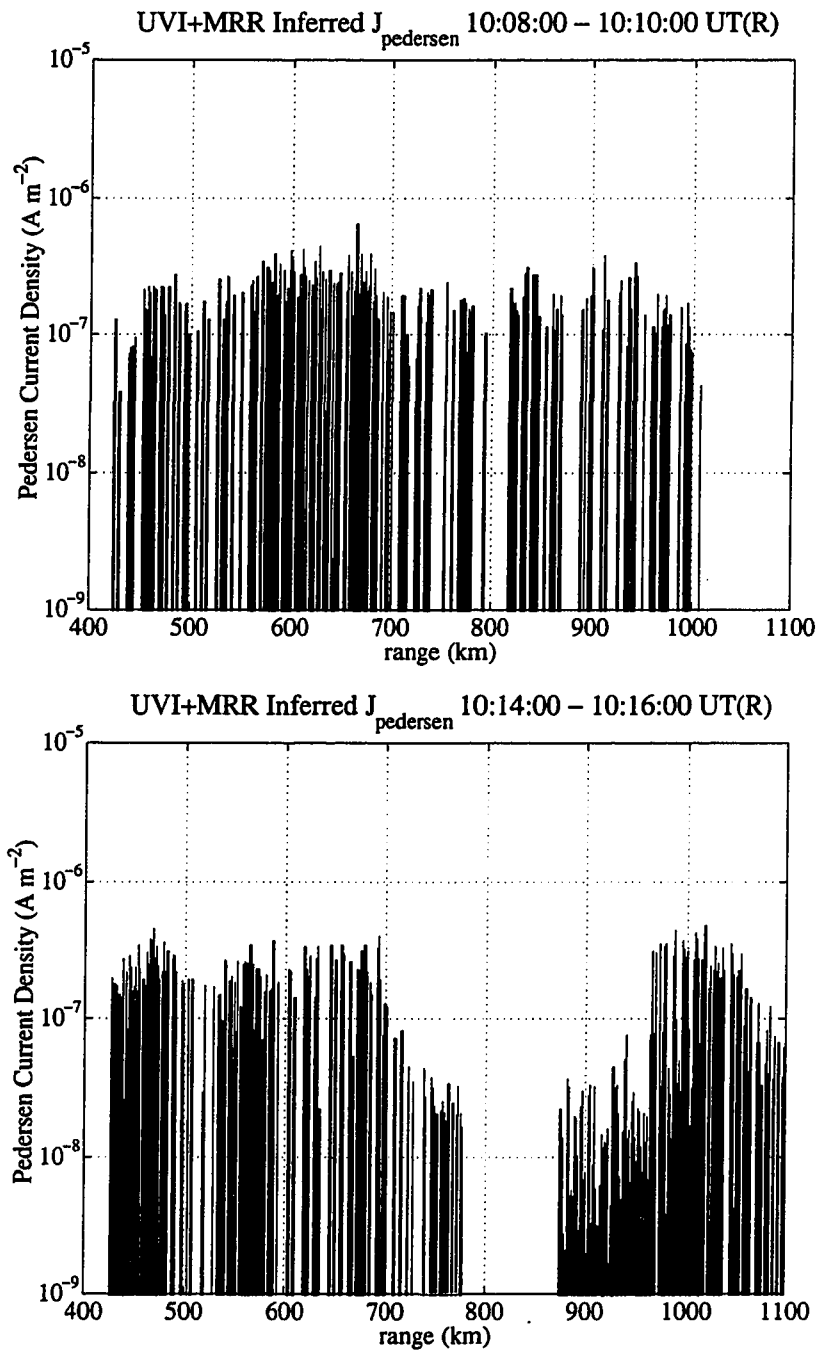


Figure 9.12: The lower bound magnitude of the Pedersen current is estimated to be an order of magnitude smaller than the Hall current along the radar view line.

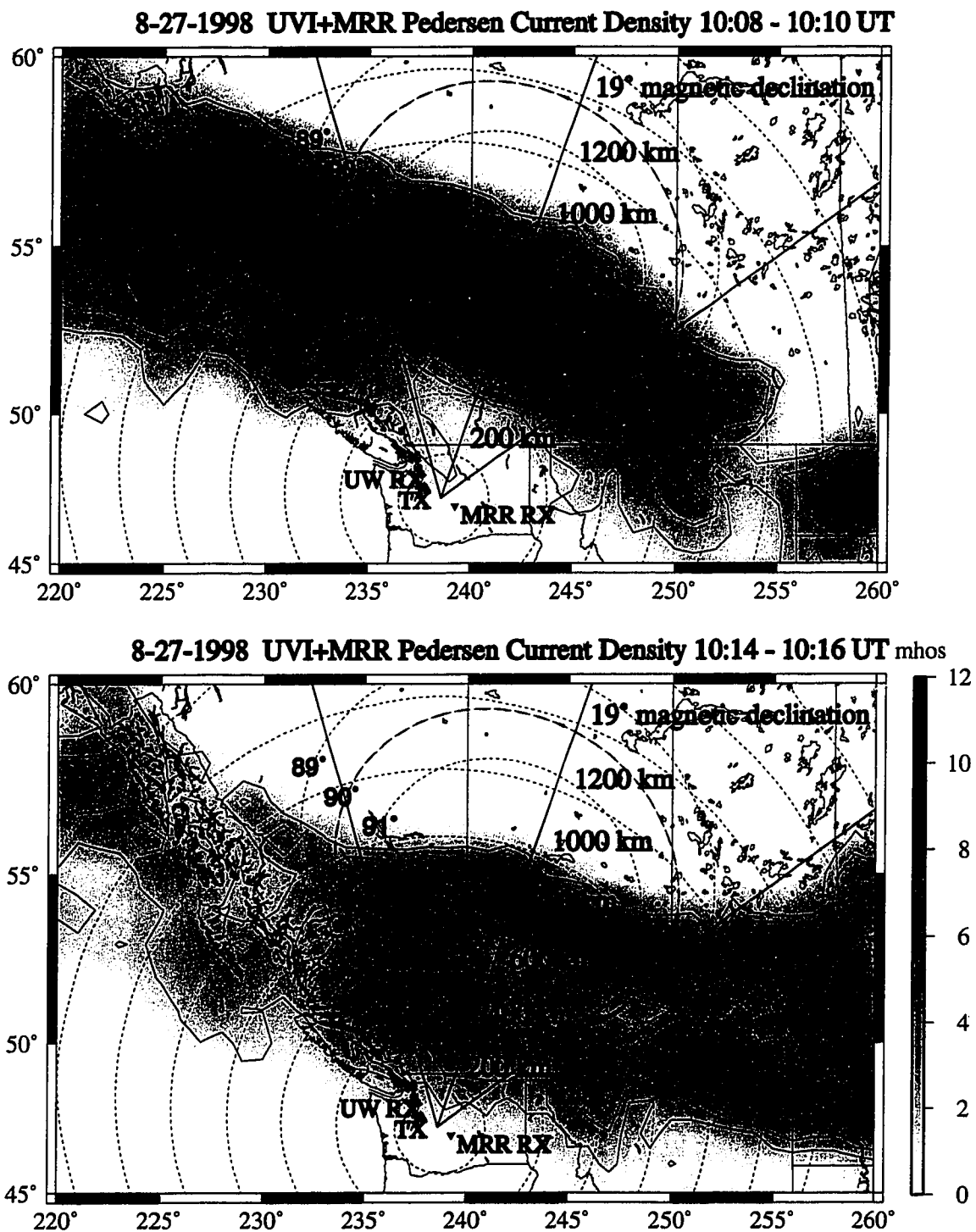


Figure 9.13: The vector direction and magnitude of the Pedersen current density is overlaid on the UVI Pedersen conductance estimate and the radar view volume.

focus on interferometric location of the irregularities along multiple baselines to ensure greater accuracy, wider spatial coverage, and current density estimates that are absolute values and not lower bounds.

## Chapter 10

### FUTURE DIRECTIONS AND CONCLUSION

Passive radar is a novel new technology where signals are intercepted from the environment and used to make radar observations. This newly developed technology has many possible ways it can develop in the future. I briefly discuss the role of passive radar in radio science. Following this I conclude with an overview of this work.

#### *10.1 Passive Radar*

Intercepting signals from the environment and utilizing them to synthesize radar observations is useful well outside the realm of radio science. Applications to aircraft tracking and surveillance have been under investigation for some time in the defense community. In the future, air traffic control and navigation may find passive radar a great complement to active radar and beacon techniques. Ultimately though, the transmitter portion of complicated military and civilian infrastructure systems is a relatively small fraction of their total cost. So passive radar, while potentially useful in some situations, will never truly be necessary where the public interest is sufficiently great and adequate resources are available.

In radio science, however, the costs of operating powerful transmitters is very large compared to the budgets that are involved. The savings and expanded possibilities provided by passive radar is therefore of the greatest benefit to the radio science community. In order for this potential to be realized, passive radar must evolve substantially from its early developmental state.

Fortunately, this approach to radar exploits many powerful trends in current technological development. The rapid advance of computational power is substantially reducing the difficulty of cross-correlating and analyzing intercepted signals. Global positioning systems have essentially solved the problems underlying the synchronization of widely separated receivers, and the development of a global high-speed data network infrastructure will eliminate the difficulties of communicating receiver information between any two points on the globe.

These developments will soon make possible the deployment of a multistatic distributed radar network composed of low-cost receivers. These receivers will be individually quite compact, but together they will form a very capable ionospheric observation network. Such a system could be developed in incremental stages by a diverse cross-section of participants. It could then be operated cooperatively by exploiting the powerful computer networks that make the system possible.

There are several key areas that can be identified in which significant progress must be made in order to realize the potential of passive radar. Receiver improvements are perhaps the most immediate place in which significant benefits can be realized. The current receivers systems of the Manastash Ridge Radar have many limitations including relatively large size, limited tuning range, lack of flexible gain control, and the use of several high-cost components such as external GPS receivers and digitizers. Although novel due to the use of GPS for precise synchronization, the underlying technology is certainly not state-of-the-art for receiver design.

By utilizing many of the latest digital receiver techniques it should be relatively straightforward to develop very compact receivers which mount on the antennas, have the ability to simultaneously observe several widely separated frequencies, perform digitization as an integral part of their design, and self-synchronize by intercepting GPS signals as part of their native operation.

Such receivers would then be combined with an appropriately wide bandwidth

antenna system. These individual radar receiver units could then be deployed in arrays where the signals are combined digitally to synthesize appropriate antenna patterns.

Phased arrays are also important for rejecting clutter from the radar system by synthesizing antenna patterns that dynamically null strong clutter sources. This is especially important when intercepting continuous wave signals, such as those transmitted by FM radio stations, because the signals continuously illuminate clutter sources. The scatter from mountains and aircraft can interfere with observations of ionospheric plasma irregularities.

It is also important to consider what signals such a system will be intercepting, where its deployment is most technologically feasible, and where its observations would be most scientifically useful.

North America is a particularly good choice for the deployment of a passive radar network. There are a large number of FM radio and digital television stations covering much of the continent. These stations broadcast powerful signals over a wide range of frequencies. The coverage is very well distributed as can be seen for FM radio stations in Figure 10.1. A North American deployment also has the advantage of the relative accessibility of high speed Internet connections to provide data transport.

To maximize the scientific output of a passive radar network it should be deployed so that a large section of the auroral oval can be observed simultaneously, at multiple wavelengths, and with multiple overlapping baselines. An interferometric capability at each receiver site is also necessary to allow the location of the E-region irregularities to be precisely measured.

A passive radar network could provide long term observations of E-region irregularities and would contribute substantially to the experimental study of ionospheric turbulence, electric fields, and energy dissipation by ionospheric current systems.

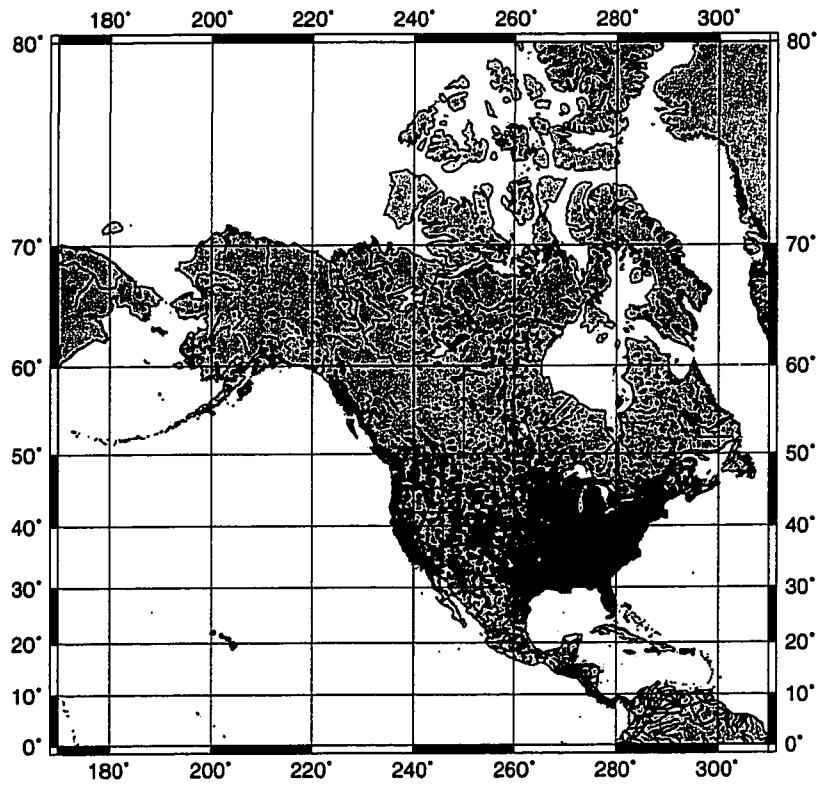


Figure 10.1: A national map of FM radio stations from the Federal Communications Commission database. Each dot on the map represents a single FM radio station.



The network could also derive ionospheric electric fields and convections patterns during disturbed conditions with wide coverage at relatively low cost. This would be complementary to observations such as those by SuperDARN because HF radars have difficulty estimating electric fields during strong auroral events due to absorption of their signals in the D-region of the ionosphere.

## **10.2 Conclusion**

In this dissertation I have presented the first results from the Manastash Ridge Radar system. This system is the first passive radar constructed for scientific purposes. Its performance substantially exceeds that of other contemporary coherent scatter radars used for observing E-region irregularities at a substantially lower cost.

The initial observations using the radar system were made during a strong geomagnetic event on August 27, 1998. During this period the auroral oval expanded equatorward bringing it and the associated auroral electrojet into the view volume of the radar. The observations taking during this event are the first reported for 1.5 m irregularities.

By making several assumptions I have determined the probable location of the irregularities in the radar's view volume and inferred a lower bound for the electric field in the E-region during the event. There are several ambiguities in this process and in the future it would be very useful to develop passive radar systems that provide a full interferometric capability or at the very least use a narrow antenna pattern.

The August 27, 1998 event was also observed by the Ultraviolet Imager aboard NASA's Polar spacecraft. For a period from 10:08:00 to 10:27:00 UT the imager observed auroral emissions directly over the view volume of the radar system. The imager used several different filters during this time and this allows the ionospheric conductance to be derived for two periods during these observations.

I have compared the imager observations directly to those of the radar by mapping the imager photon fluxes onto the radar view volume. The general evolution of the event is the same in both instruments. In several cases the structures seen by the radar are reflected in the structure of ultraviolet emission from the ionosphere. In most cases the strongest E-region irregularities appear to be located on the equatorward side of the auroral arc.

To complete the analysis of the August 27, 1998 event I have combined the imager derived ionospheric conductances with the radar inferred electric fields to compute a lower bound for the Hall and Pedersen current densities flowing in the ionosphere. The estimates are somewhat crude due to uncertainty in the location of the E-region irregularities. This approach should be attempted again using radars with greater angular resolution. A good choice for such an experiment would be an incoherent scatter radar system.

In addition to the radar observations and their analysis, I have included some work on a linear three fluid theory for E-region irregularities. This theory is unique in that it does not make the simplifying assumption that the E-region consists of a single ion species. The dispersion relation that is analytically derived from this model is analyzed numerically by evaluating its roots for appropriate parameter variations and using a realistic model ionosphere.

The theory predicts the phase velocities and growth rates for several wave modes produced by the system. The familiar "type-1" Farley-Buneman two stream wave mode is recovered. It is shown that for a sufficiently high ion-neutral collision frequency this mode may also explain the "type-3" radio aurora. Several other weakly damped wave modes that may be important for the "type-3" radio aurora and for energy dissipation in the turbulent E-region are also explored. Future directions of investigation for this theory include an expansion to include non-linear terms, application to sporadic E-layers formed by meteors, and investigations of plasma

regimes outside those of the E-region of the ionosphere.

## BIBLIOGRAPHY

- [*Abel and Newell*] Abel, W. G., R. E. Newell, Measurements of the afternoon radio aurora at 1295 MHz, *J. Geophys. Res.*, *74*, 231, 1969.
- [*Andre*] Andre, D., The dependence of the relative backscatter cross section of 1m density fluctuations in the auroral electrojet on the angle between electron drift and radar wave vector, *J. Geophys. Res.*, *88*, 8043, 1983.
- [*Albert and Sudan*] Albert, J. M., and R. N. Sudan, Three-wave interaction and type II irregularities in the equatorial electrojet, *Phys. Fluids B*, *3*, 495, 1991.
- [*Alport et al.*] Alport, M. J., N. D'Angelo, H. L. Pecseli, A laboratory experiment on EM backscatter from Farley-Buneman and gradient drift waves, *J. Geophys. Res.*, *86*, 7694, 1981.
- [*Bagaryatskii*] Bagaryatskii, B. A., Radar reflections from aurorae, *Soviet Phys. Usp.*, *4*, 70, 1961.
- [*Bahnsen et al.*] Bahnsen, A., E. Ungstrup, C. G. Falthammar, V. Fahleson, J. K. Olesen, F. Primdahl, F. Spangslev, A. Pedersen, Electrostatic waves observed in an unstable polar cap ionosphere, *J. Geophys. Res.*, *83*, 5191, 1978.
- [*Balsley and Ecklund*] Balsley, B. B., W. L. Ecklund, VHF power spectra of the radar aurora, *J. Geophys. Res.*, *77*, 4746, 1972.
- [*Balsley et al.*] Balsley, B. B., W. L. Ecklund, R. A. Greenwald, Striations, pulsa-

- tions, and substorm activity on VHF radar-auroral records, *Trans. of the AGU*, *53*, 493, 1972.
- [*Barton, C. E.*] Barton, C. E., International Geomagnetic Reference Field: The Seventh Generation, *J. Geomag. Geoelectr.*, *49*, 123, 1997.
- [*Basu et al.*] Basu, S., R. L. Vesprini, J. Aarons, Density gradients and the Farley-Buneman instability, *Radio Sci.*, *8*, 235, 1973.
- [*Basu et al.*] Basu, S., R. L. Vesprini, J. Aarons, Study of field-aligned ionospheric E-region irregularities and sporadic E at HF, *Indian J. of Radio and Space Phys.*, *3*, 70, 1974.
- [*Bearing*] Bearing, E. A., Apparent electrostatic ion cyclotron waves in the diffuse aurora, *Geophys Rees. Lett.*, *10*, 647, 1983.
- [*Bearing*] Bearing, E. A., The plasma wave environment of an auroral arc: electrostatic ion cyclotron waves in the diffuse aurora, *J. Geophys. Res.*, *89*, 1635, 1984.
- [*Beley et al.*] Beley, V. S., V. G. Galushko, Y. M. Yampolski, Traveling ionospheric disturbance diagnostics using HF signal trajectory parameter variations, *Radio Sci.*, *30*, 1739, 1995.
- [*Bilitza et al.*] Bilitza, D., K. Rawer, L. Bossy, T. Gulyaeva, International Reference Ionosphere - Past, Present, Future, *Adv. Space Res.*, *13*, 3, 1993.
- [*Bone*] Bone, N., The Aurora: Sun-Earth Interactions, *Ellis Horwood Limited Library of Space Science and Space Technology, series in Astronomy*, 1991.

- [Booker] Booker, H. G., A theory of scattering by nonisotropic irregularities with application to radar reflections from the aurorae, *J. Atm. Terr. Phys.*, *8*, 204, 1956.
- [Booker, et. al.] Booker, H. G., C. W. Gartlein, B. Nichols, Interpretation of radio reflections from the aurora, *J. Geophys. Res.*, *60*, 1, 1955.
- [Bowles] Bowles, K. L., Doppler shifted radio echoes from the aurora, *J. Geophys. Res.*, *59*, 553, 1954.
- [Bowles] Bowles, K. L., Observations of vertical incidence scatter from the ionosphere at 41 Mc/sec, *Phys. Rev. Lett.*, *1*, 454, 1958.
- [Bowles] Bowles, K. L., Radio Echoes from field aligned ionization above the magnetic equator and their resemblance to auroral echoes., *J. Geophys. Res.*, *65*, 1853, 1960.
- [Bowles et al.] Bowles, K. L., B. B. Balsley, R. Cohen, Field aligned E region irregularities identified with ion acoustic waves, *J. Geophys. Res.*, *68*, 2485, 1963.
- [Brekke] Brekke, A., Physics of the Upper Polar Atmosphere, *John Wiley and Sons, Inc., New York*, 1997.
- [Breit and Tuve] Breit, G., M. A. Tuve, A test of the existence of the conducting layer, *Phys. Rev.*, *28*, 554, 1926.
- [Brittnacher et al.] Brittnacher, M., J. Spann, G. Parks, G. Germany, Auroral observations by the Polar Ultraviolet Imager UVI, *Adv. Space. Res.*, *20*, 1037, 1997.

- [*Bullough and Kaiser*] Bullough, K., T. R. Kaiser, Radio reflections from the aurorae, *J. Atm. Terr. Phys.*, 5, 189, 1954.
- [*Bullough et al.*] Bullough, K., T. Davidson, T. R. Kaiser, C. D. Watkins, Radio reflections from the aurorae, 3: The association with geomagnetic phenomena, *J. Atm. Terr. Phys.*, 11, 237, 1957.
- [*Buneman*] Buneman, O., Excitation of field-aligned sound waves by electron streams, *Phys. Rev. Lett.*, 10, 285-287, 1963.
- [*Chaturvedi and Kaw*] Chaturvedi, P. K., P. K. Kaw, Current driven ion cyclotron waves in collisional plasma, *Plasma Phys.*, 17, 447, 1975.
- [*Chaturvedi*] Chaturvedi, P. K., Collisional ion cyclotron waves in the auroral ionosphere.
- [*Chaturvedi and Ossakow*] Chaturvedi, P. K., S. L. Ossakow, Nonlinear stabilization of the current convective instability in the diffuse aurora, *Geophys. Res. Lett.*, 9, 957, 1979.
- [*Chaturvedi and Ossakow*] Chaturvedi, P. K., S. L. Ossakow, The current convective instability as applied to the auroral ionosphere, *J. Geophys. Res.*, 86, 4811, 1981.
- [*Chaturvedi et al.*] Chaturvedi, P. K., J. D. Huba, S. L. Ossakow, P. Satyanarayana, J. A. Fedder, Parallel current effects on two-stream electrojet plasma instabilities, *J. Geophys. Res.*, 92, 8700, 1987.
- [*Cummer et al.*] Cummer, S. A., T. F. Bell, U. S. Inan, L. J. Zanetti, VLF remote sensing of the auroral electrojet, *J. Geophys. Res.*, 101, 5381, 1996.

- [D'Angelo] D'Angelo, N., Type II spectra of the radio aurora, *J. Geophys. Res.*, *78*, 3987, 1973.
- [D'Angelo et al.] D'Angelo, N., H. L. Pecseli, P. I. Petersen, The Farley instability: A laboratory test, *J. Geophys. Res.*, *79*, 4747, 1974.
- [D'Angelo et al.] D'Angelo, N., H. L. Pecseli, P. I. Petersen, The k spectrum of ionospheric irregularities, *J. Geophys. Res.*, *80*, 1854, 1975.
- [D'Angelo] D'Angelo, N., On plasma instabilities in the high-latitude ionospheric E region, *Relation Between Laboratory and Space Plasmas. Proc. of the Inter. Workshop Reidel, Dordrecht, Netherlands*, 1981
- [del Pozo et al.] del Pozo, C. F., J. C. Foster, J. P. St-Maurice, Dual-mode E region plasma wave observations from Millstone Hill, *J. Geophys. Res.*, *98*, 6013, 1993.
- [del Pozo] del Pozo, C. F., Polarization electric field and Farley-Buneman instability during a precipitation event, *J. Atm. Terr. Phys.*, *56*, 509, 1994.
- [del Pozo et al.] del Pozo, C. F., J. K. Hargreaves, A. D. Aylward, Ion composition and effective ion recombination rate in the nighttime auroral lower ionosphere, *J. Atm. Terr. Phys.*, *59*, 1919, 1997.
- [Dickinson et al.] Dickinson, P. H. G., R. Grabowski, C. Hanuise, D. J. Mackinnon, E. Nielsen, E. V. Thrane, J.P. Villain, H. Wolf, O. Andreassen, Simultaneous observations of E-region irregularities by ground-based and rocket-borne techniques, *J. Atm. Terr. Phys.*, *47*, 265, 1985.
- [Dimant and Sudan] Dimant, Y. S., R. N. Sudan, Kinetic theory of the Farley-Buneman instability in the E region of the ionosphere, *J. Geophys. Res.*, *100*, 14605, 1995.



- [*Donovan and Moorcroft*] Donovan, E. F., D. R. Moorcroft, The effect of multiple scattering on the aspect sensitivity and polarization of radio auroral echoes, *Radio Sci.*, 27, 169, 1992.
- [*Dougherty*] Dougherty, J. P., The conductivity of a partially ionized gas in alternating electric fields, *J. Fluid Mech.*, 16, 126, 1963.
- [*Dum and Dupree*] Dum, C. T., T. H. Dupree, Nonlinear stabilization of high-frequency instabilities in a magnetic field, *Phys. Fluids*, 13, 20064, 1970.
- [*Eckersley*] Eckersley, T. L., Irregular ionic clouds in the E layer of the ionosphere, *Nature*, 140, 846, 1937.
- [*Ecklund et al.*] Ecklund, W. L., D. A. Carter, J. G. Keys, R. S. Unwin, Conjugate auroral radar observations of a substorm, *J. Geophys. Res.*, 79, 3211, 1974.
- [*Eglitis et al.*] Eglitis, P., T. R. Robinson, I. W. McCrea, K. Schlegel, T. Nygren, A. S. Rodger, Doppler spectrum statistics obtained from three different-frequency radar auroral experiments, *Ann. Geophys.*, 13, 56, 1995.
- [*Eglitis et al.*] Eglitis, P., I. W. McCrea, T. R. Robinson, T. B. Jones, K. Schlegel, T. Nygren, Flow dependence of COSCAT spectral characteristics, *J. Atm. Terr. Phys.*, 58, 189, 1996.
- [*Eglitis et al.*] Eglitis, P., I. W. McCrea, T. R. Robinson, T. Nygren, K. Schlegel, T. Turunen, New techniques for auroral irregularity studies with COSCAT, *Ann. Geophys.*, 16, 1241, 1998.
- [*Farley*] Farley, D. T., A theory of electrostatic fields in a horizontally stratified ionosphere subject to a vertical magnetic field, *J. Geophys. Res.*, 64, 1225, 1959.

- [Farley] Farley, D. T., A theory of electrostatic fields in the ionosphere at nonpolar geomagnetic latitudes, *J. Geophys. Res.*, *65*, 869, 1960.
- [Farley] Farley, D. T., A plasma instability resulting in field-aligned irregularities in the ionosphere, *J. Geophys. Res.*, *68*, 6083, 1963.
- [Farley] Farley, D. T., Two-stream plasma instability as a source of irregularities in the ionosphere, *Phys. Rev. Letters*, *10*, 279, 1963.
- [Farley and Fejer] Farley, D. T., B. G. Fejer, The effect of the gradient drift term on the type 1 electrojet irregularities, *J. Geophys. Res.*, *80*, 3087, 1975.
- [Farley] Farley, D. T., Theory of equatorial electrojet plasma waves: new developments and current status, *J. Atm. Terr. Phys.*, *47*, 729, 1985.
- [Farley and Providakes] Farley, D. T., J. F. Providakes, The variation with  $T_e$  and  $T_i$  of the velocity of unstable ionospheric two-stream waves, *J. Geophys. Res.*, *94*, 15415, 1989.
- [Farley et al.] Farley, D. T., J. D. Sahr, J. F. Providakes, Ion cyclotron harmonics in auroral radar echoes: Real effect or statistical artifact?, *Geophys. Res. Lett.*, *18*, 709, 1991.
- [Farley] Farley, D. T., The origin of type-4 auroral radar echoes, *Ann. Geophys.*, 1994.
- [FCC 47CFR73.322] Federal Communications Commission, FM Stereophonic Sound Transmission Standards, *47CFR73.322*, USGPO, 1998.
- [Fejer and Kelly] Fejer, B. G., M. C. Kelley, Ionospheric irregularities, *Rev. Geophys.*, *18*, 401, 1980.

- [*Fejer and Providakes*] Fejer, B. G., J. F. Providakes, High latitude E region irregularities: New results, *Phys. Scr.*, *T18*, 169, 1987.
- [*Fejer et al.*] Fejer, B. G., J. F. Providakes, and D. T. Farley, Theory of plasma waves in the auroral E region, *J. Geophys. Res.*, *89*, 7487, 1984.
- [*Fejer et al.*] Fejer, B. G., R. W. Reed, D. T. Farley, W. E. Swartz, and M. C. Kelly, Ion cyclotron waves as a possible source of resonant auroral radar echoes., *J. Geophys. Res.*, *89*, 187, 1984.
- [*Fejer et al.*] Fejer, B. G., J. F. Providakes, D. T. Farley, W. E. Swartz, Auroral E region plasma waves and elevated electron temperatures, *J. Geophys. Res.*, *91*, 13583, 1986.
- [*Fejer and Providakes*] Fejer, B. G., and J. F. Providakes, High latitude E-region irregularities: New results, *Phys. Scr.*, *T18*, 167, 1987.
- [*Fel'dshteyn*] Fel'dshteyn, A. Ya., Effect of the upper ionosphere on the Farley-Buneman instability, *Geomag. Aeron.*, *20*, 180, 1980.
- [*Flood*] Flood, W. A., Simultaneous VHF auroral backscatter measurements, *J. Geophys. Res.*, *65*, 2261, 1960.
- [*Forsyth et. al.*] Forsyth, P. A., W. Petrie, F. Vawter, B. W. Currie, Radar reflexions from auroras, *Nature*, *165*, 561, 1950.
- [*Forsyth and Fulford*] Forsyth, P. A., J. A. Fulford, A rocket-borne radar study of aurora, *Canadian J. Phys.*, *57*, 1503, 1979.
- [*Foster and Tetenbaum*] Foster, J. C., D. Tetenbaum, High-resolution backscatter observations of 440-MHz E region coherent echoes at Millstone Hill, *J. Geophys. Res.*, *96*, 1251, 1991.

- [*Foster and Tetenbaum*] Foster, J. C., D. Tetenbaum, Phase velocity studies of 34-cm E-region irregularities observed at Millstone Hill, *J. Atm. Terr. Phys.*, *54*, 759, 1992.
- [*Foster et al.*] Foster, J. C., D. Tetenbaum, C. F. del Pozo, J. P. St-Maurice, D. R. Moorcroft, Aspect angle variations in intensity, phase velocity, and altitude for high-latitude 34-cm E region irregularities, *J. Geophys. Res.*, *97*, 8601, 1992.
- [*Fremouw et al.*] Fremouw, E. J., J. A. Secan, B. M. Howe, Application of stochastic inverse theory to ionospheric tomography, *Radio Sci.*, *27*, 721, 1992.
- [*Gartlein et al.*] Gartlein, C. W., G. Sprague, R. C. Wang, 41 Mc/s IGY Auroral Radar at Ithaca, New York, *J. Geophys. Res.*, *65*, 2255, 1960.
- [*Germany et al.*] Germany, G. A., D. G. Torr, P. G. Richards, M. R. Torr, S. John, Determination of ionospheric conductivities from FUV auroral emissions, *J. Geophys. Res.*, *99*, 23297, 1994.
- [*Gordon*] Gordon, W. E., Incoherent scattering of radio waves by free electrons with application to space exploration by radar, *Proc. TRE*, *46*, 1824, 1958.
- [*Greenwald et al.*] Greenwald, R. A., W. E. Ecklund, B. B. Balsley, Auroral currents, irregularities and luminosity, *J. Geophys. Res.*, *78*, 8193, 1973.
- [*Greenwald*] Greenwald, R. A., Diffuse radar aurora and the gradient drift instability, *J. Geophys. Res.*, *79*, 4807, 1974.
- [*Greenwald et al.*] Greenwald, R. A., W. L. Ecklund, B. B. Balsley, Diffuse radar aurora: Observations of non-two-stream irregularities, *J. Geophys. Res.*, *80*, 131, 1975.

- [Greenwald et al.] Greenwald, R. A., W. L. Ecklund, B. B. Balsley, Diffuse radar aurora: Spectral observations of non-two-stream irregularities, *J. Geophys. Res.*, *80*, 4807, 1975.
- [Greenwald et al.] Greenwald, R. A., W. L. Ecklund, B. B. Balsley, Radar observations of auroral electrojet currents, *J. Geophys. Res.*, *80*, 3642, 1975.
- [Greenwald et al.] Greenwald, R. A., W. Weiss, E. Nielsen, STARE: a new radar auroral backscatter experiment in northern Scandinavia, *Radio Sci.*, *13*, 1021, 1978.
- [Griffiths et al.] Griffiths, H. D., A. J. Garnett, C. J. Baker, S. Keaveney, Bistatic radar using satellite-borne illuminators of opportunity, in *International conference Radar 92*, pp. 276-279, *IEE, London*, 1992.
- [Gurevich and Zybin] Gurevich, A. V., K. P. Zybin, Saturation of the Farley-Buneman instability due to the interaction with atmospheric turbulence, *Phys. Lett. A.*, *205*, 55, 1995.
- [Gurevich et al.] Gurevic, A. V., N. D. Borisov, A. N. Karashtin, K. P. Zybin, Plasma density perturbations in the ionospheric E region, *Phys. Lett. A.*, *208(3)*, 214, 1995.
- [Hagen] Hagen, J. B., *Radio Frequency Electronics: Circuits and Applications*, Cambridge University Press, 1996.
- [Hagfors et al.] Hagfors, T., R. G. Johnson, R. A. Power, Simultaneous observation of proton precipitation and auroral radar echoes, *J. Geophys. Res.*, *76*, 6093, 1971.

- [*Hagfors*] Hagfors, T., Some properties of radar auroral echoes as observed at a frequency of 1295 MHz, *AGARD Conf. Proc.*, 97, 9, 1972.
- [*Hagfors and Kofman*] Hagfors, T., W. Kofman, Mapping of overspread targets in radar astronomy, *Radio Sci.*, 26, 403, 1991.
- [*Haldoupis and Sofko*] Haldoupis, C. I., G. J. Sofko, VHF double-peaked spectra at negative Doppler shifts in the morning sector of radio aurora, *Planet Space Sci.*, 27, 233, 1979.
- [*Haldoupis et al.*] Haldoupis, C. I., E. Nielsen, H. M. Ierkic, STARE Doppler spectral studies of westward electrojet radar aurora, *Planet. Space Sci.*, 32, 1291, 1984.
- [*Haldoupis et al.*] Haldoupis, C. I., P. Prikryl, G. J. Sofko, J. A. Koehler, Evidence for 50 MHz bistatic radio observations of electrostatic ion cyclotron waves in the auroral plasma, *J. Geophys. Res.*, 90, 10983, 1985.
- [*Haldoupis et al.*] Haldoupis, C. I., G. J. Sofko, J. A. Koehler, On ion acoustic plasma waves at large magnetic aspect angles in the high-latitude E region of the ionosphere, *J. Geophys. Res.*, 91, 5755, 1986.
- [*Haldoupis and Nielsen*] Haldoupis, C. I., E. Nielsen, Doppler spectrum observations of long discrete echoes, *Planet. Space Sci.*, 35, 135, 1986.
- [*Haldoupis et al.*] Haldoupis, C. I., G. J. Sofko, J. A. Koehler, P. Prikryl, A. G. McNamara, High resolution doppler spectrum measurements of 3m auroral irregularities at large magnetic aspect angles, *Phys. Scripta*, 35, 910, 1987.
- [*Haldoupis*] Haldoupis, C. I., A review on radio studies of auroral E region ionospheric irregularities, *Ann. Geophys.*, 7, 239, 1989.

- [*Haldoupis and Nielsen*] Haldoupis, C. I., and E. Nielsen, 140 MHz auroral backscatter: Evidence for characteristic phase velocities below and above the ion acoustic speed, *Geophys. Res. Lett.*, *16*, 723, 1989.
- [*Haldoupis and Nielsen*] Haldoupis, C. I., and E. Nielsen, Very large phase velocities of non two-stream, meter scale irregularities in the high latitude E region ionosphere, *J. Geophys. Res.*, *94*, 13489, 1989.
- [*Haldoupis et al.*] Haldoupis, C. I., E. Nielsen, K. Schlegel, Dependence of radar auroral scattering cross section on the ambient electron density and the destabilizing electric field, *Ann. Geophys.*, *8*, 195, 1990.
- [*Haldoupis and Schlegel*] Haldoupis, C. I., K. Schlegel, Direct comparison of 1-m irregularity phase velocities and ion acoustic speeds in the auroral E region ionosphere, *J. Geophys. Res.*, *95*, 18989, 1990.
- [*Haldoupis et al.*] Haldoupis, C. I., G. J. Sofko, J. A. Koehler, D. W. Danskin, A new look at type 4 echoes of radar aurora, *J. Geophys. Res.*, *96*, 11353, 1991.
- [*Haldoupis et al.*] Haldoupis, C. I., K. Schlegel, and E. Nielsen, On type 3 auroral VHF coherent radar backscatter, *J. Geophys. Res.*, *97*, 4109, 1992.
- [*Haldoupis et al.*] Haldoupis, C. I., K. Schlegel, E. Nielsen, Some observations of radio auroral backscatter at 140 MHz during E-region electron gas heating, *Ann. Geophys.*, *11*, 283, 1993.
- [*Haldoupis et al.*] Haldoupis, C. I., J. A. Koehler, G. J. Sofko, D. W. Danskin, M. J. McKibben, D. Andre, Preferential phase velocities for type-4 irregularities in the auroral E region plasma, *J. Geophys. Res.*, *98*, 6173, 1993.

- [*Haldoupis and Schlegel*] Haldoupis, C. I., K. Schlegel, A 50 Mhz radio Doppler experiment for midlatitude E region coherent backscatter studies: System description and first results, *Radio Sci.*, *28*, 959, 1993.
- [*Haldoupis*] Haldoupis, C. I., Possible evidence for partial demagnetization of electrons in the auroral E-region plasma during electron gas heating, *Ann. Geophys.*, *12*, 40, 1994.
- [*Haldoupis et al.*] Haldoupis, C. I., G. J. Sofko, G. C. Hussey, and J. Mu, An overview of type-3 radar auroral research: basic observational properties and new interpretation propositions, *Ann. Geophysicae*, *13*, 10-24, 1995.
- [*Haldoupis et al.*] Haldoupis, C. I., J. A. Koehler, G. J. Sofko, D. W. Danskin, D. Andre, J. Mu, Localized and strongly unstable plasma regions in the auroral E Region ionosphere and implications for radar experiments, *J. Geophys. Res.*, *100*, 7771, 1995.
- [*Hall and Moorcroft*] Hall, G. E., D. R. Moorcroft, Doppler spectra of the UHF diffuse radio aurora, *J. Geophys. Res.*, *93*, 7425, 1988.
- [*Hall et al.*] Hall, G. E., D. R. Moorcroft, L. L. Cogger, D. Andre, Spatial relationship between large aspect angle VHF radio aurora and 557.7-nm emissions: Evidence from refraction, *J. Geophys. Res.*, *95*, 15281, 1990.
- [*Hall and Moorcroft*] Hall, G. E., D. R. Moorcroft, Magnetic aspect angle effects in radar aurora at 48.5 MHz, corrected for refraction, *J. Geophys. Res.*, *97*, 19471, 1992.
- [*Hall*] Hall, P. W., Correlative range-Doppler detectors and estimators in bistatic radar using commercial FM broadcasts, MS thesis, Univ. of Wash., Seattle, 1995.



- [*Hamza and St.-Maurice*] Hamza, A. M., and J.-P. St.-Maurice, A self consistent fully turbulent theory of auroral E region irregularities, *J. Geophys. Res.*, *98*, 11601, 1993a.
- [*Hamza and St.-Maurice*] Hamza, A. M., and J.-P. St.-Maurice, A turbulent theoretical framework for the study of current-driven E region irregularities at high latitudes: basic derivation and application to gradient-free situations, *J. Geophys. Res.*, *98*, 11587, 1993b.
- [*Hamza and St.-Maurice*] Hamza, A. M., and J.-P. St.-Maurice, A fully self-consistent fluid theory of anomalous transport in Farley-Buneman turbulence, *J. Geophys. Res.*, *100*, 9563, 1995.
- [*Hansen*] Hansen, J. M., A new radar technique for remote sensing of atmospheric irregularities by passive observation of the scattering of commercial FM broadcasts, MS thesis, Univ. of Wash., Seattle, 1994.
- [*Hanuse et al.*] Hanuse, C., J. P. Villain, J. C. Cerisier, C. Senior, J. M. Rouhoniemi, R. A. Greenwald, K. B. Baker, Statistical study of high latitude E region Doppler spectra obtained with SHERPA HF radar, *Ann. Geophys.*, *9*, 273, 1991.
- [*Hanuse*] Hanuse, C., High-latitude ionospheric irregularities: A review of recent radar results, *Radio Sci.*, *18*, 1093, 1983.
- [*Hanuse et al.*] Hanuse, C., J. P. Villain, D. Gresillon, C. Cabrit, R. A. Greenwald, K. B. Baker, Interpretation of HF radar ionospheric Doppler spectra by collective wave scattering theory, *Ann. Geophys.*, *11*, 29, 1993.
- [*Harang and Stoffregen*] Harang, L., W. Stoffregen, Scattered reflections of radio waves from a height of more than 1000 km, *Nature*, *142*, 832, 1938.

- [*Harang and Landmark*] Harang, L., B. Landmark, Radio echoes observed during aurorae and terrestrial magnetic storms using 35 and 74 mc./s waves simultaneously, *Nature*, 171, 1017, 1953.
- [*Harang and Landmark*] Harang, L., B. Landmark, Radio echoes observed during aurorae and terrestrial magnetic storms using 35 and 74 mc./s waves simultaneously, *J. Atm. Terr. Phys.*, 4, 322, 1954.
- [*Harang and Troim*] Harang, L., J. Troim, Investigation of auroral echoes, 2, *Planet. Space Sci.*, 5, 105, 1961.
- [*Hedin, A. E.*] Hedin, A. E., Extension of the MSIS Thermospheric Model into the Middle and Lower Atmosphere, *J. Geophys. Res.*, 96, 1159, 1991.
- [*Hellgren and Meos*] Hellgren, G., J. Meos, *Tellus*, 249, 1952.
- [*Howland*] Howland, P. E., A passive metric radar using a transmitter of opportunity. in *International Conference on radar*, pp. 251-256, Paris, France. *Soc Electr. & Electron*, 1994.
- [*Huba et al.*] Huba, J. D., S. L. Ossakow, P. Satyanarayana, P. N. Guzdar, Linear theory of the ExB instability with an inhomogenous electric field, *J. Geophys. Res.*, 88, 425, 1983.
- [*Hultqvist and Egeland*] Hultqvist, B., A. Egeland, Radio aurora, *Space Sci. Rev.*, 3, 27, 1964.
- [*Huuskonen et al.*] Huuskonen, A., T. Nygren, L. Jalonen, N. Bjorna, T. L. Hansen, A. Brelle, T. Turunen, Ion composition in sporadic E layers measured by the EISCAT UHF radar, *J. Geophys. Res.*, 93, 14603, 1988.

- [*Ierkic et al.*] Ierkic, H. M., C. Haldoupis, D. R. Moorcroft, E. Nielsen, Coherent radar interferometry of vertical irregularity structures in the auroral E region, *Radio Sci.*, *27*, 743, 1992.
- [*Inan et al.*] Inan, U. S., A. Slingeland, V. P. Pasko, J. V. Rodriguez, VLF and LF signatures of mesospheric/lower ionospheric response to lightning discharges, *J. Geophys. Res.*, *101*, 5219, 1996.
- [*Janhunen*] Janhunen, P., Three-dimensional stabilization mechanism for the auroral Farley-Buneman instability, *J. Atm. Terr. Phys.*, *54*, 1633, 1992.
- [*Janhunen*] Janhunen, P., Perpendicular particle simulation of the E region Farley-Buneman instability, *J. Geophys Res.*, *99*, 11461, 1994.
- [*Janhunen*] Janhunen, P., Implications of flow angle stabilization on coherent E region spectra, *J. Geophys. Res.*, *99*, 13203, 1994.
- [*Janhunen*] Janhunen, P., On recent developments in E-region irregularity simulations and a summary of related theory, *Ann. Geophys.*, *13*, 791, 1995.
- [*Jaye et al.*] Jaye, W. E., W. G. Chestnut, G. Craig, Analysis of auroral data from the Prince Albert Radar Laboratory, report, *Stanford Res. Inst., Stanford, Calif.*, 1969.
- [*John and Saxena*] John, P. I., Y. C. Saxena, Observation of the Farley-Buneman instability in laboratory plasma, *Geophys. Res. Lett.*, *2*, 251, 1975.
- [*Jones et al.*] Jones, T. B., C. Spracklen, C. P. Stewart, E. C. Thomas, SABRE-a UK-German auroral radar, *Second International Conference on Antennas and Propagation. IEE, London, UK*, 1981.

- [*Jones et al.*] Jones, B., P. J. S. Williams, K. Schlegel, T. Robinson, I. Haggstrom, Interpretation of enhanced electron temperatures measured in the auroral E-region during the ERRRIS campaign, *Ann. Geophys.*, 9, 55, 1991.
- [*Kelly et al.*] Kelly, P. E., D. R. Hansen, P. E. Forsyth, The azimuthal distribution of ultra-high frequency radar echoes from the aurora, *Can. J. Phys.*, 39, 1535, 1961.
- [*Kelley*] Kelly, M. C., The Earth's Ionosphere : Plasma Physics and Electrodynamics, Academic Press Inc., 1989.
- [*Karashtin and Tsimring*] Karashtin, A. N., M. Sh. Tsimring, Low-frequency current instabilities in nonisothermal magnetoactive plasma, *Radiophys. and Quant. Elec.*, 36, 15, 1993.
- [*Keskinen*] Keskinen, M. J., Nonlinear stabilization of the Farley-Buneman instability by strong ExB turbulence in a plasma, *Phys. Rev. Lett.*, 47, 344, 1981.
- [*Keskinen and Ossakow*] Keskinen, M. J., S. L. Ossakow, High latitude ionospheric irregularities: A review, *Radio Sci.*, 18, 1077, 1983.
- [*Keys*] Keys, J. G., The association between X-rays and auroral radar echoes in the southern auroral zone, *J. Atmos. Terr. Phys.*, 32, 1975, 1970.
- [*Keys and Johnstont*] Keys, J. G., P. V. Johnstont, Radio aurora dynamics as seen by Doppler radar, *Geophys. Res. Lett.*, 6, 97, 1979.
- [*Keys and Andrews*] Keys, J. G., M. K. Andrews, Gravity wave and sporadic-E echo signatures on VHF backscatter radar systems, *Planetary and Space Sci.*, 32, 1455, 1984.

- [*Kissack et al.*] Kissack, R. S., J. P. St.-Maruice, D. R. Moorcroft, Electron thermal effects on the Farley-Buneman fluid dispersion relation, *Phys. Plasmas*, *2*, 1032, 1995.
- [*Kissack et al.*] Kissack, R. S., J. P. St.-Maruice, D. R. Moorcroft, The effect of electron-neutral energy exchange on the fluid Farley-Buneman instability threshold, *J. Geophys. Res.*, *102*, 24091, 1997.
- [*Koehler et al.*] Koehler, J. A., G. J. Sofko, V. Mehta, A. G. McNamara, D. R. McDiarmid, Observations of magnetic aspect effects in auroral radar backscatter, *Can. J. Phys.*, *63*, 402, 1985.
- [*Koehler et al.*] Koehler, J. A., G. J. Sofko, V. Mehta, A statistical study of magnetic aspect effects associated with VHF auroral backscatter, *Radio Sci.*, *20*, 689, 1985.
- [*Koehler et al.*] Koehler, J. A., G. J. Sofko, J. Watermann, A. G. McNamara, D. McDiarmid, D. Andre, P. Prikryl, M. McKibben, K. H. Helgeson, Frequency dependence of Doppler shift for type III coherent radar echoes, *Radio Sci.*, *25*, 791, 1990.
- [*Koehler et al.*] Koehler, J. A., G. J. Sofko, J. Mu, Type-III echoes of radar aurora: observational aspects, *Ann. Geophys.*, *13*, 2, 1995.
- [*Koehler et al.*] Koehler, J. A., G. J. Sofko, D. Andre, M. Maguire, R. Osterried, M. McKibben, J. Mu, D. Danskin, A. Ortlepp, The SAPPHERE auroral radar system, *Can. J. Phys.*, *73*, 3-4, 211, 1995.
- [*Kunitake et al.*] Kunitake, M., T. Tanaka, K. Igarashi, S. Yamamoto, H. Maeno, T. Ogawa, New-type echoes observed with the 50 MHz auroral Doppler radar

at Syowa Station (extended abstract), *Proc. Natl. Inst. Polar Res. Symp. Upper Atmos. Phys.*, 6, 42, 1993.

[*Kustom et al.*] Kustom, B., N. D'Angelo, R. L. Merlino, A laboratory investigation of the high-frequency Farley-Buneman instability, *J. Geophys. Res.*, 90, 1698, 1985.

[*Kustov et al.*] Kustov, A. V., M. V. Uspenskiy, F. J. S. Williams, The effects of the saturation of the turbulence of the auroral electrojet, *Geomag. Aeron.*, 28, 800, 1988.

[*Kustov et al.*] Kustov, A. V., M. Uspensky, J. Kangas, A. Huuskonen, E. Nielsen, On the threshold electric field for the approximately 1-m auroral irregularity appearance, *J. Geophys. Res.*, 94, 1989.

[*Kustov et al.*] Kustov, A. V., M. V. Uspensky, G. O. L. Jones, P. J. S. Williams, G. J. Sofko, J. A. Koehler, Electric field and electron density thresholds for coherent auroral echo onset, *J. Geophys. Res.*, 98, 7729, 1993.

[*Kustov et al.*] Kustov, A. V., M. Uspensky, G. J. Sofko, J. A. Koehler, J. Mu, Aspect angle dependence of the radar aurora doppler velocity, *J. Geophys. Res.*, 99, 2131, 1994.

[*Kustov et al.*] Kustov, A. V., G. J. Sofko, J. A. Koehler, M. V. Uspensky, Flow angle dependence for the asymmetry of broad 50-MHz coherent echoes at large magnetic aspect angles, *Ann. Geophys.*, 15, 760, 1997.

[*Leadabrand et al.*] Leadabrand, R. L., L. Dolphin, A. M. Peterson, Preliminary results of 400 Mc/s radar investigations of auroral echoes at College, Alaska, *IRE Trans.*, AP-7, 127, 1959.

- [*Leadabrand et al.*] Leadabrand, R. L., J. C. Schlobohm, M. J. Baron, Simultaneous very high frequency and ultra high frequency observations of the aurora at Fraserburgh, Scotland, *J. Geophys. Res.*, *70*, 4235, 1965.
- [*Lee et al.*] Lee, K., C. F. Kennel, J. M. Kindel, High frequency Hall current instability, *Radio Sci.*, *6*, 209, 1971.
- [*Lee and Kennel*] Lee, K., C. F. Kennel, Effects of propagation parallel to the magnetic field on the Type 1 electrojet irregularity instability, *Planet. Space Sci.*, *21*, 1339, 1973.
- [*Lehtinen and Haggstrom*] Lehtinen, M., I. Haggstrom, A new modulation principle for incoherent scatter, *Radio Sci.*, *22*, 625, 1987.
- [*Leitinger et al.*] Leitinger, R., H. P. Ladreiter, G. Kirchengast, Ionosphere tomography with data from satellite reception of Global Navigation Satellite System signals and ground reception of Navy Navigation satellite System signals, *Radio Sci.*, *32*, 1657, 1997.
- [*Levanon*] Levanon, N., Radar Principles, *John Wiley, New York*, 1988.
- [*Leonard*] Leonard, R. S., A Low Power VHF Radar for Auroral Research, *Proc. IRE*, *47*, 320, 1959.
- [*Lind et al.*] Lind, F. D., J. D. Sahr, D. M. Gidner, First passive radar observations of auroral E-region irregularities, *Geophys. Res. Lett.*, *26*, 14, 2155, 1999.
- [*Liperovsky et al.*] Liperovsky, V. A., A. V. Kustov, C. V. Meister, Some ideas concerning the problem of anomalous polar E region heating due to Farley-Buneman turbulence, *Astronomische-Nachrichten*, *317*, 353, 1996.

- [Liperovsky et al.] Liperovsky, V. ., C. V. Meister, S. A. Senchenkov, K. V. Popov, M. A. Oleynik, E. V. Liperovskaya, Quasi-three-dimensional model of current generation in the ionosphere caused by neutral wind action on E/sub s/-clouds, *Radiophys. and Quant. Elec.*, *39*, 166, 1996.
- [Lovell et al.] Lovell, A. C. B., J. A. Clegg, C. D. Ellyett, Radio echoes from the Aurora Borealis, *Nature*, *160*, 372, 1947.
- [Machida and Goertz] Machida, S., C. K. Goertz, Computer simulation of the Farley-Buneman instability and anomalous electron heating in the auroral ionosphere, *J. Geophys. Res.*, *93*, 9993, 1988.
- [Margot and McNamara] Margot, J., A. G. McNamara, High-frequency coherent plasma waves observed in the lower auroral ionosphere, *Canadian J. Phys.*, *69*, 941, 1991.
- [Mattin and Jones] Mattin, N., T. B. Jones, Propagation angle dependence of radar auroral E-region irregularities, *J. Atm. Terr. Phys.*, *49*, 115, 1987.
- [McDiarmid and McNamara] McDiarmid, D. R., A. G. McNamara, A physical model of a radio aurora event, *Can. J. Phys.*, *47*, 1271, 1969.
- [McDiarmid] McDiarmid, D. R., On the aspect sensitivity of radio aurora, *Can. J. Phys.*, *50*, 2557, 1972.
- [McDiarmid and McNamara] McDiarmid, D. R., A. G. McNamara, Periodically varying radio aurora, *Ann. Geophys.*, *7*, 239, 1972.
- [McDiarmid] McDiarmid, D. R., On errors in the measurement of the aspect sensitivity of radio aurora, *J. Geophys. Res.*, *81*, 4007, 1976.



- [*McNamara*] McNamara, A. G., Double-Doppler radar investigation of aurora, *J. Geophys. Res.*, 60, 257, 1955.
- [*McNamara*] McNamara, A. G., Rocket measurements of plasma densities and temperatures in the visual aurora, *Can. J. Phys.*, 47, 47, 1969.
- [*McNamara et al.*] McNamara, A. G., D. R. McDiarmid, G. J. Sofko, J. A. Koehler, P. A. Forsyth, D. R. Moorcroft, Bars-a dual bistatic auroral radar system for the study of electric fields in the canadian sector of the auroral zone, *Adv. Space. Res.*, 2, 145, 1982.
- [*Moorcroft and Tsunoda*] Moorcroft, D. R., R. T. Tsunoda, Rapid scan Doppler velocity maps of the UHF diffuse radar aurora, *J. Geophys. Res.*, 83, 1482, 1978.
- [*Moorcroft*] Moorcroft, D. R., Dependence of radio aurora at 398 MHz on electron density and electric field, *Can. J. Phys.*, 57, 688, 1979.
- [*Moorcroft*] Moorcroft, D. R., Comparison of radio auroral spectral characteristics at 398 MHz with incoherent scatter measurements of electric field, *Can. J. Phys.*, 58, 232, 1980.
- [*Moorcroft*] Moorcroft, D. R., An examination of radio-auroral aspect sensitivity, *Can. J. Phys.*, 63, 1005, 1985.
- [*Moorcroft*] Moorcroft, D. R., Estimates of absolute scattering coefficients of radar aurora, *J. Geophys. Res.*, 92, 8723, 1987.
- [*Moorcroft and Ruohoniemi*] Moorcroft, D. R., J. M. Ruohoniemi, Nearly simultaneous measurements of radar auroral heights and Doppler velocities at 398 MHz., *J. Geophys. Res.*, 92, 3333, 1987.

- [*Moorcroft and Schlegel*] Moorcroft, D. R., K. Schlegel, E region coherent backscatter at short wavelength and large aspect angle, *J. Geophys. Res.*, *93*, 2005, 1988.
- [*Moorcroft*] Moorcroft, D. R., Reflection and refraction by tilted layers: An explanation for VHF auroral backscatter at large aspect angles, *Geophys. Res. Lett.*, *16*, 235, 1989.
- [*Moorcroft and Schlegel*] Moorcroft, D. R., K. Schlegel, Height and aspect sensitivity of large aspect angle coherent backscatter at 933 MHz, *J. Geophys. Res.*, *95*, 19011, 1990.
- [*Nielsen et al.*] Nielsen, E., J. D. Whitehead, L. A. Headberg, T. B. Jones, A test of the cosine relationship using three-radar velocity measurements, *Radio Sci.*, *18*, 230, 1983.
- [*Nielsen et al.*] Nielsen, E., C. I. Haldoupis, B. G. Fejer, H. M. Ierkic, Dependence of auroral power spectra variations upon electron drift velocity in the eastward electrojet, *J. Geophys. Res.*, *89*, 253, 1984.
- [*Nielsen and Schlegel*] Nielsen, E., K. Schlegel, Coherent radar Doppler measurements and their relationship to the ionospheric electron drift velocity, *J. Geophys. Res.*, *90*, 3498, 1985.
- [*Nielsen*] Nielsen, E., Aspect angle dependence of mean Doppler velocities of 1-m auroral plasma waves, *J. Geophys. Res.*, *93*, 4119, 1988.
- [*Nielsen et al.*] Nielsen, E., M., Uspensky, A. Kustov, A. Kuuskonen, J. Kangas, On the dependence of the Farley-Buneman turbulence level on ion sphericoelectric field, *J. Atm. Terr. Phys.*, *50*, 601, 1988.

- [*Nygren et al.*] Nygren, T., A. Huuskonen, P. Pollari, Alternating-coded multipulse codes for incoherent scatter experiments, *J. Atm. Terr. Phys.*, 58, 465, 1996.
- [*Opgenoorth et al.*] Opgenoorth, H., J. Haggstrom, P. J. S. Williams, G. O. Jones, Regions of strongly enhanced perpendicular electric fields adjacent to auroral arcs, *J. Atmos. Terr. Phys.*, 52, 449, 1990.
- [*Oppenheim*] Oppenheim, M., Nonlinear Simulations and Theory of the Farley-Buneman Instability in the E-region Ionosphere, Ph.D. thesis, Cornell Univ., Ithaca, NY, 1995.
- [*Oppenheim et al.*] Oppenheim, M., N. Otani, C. Ronchi, Hybrid simulations of the saturated Farley-Buneman instability in the ionosphere, *Geophys. Res. Lett.*, 22, 353, 1995.
- [*Oppenheim et al.*] Oppenheim, M., N. Otani, C. Ronchi, Saturation of the Farley-Buneman instability via nonlinear electron ExB drifts, *J. Geophys. Res.*, 101, 17273, 1996.
- [*Oppenheim and Otani*] Oppenheim, M., N. Otani, Spectral characteristics of the Farley-Buneman instability: Simulations versus observations, *J. Geophys. Res.*, 101, 24573, 1996.
- [*Ossakow et al.*] Ossakow, S. L., K. Papadopoulos, J. Orens, T. Coffey, Parallel propagation effects on the type 1 electrojet instability, *J. Geophys. Res.*, 80, 141, 1975.
- [*Ossakow and Chaturvedi*] Ossakow, S. L., P. K. Chaturvedi, Current convective instability in the diffuse aurora, *Geophys. Res. Lett.*, 6, 332, 1979.

- [*Otani and Oppenheim*] Otani, N. F., M. Oppenheim, A saturation mechanism for the Farley-Buneman instability, *Geophys. Res. Lett.*, *25*, 1998.
- [*Ogawa et al.*] Ogawa, T., B. B. Balsley, W. L. Ecklund, D. A. Carter, P. E. Johnston, Aspect angle dependence of irregularity phase velocities in the auroral electrojet, *Geophys. Res. Lett.*, *7*, 1081, 1980.
- [*Ogawa et al.*] Ogawa, T., K. T. Igarashi, M. Ose, Y. Kuratani, R. Fujii, Hirasawa, Preliminary results of new 50 MHz Doppler radar experiment at Syowa Station, *Mem. Natl. Inst. Polar Res. Spec. Issue Jpn.*, *22*, 193, 1982.
- [*Ogawa*] Ogawa, T., Radar observations of ionospheric irregularities at Syowa Station, Antarctica: a brief overview, *Ann. Geophys.*, *14*, 1454, 1996.
- [*Pasko and Inan*] Pasko, V. P., U. S. Inan, Recovery signatures of lightning associated VLF perturbations as a measure of the lower ionosphere, *J. Geophys. Res.*, *99*, 17523, 1994.
- [*Pecseli et al.*] Pecseli, H. L., F. Primdahl, A. Bahnsen, Low frequency electrostatic turbulence in the polar cap E region, *J. Geophys. Res.*, *94*, 5337, 1989.
- [*Pfaff*] Pfaff, R. F., Rocket Studies of Plasma Turbulence in the Equatorial and Auroral Electrojets, Ph.D. thesis, Cornell Univ., Ithaca, N.Y., 1986.
- [*Pfaff, et al.*] Pfaff, R. F., J. Sahr, J. F. Providakes, W. E. Swartz, D. T. Farley, P. M. Kintner, I. Haggstrom, A. Hedberg, H. Opgenoorth, G. Holmgren, A. McNamara, D. Wallis, B. Whalen, A. Yau, S. Watanabe, F. Creutzberg, P. Williams, E. Nielsen, K. Schlegel, T. R. Robinson, The E region rocket/radar instability study (ERRRIS): scientific objectives and campaign overview, *J. Atmos. Terr. Phys.*, *54*, 779, 1992.

- [Pivovarov *et al.*] Pivovarov, V. G., Yu. L. Sverdlov, N. G. Sergeeva, V. N. Lytkin, A new approach to the determination of the E-region drift velocity using radar aurora Doppler spectral shape, *J. Atm. Terr. Phys.*, *58*, 489, 1996.
- [Popple *et al.*] Popple, M., P. J. Chapman, E. C. Thomas, T. B. Jones, RAPIER: a new relocatable VHF coherent radar, *J. Atm. Terr. Phys.*, *59*, 1035, 1997.
- [Prikryl *et al.*] Prikryl, P., J. A. Koehler, G. J. Sofko, D. J. McEwen, D. Steele, Ionospheric ion cyclotron wave generation inferred from coordinated Doppler radar, optical, and magnetic observations, *J. Geophys. Res.*, *92*, 3315, 1987.
- [Prikryl *et al.*] Prikryl, P., D. Andre, G. J. Sofko, J. A. Koehler, Doppler radar observations of harmonics of electrostatic ion cyclotron waves in the auroral ionosphere, *J. Geophys. Res.*, *93*, 7409, 1988.
- [Prikryl *et al.*] Prikryl, P., G. J. Sofko, J. A. Koehler, J. Mu, D. Andre, Steep electron density gradients associated with discrete aurorae explaining the diversity of auroral VHF Doppler spectra, *Ann. Geophys.*, *13*, 25, 1995.
- [Primdahl *et al.*] Primdahl, F., J. K. Olesen, F. Spangselv, Backscatter from a postulated plasma instability in the polar cap ionosphere and the direct measurement of a horizontal E region current, *J. Geophys. Res.*, *79*, 4262, 1974.
- [Primdahl *et al.*] Primdahl, F., J. K. Olesen, F. Spangselv, The Farley instability and the polar cap E-field, *J. Geophys. Res.*, *80*, 2698, 1975.
- [Primdahl and Bahnsen] Primdahl, F., A. Bahnsen, Auroral E region diagnosis by means of non linearly stabilized plasma waves, *Ann. Geophys.*, *3*, 57, 1985.
- [Providakes *et al.*] Providakes, J. F., W. E. Swartz, D. T. Farley, B. G. Fejer, First

VHF auroral radar interferometer observations, *Geophys. Res. Lett.*, *10*, 401, 1983.

[*Providakes*] Providakes, J. F., Radar interferometer observations and theory of plasma irregularities in the auroral ionosphere, Ph.D. thesis, Cornell Univ., Ithaca, NY, 1985.

[*Providakes et al.*] Providakes, J. F., D. T. Farley, W. E. Swartz, D. Riggan, Plasma irregularities associated with a morning discrete auroral arc: Radar interferometer observations and theory, *J. Geophys. Res.*, *90*, 7513, 1985.

[*Providakes et al.*] Providakes, J. F., D. T. Farley, B. G. Fejer, J. Sahr, W. E. Swartz, I. Häggström, Å. Hedberg, and J. A. Nordling, Observations of auroral E-region plasma waves and electron heating with EISCAT and a VHF radar interferometer, *J. Atm. Terr. Phys.*, *50*, 339, 1988.

[*Ratcliffe*] Ratcliffe, J.A., Sun Earth and Radio, *World University Library, London*, 1970.

[*Reinleitner, and Nielsen*] Reinleitner, L. A., E. Nielsen, Self-consistent analysis of electron drift velocity measurements with the STARE/SABRE system, *J. Geophys. Res.*, *90*, 8477, 1985.

[*Rietveld et al.*] Rietveld, M. T., P. N. Collis, J. P. St.-Maurice, Naturally enhanced ion acoustic waves in the auroral ionosphere observed with the EISCAT 933 MHz radar, *J. Geophys. Res.*, *96*, 19291, 1991.

[*Robinson*] Robinson, T. R., Toward a self-consistent non linear theory of radar auroral backscatter, *J. Atm. Terr. Phys.*, *48*, 417, 1986.

- [*Robinson and Honary*] Robinson, T. R., F. Honary, A resonance broadening kinetic theory of the modified two-stream instability: Implications for radar auroral backscatter experiments, *J. Geophys. Res.*, *95*, 1073, 1990.
- [*Robinson*] Robinson, T. R., The effects of the resonance broadening of Farley-Buneman waves on electron dynamics and heating in the auroral E-region, *J. Atm. Terr. Phys.*, *54*, 749, 1992.
- [*Robinson*] Robinson, T. R., Simulation of convection flow estimation errors in VHF bistatic auroral radar systems, *Ann. Geophys.*, *11*, 1033, 1993.
- [*Robinson and Honary*] Robinson, T. R., F. Honary, Adiabatic and isothermal ion-acoustic speeds of stabilized Farley-Buneman waves in the auroral E-region, *J. Atm. Terr. Phys.*, *55*, 65, 1993.
- [*Robinson*] Robinson, T. R., The role of natural E-region plasma turbulence in the enhanced absorption of HF radio waves in the auroral ionosphere: implications for RF heating of the auroral electrojet, *Ann. Geophys.*, *12*, 316, 1994.
- [*Robinson*] Robinson, T. R., The effects of small scale field aligned irregularities on E-region conductivities: implications for electron thermal processes, *Adv. Space Res.*, *22*, 1357, 1998.
- [*Robinson et al.*] Robinson, T. R., G. Bond, P. Eglitis, F. Honary, M. T. Rietveld, RF heating in a strong auroral electrojet, *Adv. Space Res.*, *21*, 689, 1998.
- [*Rose et al.*] Rose, G., K. Schlegel, K. Rinnert, H. Kohl, E. Nielsen, G. Dehmel, A. Friker, F. J. Lubken, H. Luhr, E. Neske, A. Steinweg, The ROSE project. scientific objectives and discussion of first results, *J. Atmos. Terr. Phys.*, *54*, 657, 1992.

- [*Rosenberg and Chow*] Rosenberg, M., V. W. Chow, Farley-Buneman instability in a dusty plasma, *Planetary and Space Sci.*, *46*, 103, 1998.
- [*Rosenbluth and Sudan*] Rosenbluth, M. N., R. N. Sudan, Almost two-dimensional strong turbulence in a magnetized plasma, *Phys. Fluids*, *29*, 2347, 1986.
- [*Ruohoniemi and Moorcroft*] Ruohoniemi, J. M., D. R. Moorcroft, Radar auroral echo heights as seen by a 398 MHz phased array radar operated at Homer Alaska, *Radio Sci.*, *20*, 719, 1985.
- [*Ruzhin et al.*] Ruzhin, Yu Ya., I. I. Shagimuratov, V. E. Kunitsyn, A. Kh., Dupueva, O. G. Razinkov, GPS-based tomographic reconstruction of the ionosphere, *Adv. in Space Res.*, *21*, 521, 1998.
- [*Sahr*] Sahr, J. D., Observation and theory of the radar aurora, Ph.D. thesis, Cornell Univ., Ithaca, NY, 1990.
- [*Sahr et al.*] Sahr, J. D., D. T. Farley, W. E. Swartz, and J. F. Providakes, On the origin of type 3 auroral irregularities: CUPRI vertical interferometer observations, *J. Geophys. Res.*, *96*, 17805, 1991.
- [*Sahr and Farley*] Sahr, J. D., and D. T. Farley, Three wave coupling in the auroral E region, *Ann. Geophys.*, *13*, 38, 1995.
- [*Sahr and Fejer*] Sahr, J. D., and B. G. Fejer, Auroral electrojet plasma irregularity theory and experiment: A critical review of present understanding and future directions, *J. Geophys. Res.*, *101*, 26893, 1996.
- [*Sahr and Lind*] Sahr, J. D., F. D. Lind, The Manastash Ridge Radar: A passive bistatic radar for upper atmospheric radio science, *Radio Sci.*, *32*, 2345, 1997.



- [*Saxena*] Saxena, Y. C., Laboratory experiments related to plasma instabilities in the electrojets, *Relation Between Laboratory and Space Plasmas. Proc. of the Inter. Workshop Reidel, Dordrecht, Netherlands*, 1981.
- [*Schunk and Nagy*] Schunk, R. W., A. F. Nagy, Ionospheres of the terrestrial planets, *Rev. Geophys. Space Res.*, 18, 813, 1980.
- [*Schlegel and St.-Maurice*] Schlegel, K., J. P. St.-Maurice, Anomalous heating of the polar E region by unstable plasma waves, 1, Observations, *J. Geophys. Res.*, 86, 1447, 1981.
- [*Schlegel and St.-Maurice*] Schlegel, K., J. P. St.-Maurice, Note on the parallel propagation effects of unstable Farley-Buneman waves at high latitudes, *Planetary and Space Sci.*, 30, 315, 1982.
- [*Schlegel and St.-Maurice*] Schlegel, K., J. P. St.-Maurice, Short wavelength gradient-drift waves at high latitudes, *Ann. Geophys.*, 3, 259, 1983.
- [*Schlegel*] Schlegel, K., Interpretation of auroral radar experiments using a kinetic theory of the two-stream instability, *Radio Sci.*, 18, 108, 1983.
- [*Schlegel et al.*] Schlegel, K., E. C. Thomas, D. Ridge, A statistical study of auroral radar spectra obtained with SABRE, *J. Geophys. Res.*, 91, 13483, 1986.
- [*Schlegel and Moorcroft*] Schlegel, K., D. R. Moorcroft, EISCAT as a tristatic auroral radar, *J. Geophys. Res.*, 94, 1430, 1989.
- [*Schlegel et al.*] Schlegel, K., T. Turunen, D. R. Moorcroft, Auroral radar measurements at 16-cm wavelength with high range and time resolution, *J. Geophys. Res.*, 95, 19001, 1990.

- [*Schlegel and Thiemann*] Schlegel, K., H. Thiemann, Particle-in-cell plasma simulations of the modified two-stream instability, *Ann. Geophys.*, *12*, 1091, 1994.
- [*Schmidt and Gary*] Schmidt, M. J., S. P. Gary, Density gradients and the Farley-Buneman instability, *78*, 8261, 1973.
- [*Self*] Self, S. A., Ion waves, drift waves, and instability in a weakly ionized magnetoplasma, *J. Plasma Phys.*, *4*, 693, 1970.
- [*Seyler and Providakes*] Seyler, C. E., J. F. Providakes, Particle and fluid simulations of resistive current driven electrostatic ion cyclotron waves, *Phys. Fluids*, *30*, 3113, 1987.
- [*Shalimov and Haldoupis*] Shalimov, S., and C. Haldoupis, An electron thermal diffusion instability and type-3 echoes in the auroral E-region plasma, *Ann. Geophysicae*, *13*, 45-55, 1995.
- [*Shand et al.*] Shand, B. A., M. Lester, T. K. Yeoman, The relationship between VHF radar auroral backscatter amplitude and Doppler velocity: a statistical study, *Ann. Geophys.*, *14*, 803, 1996.
- [*Siren et al.*] Siren, J. C., J. R. Doupnik, W. L. Ecklund, A comparison of auroral currents measured by the Chatanika radar with 50 MHz backscatter observed from Anchorage, *J. Geophys. Res.*, *82*, 3577, 1977.
- [*Skolnik*] Skolnik, M. (ed.), Radar Handbook, *McGraw Hill, New York*, 1990.
- [*Sofko et al.*] Sofko, G. J., J. A. Koehler, J. Gilmer, A. G. McNamara, D. R. McDiarmid, Radio aurora magnetic and streaming aspect sensitivities on 6 simultaneous links at 50 MHz, *Adv. Space Res.*, *2(7)*, 149, 1983.

- [*Stenflo*] Stenflo, L., Stimulated scattering by collisional modes in the ionosphere, *Radio Sci.*, *18*, 1379, 1983.
- [*St.-Maurice et al.*] St.-Maurice, J. P., K. Schlegel, P. M. Banks, Anomalous heating of the polar E region by unstable plasma waves. II. Theory, *J. Geophys. Res.*, *86*, 1453, 1981.
- [*St.-Maurice and Schlegel*] St.-Maurice, J. P., K. Schlegel, Estimates of plasma wave amplitudes in the turbulent high-latitude E region using electron temperature measurements, *J. Geophys. Res.*, *87*, 5197, 1982.
- [*St.-Maurice and Schlegel*] St.-Maurice, J. P., K. Schlegel, A theory of coherent radar spectra in the auroral E region, *J. Geophys. Res.*, *88*, 4087, 1983.
- [*St.-Maurice*] St.-Maurice, J. P., A nonlocal theory of the high-latitude Farley-Buneman instability, *J. Geophys. Res.*, *90*, 5211, 1985.
- [*St.-Maurice and Laher*] St.-Maurice, J. P., R. Laher, Are observed broadband plasma wave amplitudes large enough to explain the enhanced electron temperatures of the high latitude E region?, *J. Geophys. Res.*, *90*, 2843, 1985.
- [*St.-Maurice*] St.-Maurice, J. P., A unified theory of anomalous resistivity and Joule heating effects in the presence of ionospheric E Region irregularities, *J. Geophys. Res.*, *92*, 4533, 1987.
- [*St.-Maurice et al.*] St.-Maurice, J. P., J. C. Foster, J. M. Holt, C. del Pozo, First results on the observation of 440 MHz high-latitude coherent echoes from the E region with the Millstone Hill Radar, *J. Geophys. Res.*, *94*, 6771, 1989.
- [*St.-Maurice*] St.-Maurice, J. P., Wave induced diffusion in the turbulent E region,

in *Physics of Space Plasmas (1988)*, SPI Conf. Proc. Reprint Ser., vol. 8, 323, Scientific, Cambridge, Mass., 1990.

[*St.-Maurice et al.*] St.-Maurice, J.-P., P. Prikryl, D. Danskin, A. M. Hamza, G. J. Sofko, J. A. Koehler, A. Kustov, and J. Chen, On the origin of narrow non-ion-acoustic coherent radar spectra in the high latitude E-region, *J. Geophys. Res.*, *99*, 6447, 1994.

[*Stoker et al.*] Stoker, P. H., M. J. Mathews, M. W. J. Scourfield, Cosmic radio noise absorption related to structures in auroral luminosity, *J. Geophys. Res.*, *102*, 7439, 1997.

[*Stubbe*] Stubbe, P., Theory of electrostatic waves in an E region plasma, 1, General formulation, *J. Geophys. Res.*, *94*, 5303, 1989.

[*Sudan, et al.*] Sudan, R. N., J. Akinrimisi, D. T. Farley, Generation of small scale irregularities in the equatorial electrojet, *J. Geophys. Res.*, *78*, 240, 1973.

[*Sudan and Keskinen*] Theory of strongly turbulent two-dimensional convection of low pressure plasma, *Phys. Fluids*, *22*, 2305, 1979.

[*Sudan*] Sudan, R. N., Unified theory of type I and type II irregularities in the equatorial electrojet, *J. Geophys. Res.*, *88*, 4853, 1983.

[*Sudan*] Sudan, R. N., Nonlinear theory of type I irregularities in the equatorial electrojet, *Geophys. Res. Lett.*, *10*, 983, 1983.

[*Sulzer*] Sulzer, M. P., A radar technique for high range resolution incoherent scatter autocorrelation function measurements utilizing the full average power of klystron radars, *Radio Sci.*, *21*, 1033, 1986.

- [*Sverdlov*] Sverdlov, Yu. L., Space-time approach to the analysis of the Farley-Buneman instability. I. Evolution of plasma nonuniformities in crossed magnetic and electric fields, *Radiophys. and Quant. Elec.*, *31*, 573, 1988.
- [*Tanaka et al.*] Tanaka, T., T. Ogawa, H. Maeno, S. Yamamoto, Type 5 echoes observed by 50 MHz VHF Doppler radar at the auroral ionosphere, *Proc. Natl. Inst. Polar Res. Symp. Upper Atmos. Phys.*, *3*, 86, 1990.
- [*Tellegen*] Tellegen, B. D. H., Interaction between radio waves, *Nature*, *131*, 840, 1933.
- [*Timofeev and Miroshnikov*] Timofeev, E., Y. Miroshnikov, Altitude characteristics of radar aurora as seen by a 90 MHz double altitude radar system operated at Karmaselga Karelia, *J. Geophys Res.*, *51*, 44, 1982.
- [*Tsunoda et al.*] Tsunoda, R. T., R. I. Presnell, R. L. Leadabrand, Radar auroral echo characteristics as seen by a 398 MHz phased array radar operated at Homer, Alaska, *J. Geophys. Res.*, *79*, 4709, 1974.
- [*Tsunoda*] Tsunoda, R. T., Electric field measurements above a radar scattering volume producing 'diffuse' auroral echoes, *J. Geophys. Res.*, *80*, 4297, 1975.
- [*Tsunoda*] Tsunoda, R. T., Doppler velocity maps of the diffuse radar aurora, *J. Geophys. Res.*, *81*, 425, 1976.
- [*Tsunoda and Presnell*] Tsunoda, R. T., R. I. Presnell, On a threshold electric field associated with the 398-MHz diffuse radar aurora, *J. Geophys. Res.*, *81*, 88, 1976.
- [*Ungstrup*] Ungstrup, E., Electrostatic waves in the ionosphere, in *Exploration of*

*the Polar Upper Atmosphere*, edited by C. S. Deehr and J. A. Holtet, p. 395, D. Reidel, Norwell, Mass., 1973.

[*Unwin*] Unwin, R. S., The morphology of the VHF radio aurora at sunspot maximum, I, Diurnal and seasonal variations, *J. Atm. Terr. Phys.*, *28*, 1167, 1966.

[*Unwin*] Unwin, R. S., The morphology of VHF radio aurora at sunspot maximum, III, movement of echoes, *J. Atm. Terr. Phys.*, *29*, 1581, 1967.

[*Unwin*] Unwin, R. S., On the origin of the diffuse radio aurora, *Ann. de Geophysique*, *24*, 201, 1968.

[*Unwin and Baggaley*] Unwin, R. S., W. J. Baggaley, The radio aurora, *Ann. Geophys.*, *28*, 111, 1972.

[*Unwin and Keys*] Unwin, R. S., J. G. Keys, Characteristics of the radio aurora during the expansive phase of polar substorms, *J. Atm. Terr. Phys.*, *37*, 55, 1975.

[*Unwin and Johnston*] Unwin, R. S., P. V. Johnston, Height dependence in power spectrum of diffuse radar aurora, *J. Geophys. Res.*, *86*, 5733, 1981.

[*Uspensky*] Uspensky, M. V., On the altitudinal profile of auroral radar backscatter, *Radio Sci.*, *20*, 735, 1985.

[*Uspensky and Williams*] Uspensky, M. V., P. J. S. Williams, The amplitude of auroral backscatter, I, Model estimates of the dependence on electron density, *J. Atm. Terr. Phys.*, *50*, 73, 1988.

[*Uspensky et al.*] Uspensky, M. V., A. V. Kustov, P. J. S. Williams, The amplitude of auroral backscatter-III. Effect of tilted ionospheric layer, *J. Atm. Terr. Phys.*, *55*, 1383, 1993.

- [*Villain et al.*] Villain, J. P., R. A. Greenwald, K. B. Baker, J. M. Rouhoniemi, HF radar observations of E region plasma irregularities produced by oblique electron streaming, *J. Geophys. Res.*, *92*, 12327, 1987.
- [*Villain et al.*] Villain, J. P., C. Hanuise, R. A. Greenwald, K. B. Baker, J. M. Rouhoniemi, Obliquely propagating ion acoustic waves in the auroral E region: Further evidence of irregularity production by field aligned electron streaming, *J. Geophys. Res.*, *95*, 7833, 1990.
- [*Volosevich and Gel'berg*] Volosevich, A. V., M. G. Gel'berg, Nonlinear interaction of electrostatic waves in the E region of the ionosphere, *Radiophys. and Quant. Elect.*, *31*, 399, 1988.
- [*Volsoevich and Galperin*] Volosevich, A. V., Yu. I. Galperin, Nonlinear wave structures in collisional plasma of auroral E-region ionosphere, *Ann. Geophys.*, *15*, 890, 1997.
- [*Waldock et al.*] Waldock, J. A. T. B. Jones, E. Nielsen, Statistics of 1-m wavelength plasma irregularities and convection in the auroral E region, *Radio Sci.*, *20*, 709, 1985.
- [*Wang and Tsunoda*] Wang, T. N. C., R. T. Tsunoda, On a crossed field two-stream plasma instability in the auroral plasma, *J. Geophys. Res.*, *80*, 2172, 1975.
- [*Watermann et al.*] Watermann, J., D. R. McDiarmid, A. G. McNamara, J. A. Koehler, and G. J. Sofko, Are type III radio aurorae directly excited by electrostatic ion cyclotron waves?, *J. Geophys. Res.*, *94*, 13479, 1989.
- [*Watermann et al.*] Watermann, J., D. R. McDiarmid, J. A. Koehler, G. J. Sofko, A. G. McNamara, Magnetic aspect angle dependence of spectra from coherent radio aurora backscatter, *J. Geophys. Res.*, *94*, 3663, 1989.

- [*Watermann*] Watermann, J., Refraction of 50-MHz radar waves in a realistic ionospheric model, *Radio Sci.*, *25*, 805, 1990.
- [*Watermann*] Watermann, J., A decade of type-3 radio auroral studies: Towards and away from the EIC interpretation, *J. Geomagn. Geoelec.*, *46*, 285-296, 1994.
- [*Watt et al.*] Watt, T. M., L. L. Newkirk, E. G. Shelley, Joint radar satellite determination of the effective recombination coefficient in the auroral E region, *J. Geophys. Res.*, *79*, 4725, 1974.
- [*Whitehead*] Whitehead, J. D., The future of coherent radars in the study of E-region irregularities, *Ann. Geophys.*, *10*, 278, 1992.
- [*Williams et al.*] Williams, P. J. S., B. Jones, G. O. L. Jones, The measured relationship between electric field strength and electron temperature in the auroral E region, *J. Atm. Terr. Phys.*, *54*, 741, 1992.
- [*Zarnitskiy*] Zarnitskiy, Yu. F., A contribution to the theory of Doppler spectra of auroral scattering, *Geomag. Aeron.*, *27*, 689, 1987.



## Appendix A

### DERIVATION OF A 3-FLUID MODEL FOR AURORAL E-REGION IRREGULARITIES

The derivation of the three fluid model for the irregularities is difficult primarily due to its algebraic complexity. This complexity can be managed by appropriately organizing the derivation. To do this I adopt the approach of *Oppenheim* [1995] who solved a system of fluid electrons and kinetic ions for the equatorial electrojet. His approach results in a density response function for each species that can be combined using Gauss' law to obtain the dispersion relation for the irregularities. It is straightforward to generalize this method to multiple ion species and I do so below using a purely fluid approach.

I begin the problem using the linear fluid theory for both the ions and electrons and my assumptions are most appropriate for the auroral E-region ionosphere. The resulting fifth order dispersion relation can be evaluated either by analytic approximations or by numerical evaluation. I adopt the numerical approach because this allows the use of a model ionosphere that illuminates the system's response to realistic parameters. The results of this evaluation are presented in chapter 5.

#### **A.1 Assumptions**

Many assumptions are necessary in order to simplify the system of equations sufficiently for a solution. The most fundamental assumption is that magnetic perturbations are negligible and that the system is purely electrostatic. The ions are taken to be demagnetized and the electrons magnetized. Electron momentum is neglected

as the electron mass is much less than the ion mass. Pressure is taken to follow an ideal gas law, and non-linear effects ignored.

Several assumptions are useful approximations to E-region conditions that simplify the solution without masking the fundamental underlying physics. The ions are taken to be sufficiently coupled to the neutral background gas by collisions so that thermal equilibrium is maintained between different ion species. Production, recombination, and attachment are assumed to be balanced and their effects are neglected on the time scale of irregularity formation and decay. Neutral background winds, ion drifts, and velocity shear effects are taken as not important for the basic system.

Finally I will evaluate the system in one dimension for meter scale irregularities. I will also neglect plasma density gradients even though they are often important for irregularity growth and damping. Their primary impact is to enhance wave growth when their direction is parallel to the ambient electric field and inhibit it when their direction is opposite.

## ***A.2 Initial Equations***

I begin the derivation using the fluid equations for a magnetized plasma. The continuity relation for a species  $\alpha$  is

$$\frac{\partial n_\alpha}{\partial t} + \nabla \cdot (n_\alpha \mathbf{V}_\alpha) = 0 \quad (\text{A.1})$$

where production, recombination, and attachment are neglected as being unimportant on the time scale of the growth and decay of the irregularities. I also use a momentum relation assuming an ideal gas law  $P = \gamma n T_\alpha$ . Neglecting the convective portion of the total derivative and taking the density to be independent of the time variation, the momentum relation is given by

$$n_\alpha \frac{\partial V_\alpha}{\partial t} = \frac{qn_\alpha}{m_\alpha} (\mathbf{E} + \mathbf{V}_\alpha \times \mathbf{B}) - \nu_\alpha n_\alpha \mathbf{V}_\alpha - \frac{\gamma T_\alpha}{m_\alpha} \nabla n_\alpha \quad (\text{A.2})$$

where I include the Lorentz force, collisions, and the pressure force. For the three fluid model the system of equations consists of three species: electrons ( $\alpha = e$ ), ion one ( $\alpha = i1$ ), and ion two ( $\alpha = i2$ ).

Because the ion gyro-collision ratio is low a good assumption in the E-region is that the ion species are demagnetized. I also take the ion neutral collision frequency and the ion temperatures to be identical between ion species due to their strong collisional coupling to the neutral background gas. For the two ion species the momentum relation is identical, and is given by

$$n_i \frac{\partial V_i}{\partial t} = \frac{en_i}{m_i} \mathbf{E} - \nu_i n_i \mathbf{V}_i - \frac{\gamma T_i}{m_i} \nabla n_i \quad (\text{A.3})$$

where the  $\alpha = i$  can represent either  $\alpha = i1$  or  $\alpha = i2$  as is necessary.

I also be assume that the electrons carry no momentum because of the large ion-electron mass ratio. This results in an electron momentum equation where only the force terms remain.

$$\frac{-en_e}{m_e} (\mathbf{E} + \mathbf{V}_e \times \mathbf{B}) - \nu_e n_e \mathbf{V}_e - \frac{\gamma T_e}{m_e} \nabla n_e = 0 \quad (\text{A.4})$$

Now taking these equations and using a perturbation approach it is not difficult to find a dispersion relation for the irregularities.

### A.3 Perturbed Equations

Assuming small amplitude wave like solutions of the form  $e^{i\mathbf{k}\cdot\mathbf{r}-\omega t}$ , and taking the Fourier transform of the continuity and momentum equations such that  $\frac{\partial}{\partial t} \Rightarrow -i\omega$  and  $\nabla \Rightarrow i\mathbf{k}$ . I perform a perturbation expansion where  $\mathbf{E} \rightarrow \mathbf{E}_0 + \mathbf{E}_1$ ,  $n_\alpha \rightarrow n_{\alpha 0} + n_{\alpha 1}$ , and  $\mathbf{V}_\alpha \rightarrow \mathbf{V}_{\alpha 0} + \mathbf{V}_{\alpha 1}$ .

First order terms in the perturbation expansion are retained, while higher order terms are neglected. Zero order terms are also neglected so long as they are not directly relevant to the production of the irregularities.

#### A.3.1 Continuity Relations

Because under these approximations the continuity relation has the same form for all species, it is only necessary to perturb it once and then obtain a solution for each species through a change of variables.

$$-i\omega(n_{\alpha 0} + n_{\alpha 1}) + i\mathbf{k} \cdot [(n_{\alpha 0} + n_{\alpha 1})(\mathbf{V}_{\alpha 0} + \mathbf{V}_{\alpha 1})] = 0 \quad (\text{A.5})$$

Then keeping only first order terms it follows that

$$-i\omega n_{\alpha 1} + i\mathbf{k} \cdot (n_{\alpha 1}\mathbf{V}_{\alpha 0} + n_{\alpha 0}\mathbf{V}_{\alpha 1}) = 0 \quad (\text{A.6})$$

which by manipulation yields the perturbed frequency domain continuity relation.

$$i\mathbf{k} \cdot \mathbf{V}_{\alpha 1} = (i\omega - i\mathbf{k} \cdot \mathbf{v}_{\alpha 0}) \frac{n_{\alpha 1}}{n_{\alpha 0}} \quad (\text{A.7})$$

By changing variables the three fluid system results in the following perturbed con-

tinuity relations.

$$i\mathbf{k} \cdot \mathbf{V}_{e1} = (i\omega - i\mathbf{k} \cdot \mathbf{v}_{e0}) \frac{n_{e1}}{n_{e0}} \quad (\text{A.8})$$

$$i\mathbf{k} \cdot \mathbf{V}_{i11} = (i\omega - i\mathbf{k} \cdot \mathbf{v}_{i10}) \frac{n_{i11}}{n_{i10}} \quad (\text{A.9})$$

$$i\mathbf{k} \cdot \mathbf{V}_{i21} = (i\omega - i\mathbf{k} \cdot \mathbf{v}_{i20}) \frac{n_{i21}}{n_{i20}} \quad (\text{A.10})$$

### A.3.2 Ion Momentum Equations

By taking the same approach for the ion momentum equation it is possible to again only Fourier transform, perturb, and manipulate one equation and then obtain solutions for each ion species by changing variables.

$$\begin{aligned} -i\omega(\mathbf{V}_{i0} + \mathbf{V}_{i1})(n_{i0} + n_{i1}) - \frac{\Omega_i}{B}(\mathbf{E}_0 + \mathbf{E}_1)(n_{i0} + n_{i1}) \\ + \nu_i(n_{i0} + n_{i1})(\mathbf{V}_{i0} + \mathbf{V}_{i1}) + i\mathbf{k} \frac{\gamma T_i}{m_i}(n_{i0} + n_{i1}) = 0 \end{aligned} \quad (\text{A.11})$$

Neglecting the zeroth order ion drift and electric field I then retain only first order terms in the equation.

$$-i\omega n_{i0} \mathbf{V}_{i1} - \Omega_i n_{i0} \frac{\mathbf{E}_1}{B} + \nu_i n_{i0} \mathbf{V}_{i1} + i\mathbf{k} \frac{\gamma T_i}{m_i} n_{i1} = 0 \quad (\text{A.12})$$

Taking  $\mathbf{k} \cdot$  all terms results in

$$(i\omega - \nu_i)n_{i0}\mathbf{k} \cdot \mathbf{V}_{i1} + \Omega_i n_{i0} \frac{\mathbf{k} \cdot \mathbf{E}_1}{B} - ik^2 \frac{\gamma T_i}{m_i} n_{i1} = 0 \quad (\text{A.13})$$

which is a useful form for making substitution of the continuity relations. Next I solve for  $n_{i1}$  prior to making any substitutions.

$$n_{i1} = \frac{(i\omega - \nu_i)n_{i0}\mathbf{k} \cdot \mathbf{V}_{i1} + \Omega_i n_{i0} \frac{\mathbf{k} \cdot \mathbf{E}_1}{B}}{ik^2 \frac{\gamma T_i}{m_i}} \quad (\text{A.14})$$

Multiplying by  $\frac{i}{i}$  and substituting the perturbed ion continuity relationship results in

$$n_{i1} = \frac{(i\omega - \nu_i)n_{i0}(i\omega - i\mathbf{k} \cdot \mathbf{V}_{i0})\frac{n_{i1}}{n_{i0}} + \Omega_i n_{i0} i \frac{\mathbf{k} \cdot \mathbf{E}_1}{B}}{-k^2 \frac{\gamma T_i}{m_i}} \quad (\text{A.15})$$

Now using the approximation that the ion drift  $\mathbf{V}_{i0} = 0$  and solving for  $n_{i1}$  gives the ion density response function to the perturbation. At this point I also make a substitution of the ion thermal velocity  $V_{ti}^2 = \frac{\gamma T_i}{m_i}$ .

$$n_{i1} = \frac{\Omega_i n_{i0} \frac{i\mathbf{k} \cdot \mathbf{E}_1}{B}}{i\nu_i \omega - k^2 V_{ti}^2 + \omega^2} \quad (\text{A.16})$$

Specializing the response function to each of the two ion species, it is also useful to multiply by  $\frac{e}{\epsilon_0}$  and convert to the plasma frequency of each ion species in the numerator.

$$\frac{e}{\epsilon_0} n_{i11} = \frac{\omega_{pi1}^2 i\mathbf{k} \cdot \mathbf{E}_1}{\omega^2 + i\nu_i\omega - k^2 V_{ti1}^2} \quad (\text{A.17})$$

$$\frac{e}{\epsilon_0} n_{i21} = \frac{\omega_{pi2}^2 i\mathbf{k} \cdot \mathbf{E}_1}{\omega^2 + i\nu_i\omega - k^2 V_{ti2}^2} \quad (\text{A.18})$$

From this we can see immediately that the density response of the two ion species to the perturbation is only different due to differences in their plasma frequencies and thermal velocities. For identical ion temperatures this reduces to a dependence on the masses of the ion species.

### A.3.3 Electron Momentum Equations

Next I treat the electron momentum equation in a similar manner. This equation is the most complicated because it involves the magnetic field. First I define the gyro-collision ratio  $\kappa_e = \frac{\Omega_e}{\nu_e}$  and use this to define the gyro-collision tensor after the approach of *Sahr* [1990].

$$\overset{\leftrightarrow}{\kappa}_e \equiv \begin{pmatrix} 1 & -\kappa_e & 0 \\ \kappa_e & 1 & 0 \\ 0 & 0 & 1 \end{pmatrix} \quad (\text{A.19})$$

with inverse

$$\overset{\leftrightarrow}{\kappa}_e^{-1} \equiv \frac{1}{1 + \kappa_e^2} \begin{pmatrix} 1 & \kappa_e & 0 \\ \kappa_e & 1 & 0 \\ 0 & 0 & 1 + \kappa_e^2 \end{pmatrix} \quad (\text{A.20})$$

The purpose of the gyro-collision tensor is to express the cross product of the electron velocity with the magnetic field in a compact manner. Here I assume that the field is given by  $\mathbf{B} = -B\hat{z}$ . Using this definition the unperturbed electron momentum equation becomes

$$n_e \overset{\leftrightarrow}{\kappa}_e \cdot \mathbf{V}_e + n_e \kappa_e \frac{\mathbf{E}}{B} - \nu_e n_e \mathbf{V}_e - \frac{T_e}{m_e} \nabla n_e = 0 \quad (\text{A.21})$$

which is just the expression of the momentum equation in terms of the gyro-collision tensor. Perturbing this equation and taking linear wave like solutions results in

$$\begin{aligned} (n_{e0} + n_{e1}) \overset{\leftrightarrow}{\kappa}_e \cdot (\mathbf{V}_{e0} + \mathbf{V}_{e1}) + (n_{e0} + n_{e1}) \kappa_e (\mathbf{E}_0 + \mathbf{E}_1) \\ - \nu_e (n_{e0} + n_{e1}) (\mathbf{V}_{e0} + \mathbf{V}_{e1}) - \frac{T_e}{m_e} i\mathbf{k} (n_{e0} + n_{e1}) = 0 \end{aligned} \quad (\text{A.22})$$

and after retaining only first order terms this yields

$$\begin{aligned} n_{e0} \overset{\leftrightarrow}{\kappa}_e \cdot \mathbf{V}_{e1} + n_{e1} \overset{\leftrightarrow}{\kappa}_e \cdot \mathbf{V}_{e0} + \kappa_e (n_{e0} \frac{\mathbf{E}_1}{B} + n_{e1} \frac{\mathbf{E}_0}{B}) \\ - \nu_e (n_{e0} \mathbf{V}_{e1} + n_{e1} \mathbf{V}_{e0}) - i\mathbf{k} n_{e1} \frac{T_e}{m_e} = 0 \end{aligned} \quad (\text{A.23})$$

Now multiply through by  $\overset{\leftrightarrow}{\kappa}_e^{-1}$



$$\begin{aligned}
& \mathbf{V}_{e1}n_{e0} + \mathbf{V}_{e0}n_{e1} + \frac{\kappa_e}{B}(n_{e0} \overset{\leftrightarrow}{\kappa}_e^{-1} \cdot \mathbf{E}_1 + n_{e1} \overset{\leftrightarrow}{\kappa}_e^{-1} \cdot \mathbf{E}_0) \\
& + \nu_e(n_{e0} \overset{\leftrightarrow}{\kappa}_e^{-1} \cdot \mathbf{V}_{e1} + n_{e1} \overset{\leftrightarrow}{\kappa}_e^{-1} \cdot \mathbf{V}_{e0}) + i \overset{\leftrightarrow}{\kappa}_e^{-1} \cdot \mathbf{k} \frac{\gamma T_e}{m_e} n_{e1} = 0
\end{aligned} \tag{A.24}$$

At this point it is necessary to simplify the system of equations in order to find an analytically tractable solution. The easiest approach is to take a 1-D solution where  $k \rightarrow k\hat{y}$ ,  $\mathbf{E}_0 \rightarrow E_{0x}\hat{x}$ ,  $\mathbf{E}_1 \rightarrow E_{1y}\hat{y}$ ,  $\mathbf{V}_{e0} \rightarrow V_{e0y}\hat{y}$ , and  $\mathbf{V}_{e1} \rightarrow V_{e1y}\hat{y}$ .

It is possible to solve for a 2-D solution in the plane perpendicular to  $\mathbf{B}$ . While this does allow analysis of the dispersion relation as a function of flow angle it makes the derivation of the electron density response function significantly more complicated.

Turning to the 1-D system and evaluating the inverse gyro-collision tensor products we multiply all terms by  $i\mathbf{k} \cdot$  to obtain an expanded relation.

$$\begin{aligned}
& ik_y V_{e1y} n_{e0} + ik_y n_{e1} V_{e0y} + \frac{\kappa_e}{B(1 + \kappa_e^2)} (n_{e0} ik_y E_{1y} + n_{e1} \kappa_e ik_y E_{0x}) \\
& + \frac{\nu_e}{1 + \kappa_e^2} (n_{e0} ik_y V_{e1y} + n_{e1} ik_y V_{e0y}) + \frac{k_y^2}{1 + \kappa_e^2} \frac{\gamma T_e}{m_e} n_{e1} = 0
\end{aligned} \tag{A.25}$$

Now simplifying the perturbed electron continuity relationship to 1-D results in

$$ik_y V_{e1y} = (i\omega - ik_y V_{e0y}) \frac{n_{e1}}{n_{e0}} \tag{A.26}$$

Substituting this into A.25 and solving for  $n_{e1}$  gives the electron density perturbation response function after a great deal of algebra.

$$n_{e1} = \frac{n_{e0} i k_y \kappa_e \mathbf{E}_{y1}}{-i \nu_e \kappa_e^2 (\omega - k_y \frac{E_{x0}}{B}) + k^2 V_{te}^2} \quad (\text{A.27})$$

This can be rewritten in terms of the electron plasma frequency by multiplying by  $\frac{e}{\epsilon_0}$ . It is also useful substitute the drift velocity  $V_d = \frac{E_{0x}}{B}$ .

$$\frac{e}{\epsilon_0} n_{e1} = \frac{\omega_{pe}^2 i k_y E_{1y}}{-i \nu_e \kappa_e^2 (\omega - k_y V_d) + k^2 V_{te}^2} \quad (\text{A.28})$$

#### A.4 The Three Fluid Dispersion Relation

Now in order to derive the dispersion relation it is necessary to close the system of equations. The normal method is to use quasi-neutrality but following *Oppenheim* [1995] I use Gauss' law

$$\nabla \cdot \mathbf{E} = \frac{e}{\epsilon_0} (n_{i1} + n_{i2} - n_e) \quad (\text{A.29})$$

This approach has the virtue of neatly combining the response of each ion species with that of the electrons. Now, Fourier transforming A.29, perturbing, and taking the 1-D approximation yields our closure relation.

$$i k_y E_{1y} = \frac{e}{\epsilon_0} (n_{i1} + n_{i2} - n_e) \quad (\text{A.30})$$

Substituting the ion and electron response functions gives the dispersion relation directly.

$$1 - \frac{\omega_{pi1}^2}{-k_y^2 V_{ti1}^2 + \omega^2 + i\nu_i \omega} - \frac{\omega_{pi2}^2}{-k_y^2 V_{ti2}^2 + \omega^2 + i\nu_i \omega} + \frac{\omega_{pe}^2}{-i\nu_e \kappa_e^2 (\omega - k_y V_d) + k_y^2 V_{te}^2} = 0 \quad (\text{A.31})$$

The dispersion relation can be reorganized into a fifth order polynomial purely through algebraic manipulation. I recommend using a symbolic mathematics program to avoid mistakes. While the result is not organized in a particularly appealing manner it is useful for numeric root finding.

$$a\omega^5 + b\omega^4 + c\omega^3 + d\omega^2 + e\omega + f = 0 \quad (\text{A.32})$$

$$a = -i\nu_e \kappa_e^2 \quad (\text{A.33})$$

$$b = 2\nu_i \nu_e \kappa_e^2 + \omega_{pe}^2 + i\nu_e \kappa_e^2 k V_d + k^2 V_{te}^2 \quad (\text{A.34})$$

$$c = (2\nu_i k^2 V_{te}^2 + 2\omega_{pe}^2 i\nu_i + ik^2 V_{ti1}^2 \nu_e \kappa_e^2 + ik^2 V_{ti2}^2 \nu_e \kappa_e^2 + i\omega_{pi2}^2 \nu_e \kappa_e^2 - 2\nu_i \nu_e \kappa_e^2 k V_d + i\omega_{pi1}^2 \nu_e \kappa_e^2 + i\nu_i^2 \nu_e \kappa_e^2) \quad (\text{A.35})$$

$$\begin{aligned}
d = & -ik^3 V_{ti2}^2 \nu_e \kappa_e^2 V_d - \omega_{pi2}^2 k^2 V_{te}^2 - ik^3 V_{ti1}^2 \nu_e \kappa_e^2 V_d - i\omega_{pi1}^2 \nu_e \kappa_e^2 k V_d \\
& - \omega_{pe}^2 k^2 V_{ti2}^2 - \nu_i k^2 V_{ti2}^2 \nu_e \kappa_e^2 + i\omega_{pi2}^2 i\nu_i \nu_e \kappa_e^2 - \omega_{pi1}^2 k^2 V_{te}^2 \\
& - i\omega_{pi2}^2 \nu_e \kappa_e^2 k V_d - k^4 V_{ti1}^2 V_{te}^2 - k^4 V_{ti2}^2 V_{te}^2 + ik^2 V_{ti1}^2 i\nu_i \nu_e \kappa_e^2 \\
& - \omega_{pe}^2 k^2 V_{ti1}^2 + i\omega_{pi1}^2 i\nu_i \nu_e \kappa_e^2 + \omega_{pe}^2 i^2 \nu_i^2 + i^2 \nu_i^2 k^2 V_{te}^2 \\
& - i\nu_i^2 \nu_e \kappa_e^2 k V_d
\end{aligned} \tag{A.36}$$

$$\begin{aligned}
e = & -ik^4 V_{ti1}^2 V_{ti2}^2 \nu_e \kappa_e^2 - i\omega_{pi2}^2 k^2 V_{ti1}^2 \nu_e \kappa_e^2 + k^3 V_{ti1}^2 \nu_i \nu_e \kappa_e^2 V_d - i\omega_{pi1}^2 k^2 V_{ti2}^2 \nu_e \kappa_e^2 \\
& + \omega_{pi2}^2 \nu_i \nu_e \kappa_e^2 k V_d + \omega_{pi1}^2 \nu_i \nu_e \kappa_e^2 k V_d - \omega_{pe}^2 i\nu_i k^2 V_{ti2}^2 - \omega_{pi1}^2 i\nu_i k^2 V_{te}^2 \\
& - \omega_{pe}^2 k^2 V_{ti1}^2 i\nu_i + \nu_i k^3 V_{ti2}^2 \nu_e \kappa_e^2 V_d - i\nu_i k^4 V_{ti2}^2 V_{te}^2 - \omega_{pi2}^2 i\nu_i k^2 V_{te}^2 \\
& - k^4 V_{ti1}^2 i\nu_i V_{te}^2
\end{aligned} \tag{A.37}$$

$$\begin{aligned}
f = & \omega_{pi1}^2 k^4 V_{ti2}^2 V_{te}^2 + k^6 V_{ti1}^2 V_{ti2}^2 V_{te}^2 + ik^5 V_{ti1}^2 V_{ti2}^2 \nu_e \kappa_e^2 V_d + \omega_{pe}^2 k^4 V_{ti1}^2 V_{ti2}^2 \\
& + i\omega_{pi1}^2 k^3 V_{ti2}^2 \nu_e \kappa_e^2 V_d + \omega_{pi2}^2 k^4 V_{ti1}^2 V_{te}^2 + i\omega_{pi2}^2 k^3 V_{ti1}^2 \nu_e \kappa_e^2 V_d
\end{aligned} \tag{A.38}$$

By solving for the real and imaginary parts of A.32 it is possible to determine wave frequency and growth rate for conditions given by the free parameters. The evaluation of this model and its results are discussed in Chapter 5.

## Appendix B

### THE MANASTASH RIDGE RADAR DESIGN

The Manastash Ridge Radar is a distributed radar system where two relatively simple receivers are located 150 km apart and synchronized using the Global Positioning System. The radar is a system of components whose operation is coordinated through software and computer networks. Information on the design of the radar system is primarily useful for individuals or groups interested in constructing similar radars.

#### *B.1 Antenna Design*

The radar system utilizes two types of antennas, one in a strong signal environment at the UW for receiving the FM broadcast signal, and the other in a weak signal environment such as at the Manastash Ridge Observatory. The UW antenna is a standard half wave dipole FM radio antenna. This antenna is more than sufficient for transmitter signal interception in a strong signal environment where directivity is not required. At MRO where signals are relatively weak it is desirable to have an antenna with more directive gain.

The observations presented here were made using a log periodic antenna (LPA) with about 6 dB of gain at 100 MHz. The antenna pattern is shown in Figure B.1 in both azimuth and elevation.

The LPA antenna is extraordinarily modest by the standards of other coherent scatter radars. This is not completely unprecedented as many early irregularity observations were made with relatively simple Yagi antennas. A Yagi antenna tuned

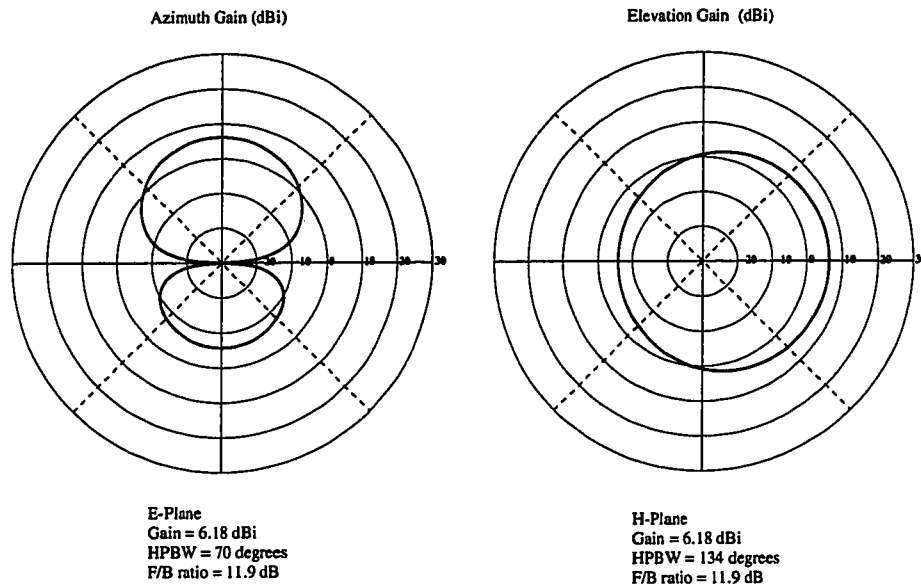


Figure B.1: The antenna pattern for the log periodic antenna used by the Manastash Ridge Radar.

to 99.9 MHz with 14 dB of gain has recently been deployed on an antenna tower to replace the LPA for future observations.

## B.2 Receiver Design

The basic purpose of any radio receiver system is to detect and convert the information carried by electromagnetic waves to a more useful form. In the case of many applications the information conveyed by the waves is converted to audio and then conveyed to the ear. In the case of modern radar systems the most useful form for the data is as a series of digital samples. In an ideal sense these samples, usually a voltage versus time, should be linearly related in form to the electromagnetic wave that was incident upon the system's antenna. In practice there are deviations from this ideal due to noise in the system, limitations of design, and imperfections in the physical devices. A good reference for RF design is *Hagen* [1996].

The receiver design of the radar is in unique only in its precise synchronization

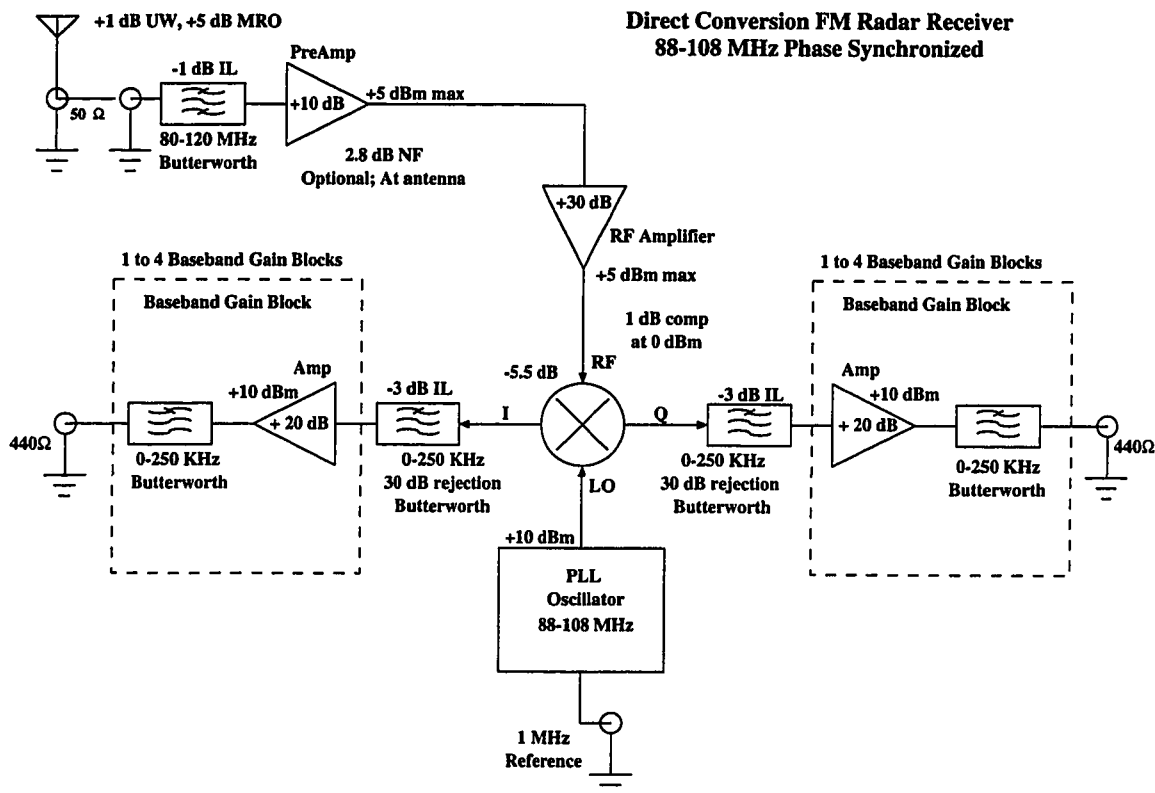


Figure B.2: The radar receiver design.

to other receivers in the system. This phase coherence is one of the fundamental properties of a multi-static radar system intended for high resolution range and doppler observations.

The receiver signal chain is shown in Figure B.2 and is a simple direct conversion quadrature receiver. In such a system an appropriate bandwidth of the RF signal is amplified and then shifted in frequency to the baseband in a single mixing step. As part of this step the phase of the signal is preserved in a complex representation of the received voltage using an IQ demodulator. The simplicity of this design, involving only a single heterodyne stage, is useful for the ease with which it allows synchronization to the GPS reference signal. Only a single local oscillator needs to be synchronized, instead of several as would be required in the dual conversion design that is typical of most FM radio receivers.

### ***B.3 Data Acquisition and Transport***

Analog to digital conversion of voltages at the baseband outputs of the receiver is currently done using a Datel PCI-416J digitizer. This 12 bit digitizer is hosted on a normal PC running the Linux operating system and uses a custom device driver. The digitizer is capable of sampling at 250 kHz on 8 channels and allows an external sampling clock and trigger.

The external clock and trigger are critical because the data acquisition must also be synchronized between the receivers in the system. The data acquisition is made synchronous by driving the sampling clock with a digital reference divided down from a 1 MHz GPS synchronized oscillator and using a 1 PPS GPS output as a trigger. Synchronization of digital data acquisition will become more important as passive radar systems progress to the use of IF or RF sampling.

In a multistatic radar system data must be transported to a central location for processing. This data transport is facilitated in the Manastash Ridge Radar by the use of the Internet at both the reference and remote sites. The reference receiver is connected at the UW using a 10 Mbps ethernet connection. The remote receiver utilizes a 500 Kbps TCP/IP microwave bridge to Central Washington University. The use of the Internet allows remote control and monitoring of the radar and also prevents frequent trips to the remote receiver site.

### ***B.4 Signal Processing***

The signal processing of the radar data is relatively simple despite the large computational burden. The initial processing is applied separately to the reference  $x(t)$  and remote  $y(t)$  signal as is shown in Figure B.3. A block of received data has its mean removed using an AR(1) model with a user selected correlation time. The orthogonality of the I and Q channels is then corrected for the same model. The covariance of the channels is estimated over the model correlation time and this is



### Received Signal Correction

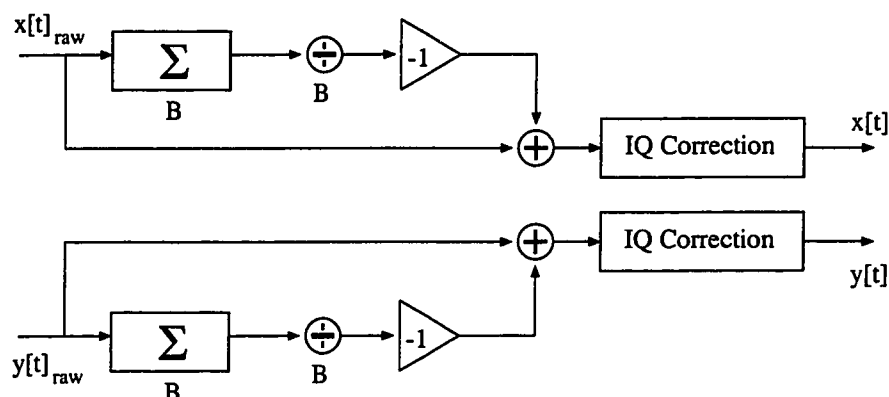


Figure B.3: Blocks of raw data from the receivers are corrected by removing the mean and ensuring that the I and Q channels are orthogonal.

### Ambiguity Computation for a Single Range

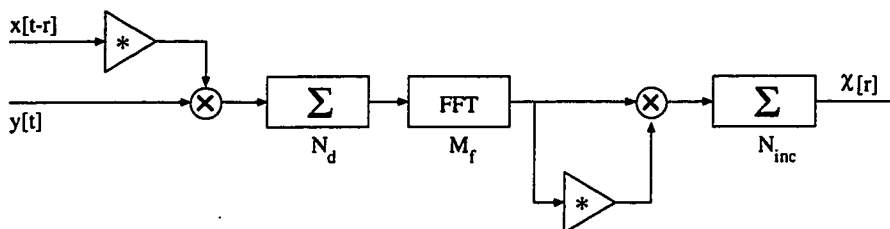


Figure B.4: Each range of data is processed by forming the received sequence for a given range offset, decimating to a desired signal bandwidth, evaluating the correlation using the Fast Fourier Transform, and finally incoherently integrating.

used to compute a correction that makes I and Q orthogonal.

After the received data has been corrected it must be processed to form the cross ambiguity function. Figure B.4 shows this process for a single range of data.

The reference and remote signals are combined and  $N_d$  samples are coherently averaged (decimated) to produce the detected signal  $YX(t)$ . This signal is Fourier transformed over a window length  $M_f$  and the power spectrum is computed. The spectra from successive FFTs are combined for a given range by incoherent averaging to reduce the variance of the estimate. The result of this process is the cross

ambiguity function for a given range  $\chi[r]$ . Typically the radar repeats this process for about 2000 ranges in order to examine a typical view volume.

### ***B.5 Computational Systems***

A significant portion of the Manastash Ridge Radar system consists of the computational systems that perform data acquisition, data transport, signal processing, and data presentation. At the present time a large cost associated with the radar is that of the computers used to acquire and manage data. It is likely that this will remain the case in future passive radar systems because it is very easy to increase the capability of these radars if more computational power is available.

The data acquisition is currently done using a single computer at each receiver site. The data is stored directly to disk in a raw data format that facilitates streaming data from the receiver without interruption. The amount of computational power necessary at the receivers depends strongly on the the sophistication of the passive radar design. With sufficient computational power receiver correction, data compression, and even software receivers become possible.

After data has been acquired and transported to the University of Washington a Linux based cluster computer is used to process the data. This system runs the Linux operating system, uses a dedicated fast ethernet switch, and currently has nine CPUs available for data processing and presentation. The system is not powerful enough to process data in real time and current software limitations allow processing at only about 1/60th real time.

Because of the limited bandwidth from the remote receiver site uncompressed data can currently be delivered at 1/20th real time at best. By rewriting portions of the data processing software it should be possible to process uncompress data in 1/15th real time with the current cluster configuration. To progress beyond this data compression, a faster data link, or a reduction in receiver bandwidth will be

Table B.1: Useful software tools

Program	Purpose
ACE + TAO	C++ distributed object programming library
Apache	web server
CVS	source code version control system
CVS web	web based CVS repository browsing
Xilinx Foundation	FPGA Programming
Generic Mapping Tools	data plotting
GCC	C++ complier
Image Magick	graphics conversion and formatting
Linux	operating system for all radar components
Matlab	data analysis and plotting
MPEG Encode	mpeg movie production
NetCDF	standard network data format
Perl	scripting language
Protel	Schematic capture, PCB layout, Mixed Simulation
SSH	secure shell protocol
Tgif	vector graphics and layout program
XNTP	network time synchronization

necessary.

Approximately half of the total processing time is occupied by the production of graphical output from the radar data. It should be possible to optimize this process significantly, but future passive radar designs should take account of this overhead in the design of their computational systems. It is also very useful to provide additional computational power for post-processing analysis of the radar data.

## ***B.6 Software Systems***

During the development of the radar it became rapidly apparent that an extensive set of software tools was necessary to automate the system. Table B.1 gives a list of these tools and their primary use in the radar system. Almost all of the tools are freely available with source code. The only exceptions to this are electronic design tools for PCB layout, simulation, and FPGA programming. There are currently no

good open source alternatives for these applications.

The Manastash Ridge Radar is controlled by approximately 25,000 lines of software written in C, C++, and Perl. This software consists of low level device drivers, routines for transporting, reading and writing data, signal processing code, utilities for automatically creating images and animations from the radar data, and control scripts to run the whole system.

The effort involved in developing the software was comparable to that of designing and building the radar hardware. Figure B.5 shows the organization of software components in the radar system. The software operates the radar by communicating over the Internet using TCP/IP and a custom protocol. In future incarnations of the software a distributed object system such as CORBA will be used.

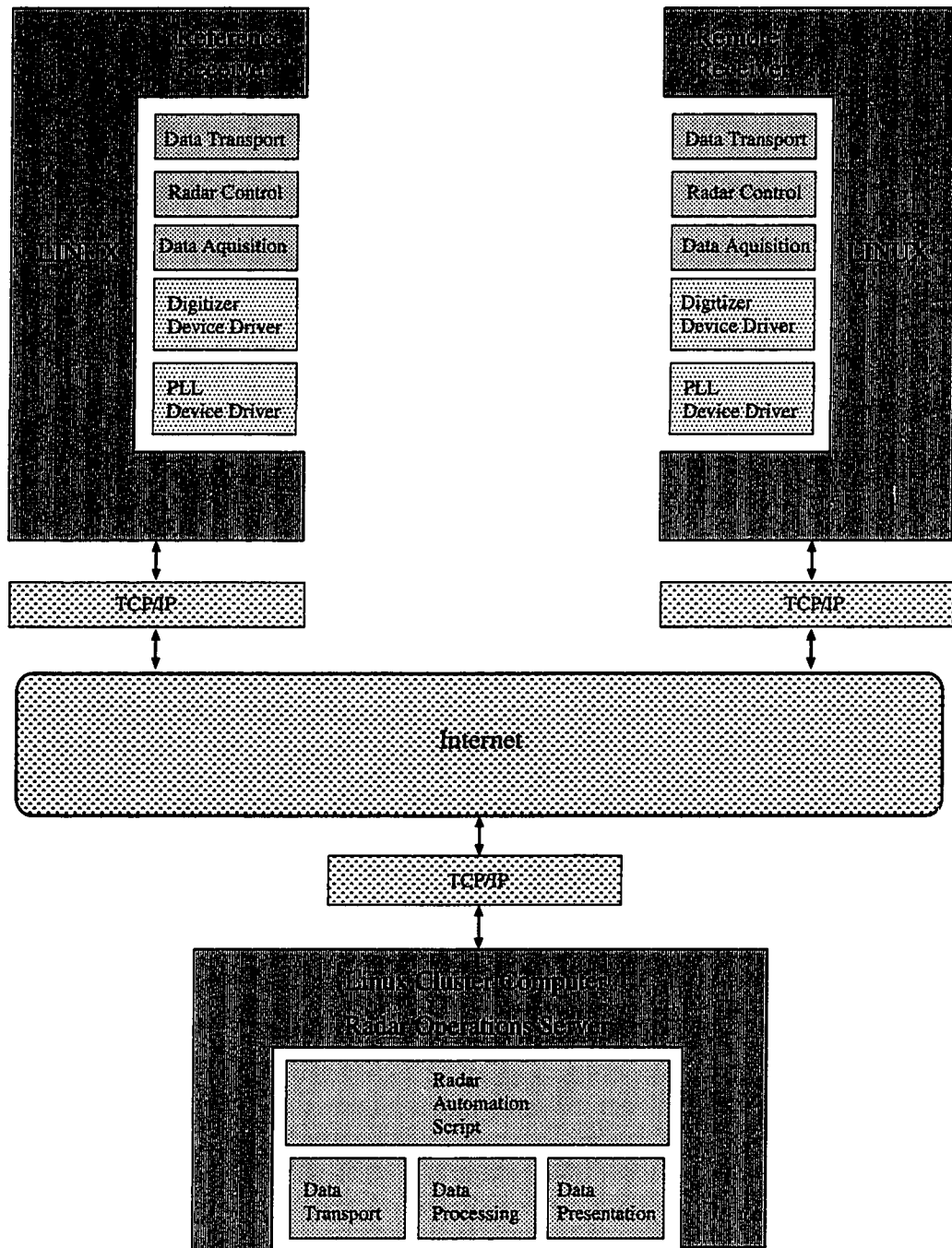


Figure B.5: The software for the Manastash Ridge Radar is divided between the receiver control computers and the radar operations server. Data processing and output is done on a cluster computer under the control of Perl scripts. The network time protocol and external web servers are not shown.

## VITA

Frank David Lind was born near Portland, Oregon in 1971. After attending high school in Seattle Washington, he studied at the University of Washington where he received a Bachelor of Science in Physics (with honors) and a Bachelor of Science in Computer Science in 1994. He subsequently joined the Geophysics Program and pursued studies leading to the Doctor of Philosophy in Geophysics in 1999.